Carbon-based neural interfaces to probe retinal and cortical circuits with functional ultrasound imaging in vivo

Julie Meng Zhang

THÈSE DE DOCTORAT EN NEUROSCIENCES

Sorbonne Université – Faculté de Médecine

École doctorale Cerveau – Cognition – Comportement (ED 158)

CARBON-BASED NEURAL INTERFACES TO PROBE RETINAL AND CORTICAL CIRCUITS WITH FUNCTIONAL ULTRASOUND IMAGING *IN VIVO*

Présentée par Julie Meng Zhang

Dirigée par Serge Picaud

Institut de la Vision

Équipe « Transmission de l'information visuelle : codage et restauration visuelle »

Soutenue le 04.12.2023 à Paris (12e) devant un jury composé de :

Valérie Crépel	Rapportrice
Stéphanie Lacour	Rapportrice
Diego Ghezzi	Examinateur
Pierre Pouget	Examinateur - Président du jury
Blaise Yvert	Examinateur
Serge Picaud	Directeur de thèse

Résumé en français

Les **interfaces cerveau-machine (ICMs)** peuvent **stimuler** électriquement les neurones par injection de courant et/ou **enregistrer** leurs signaux. Porteur d'espoirs chez les patients atteints de maladies neurologiques ou de handicaps, les dispositifs actuels sont composés de larges électrodes métalliques susceptibles de provoquer une inflammation des tissus conduisant à des fibroses, ce qui réduit in fine l'efficacité. Les recherches récentes se portent sur les électrodes à base de **matériaux carbonés,** attractifs de par leurs propriétés mécaniques, électriques et électrochimiques.
Pouvons-nous utiliser ces matériaux pour stimuler et/ou enregistrer efficacement les signaux neuronaux ? En collaboration avec trois équipes européennes, cette thèse explore les fonctionnalités de trois ICM différents. Deux de mes trois projets font appel à **l'imagerie fonctionnelle par ultrasons** (fUS) pour vérifier l'activation neuronale en profondeur dans le cerveau. Cette technique repose sur la mesure du volume sanguin cérébral (CBV), corrélé à l'activité neuronale du fait de l'existence du couplage neurovasculaire (NVC).

Dans le cadre du projet NEURODIAM (projet 1) financé par l'Union européenne (EU Horizon 2020), j'ai travaillé sur la preuve de concept d'un **implant d'électrocorticographie (ECoG) tout-diamant**, combinant à la fois les propriétés isolantes du diamant intrinsèque en tant que couche de passivation et la forte conductivité du diamant dopé au bore. Après la caractérisation *in vitro* des électrodes, j'ai enregistré des potentiels évoqués visuels (PEVs) à l'aide de tels implants chez deux modèles rongeurs. L'observation de faibles impédances (dizaines de kΩ), d'une large fenêtre de potentiel électrochimique (3 V), ainsi que le rapport signal/bruit raisonnable obtenu confirment leur fonctionnalité.

Dans le cadre du projet Graphene Flagship financé par l'UE (projet 2), j'ai utilisé des **transistors à effet de champ à grille de graphene (gFETs)** et le fUS simultanément pour enregistrer sur rongeurs des ondes lentes de dépolarisations corticales (CSDs) et des crises épileptiques chez un modèle d'épilepsie induite. Pendant les CSDs, les variations biphasiques de CBV se propagent vers des régions sous-corticales telles que l'hippocampe, en plus des régions corticales habituellement observées. Nous mesurons également une forte synchronisation de phase entre les oscillations ultralentes et le CBV pendant les crises, mais aussi une oscillation anticipée du CBV en amont d'une crise épileptique. Cette plateforme multimodale permettrait l'investigation poussée du NVC dans diverses pathologies.

L'oxyde de graphène réduit (rGO) présente une capacité élevée d'injection de charge électrique adaptée aux prothèses rétiniennes pour les patients aveugles (projet 3). Notre étude de biocompatibilité a mis en évidence aucune différence de nombre de microglies entre les rétines implantées avec du rGO et les rétines témoins, suggérant une réaction non inflammatoire. La stimulation électrique sous-rétinienne *in vivo* de l'implant active également les structures visuelles, observées grâce au fUS. Nos résultats confirment l'aptitude du rGO à stimuler les neurones rétiniens mais suggèrent également l'enregistrement de signaux dans l'optique d'une prothèse bimodale.

En résumé, j'ai travaillé sur trois projets différents impliquant différentes électrodes en carbone pour la stimulation ou l'enregistrement neuronal *in vivo*. J'ai d'abord établi la preuve de concept d'un ECoG tout-diamant, potentiellement plus durable de par la non-réactivité du diamant. J'ai ensuite enregistré et analysé les CSDs et les crises épileptiques à l'aide des gFETs et du fUS simultanément. Enfin, j'ai confirmé *in vivo* la biocompatibilité à long terme et la fonctionnalité des électrodes sous-rétiniennes en rGO pour la restauration visuelle. Tous ces résultats renforcent la légitimité des électrodes carbonées pour une translation clinique future.

Abstract

Brain-computer interfaces (BCIs) based on electrode arrays can either **stimulate/write** information to neurons through electrical current injection, **record/read** from neurons. Such BCIs have created great hopes in patients with neurological diseases or handicaps but current interfaces display large metallic electrodes facing tissue inflammation leading to gliotic and fibrotic reactions, which in the end limits the device efficacy. In contrast, **carbon-based electrodes** gained interest because of their combined mechanical, electrical and electrochemical properties.

My project focuses on this question: can we use carbon-based electrodes for reading and/or writing efficiently information to neurons? In collaboration with 3 research teams across Europe, this doctoral work explores three different BCIs for different neural applications, with the help of **functional ultrasound imaging** (fUS) to monitor activity in cortical and subcortical regions. This brain imaging technique relies on the measure of cerebral blood volume (CBV) which correlates with neural activity through neurovascular coupling.

In the scope of NEURODIAM (project 1), a European Union (EU) Horizon 2020 funded project, I worked on the proof-of-concept of **a full-diamond electrocorticography array** (ECoG), combining the insulating properties of intrinsic diamond as passivation layer and the high conductivity of boron-doped diamond for neural interfacing. Upon *in vitro* characterization of the electrodes, I recorded visual evoked potentials (VEPs) using such implants during light flashes on anesthetized rats and mice. We report impedances in the range of the tens of kΩ and an electrochemical potential window of 3 V for electrodes of 200, 400 or 600 µm of diameter. Observation of the classical shape of VEPs and the reasonable signal-to-noise ratio give us confidence in the functionality of such electrodes.

In the scope of the EU-funded Graphene Flagship Core 3 (project 2), I used simultaneously **graphene-solution-gated field-effect transistors (gFETs)** and **fUS** to record cortical spreading depolarizations (CSDs) and seizures in acute models of epileptic rats. During CSDs, the biphasic variation of CBV spreads to subcortical areas such as hippocampus, in addition to cortical regions. We also observe a tight phase coupling during seizures between infra-slow brain signals and CBV but also oscillations of CBV prior to seizures onset. This new technological platform can help to investigate how both fast and infraslow brain signals contribute to NVC in neurological diseases.

In its **reduced graphene oxide (rGO)** form, graphene has a high charge injection capacity and stability, hence a potential application to retinal prostheses for visually impaired patients (project 3). Our biocompatibility study highlighted no difference in microglia number between controls and rGO-implanted retinas, suggesting a non-inflammatory reaction. *In vivo* subretinal electrical stimulation of the implant with 10 ms pulses activated the visual structures, observed thanks to fUS. Spatial extent of the activation in the superior colliculus was dependent on the electrode size only at high current amplitudes. Our results suggest that rGO is a reliable material for neural stimulation but can also be applied for neural recording in bimodal prosthetics.

In summary, I worked on three different projects involving different carbon-based interfaces for either reading or writing neural activity *in vivo*. I first established the proof-of-concept of a full-diamond ECoG for neural recording. I then focused on the multimodal recording and analysis CSDs and seizures using gFETs and fUS. Finally, I confirmed the *in vivo* long-term biocompatibility and functionality of rGO electrodes for subretinal prostheses. All together, these results provide great confidence in carbon-based technology for translation in clinical applications and for the elaboration of future-generation BCIs.

This doctoral work has been funded by the enTRAIN Vision innovative training network (ITN), as part of the European Union's Horizon 2020 research and innovation programme under the Marie Skłodowska-Curie grant agreement N° 861423.

Keywords: brain-computer interfaces, carbon-based electrodes, graphene, diamond, electrocorticography, subretinal implant, functional ultrasound imaging, rodents

Acknowledgments

Il y a trois ans et demi, je finissais mon Master européen de Food Technology et j'empochais dans la foulée mon diplôme d'ingénieur ESPCI, me laissant toujours plus indécise sur mon avenir et pas moins imposteur dans l'âme. Il y a trois ans, je démarrais une nouvelle aventure neuroscientifique à l'Institut de la Vision dans l'équipe S8 encore dirigée par Serge Picaud sous l'égide de Marie Sklodowska-Curie, aux côtés également de 14 autres Early Stage Researchers (code name : enTRAIN Vision) éparpillés en Europe et dont les premières retrouvailles post-Covid à Paris ont scellé le début d'une complicité facile. Il y a deux ans je me formais en électrochimie et électrophysiologie in vivo aux côtés d'Eleonora à l'EPFL tout en m'intégrant à la vie de labo suisse. Il y a un an et demi je m'envolais pour Ventura aux US (avion, 3,1 t de CO_2) pour assister à ma première conférence qui restera finalement la plus marquante, la Neuroelectronic interfaces Gordon Research Conference. Se sont ensuite ensuivis divers déplacements internationaux et retrouvailles, telles que les summer school enTRAIN Vision à Helsinki (Finlande, juin 2022) (avion, 0,7 t de CO_2) ou Elche (Espagne, mars 2023) (train+bus, 6,2 kg de CO_2), les trainings enTRAIN Vision à Prague (mai 2022, avion, 0,4 t de CO_2) ou à Vienne (Juin 2023, avion + train, 0,2 t de CO_2), les Graphene Flagship meetings à Venise (Italie, avril 2022, train+avion, 0,2 t de CO_2) ou à Rome (avril 2023, train, 40 kg de CO2). J'ai aussi eu l'opportunité de présenter mes travaux à maintes reprises lors de la conférence fUSBrain à Cargèse en Corse (mai 2022, avion, 0,4 t de CO_2), à la SFN à San Diego aux US (novembre 2022, avion, 3,3 t de CO_2) à la JNSS à Sendai au Japon (août 2023, avion, 3,2 t de CO_2) et enfin à l'ERM à Tübingen en Allemagne (septembre 2023, train, 6,0 kg de CO_2).

Ma thèse, c'est donc ça, trois projets dont deux en collaboration européenne sur trois ans, une quarantaine de rats imagés, des nouvelles rencontres et des amitiés qui restent, 5 conférences internationales au prix de 14 tonnes de CO_2 émises rien qu'en transport, un peu moins d'un To de données à ré-organiser, divers résultats technologiques à publier, synthétisés en un manuscrit que j'espère concis après deux mois et demi de rédaction inégalement répartis.

Alors merci **Serge** pour m'avoir assuré ta confiance du jour 1 jusqu'aujourd'hui et j'espère demain, merci pour ta bonté, ton optimisme et ta disponibilité malgré ton calendrier de ~~ministre~~ directeur, merci pour m'avoir offert l'opportunité de me former en neurosciences, en électrophysiologie tout en voyageant aux quatre coins de la Terre. J'y ai rencontré non sans admiration les « personnalités influentes » du monde des neuroprothèses. Thank you, **Rob, Anton, Edu** for introducing me to the epilepsy world and guiding my chaotic self throughout the gFET/fUS project no matter the time of the day/night, I really enjoyed working with you and I do hope the collaboration will last. Thank you, **Jose, Taygun** for the thorough discussion on implants, for your attentiveness and cheerful welcome at ICN2. Merci **Lionel**, **Gaëlle** et **Claudia** pour la concrétisation du beau projet Neurodiam. Thank you **Ele** for being my chaperone in the Campus Biotech ecosystem and thank you **Diego** for the secondment opportunity which taught me a lot. A l'IDV, merci **Diep** pour une passation aux petits oignons ; merci **Julie D**. et **Ruben** sans qui cette thèse n'aurait juste pas eu lieu ; merci **Vi** pour ton travail de stage minutieux et passionné, merci **Jean-Charles** pour les formations fUS précieusement prises en notes. Mes plus sincères mercis à mes collègues (**Grégory, Fabrice, Corentin, Antouine, Amine, Louiza, Ignacio, Erwan**) pour vos réguliers inputs qui frappent juste. Tout particulièrement merci **Matthieu** pour nos fous rires nerveux impromptus et complètement absurdes ; merci **Florian** pour ton soutien moral indispensable et ton oreille attentive, merci **Audrey** pour supporter mes blagues nulles et nous gâter en petits gâteaux « pas trop sucrés ». Thank you to those who proof-read my thesis and brought their critical insight, thank you to those who offered a warm shelter for the suburban-me, in Paris but also abroad. Merci ***les Meilleurs***, merci les amis ***Dinner***, merci **les copains ESPCI**, merci ***les filles*** pour avoir rythmé ma vie parisienne entre deux déplacements et dix mille questionnements ; merci **ma famille** pour votre protection inconditionnelle. Thank you **dear ESRs** (**Samuele, Sandrine, Dharm, Andreea, Cristina, Krishna, Fabrizio, Dorota, David, Luca, Jasnoor, Marlene** and **Alireza**), thank you dear project managers **Aurélie**, **Sarah**, for making neuroscience and vision such a fun game without frontiers.

C'est avec la gorge nouée que je clos le bal de soutenances des copains ESPCI (amorcé par Chloé en Mars 2022 et Lola en Oct. 2022) et avec fierté que j'ouvre la voie pour les présentations finales de mes camarades enTRAIN Vision.

Table of contents

Abbreviations

4-AP	4-Amino Pyridine
AC	Alternative current
Au	Gold
BCI	Brain-Computer Interface
BDD	Boron-Doped Diamond
C*	intrinsic Carbon
CBV	Cerebral Blood Volume
CE	Counter Electrode
CIC	Charge Injection Capacity
CNM	Institute of Microelectronics of Barcelona
CNS	Central Nervous System
CSC	Charge Storage Capacity
CSD	Cortical Spreading Depolarisation
CV	Cyclic Voltammetry
CVD	Chemical Vapour Deposition/Deposited
DBS	Deep Brain Stimulation
DC	Direct current
E	Young Modulus
ECoG	Electrocorticography
EDL	Electrochemical Double-Layer
EEG	Electroencephalography
ESIEE	École supérieure d'ingénieurs en électrotechnique et électronique
FBR	Foreign Body Reaction
FDA	Food and Drug Administration (US)
fMRI	functional Magnetic Resonance Imaging
fUS	functional UltraSound imaging
GFAP	Glial Fibrillary Acid Protein
gFET	graphene-based Field Effect Transistor
GLM	Global Linear Model
GO	Graphene Oxide
Hip	Hippocampus
HRF	Haemodynamic Response Function
Iba-1	Ionized calcium Binding Adaptor molecule 1
ICN2	Catalan Institute of Nanoscience and Nanotechnologies
IDV	Institut de la Vision
IrOx	Iridium Oxide
ISO	Infraslow Oscillations
KCl	Potassium Chloride
LFP	Local Field Potential
LGN	Lateral Geniculate Nucleus
MEA	Multi-Electrode Array
MO	Molecular Orbitals
N-UNCD	Nitrogen-doped-Ultra-Nano-Crystallin Diamond
NO	Nitric Oxide
NVC	Neurovascular Coupling

ON	Optic Nerve
PBS	Phosphate Buffer Saline
PDMS	Polydimethylsiloxane
PEDOT	Poly(3,4-ethylenedioxythiophene)
PI	Polyimide
PSS	Poly(styrene sulfonate)
Pt	Platinum
RE	Reference Electrode
RGC	Retinal Ganglion Cell
rGO	reduced Graphene Oxide
RPE	Retinal Pigment Epithelium
S1	Somatosensory Cortex (primary)
SCc, SCi	Superior Colliculus contralateral, ipsilateral (to stimulated eye)
SEM	Scanning Electron Microscope
SMC	Smooth Muscle Cells
SNR	Signal-to-Noise Ratio
SVD	Singular Value Decomposition
TiN	Titanium Nitride
V1	Visual Cortex (primary)
WE	Working Electrode
Z	Impedance
Φ	Phase (electrochemical)

I. Introduction

Concomitant with the debut of electrophysiology in the 19th century, **electronic neural interfaces** were first developed to decipher brain signals and circuitry. As the name entails, they sit at the interface between neurons and electronic circuitry controlled by us. Eventually, these interfaces have evolved during the 20th century to stimulate neuronal circuits. As a consequence, a **brain-computer interface** (**BCI**) is a *"system that records central nervous system (CNS) activity and translates it into artificial output that replaces, restores, enhances, supplements, or improves natural CNS outputs [...]"* (Wolpaw et al., 2020). Compared to neural interfaces, modern BCIs are evolving towards a bi-directional dimension not necessarily found in initial neural interfaces.

The wording "electronic neural interfaces" is often substituted by the concept of "implant". Strictly speaking, an **implant** is a generic term designating an object which is inserted in the body during a surgery, to improve appearance or treat a medical condition (Cambridge University Press, n.d.). Neural implants are by definition in contact with neural tissues, and the wording implies interaction between the device and neurons. Therefore, it is common to interchange the 3 concepts in the context of neural rehabilitation. The field of n**europrosthetics**, at the crossroads of engineering and neuroscience, emerged with progress in both microfabrication and material science, and with better understanding of the nervous system. Neural prostheses were first envisioned to restore lost sensory or motor functions: they are generally composed of a BCI component with external power supply.

Depending on the final application, neural implants have 3 main working mode: they can either **stimulate/write** information to neurons through electrical current injection, **record/read** from neurons they are interfaced with or **sense** neurotransmitters. We will cover in this thesis only the first two functions, which have been exploited in medicine as palliative treatments for neurological diseases with sensory/motor malfunctions or clinical diagnosis tools. Indeed, the **READ** mode is already widely used to monitor brain activities as in epilepsy to localize the epileptic focus prior to brain tissue resection. The **WRITE** mode is applied in deep brain stimulation (DBS) as for the Parkinson disease or in prostheses to stimulate a deficient sensory organ as in deaf or blind patients. For example, cochlear implants are one of the most advanced brain-computer interfaces (BCI) developed, technologically speaking. Recently, intracortical Utah arrays were even used in a bimodal function: the cortical activity was monitored in order to optimize in the future the write mode to enter visual information at the level of the visual cortex in a closed-loop fashion (X. Chen et al., 2020, p. 202).

Such BCIs have created great hopes in patients with neurological diseases or handicaps. However, current interfaces display large metallic electrodes facing tissue reactions leading to gliotic and fibrotic reactions (X. Chen et al., 2023), which in the end limits long-term efficacy of the devices and their life time. The possibility to fabricate **carbon-based** electrodes generates great interest because the carbon atom is one of the main constituents of cells suggesting that such materials could be more biocompatible, hence less reactive. Moreover, their semi-conductive properties could reduce the size of electrodes and thus the device flexibility to match that of the brain.

This doctoral thesis focuses on the exploration of carbon-based (graphene and diamond) BCIs to different neurological diseases in a preclinical setting in both the READ and the WRITE mode. The READ mode was assessed both on the visual cortex by recording physiological brain state during light stimulation experiments and pathophysiological phenomena in an acute model of epilepsy. The WRITE mode was investigated in the retina in the context of vision restoration.

Therefore, the first chapter (§I.A) aims at describing the physical, chemical and electrochemical requirements for BCIs in both modes. We also give a state-of-the-art of past and present materials in use with a particular emphasis on blindness and epilepsy. We then set the background for both diseases. For **vision restoration** and visual prostheses (§I.B), we define leading causes of blindness before describing past and current visual prosthesis under development and electrical stimulation strategies. For **epilepsy research** (§I.C), we present the epidemiology, the aetiology, the current electrophysiology tools for diagnosis or treatment, and the physio-pathological mechanisms at play to stress the urgent need to tackle the too many unknowns in epilepsy-related diseases.

I.A. Implant design

Second generation electronic neural interfaces, also called multichannel neural interfaces (M. Zhang et al., 2020) are traditionally composed of 3 main parts: the **electrodes** which conduct currents, linked to the **conductor pads** (transferring information into the digital world) through **conductive tracks**. All except the active areas of electrodes are coated in an insulating material also referred as **coating** which is in contact with the neural tissue. Sometimes, adhesive aids films are added between metal and coating to improve overall layers adhesion and reliability.

The optimal recording/stimulation electrode design should ensure maximum efficiency within biological safety limits and without degradation of the electrode material. The different electrochemical phenomena occurring at the interface have to be studied with adequate instruments to meet the electrical requirements, described in §I.A.1. We will then emphasize the importance of biocompatibility validation in §I.A.2 and the mechanisms at play during foreign body reaction, before providing an overview on classically used metal electrodes (§I.A.3).

However, current and future trends for recording and stimulation probes involve novel biocompatible materials in many different configurations, from mesh grids to stretchable implants, possibly in closed-loop fashion. The recent development of carbon-based materials (§I.A.4) and soft polymers (§I.A.5) already open a new door for the neuroprosthetics field, where much is left to explore. Here, we illustrate this electrode roadmap with applications in visual prostheses or electrocorticography (ECoGs) research.

I.A.1. Electrical requirements

Neural implants are in contact with neural tissue. In recording mode (Fig. 1, blue circle), the electrical current of cellular origin is transduced into electrons in the electrode and is amplified before its analysis. As the surrounding noise is equally amplified using passive electrodes, a **high signal-to-noise ratio (SNR)** is desirable for good fidelity recordings. If the impedance of the electrode/electrolyte interface is too high or if the electrode capacitance is too high, the depolarised neurons cannot convey the voltage change up to the electrode. In stimulation mode (Fig. 1, orange circle), electrical current controlled by the neurostimulator is injected from the electrode to the neural tissue and returns to the ground which is either distant (monopolar stimulation) or to a nearby electrode (bipolar stimulation, used in this work). The ability to inject enough charge into the tissue so that the cells can depolarize and trigger an action potential is sought. To ensure this, **charge injection capacity (CIC)** and **charge storage capacity (CSC)** are often calculated. For both modes, **Electrochemical Impedance Spectroscopy (EIS)** and **Cyclic Voltammetry (CV)** measurements are essential for the understanding of mechanisms occurring at the electrode/electrolyte interface.

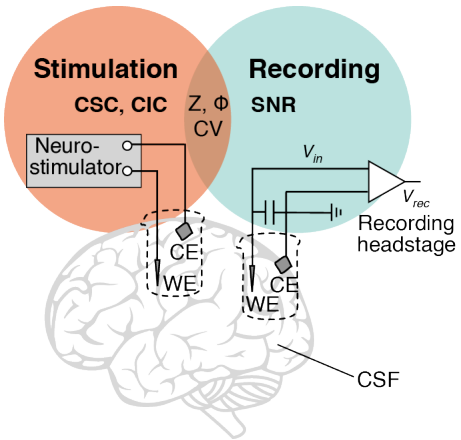

Fig. 1 Electrical requirements for stimulation and recording electrodes. Modified from (Boehler et al., 2020). CSC = Charge storage capacity, CIC = Charge injection capacity, Z = impedance, φ = phase, CV = cyclic voltammetry, SNR = signal-to-noise ratio, CE = counter electrode, WE = working electrode, CSF = cerebrospinal fluid.

The electrodes have first to be conductive in order to be able to record neural activity or stimulate neurons. This is why we start the section with a brief description of band theory and molecular orbitals (§I.A.1.a), in order to understand the origins of electrochemical properties in the different conductive materials at play. Then, we describe the interface between electrode and electrolyte (§I.A.1.b) and detail the principles behind the key electrochemical characteristics at stake (§I.A.1.c-e).

a. Band theory and conduction

In fundamental physics concepts, atomic orbitals Φ(n,l,m) are wave functions solutions of Schrodinger's equation characterised by different quantic numbers n, l, m, ms. They describe the density probability of electrons, with discrete energy levels $E_{n,l}$, Φ(n,0,0) functions correspond to sharp atomic spectrum and are noted "s". Φ(n,1,m) functions are noted "p" for principal atomic spectrum and Φ(n,2,m) are "d" for diffuse atomic spectrum. The abbreviation ms stands for the magnetic spin number. In the ground state, the electrons are distributed in the orbitals in the most stable electronic configuration for them (corresponding to the lowest electronic energy). Electrons in non-complete levels or with the highest n number are called valence electrons and compose the outer shell. Valence electrons can form bonds with neighbouring atoms, creating **molecular orbitals** (MO).

In solids, electrical and optical properties are governed by the strong chemical bonds between the atoms. The strong bonds can be covalent (originating from the sharing of electrons between atoms), metallic or ionic (of electrostatic origins).

An example is given hereafter for metals with valence electrons in the s atomic orbitals. Atomic orbitals with the same symmetry relative to the molecule symmetry plan can combine together into new symmetric and anti-symmetric molecular orbitals. N s-type atomic orbitals combine to form N σ- and N σ*-type molecular orbitals with $N=n.N_A$, n being the number of moles and N_A the Avogadro number. The energy levels of σ and σ* orbitals are very close because of the weak coverage between s-type orbitals. This forms a s-type band of energy with N energy states very close to each other, as a continuous band (Fig. 2.A). When an electric field is applied to the material, the electrons can move from one band to the next higher energy level if it is not completely filled already. As conduction and valence band overlap in metals, a very low field amplitude can displace the electrons, hence the high conductivity of metals at room temperature. The metallic bonds are actually covalent delocalised bonds.

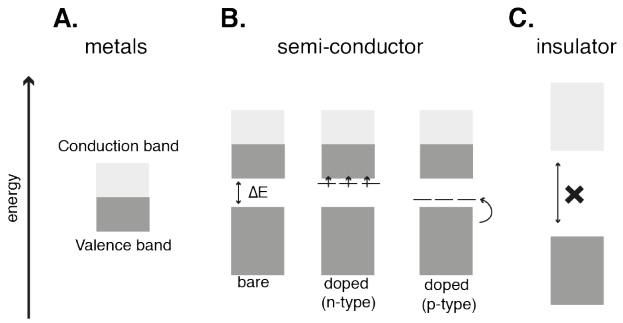

Fig. 2 Band theory for **A.** metals **B.** Semi-conductors **C.** insulators.

In semi-conductors, the valence and conduction bands are separated by an energy gap ΔE (Fig. 2.B). Their conductivity is weaker than metals but increases with increased temperature or doping with impurities. Silicon (Si, Z=14) is a semiconductor with an energy gap of 1.09 eV between its valence and conduction band. Its valence electrons have an electronic configuration written $3s^2 3p^2$. Some atoms of the solid crystal can be replaced by atoms with neighbouring electronic configurations (1 for 105 to 106 Si atoms or ~1 ppm) to add an extrinsic conductivity to the material. When atoms with higher valence electrons are introduced (phosphorus (P, Z=15) in the case of Si) and if the excess electrons they "donate" are closer to the conduction band of the semiconductor, those electrons can move effortlessly in the conduction band at normal temperatures. The main charge carriers responsible for conduction are the electrons. As they are Negative, the semiconductor is of N-type. Inversely, when trivalent atoms with lower valence electrons are introduced (aluminium (Al, Z=13), boron (B, Z=5)), they have to "accept"

one electron from the 4 valence electrons of Si, leaving there a positive hole whose energy are close to the top of the valence band. As if the conduction band was lowered, electrons can move easily to the newly created energy levels at normal temperatures. The main charge carriers being the Positive holes, the semiconductor is of P-type.

In insulators, the gap is too high to be bridged when an electrical field is applied. The electrons cannot move from the valence to the conduction band (Fig. 2.C): the material is non-conductive.

b. Description of the interface and transfer mechanisms

When a conductive electrode is immersed in a biofluid environment/electrolyte, an interface is created between them. Two main charge transfer mechanisms can occur there: a non-Faradaic or **capacitive** charge transfer and a **Faradaic** one. When there is no current flowing through the electrode, the potential in the bulk electrolyte remains constant while when current flows, a potential gradient is created.

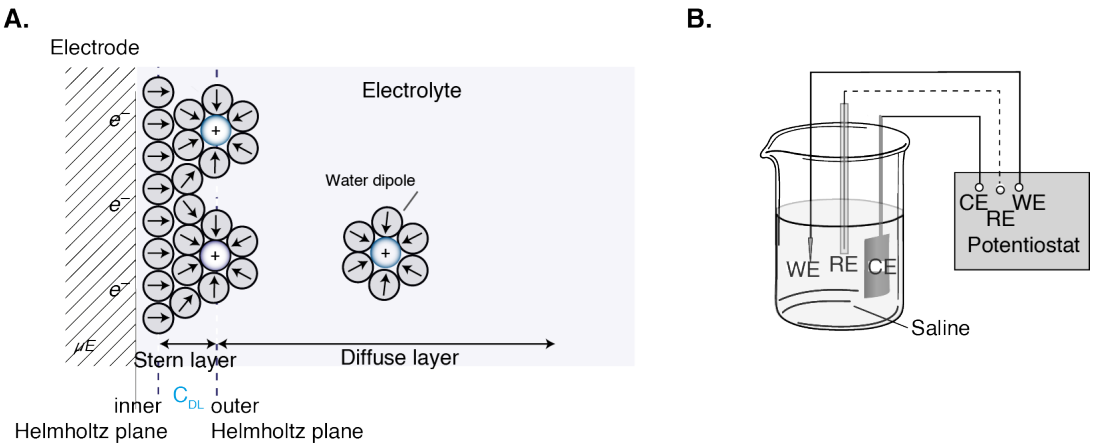

Fig. 3 Interface between electrode and electrolyte. **A**. Schematic description and *in vitro* measurement of the interface. **B**. Measurement of the interface between electrode and electrolyte. WE=working electrode, CE=counter electrode, RE=reference electrode. Modified from (Boehler et al., 2020).

The sole contact between the electrode and the biofluid creates a rearrangement of charge carriers at the interface. The accumulation of counter ions in the electrolyte at the interface to counter balance the planar build-up of electrons in the electrode at the interface is called the electrical double layer (EDL) (Merrill et al., 2005). In the Stern model, this EDL is characterised by several layers. In the Stern layer (Fig. 3.A), the charges on respective side define two Helmholtz planes and create a capacitor-like structure, characterised by the **double-layer capacitance** C_{DL} (C_{DL} ~10 to 40 μF/cm², (Faulkner & Bard, 2001)), also called the Helmholtz capacitance.

At the electrode/electrolyte interface, electrons (in metals) or positive holes (in semiconductors) from the electronic device can also be transduced into ions of the electrolyte. Transfer of electrons across the interface result in oxydo-reduction relations in the electrolyte which amount is proportional to the amount of current passed (Faraday's law) when electrode potentials are thermodynamically or kinetically favourable to such reactions. This is called the Faradaic charge transfer. Faradaic reactions can be reversible or irreversible.

When small amount of charge is injected, it is possible that no electron transfers from the electrode to the ionic solution. This capacitive or non-Faradaic charge transfer mechanism originate mainly from the adsorption/desorption of ions (Cl-, Br-, …) and the transient transfer of electrons between the electrode and the electrolyte at the interface. The stored charge at the surface of the electrode can be redistributed upon inverse current flow, in order to avoid accumulation of charges at the surface. For neural stimulation applications, capacitive mechanisms are preferred as they do not generate oxydo-reduction products which could potentially damage the neural tissue.

In vitro, the mechanisms at the electrode interface are usually studied a three-electrode electrochemical cell, composed of the electrode of interest or working electrode (WE), the counter

electrode (CE) where the current flow back and the reference electrode (RE) defining the electrical potential reference, all bathed in an electrolyte solution (Fig. 3.B).

c. Electrochemical Impedance Spectroscopy (EIS)

The impedance of an electrode corresponds the opposition of flow of current in the electrode. For both recording and electrical stimulation electrodes, a low impedance is favourable to better transduction of the charges. For recording electrodes especially, the impedance is a good indicator of the thermal noise as the noise is proportional to $\sqrt{Re(Z)}$ (Boehler et al., 2020). For metal electrodes, the impedance and phase at 1 kHz is commonly given as neuron spikes occur mostly at that frequency, although it is recommended for flexible probes and novel materials to describe the whole spectrum because of the interface complexity (Schiavone et al., 2020).

EIS measurements consist in sending a small amplitude sinusoidal signal is sent between the WE and the CE at different frequencies, usually by a potentiostat and measuring the resulting sinusoidal response. The complex impedance Z corresponds to the transfer function between the output and input: $Z = \frac{I_{out}}{V_{in}} = |Z|e^{j\varphi}$, with $|Z|$ the impedance modulus and $\varphi = \omega t$ the phase.

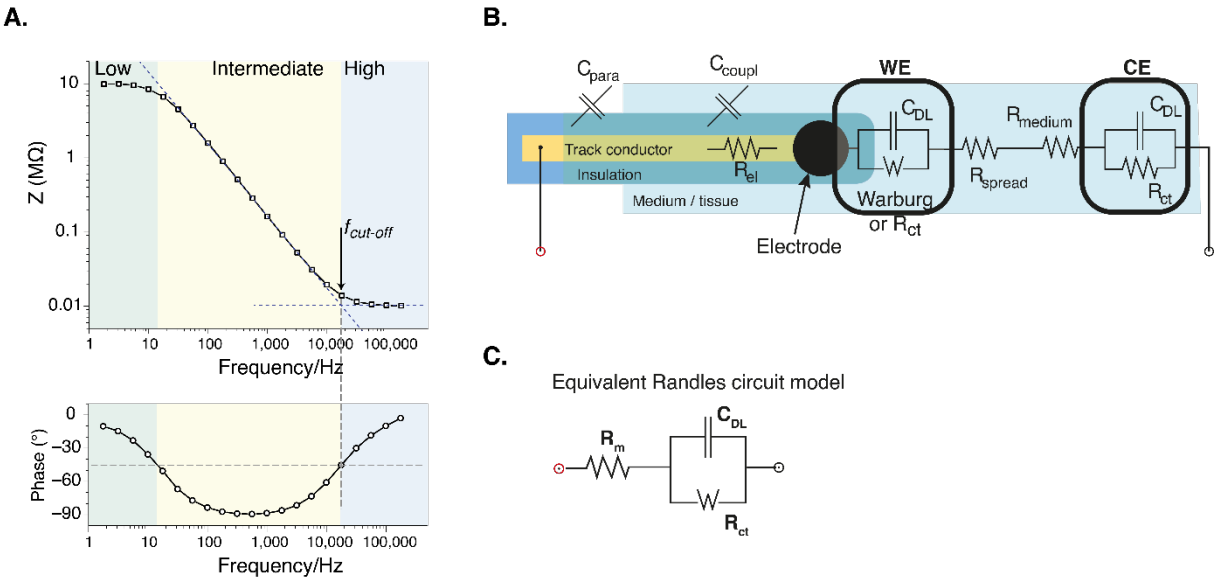

Fig. 4 Description of Electrochemical Impedance Spectroscopy (EIS) of neural electrodes. **A.** Typical EIS for metal electrodes (Boehler et al., 2020). **B.** Model of the interface between tissue and the different components of the neural implant. CDL is the capacitance of the double-layer formed. Modified from (Schiavone et al., 2020).

A typical EIS plot for metal electrodes is presented in Fig. 4.A. The system acts as a high-pass filter. Indeed, at low frequencies the impedance is high, preventing passing of the electrons while at high frequencies, the impedance is low and the phase (delay between in and out signals) is close to zero. Different circuit models exist to describe the interface. In Fig. 4.B, the interface between the working electrode (WE) and the biological medium is modelled by a C_{DL} stores a charge dq when the difference of potential dV between the electrode and the reference potential is non-null such as $C_{DL} = {dq}/{dV} = {\varepsilon_0 . A}/{d}$, with ε_0 the relative permittivity, A the interfacial surface and d the distance between the plates. The corresponding impedance is $Z_{DL} = {1}/{j\omega C_{DL}}$. Further away the diffuse layer is composed of solvated ions distributed uniformly. As $C_{DL} \propto A$, the larger the electrode surface and the larger the charge accumulated at the interface and the higher the charge injection capacity. In practice, the impedance at the double-layer capacitance is corrected with a constant phase element (CPE) such as $Z_{CPE} = {1}/{(j\omega)^{\alpha} Q_0}$, with $\alpha \in [0\ 1]$ and Q_0 a constant. When faradaic contributions cannot be neglected, the impedance can be modelled using Warburg model, depending on a diffusional time constant and a pseudo-capacitance.

A simpler equivalent circuit model is the Randles model (Fig. 4.C). R_m models the resistance of the medium/tissue, C_{DL} is the double-layer capacitance as described above and R_{ct} is the charge transfer resistance. Electrical circuits calculation gives the following impedance:

$$Z = R_m + \frac{R_{ct}}{jwC_{DL}R_{ct}+1} \text{ or } Z_{CPE} = R_m + \frac{R_{ct}}{(jw)^{\alpha}C_{DL}R_{ct}+1} \quad \text{(Eq. 1)}$$

from which it is possible to characterize the interface. The impedance at the counter electrode (CE) is negligible as its surface is much larger than the one of the WE, therefore $C_{CE} >> C_{DL}$ so $Z_{CE} << Z_{DL}$ based on Eq. 1.

d. Cyclic voltammetry (CV)

Cyclic voltammetry is an electrochemical method which informs on the reduction and oxidation reactions occurring at the neural interface. It measures the current flow between the WE and CE when applying sweeping potentials linearly between the WE and RE, at a certain sweep rate. The concentration of ions at the interface depends on the Nernst equation:

$$E = E_0 + \frac{RT}{F}.\ln\left(\frac{[ox]}{[Red]}\right) \quad \text{(Eq. 2)}$$

Cyclic voltammograms are useful for estimation of the **'water window'** which corresponds to the potential boundaries above which, water is electrolysed. If faradaic interactions occur, they appear in the form of peaks in the voltammograms at specific voltages. Such interactions can become harmful for the neural tissue only if irreversible. Finally, it is possible to estimate the cathodic or anodic **charge storage capacity (CSC)** of an electrode by calculating respectively the negative or positive area of the CV plot, corresponding to the sum of transferred charge. However, not all the charge effectively transferred can be used in practice for charge injection. This is why voltage transients (VTs) measurements are usually performed for stimulating electrodes.

e. Voltage transients (VTs)

VTs give an idea of the **charge injection capacity (CIC)** of the electrodes. For VTs measurements, the potentiostat typically sends charge-balanced biphasic pulses at increased current amplitude (I) between the WE and RE, and record the response in potentials between the WE and CE. The real electrode polarization VE is calculated by subtracting the access voltage VA, which is defined as an almost-instantaneous drop in voltage due to electrical resistance from conductive tracks and electrolyte. The intersection between water window potentials and linear fitting of VE = f(I) for both anodic and cathodic corresponds to their respective maximum CIC allowed.

I.A.2. Biocompatibility requirements

Biocompatibility is defined as "the ability of a device material to perform with an appropriate host response in a specific situation" (Black & Black, 2005). It is a critical property, which has to be insured for both human health safety and efficient functionality. The biological reactions in the body in response to the contact with the implanted device is highly dependent on the material composing the implant. Design of the implant should consider the biological mechanisms occurring during foreign body implantation acutely and on the long term. We describe below the main general mechanisms at play and focus on the role of retinal microglia in the context of retinal implants for vision restoration.

a. Foreign body reaction (FBR)

In vitro techniques relying on cell cultures can give fast insights into the biological behaviour of the material-host interface. Most common studies look at cell survival in life/death assays (toxicity), or investigate cell growth or cellular damage (mutagenicity, carcinogenicity). However, *in vitro*

environments are too simplistic models compared to the complexity of *in vivo* environments. Indeed, biocompatibility should be verified in the conditions the implants will be used, as per the international standard ISO 10993-1 on “Biological evaluation of medical devices - Part 1: Evaluation and testing within a risk management process”. Table 1 gives an overview of the framework of biocompatibility tests for medical devices implanted at the tissue/bone interface (ISO 10993-1).

Implantation of a foreign body *in vivo* creates *de facto* a local injury, and therefore a local inflammation with activation of the innate immune system: blood monocytes migrating to the tissue lesion parts (Fig. 5.A). Other systems (platelets, fibrinolytic system, complement system) are also activated, leading to release of blood proteins onto the foreign body and formation of a provisional matrix (Fig. 5.B).

Table 1 Relevant framework for biocompatibility testing of a medical device at the tissue/bone interface (ISO 10993-1).

Biological Effect	Limited Duration	Prolongated Duration	Permanent
Cytotoxicity			
Sensitization			
Irritation or Intracutaneous Reactivity			
Acute Systemic Toxicity			
Material-Mediated Pyrogenicity			
Subacute/Subchronic Toxicity			
Genotoxicity			
Implantation			
Chronic Toxicity			
Carcinogenicity			

However, macrophages are not able to engulf the whole implant hence a “frustrated phagocytosis” happens (Ratner, 2015): while trying in vain to phagocytose the material, the macrophages spread over, adhere to protein coated on the foreign body surface, fuse with neighbouring ones to become foreign body giant cells (FBGCs) thanks to diffusion of cytokines such as IL-4 and IL-13 and release lysosomes. This failed phagocytosis results in a thin layer of cells creating a fibrotic capsule around the implant (Fig. 5.D). The whole process is called the **foreign body reaction** (FBR). Chronic inflammation usually resorbs after one week. Worsening of the inflammation (often synonym of infection) can lead a too thick fibrous encapsulation around the foreign body (Fig. 5.E), which impedes the efficient electrical stimulation as the glial cells build up an insulating layer between the retinal implant and the neurons to be stimulated. This results in a less efficient stimulation, and on the long-term, failure of the implant.

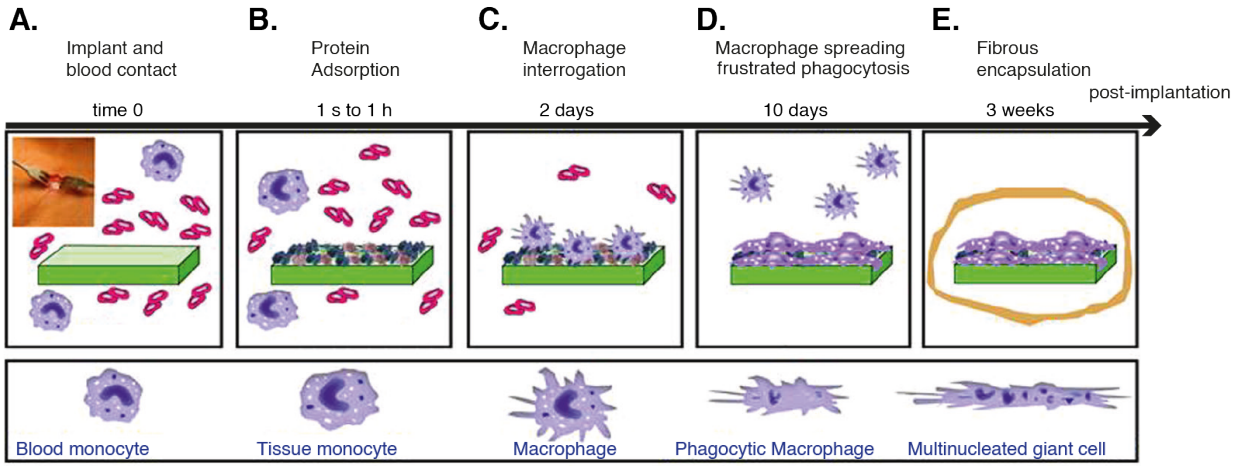

Fig. 5 Evolution of the foreign body reaction from implantation time to 3 weeks post-implantation (wpi). The introduction of a foreign body (green) induces an innate primary immune reaction with monocytes migrating from blood (**A**) to tissue (**B**) while releasing antigens (proteins). The monocytes evolve into macrophage (**C**) after around 2 days with release of diverse inflammatory cytokines

such as tissue necrosis factor alpha (TNFα), interleukin-1β (IL-1β). Failure to engulf the foreign body leads to frustrated phagocytosis (**D**) and macrophage spreading and fusing together into a thin layer of fibrotic tissue (**E**). Modified from (Ratner et al. 2015).

Today, devices which implantation only create on the long-term a thin layer of non-adherent capsule around are targeted as "biocompatible" (Ratner, 2015). Metal leakage, material degradation, material contamination, modulus mismatch between neural interface and the neural tissue (E_{dura} ~10 MPa) and interactions of the electrodes material with proteins can all influence the evolution of the FBR, imposing challenges for implant design. Immunoassays studies of cytokine release upon chronic *in vivo* implantation showed that levels of cytokines produced by macrophages ongoing frustrated phagocytosis are dependent on the material of the implant (Rodriguez et al., 2008). Careful choice of the material interfacing with the body could stop macrophages fusion and therefore lower fibrous encapsulation.

b. Macroglia and microglia cells

Astrocytes and microglia cells play a critical role in the long-term foreign body reaction in the retina.

i. Astrocytes

Astrocytes are star-shaped glial cells present in the central nervous system (CNS) and make up 30 to 65% of CNS glial cells (Nathaniel & Nathaniel, 1981). They are composed of a main round body with thousands of fine branches/processes which interact with other cells and some large branch extending into endfeet which wrap around blood vessels. Their involvement in the neurovascular coupling is slowly getting a foothold in the field (see §I.D.1).

Astrocytes are composed of 8-10-nm-diameter filaments of **glial fibrillary acid protein** (**GFAP**). Upon foreign body insertion, astrocytes become activated and are recruited in the encapsulation glial layer around the implant. Their processes proliferate and show hypertrophy with increasing amount of GFAP. A study with non-functional silicon probes brought precision to the timeline of glial scarring: at around 6 weeks post-implantation in the cortex, the glial capsule reached a stabilised and final size (Turner et al., 1999; Szarowski et al., 2003).

In the retina, astrocytes are mainly located close to the RGCs and the nerve fibre layer.

ii. Müller cells

Müller cells are the largest macroglia cells in the retina, located all over the retinal layers. Just like astrocytes, they play a critical role in the cell homeostasis and metabolism, but also participate in the retinal cell survival and microglia cells activation. Additionnally, Müller cells also become activated upon foreign body insertion, and undergo gliosis.

iii. Microglia

Microglia were first discovered in 1919 by Pio del Rio-Hortega. These glial cells can be found in the central nervous system (CNS) and are produced by foetal macrophages. The past decades witnessed a large increasing interest for research on microglia, often labelled as the immune cells of the nervous system. They fulfil many functions at different stages in life. Not only do they participate in inflammation, but they are also linked to synaptic functions. In wild-type healthy rats, they have a ~30 to 50 µm-perimeter somas (Beynon & Walker, 2012; Jinno et al., 2007) with 4 to 6 ramified long processes, several order of magnitude larger than the soma (Fig. 6.A). Microglia are highly motile: the processes extend and retract, such that the microglia survey their environment. Their morphology can change depending on the conditions (pathology, ageing, adulthood…) and the regions: they can for instance be ramified, amoeboid, hypertrophic, rod, dystrophic, or satellite (Savage et al., 2019).

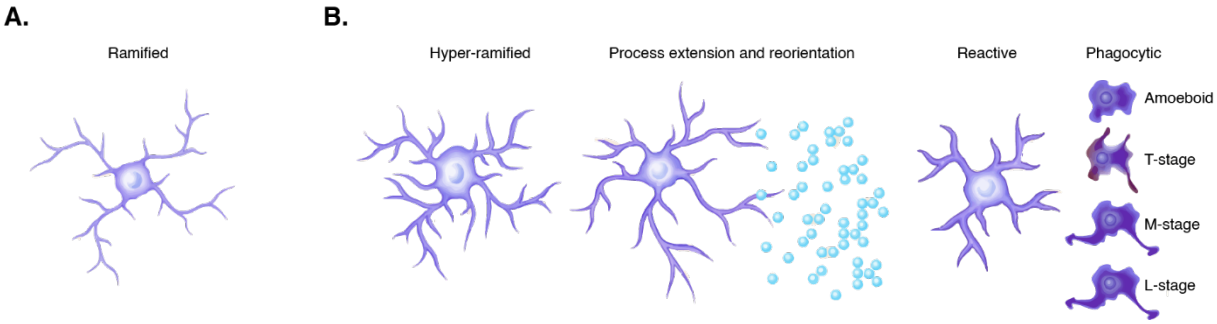

Fig. 6 Microglia morphologies under normal or pathological situations. Modified from (Beynon et al. 2012). **A.** Ramified microglia. **B.** In response to injury, microglia cells become hyper-ramified, extend their process and re-orient towards the injury site. Then, they become reactive and phagocytic. Further transformation into transitional (T-stage), motile (M-stage) or locomotor (L-stage) microglia have been reported (Modified from Stence et al. 2001).

The insertion of a foreign component into the human body breaks the blood brain barrier and causes irrevocably tissue injuries. This breaking activates the microglia and causes both local inflammation and neural degeneration. The physiological mechanism has been studied extensively yet the immunological pathways are still not so clear. An external injury site triggers the increase of cytokines or free radicals which signal the inflammation to the microglia. They first extend their processes and reorient towards the injury site (Davalos et al., 2005; Nimmerjahn et al., 2005). Only after do they shorten and transform into phagocytic **amoeboid** cells (Fig. 6.B). Half an hour after the insertion of the electrodes, microglia cells slowly encapsulate the device with a protein actin called lamellipodia. The amoeboid microglia might later transition to 3 different types, know the transitional-stage (T-stage), the motile stage (M-stage) or the locomotor stage (L-stage) (Stence et al., 2001). By one day, the microglia become fully active and surround the device the same way as macrophages, creating a wall impeding the correct interfacing with the neurons (Kozai et al., 2015).

In the retina of P23H rats, a genetically modified model of RP disease, both ramified and amoeboid microglia cells are found in the all retinal layers (Noailles et al., 2014, 2016).

c. Immunohistology tests for biocompatibility studies

In vivo testing on animals remain a controversial yet necessary, reliable and nowadays highly regulated method to verify biocompatibility before clinical applications on humans. Rodents have been proved to be a valid model for biocompatibility studies of neuroinflammation. Both human and mouse microglia overall express similar genes (Nimmerjahn et al., 2005) and both microglial response to neurodegeneration could be highly correlated.

Most *in vivo* biocompatibility studies of chronic non-functional implants are usually carried out in similar ways. After several weeks or months of implantation, the animal model is euthanised and the tissue containing the implant is removed from its original location. The tissue is cleaned and stained with markers of interests. Indeed, immuno-histology studies performed on post-mortem explanted retinas after chronic implantation can give insights into the inflammation and chronic immune response. Using confocal imaging or fluorescence microscopy, it is possible to analyse the morphology of explanted retina to investigate thinning of the outer nuclear layer (ONL) and thus survival of photoreceptors $(Di Paolo & Ghezzi, 2015). It is also possible to visualize the extent of inflammation and immune response *in vivo* by quantifying activated microglia cells and astrocytes.

Microglia cells can be labelled with antibodies specific for cluster of differentiation 11b (CD11b) which also marks macrophages or ionized calcium binding adaptor molecule 1 (Iba-1). The advantage of Iba-1 (which we chose for our *in vivo* biocompatibility study described in §III.A) lies in its long-term fixation fluorescence and the fact that it is not expressed by astrocytes nor oligodendrocytes or neurons.

GFAP staining has been widely used to specifically mark astrocytes in CNS injuries situations. However, it has been showed that GFAP does not work as well to mark astrocytes in healthy neural tissues (Sofroniew & Vinters, 2010). The labelling is expected to occur in the main stem branches but not really on the body nor the fine processes.

Post-mortem quantification of neuron density using NeuN staining at the vicinity of the implanted zone in CNS tissues can also inform on zones with neuronal death but might not be directly linked to the implant material itself. It seems rather that neurons migrate away from the foreign body location, pushed away by the glial scar growth.

I.A.3. Metals and semi-conductors

The roadmap of electrode material starts with metal-based electrodes. The semi-conductor revolution participated in the improvement of neural interfaces in terms of functionality. However, the biocompatibility requirements are still not met and downsizing metal electrodes comes at the cost of the electrochemical/electrical properties. We compare in this section the metals and alloys featured on visual prostheses and discuss their limits.

a. Metals and alloys

i. State-of-the-art

In metals, the overlapping of the valence and conduction bands is favourable to the passage of electrons. As a result, metals are highly electrically conductive. Historically, **platinum** wires (atomic symbol Pt, atomic element Z=78) were implanted for deep brain stimulation (DBS) studies (Fritsch & Hitzig, 2009) and tungsten wires (W, Z=74) for cortical recording (Hubel, 1957). Today, commercialised electrodes for DBS, cochlear implants or clinical diagnosis are still made of metal such as tungsten, iridium (Ir, Z=77), platinum, gold (Au, Z=79) or their alloys such as platinum-iridium (PtIr), stainless steel (alloy of iron (Fe, Z=26) and chromium (Cr, Z=24). Among the past and current retinal prostheses developed in research groups worldwide, all of them contain either electrodes in metal or metal alloys. Discontinued prototypes such as the epiretinal Argus I, Argus II prototypes from SecondSight company, the epiretinal Iris II from Pixium Vision or the suprachoroidal Bionic Vision Technologies generation 1 and 2 all chose first platinum electrodes for neural stimulation.

However, Pt electrodes are limited by their maximum charge injection capacity (~0.15 mC/cm²). This is why second-generation prototypes usually feature coatings made of alloys, such as Titanium Nitride or **TiN** and Iridium Oxide or **IrOx** which have higher charge injection capacities of ~1 and ~1-5 mC/cm² respectively (Cogan, 2008). Alloys are also interesting in terms of mechanical properties. For instance, Pt is too soft for surgery implantation but its combination with iridium renders the material stiffer while lowering the electrochemical impedance (Petrossians et al., 2011). Following their development in neuroprosthetics, IrOx coatings were used in the discontinued ASR chip from Optobionics, the Alpha IMS, AMS from Retina Implant AG, and is still coating the photovoltaic pixels of the PRIMA implant from Pixium Vision and the EPIRET3 device from Aachen University. The POLYRETINA implant from EPFL chose a TiN coating on top of a Ti layer.

For neural electrical stimulation, spatial resolution is a highly desired result. Limitations in miniaturisation of metal electrodes can be bypassed by increasing the electrochemical surface area (ESA) which then differs from the geometric surface area (GSA). The larger the ESA, the higher the charge injection capacity. Metal-derived materials such as platinum black (Pt-b), Iridium oxide (IrOx) or nano-porous materials are the most common options to bypass the downsizing issues. Pt-b coating can be easily deposited electrochemically to fabricate retinal stimulating electrodes with low impedance (Watanabe et al., 2007).

ii. Metallic tracks

Additionally, the conductive tracks which carry the electrical current from the current generator to the electrodes were and are still usually made of metals because of their high conductivity and easy microfabrication patterning. The conductance G of the tracks are defined by the equation: $G = \frac{1}{R} = \frac{\sigma.A}{l}$ with R the resistance, A the cross-sectional area of the conductor, l the length of the conductor and σ

the electrical conductivity ($S.m^{-1}$). Reduction of the size of the conductor can therefore raise the question of reduction of conductance and increase Joule effect through the conductive material.

b. Semi-conductors

Downsizing the electrode size improves the spatial resolution as neurons can be targeted individually and cross-talk or parasitic axonal activation can be avoided. With the advent of semiconductor technology, electrode multiplexity increased exponentially while electrode size and mechanical stiffness decreased exponentially over the last 70 years (Woods et al., 2020). The onset of photolithography in clean rooms also pushed forward the neuroprosthetics field towards easier process and easier interfacing with microelectromechanical systems devices (MEMS) for signal amplification. Clean room micro- and nano-fabrication of implants with lithography consists in stacking nm to µm of layers of conductive and insulating materials. Openings are created at the location of the electrodes using positive or negative photoresist mask precisely aligned on the substrate.

Silicon is a semi-conductor which has been often exploited in BCIs for neural recording or stimulation. For instance, the intracortical **Utah arrays** (electrodes at the tip of silicon shanks) or **Michigan probes** (electrodes distributed along the silicon shanks) became the new standards in neurostimulation and recording experiments. In vision restoration research, Utah arrays with IrOx coatings on electrode tips are still used in the ongoing cortical prostheses CORTIVIS clinical trial (n° NCT02983370) (Fernández et al., 2021; Grani et al., 2022) and were also recently featured in chronic studies on NHPs (X. Chen et al., 2020, 2023).

Thanks to these new microfabrication technologies, wireless retinal implants based on silicon photodiodes could also be engineered, such as Pixium Vision's PRIMA subretinal photovoltaic chips (Palanker et al., 2020).

Additionally, the insulation of the conductive materials was first made of silicon oxide SiO_2 films sandwiching a silicon nitride Si_3N_4 layer (Milek, 1971). The coating should also be thin enough (< µm) to minimise overall bulkiness.

c. Biocompatibility of metals and semi-conductors

Despite high conductivity at room temperature, metal electrodes and Si-based materials are subject to biocompatibility and biodegradation issues because of their high brittleness and stiffness. There is first a clear mechanical mismatch between metal electrodes or Si and neural tissues. As schematised on Fig. 7, metal electrodes exhibit Young modulus in the range of tens to hundreds of GPa (E_{Au} ~ 80 GPa, E_{Pt} ~ 150 GPa, $E_{stainless\ steel}$ ~ 200 GPa) whereas for neural tissues, it remains below 100 kPa (Lacour et al., 2010). The Young modulus of Si is also still 8 to 9 order of magnitude higher than brain and cell tissues.

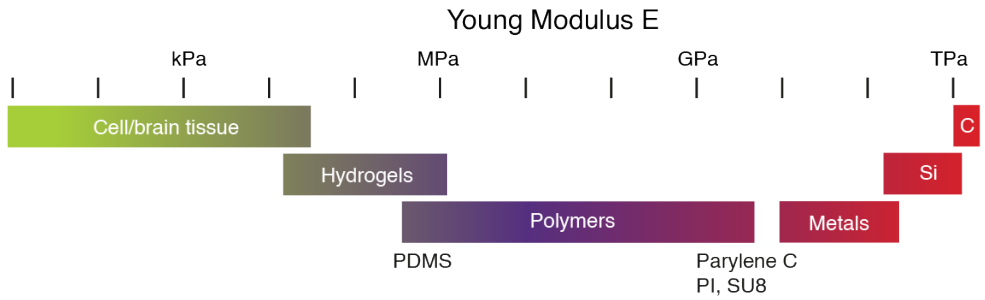

Fig. 7 Young modulus of classical materials used in electrode design

As detailed previously (§I.A.2.a), implantation causes foreign body reaction leading to gliosis and hence impeding their efficiency over time. The previously mentioned chronic study on NHPs with an intracortical prosthesis made of Utah arrays confirms once more this issue. As seen on Fig. 8.A, the explanted devices after three-year implantation in the brain of macaques show fibrotic tissue all around

the devices, but also degradation of the cortex in the implanted zone (Fig. 8.B), and degradation of the IrOx electrode tip (Fig. 8.C), all associated with loss of visual task performance and signal quality over time (X. Chen et al., 2023). In 2004, Cogan et al. already warned on the delamination risk of IrOx during *in vivo* intracortical stimulation (Cogan et al., 2004).

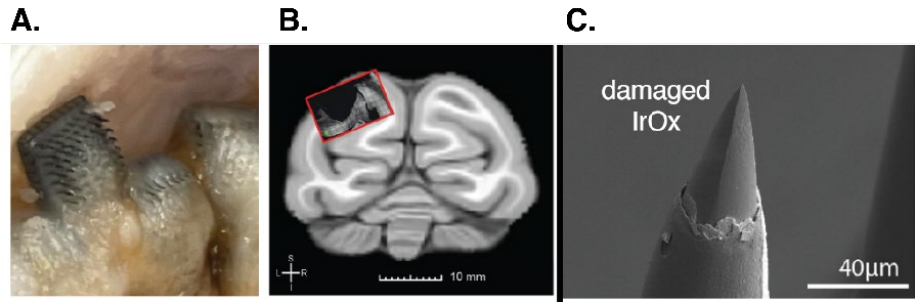

Fig. 8 Explanted Utah arrays from a macaque after three years. Modified from (X. Chen et al. 2023). **A**. Gliosis around explanted Utah arrays **B.** degradation of the implanted visual cortex seen on IRM image. **C**. Damaged Iridium oxide electrode tip seen on scanning electron microscope

Moreover, if the protective coating around the implant is not hermetic enough, water or biological fluid can also engulf in, corroding the metallic tracks and causing delamination of the electrode coating. For instance, half of the failures of the AMS subretinal photovoltaic were imputed to the CMOS corrosion (Daschner et al., 2017).

I.A.4. Carbon-based materials

Carbon (C, Z=6) is one of the most abundant elements in nature. It is composed of 6 electrons which ground electronic configuration is $1s^2 2s^2 2p^2$ with 2 valence electrons in 2s state and 2 valence electrons in 2p state (Fig. 9.A). Different distribution of electrons and different hybridizations give rise to different geometries hence different properties. Among the various allotropes of carbon, only graphite and diamond are naturally found as minerals in nature. Major advances in engineering and microfabrication led to their industrial. The facilitated access to those carbon allotropes kicked off their worldwide research as neural electrode because of their promising electrochemical and physical and chemical properties as recording or stimulating material.

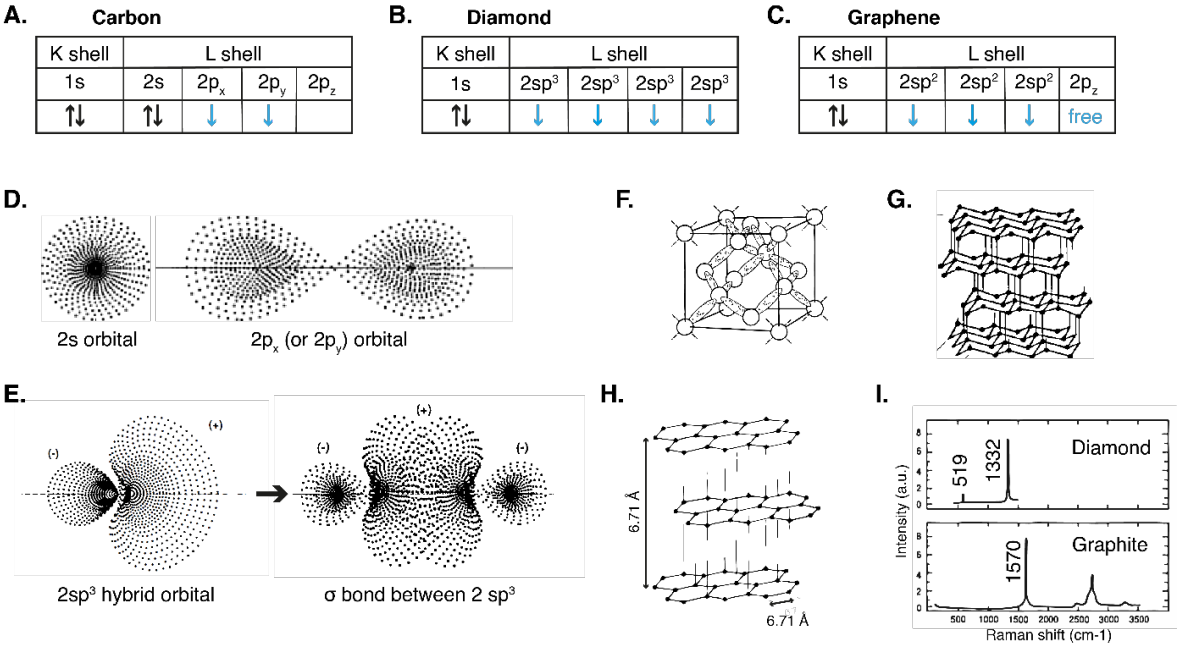

Fig. 9 Structure of carbon, diamond and graphene. Modified from (Pierson, 1993). **A.** Electronic ground configuration of carbon **B.** Electronic configuration of sp3 hybridized orbitals of carbon in diamond. **C.** Electronic configuration of sp2 hybridized orbitals of

carbon in Graphene. **D.** Distribution of electron density in a 2s orbital and a 2p orbital. **E.** Formation of σ-bond from 2 sp3 hybrid orbitals. **F.** Geometric configuration of carbon atoms in Diamond. G. Structure of cubic diamond **H.** Structure of graphite. **I.** Raman spectrum of diamond and Graphite.

a. Diamond

Diamond is one of the hardest material (rated 10 on the categorical Mohs scale) and has one of the highest molar density (0.293 g-atom/cm3) (Pierson, 1993). Its density is also high (3.515 g/cm3). While still being mostly used as gemstones in jewellery for its optical properties, diamond can be either an excellent insulator or conductor if doped with boron (hole) or nitrogen (electron donor).

i. Electronic properties

In diamond, the atomic orbitals 2s and 2p are hybridized into sp3 hybrid orbitals with 4 valence electrons (Fig. 9.B), resulting in σ-bonds with high coverage (Fig. 9.E). The covalent bonds hereby have high energy (370 kJ/mol) hence are hard to break and are short (1.5 Å), accounting for diamond's mechanical properties. The structure minimizing repulsion between atoms is tetrahedric, hence the cubic structure of diamond crystal (Fig. 9.F-G). Laser-Raman spectroscopy are often used to characterise the hybridised structures. Monocrystalline Diamond can be recognized by a high peak at 1332 cm^{-1} (Fig. 9.I) on Raman spectrum, combined usually with positive Scanning Electron Microscope (SEM) observations.

Depending on the crystallinity of diamond, the Raman band can be shifted (Yang & Narayan, 2019). Intrinsic diamond (C*) is a semi-conductor with a large gap between valence and conduction band (separated by 5.47 eV). At room temperature, it behaves as an (excellent) insulator. However, doping with boron or nitrogen can transform it in a conductive material of around 200 $\Omega^{-1}.cm^{-1}$ (Yang & Narayan, 2019).

ii. Microfabrication

Diamond can be produced by chemical vapor deposition (CVD) or under high pressure and high temperature processes. The development of CVD diamond technology started in the 70s and is nowadays fully mature and cost-effective. Inside dedicated microwave plasma reactors (MPCVD), dihydrogen H_2 decomposes into protons which react with the gas of methane (CH_4), forming under high temperature H_2 and CH_3 radicals. Those radicals deposit on a Si wafer, forming monocrystalline diamond. The addition of H_2 is necessary in order to wipe out the sp2 carbon formed along the wanted sp3 carbon by CH_4 decomposition. If the substrate is seeded with diamond nanoparticles prior to microwave exposition, the growth leads to a polycrystalline diamond of larger size (Garrett, Tong, et al., 2016).

While diamond is not complicated to fabricate if one possesses a MPCVD, the microfabrication of diamond-based microelectrode arrays is a bigger challenge. Indeed, patterning diamonds is difficult because most materials do not withstand the harsh conditions of diamond growth.

iii. Biocompatibility

The diversity of electrode designs and material used necessitates as many biocompatibility studies as close as possible to the real application. Literature attests for the biocompatibility of several diamond-based materials, knowing that diamond on its own is known to be chemically inert.

In vitro cultures of fibrogen on CVD diamond highlighted low and not significantly different percentage of adsorbed fibrogen compared to stainless steel standard, and *in vivo* implantation of CVD diamond implants in the intraperitoneal cavity revealed minimal inflammation after 7 days measured by low thickness of macrophage layer adhered to the samples (Tang et al., 1995). Nanocrystalline diamond monolayer coatings displayed similarly promising neuronal cell viability and growth (Thalhammer et al., 2010). Thin films made of ultrananocrystalline diamond had also high affinity for *in vitro* cell growth (Bajaj et al., 2007). Nanocrystalline diamond films tested *in vitro* on purified retinal ganglion cells could also survive (Bendali et al., 2014).

In vivo, BDD electrodes were analysed in histology after 2 and 4 week subcutaneous implantation in rat models (Alcaide et al., 2016) and in another study, after 15 week muscular implantation in guinea pigs (Garrett, Saunders, et al., 2016). In both cases, BDD-based samples triggered lower inflammation and thinner fibrous capsules compared to TiN or silicon control respectively, suggesting promising

capabilities for chronic BCIs. In the subretinal space as well, 3D BDD-based electrodes showed better *in vivo* biocompatibility than polyimide sham or platinum devices after 6 weeks of implantation in P23H rats (Bendali et al., 2015).

iv. Diamond as a stimulating material

Diamond holds interesting electrochemical properties for neural implant applications. Generally speaking, a wider water window is valuable for neural stimulating implants because higher current amplitudes can be injected safely. A large water window has been reported for nitrogen-doped-ultra-nano-crystallin diamond (N-UNCD) ([-1.1; 1.1], (Garrett et al., 2011), flat diamond and BDD ([-1.5; 1.5], (Hébert et al., 2014)). Fig. 10 compares the typical cyclic voltammograms from classical metal electrodes and diamond-based electrodes. The length of the water window depends on the diamond purity and fabrication process, but overall it is almost twice larger than usual metal electrodes (Nebel et al., 2007).

At the university of Melbourne, a research team is currently developing a retinal prosthesis using N-UNCD feedthroughs. *In vitro* characterization showed excellent stability over time and highlighted a charge injection capacity of 300 µC/cm² (Hadjinicolaou et al., 2012), slightly higher than platinum (~0.05 – 0.15 mC/cm²) and much lower than for IrOx (~1-5mC/cm²). A proof-of-concept of explanted retinal ganglion cell activation on MEA was established, promising enough for vision restoration prostheses.

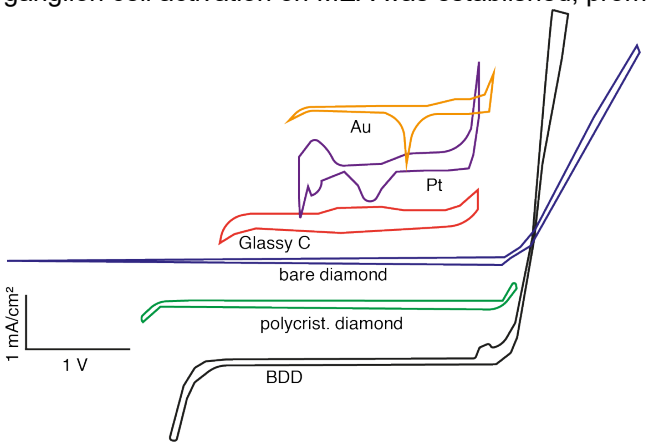

Fig. 10 Cyclic Voltammetry of diamond-based electrodes and standard passive electrodes. Modified from (Nebel et al. 2007).

v. Diamond as recording material

Diamond has mostly been used for **biosensing** neurotransmitters. Studies for neural recordings are sparse. In the past, H-terminated conductive diamond successfully recorded neural spiking activities from cell cultures (Ariano et al., 2009) and BDD-electrodes could detect local field potentials as well as multi-units (Piret et al., 2015), reporting an average impedance of 50 kΩ and very low intrinsic noise (3.1 µV). The results were very promising for future *in vivo* recordings, achieved in this thesis with an innovative fabrication process from ESIEE Paris (§II.A.1)

b. Graphene

Discovered in 2004 by Novoselov and Geim by scratching the surface of graphite with tape, graphene is a 2D carbon-based material made of repetitions of hexagonal motif of carbons (Novoselov et al., 2004; Geim & Novoselov, 2007). Graphite is made of stacked graphene layers held by weak Van der Walls interactions (Fig. 9.H).

i. Electronic properties

In graphene, a quantity N of 2s, 2px and 2py atomic orbitals hybridize to form **sp2** hybrid orbitals, resulting in 3N molecular orbitals of N σ-type, responsible for the C-C covalent bonds. They have an energy almost double the one of diamond (680 kJ/mol) and are even shorter (1.3 Å). From the $2p_z$ orbitals in which the electron remains free, N molecular orbitals of π type are created, accounting for the

delocalisation of electrons. As the π and π* bands are really close, graphene is naturally conductive. As the energy to go from one band to another is very low, graphene absorbs all the main colour wavelengths and is black.

ii. State-of-the-art of graphene-derived materials

Graphene is a semi-metal which can be fabricated by CVD technology. Graphene is also compatible with microfabrication technologies, allowing incorporation on flexible substrates which is particularly interesting for conformable neural interfaces.

Its high SNR and low impedance have been exploited extensively in (intra)cortical recordings applications. For instance, **CVD graphene** has been used as electrode coating for intracortical recording (Bourrier et al., 2019). Lim et al. also reported the use of graphene-gold-graphene electrodes for low-impedance and high SNR LFP recordings during seizures compared to bare gold (Lim et al., 2023). Graphene electrodes on flexible surface arrays can provide mapping of the brain, as successfully demonstrated by for the somatosensory and auditory cortex (M. Lee et al., 2021). Their chronic stability *in vivo* and their recording abilities have also been reported, suggesting promising applications as whole-brain neural recording electrophysiology tool in neurology, as well as biosensors or cortical micro-stimulation allowed respectively by the sensitivity of graphene to potential changes and low impedance.

Graphene has a **high electron mobility**, reported around 200 000 cm²/V.s compared to approximately 1500 cm²/V.s for Si (Kumar & Pattammattel, 2017). Combined with its high conductivity, graphene is a material of choice for field-effect transistors applications allowing direct-current (DC) low frequency signal recording, particularly suited to study cortical spreading depolarisations (§I.C.3.b.iii). However, in literature, gFETs are mostly fabricated for biosensing purposes. For instance, when functionalized with molecular linkers, gFETs can detect glucose in the concentration range of diabetes diagnosis (Kwak et al., 2012).

Optically transparent, CVD graphene can be coupled with optical imaging techniques such as calcium imaging or functional ultrasound imaging (fUS), property that we are going to exploit in this phD (see §II.B).

The synthesis of **graphene oxide** (**GO**) is a crucial step for the obtention of high-quality reduced graphene oxide. GO precursors can be obtained by oxidising graphene with strong oxidants such sulfuric acid (H_2SO_4) with nitric acid ($NaNO_3$) and permanganate ($KMnO_4$) (Hummers & Offeman, 1958). However, such reactions produce toxic gasses and residual Na^+ and NO_3^- ions complicated to remove from waste waters. Recently, more eco-friendly methods were developed without $NaNO_3$ (J. Chen et al., 2013).

Reduced graphene oxide (**rGO**) can be synthetized by reducing GO thermally at high temperatures above 1000°C (Huang et al., 2012). Generally speaking, they are water-soluble, show improved conductivity and capacitance compared to GO and finally exhibit **very high charge injection** which range from 5 mC/cm² for rGO electrodes on Ti/Au tracks (Viana et al., 2022) to 62 mC/cm² for reduced liquid crystal graphene oxide (Apollo et al., 2015). The latter implant example could also successfully record somatosensory-evoked potential. Overall, literature attests for the high potential of rGO electrodes for both neural stimulation and recording.

Other carbon-based structures such as multi-layer graphene (MLG) or carbon nanotubes (CNTs) will not be investigated in this phD.

iii. Biocompatibility

In 2008, the publication of a Nature Nanotechnology on how “Carbon nanotubes introduced into the abdominal cavity of mice show asbestos-like pathogenicity” characterised by inflammation and granulomas (lesions) in a pilot study (Poland et al., 2008) created a major scare. Shortcuts were made by the press, omitting that the study showed such cytotoxicity only for long needle-like fibres (>5 µm). This leads to a serious ban on carbon nanotubes (CNTs) in Europe and in the USA, even though the material intrinsic properties could have been exploited for medical applications. All carbon nanomaterials have been unjustifiably put into the same box yet their toxicity is very much dependent on purification process, surface modification but also dependent on the body interface in contact with (Fadeel et al., 2018).

Graphene-based materials typically fall into that class of feared materials with promising electrochemical properties. Therefore, its cytotoxicity and biocompatibility has been extensively studied to investigate their impact on human health. This classification work was a top priority for the Graphene Flagship, a European Commission project we took part in. Previous studies showed that hippocampal neurons cultures can survive on polylisine-coated graphene (Bourrier et al., 2019) as well as retinal ganglion cells culture on bare graphene (Bendali et al., 2013). However, inflammation reactions are dependent on the location of the implant in the body, hence the recommendation to test biocompatibility *in vivo* and for the meant function.

For retinal applications, biocompatibility of monolayer graphene has already been proved *in vivo* using subretinal monolayer graphene implants implanted for 3 months in the eye of blind P23H rats (Nguyen, Valet, Dégardin, Boucherit, Illa, De La Cruz, et al., 2021), but not with rGO which is the active material on our subretinal prosthesis and which structure differs from monolayer graphene. Although in some cases GO showed ecotoxicity (Evariste et al., 2020) and increased toxicity when adsorbing copper, nanoscale GO are biocompatible with more organs (Kiew et al., 2016).

Cytotoxicity and biocompatibility studies on rGO are as contrasting as those of GO, owing to the physico-chemical properties and therefore, to their inherent characteristics (dimension, porosity, concentration). Beside applications in neural implants, the proapoptotic dose- and time-dependent effect of rGO on breast cancer cells for the development of new treatments (Krętowski et al., 2021; Tabish et al., 2017). In eye applications, although exposure of GO induce ocular toxicity *in vivo*, rGO has been found to be safe (An et al., 2018). Moreover, recent *in vivo* biocompatibility study of transversal intra-fascicular microelectrode arrays with rGO were also found to be biocompatible with tibial tissue after 2 months of implantation (Viana et al., 2022).

I.A.5. Polymers

Scientists are turning nowadays towards soft and flexible materials for better conformability with neural tissue, for less tissue scarring/inflammation and hence for better biocompatibility. The chosen materials should have a Young modulus closer to the one of the implanted tissues (~kPa) but should still be rigid enough (>GPa) to be inserted or handled properly during conventional surgery (Nabaei et al., 2020).

Polymers, made of repetitions of one or several monomers, answer these requirements. Among biocompatible polymers with properties compatible with microfabrication, poly(2-chloro-p-xylylene) (**parylene C**), polydimethylsiloxane (**PDMS**), polyimide (**PI**) are the most commonly used. Their Young modulus, shown on Fig. 7 ranges respectively from 300-800 kPa for PDMS to several GPa for parylene C and PI. Despite numerous challenges of polymer adhesion on metal surface (Walton et al., 2022), cleanrooms lithography techniques can be applied for polymers as well, accelerating their integration into implant design. Additionally, conductive polymers such as Poly(3,4-ethylenedioxythiophene) (**PEDOT)** can also be integrated in neural stimulation probes as electrode

We detail in the following paragraphs and illustrate in Fig. 11 the application of the previously mentioned polymers in preclinical or clinical retinal implants or electrocorticography arrays (ECoGs).

a. Polyimide (PI)

i. State-of-the-art

PI is a polymer containing imide groups. It possesses high thermal stability (>260°C) and high insulation properties. It can be easily patterned with reactive ion etching (RIE) or deep reactive ion etching (DRIE) methods, removing the polymeric material at desired location to expose the conductive materials. The thickness can also be easily controlled via spin-coating. Its numerous advantages were first exploited in encapsulation for silicon-based probe.

Nowadays, even the substrate of retinal implants is more and more replaced by PI. For instance, the Bionic Eye Technologies subretinal implant (Shire et al., 2009), both the very large electrode arrays for epiretinal stimulation (VLARS) (Waschkowski et al., 2014) and the OPTO-EPIRET (Schaffrath et al., 2021) developed at Aachen University and shown on Fig. 11, or the subretinal graphene-based implant

we are working with all feature a PI-based substrate. A few years ago, Neuralink also reported on the use of polyimide for both encapsulation and coating material for its intracortical BCI (Musk & Neuralink, 2019).

ii. Biocompatibility

Flexible arrays with PI substrates showed no cytotoxicity when incubated with fibroblast cells for one day nor showed swelling nor water adsorption (Sun et al., 2009) and good biocompatibility *in vitro* with retinal pigment epithelial (RPE) cells (Seo et al., 2004). *In vivo* implantation of multielectrode arrays in rabbit eyes for 12 weeks (Seo et al., 2004), implantation of sham devices in blind rats eyes for 3 months (Nguyen et al., 2021) and chronic interfacing with peripheral nerves (Stieglitz et al., 2011) account for the good *in vivo* long-term biocompatibility of polyimide.

b. Parylene C

Parylene C is a transparent thermoplastic and a biocompatible polymer (FDA approved, United States Pharmacopial Class VI plastic) mostly used as coating material to protect the metals against corrosion (Golda-Cepa et al., 2020; Hassler et al., 2010). It is usually deposited in clean rooms using vacuum deposition polymerisation.

The EPI-RET and OPTO-EPIRET epiretinal prostheses are both encapsulated in parylene (Walter et al., 2005)(Schaffrath et al., 2021). In subdural neural recordings application, successful fabrication and *in vivo* validation of ECoG with parylene C coating on top of PDMS substrate presented superiority of the hybrid structure has been reported (Ochoa et al., 2013).

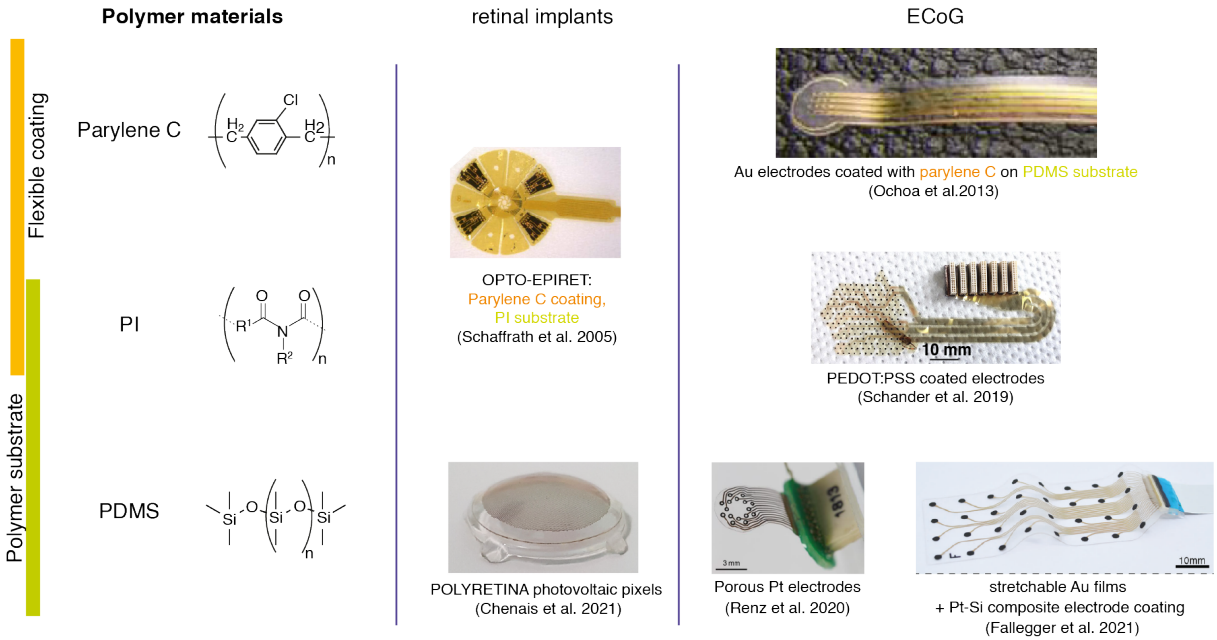

Fig. 11 Examples of Parylene C, Polyimide (PI) and polydimethylsiloxane (PDMS) polymers in substrate or coating of retinal implants and electrocorticography arrays (ECoGs) in clinical and preclinical research across the world.

c. PDMS

In visual implants preclinical research, the flexibility of PDMS shapes the epiretinal POLYRETINA implant into a contact-lense alike design (Fig. 11), improving the visual field (Chenais et al., 2021). PDMS also plays the role of hermetic case for the Australian subretinal diamond-based prosthesis (Ahnood et al., 2015).

Finally, ECoGs for neural recordings made with PDMS substrate show better conformability on brain surface such as the Opto-e-Dura developed at the University of Zurich (Renz et al., 2020) or the soft grids developed at the EPFL drawn on Fig. 11 (Fallegger et al., 2021).

d. PEDOT

Poly(3,4-ethylenedioxythiophene) (**PEDOT**) is another notable polymer with small charge transfer resistance. The oxidated form of PEDOT has higher conductivity, which is why PEDOT is usually doped with anions, the most common being poly(styrene sulfonate) (**PSS**). Its use as coating decreases the impedance and increases the charge transfer capability of metal electrodes (Castagnola et al., 2015).

Generally speaking, PEDOT demonstrates superior electrochemical characteristics compared to conventional metal electrodes (Vomero et al., 2016) but also compared to IrOx and Pt (Kigure et al., 2013) for both neural stimulation or recording. For instance, in the WRITE mode, PEDOT can be incorporated into organic material-based retinal implants as a **conductive layer** such as the SILK-PEDOT:PSS-P3HT subretinal prosthesis under *in vivo* research developed at the Italian Institute of Technology (Maya-Vetencourt et al., 2017). The POLYRETINA retinal implant previously shown (Fig. 11) also features PEDOT film below another conjugated polymer in its design for visual restoration (Chenais et al., 2021). When integrated on flexible ECoG using electrochemical deposition, PEDOT electrodes are sensitive enough to record spikes (Khodagholy et al., 2015) and can be coupled with optical imaging techniques because of their optical transparency (Donahue et al., 2018).

I.B. Writing with visual prostheses

I.B.1. Blindness, a worldwide affection

In 2020, the Lancet reported 33.6 million adults over 50 years old affected by blindness handicap (Steinmetz et al., 2021). This visual impairment condition is caused by irreversible damage which can happen at different stages of the visual pathway (Fig. 12.A), including the retina, the **optic nerve (ON)**, the **lateral geniculate nucleus (LGN)**, the **superior colliculus (SC)** and the **visual cortex (V1)**.

a. Main diseases leading to blindness

The leading causes of blindness for adults above 50 years old are cataract (15.2 million cases), uncorrected refractive errors (2.3 million cases), age-related macular degeneration (AMD) (1.8 million cases), retinitis pigmentosa (RP) (1%), glaucoma (3.6 million cases) and diabetic retinopathies (0.86 million cases) (Steinmetz et al., 2021). In developed countries, blindness mainly results from retinal diseases affecting either photoreceptors as in retinal dystrophies and AMD or the retinal output, the retinal ganglion cells, as in glaucoma and diabetic retinopathy. The large incidence goes hand in hand with socioeconomic burden, annual worldwide costs of productivity losses estimated at US$ 411 billion (WHO, 2023). For legally blind patients, even small improvements in eyesight could lead to great improvements in daily life for mobility and thus autonomy.

Humans have approximatively 100 million photoreceptors linked to 1.2 million retinal ganglion cells (RGCs) (Fig. 12.B). **Age-related macular degeneration** (AMD) and the most common retinal dystrophy, **Retinitis Pigmentosa** (RP), are both characterized by progressive loss of photoreceptors. AMD is a common disease affecting mostly people over 50. The disease starts with blurry central vision and can develop into two forms: dry and wet AMD. Dry AMD (85-90% of the cases) is characterised by the progressive thinning of the macula (region of the retina where the cone density is the highest) and the formation of subretinal deposits (drusen). The patient progressively loses its central and high acuity vision. Wet AMD is a frequent complication characterised by the growth of blood vessels from the choroid into the retina, damaging the macula and causing oedema and haemorrhages in the retina. RP is a group of inherited diseases causing the progressive loss of rod photoreceptors first, followed by a secondary degeneration of cone photoreceptors. RP patients first gradually lose their peripheral vision and night vision to ultimately lose also their central and high acuity vision. Around 30 genes have so far been associated with RP, the majority being expressed solely in rod photoreceptors and most others in

the RPE. Retinal neural remodelling occurs, leading to many physiological changes such as neurons migration, neurites sprouting from horizontal and amacrine cells (Fariss et al., 2000), bipolar cell deaths, and formation of a fibrotic glial seal isolating the remaining neurons from the RPE and choroid (Marc et al., 2003). However, in both AMD and RP, even though the outer layer cells have degenerated, many neurons of the inner retina remain (Humayun et al., 1999). In Wet AMD, 30-50% (Kim et al., 2002; Medeiros & Curcio, 2001) of RGCs are spared while there is no significant difference in dry AMD. More than 90% of the RGCs also subsist in RP patients' retina (Stone, 1992).

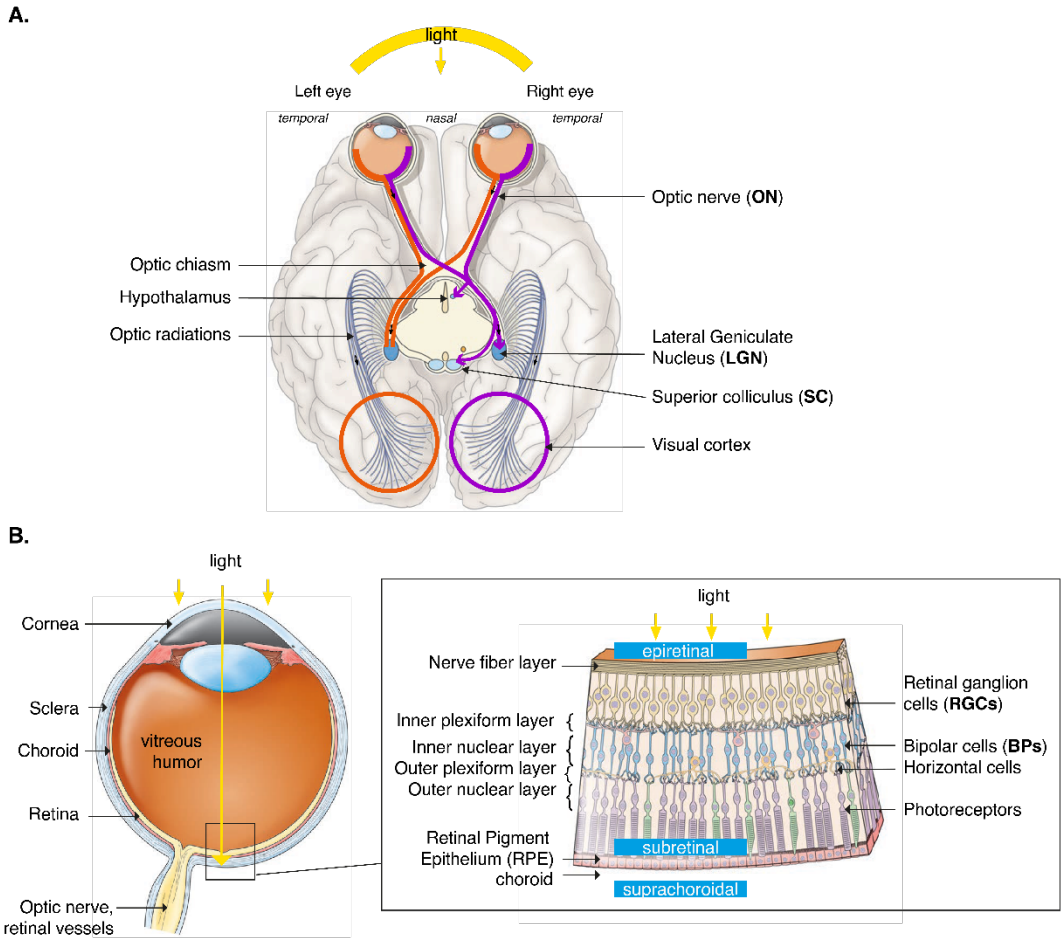

Fig. 12 Visual information processing, modified from (Purves, 2018). **A.** Visual pathway. Retinal Ganglion cells (RGCs) project onto the optic nerve (ON). At the optic chiasm, the nerves cross ("decussation") and project mostly onto the superior colliculus (SC) but also onto the lateral geniculate nucleus (LGN) in the thalamus, before going to the right/left visual cortex via the optic radiations. **B.** Anatomy of the human eye and retina. Light transduction occurs at photoreceptor cells level, protected by the retinal pigment epithelium (RPE). Depolarization is transmitted to bipolar cells (BP) which in turn depolarize the retinal ganglion cells (RGC), emitting action potentials propagating through optic nerve fibres. Depolarization is mediated by horizontal cells and amacrine cells. Classical locations of retina implantation are indicated in blue (epiretinal, subretinal and suprachoroidal).

Other common diseases are characterized by impairment at higher level on the visual pathway. For instance, **glaucoma** is a chronic disease often but necessarily characterised by an increased intraocular pressure and is also a common complication of diabetic retinopathy. Progression of the disease leads to retinal ganglion cell degeneration and the resulting degradation of the optic nerve. As the optic nerve (ON) relays the visual information from the retina to the brain, pathologies at this level similarly contribute to visual impairment and blindness development. As for AMD and RP, the higher visual areas on the visual pathway remain intact, hence the exploration of cortical prostheses directly stimulating the brain.

b. Diagnosis

i. Visual acuity

Blindness is legally defined in Europe as having a visual acuity (VA) score “less than 3/60 (0.05 decimal) or a visual field of less than 10 degrees”. This means that the patient has to stand at 3 m from the chart to perceive what healthy subjects would see at 60 m. VA translates the spatial resolution that can be seen and can be scored on different scales in ophthalmology (Snellen chart, logMAR chart, Landolt C chart). A visual acuity of around 0.4 is needed for normal reading, although the International classification of diseases already consider a person with a visual acuity lower than 6/18 (0.3) to have mild vision impairment in Europe.

ii. Visual Evoked Potentials

In ophthalmology, Visual Evoked Potentials (VEP) tests are often used to verify integrity or detect abnormalities in the visual pathway functions, which might reflect neurological disorders (Odom et al., 2016). By sending light into the eye, electroencephalograms (EEGs) are able to record in a non-invasive manner post-synaptic signals called **visually evoked potentials** (**VEPs).** In preclinical research, scientists often take advantage of the easy access and retinotopy of the visual pathway to validate the functionality of novel electrode materials and electrophysiology designs, all the more as the visual cortex is easily accessible by craniotomy and the visual pathway is relatively well-known. For instance, VEPs have been recorded on mice to evaluate flexible PDMS-based ECoGs fabricated using novel wafer processing methods (K. Y. Lee et al., 2020), on minipigs to demonstrate chronic functionality of soft and conformable grids (Fallegger et al., 2021), on white rabbits to validate printable platinum-based electrodes (Borda et al., 2022), or on NHPs to validate functionalities of the WIMAGINE platform, a 64-electrode ECoG array (Charvet et al., 2013). In line with this predicament, we recorded VEPs in two of our studies with respectively a custom full-diamond-based ECoG (see §II.A) and with a graphene-based transistor cortical array (see § II.B) to demonstrate their abilities as neural interfaces to probe cortical circuits.

Definitions of VEPs and their characteristics evolved with scientific advances. The International Society for Clinical Electrophysiology in Vision (ISCEV) standards for clinical visual evoked potentials differentiates pattern VEPs generated by checker-board stimuli from flash VEPs generated by light flashes (Odom et al., 2016). For the latter case, short 1 Hz-flash stimulation protocol with luminance at 3 cd.s.m^{-2} is preconised.

Although shapes of recorded VEPs vary depending on the preclinical or clinical set-ups, some peaks are consistent across experiments for normal VEPs. The standard nomenclature names them “P” or “N” for positive or negative peaks, followed by the number of the peak identified or by the time of the peak (Fig. 13). In practice for animal models, the N1 and P1 peaks on Fig. 13 are often missed but there has been some consistency across studies for the latency to light onset (You et al., 2011; Borda et al., 2020). In humans, N2 is often recorded around 90 ms and P2 around 110 to 120 ms for flash stimuli (Creel, 2019) while in Sprague-Dawley rats, You et al. recorded them respectively at 56.21 ms and 85.33 ms (You et al., 2011), with the last negative peak N3 occurring at 163.29 ms.

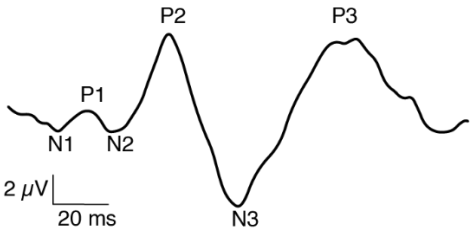

Fig. 13 Classical shape of visually evoked potentials (VEPs) and corresponding peaks.

The precise cortical regions involved in the occurrence of the different peaks are still not very clear (Creel, 2019) yet some studies showed that peaks before 100 ms originates from the primary visual cortex V1. Peak P2 can occur at an early or late time which respectively reflect signals from the dorsal extra striate cortex of the middle occipital gyrus and the ventral extra striate cortex of the fusiform gyrus.

Peak N3 also has an early and late phase which arise either in the primary visual area or from parietal lobes (Di Russo et al., 2002). For pattern-reversal stimuli induced-VEPs, 3 usual peaks named N75, P100 and N135 are found at 75 ms (negative), 100 ms (positive) and 135 ms (negative). In contrast, the amplitude of the signal measured depends strongly on the electrode material used and the experimental conditions.

c. Treatments

Treatments for these retinal diseases aim at slowing down/stopping the degeneration process. Unfortunately, many of these diseases have no treatment or many patients are still evolving up to blindness. For example, injections of antibody fragments complexing the vascular endothelial growth factor (VEGF) can successfully hinder wet AMD progression. Topical treatments can also prevent the increase in intraocular pressure leading to glaucoma and blindness. Despite these treatments, AMD and glaucoma still remain the first causes of blindness in our developed countries. Other paths enabled by modern biotechnologies are therefore being investigated, by targeting the healthy neurons closest to the pathological site in the visual pathway. Gene therapy, stem cell replacement, optogenetics are on this non-exhaustive list but visual prosthesis remains the most advanced strategy for restoring vision to date while being perhaps the most ethically acceptable one so far.

I.B.2. Past and present visual prostheses based on electrical stimulation

Visual prostheses aim at restoring some vision by electrically stimulating the visual system. Such electrical stimulation of the remaining parts of the visual pathway can generate visual percepts, called “phosphenes”, that are similar to a light flash. In 1755, Charles LeRoy was the first one to report phosphenes by stimulating the outer surface of the eye of a patient affected by cataract. During the first world war, the same observations were reported on wounded soldiers stimulated at the cortical level (Löwenstein & Borchardt, 1918)

a. Concept

Electrical stimulation in the extracellular space of neurons creates an electric field, which affects the transmembrane potential. The disturbance of the charge equilibrium leads to an influx of cation on the cathode-like membrane side (electron-receiver side). If the apparent membrane depolarisation reaches a certain threshold (-60 mV), the neuron generates action potentials or spikes. After the depolarisation, there is an outflux of potassium through classical potassium pumps to achieve again equilibrium. However, because the anode-like side cannot be depolarised by the electrical stimulation, a higher stimulation amplitude (tens of mV) compared to natural depolarisation is needed to elicit neural activity (Goetz & Palanker, 2016).

Throughout the second half of the 20th century, more than 40 international research groups attempted to restore artificially the electrical communication between neuronal circuits in the visual system at the damaged locations (Lorach et al., 2013; Lewis et al., 2015). The retina and the cortex were uncontestably the most targeted approach for visual restoration therapies based on electrical stimulation, although some strategies did succeed in the LGN (Panetsos et al., 2011; Pezaris & Eskandar, 2009) or the optic nerve (Borda et al., 2022; Delbeke et al., 2001; Sakaguchi et al., 2009). In the following section, we will introduce the retinal and cortical visual prostheses, which are both relevant to my PhD work.

b. Retinal prostheses

When photoreceptors have degenerated, retinal prostheses aim at reactivating the residual retina in patients affected by AMD or RP. Electrode arrays in contact to the residual retina generate a current stimulation pattern to elicit form perception. Three locations for the electrode array have been explored

so far: subretinal, epiretinal and suprachoroidal. Subretinal prostheses are implanted between the Retinal pigment epithelium (RPE) and outer plexiform layer (Fig. 12.B), while epiretinal prostheses are attached in the vitreous humour, onto the retinal surface close to the optic nerve fibres. Suprachoroidal prostheses are implanted behind the choroid. The implants are usually inserted the closest possible to the macula. Overall, each method has their pros and cons. For instance, the surgery for epiretinal implantation does not need to detach the already diseased retina as requested for subretinal arrays, but in the latter case the direct stimulation of bipolar cells triggers a network-mediated response by using the natural retina information processing, allowing a natural activation of amacrine and RGCs and resulting thereby in a more "natural vision". Suprachoroidal implants might also be less traumatic, but they require higher stimulating currents because of their more distant location from the retinal cells leading to greater current spreading and thus lower spatial resolution.

Fig. 14 illustrates the different retinal prostheses which entered into clinical trials. From a clinical point of view, the first subretinal array which went into clinical trials was the **Artificial Silicon Retina** (ASR) (Fig. 14.A), implanted subretinally in more than 40 American RP patients from 2000 to 2010 (Chow et al., 2010). The **Optobionics** company translating the research into the market ceased activity in 2007 because the implant was not producing any visual perception.

Meanwhile, the company **Second Sight Medical devices** (USA) entered in clinical phase for the Argus I epiretinal array (Fig. 14.B.i) showing visual perception in blind patients with only 16 electrodes (Humayun et al., 2003). The upgraded model, the **Argus II** epiretinal interface (Fig. 14.B.ii), was commercialised and implanted in more than 350 patients worldwide with variable results but always a sustained efficacy and up to letter reading (Humayun et al., 2012; Luo & Da Cruz, 2016). This retinal prosthesis, Argus II, which became the first ever commercialised product, consists of three distinct parts. An external device (part1: camera, photovoltaic captors) captures the image of the visual scene, which is then transformed by an image-processing unit (part 2) into a corresponding electrical stimulation pattern applied to the electrode arrays (part 3) interfacing with the neurons. The amplitude of the current applied is proportional to the pixel intensity, but also affects pixel resolution with lateral current spread.

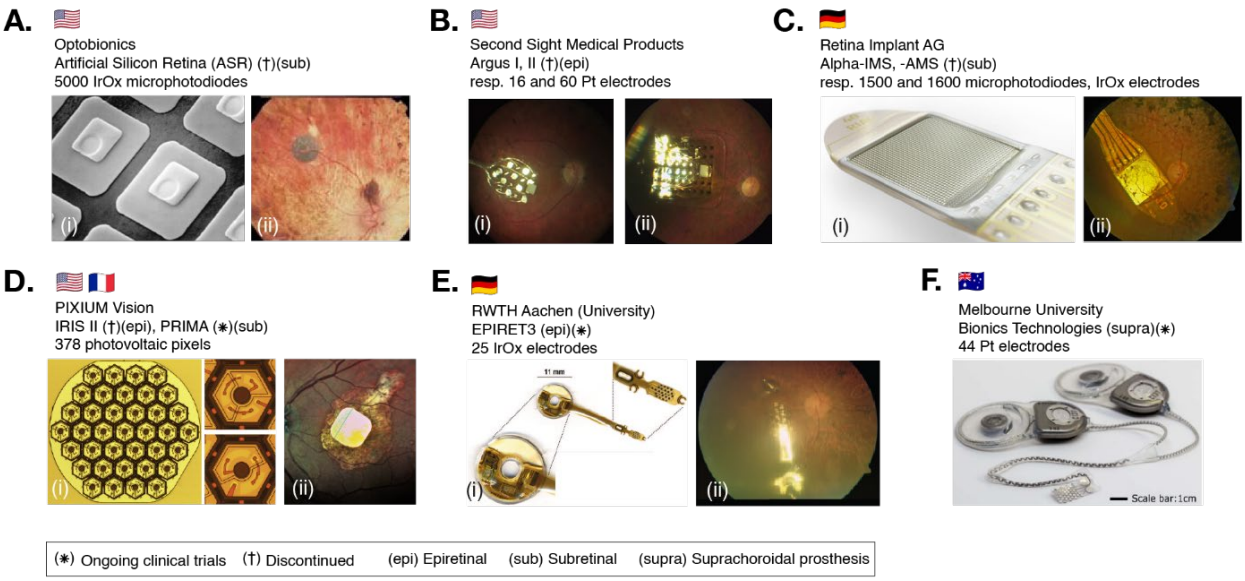

Fig. 14 Retinal prostheses which reached clinical phase. **A.** Artificial Silicon Retina (ASR) subretinal array, produced by Optobionics in the USA. (Chow et al., 2001) (i) microscopic zoom on micro-photodiodes. (ii) eye fundus of a RP patient implanted with the ASR. **B.** Epiretinal arrays produced by Second Sight Medical Products in the USA. Eye fundus of (i) Argus I and (ii) Argus II. **C.** Subetinal implant produced by Retina Implant AG in Germany. (i) eye fundus of a RP patient implanted with the alpha-AMS chip (Zrenner et al., 2017). (ii) schematics of the implant head with microphotodiodes. **D.** Photovoltaic subretinal prosthesis by Pixium Vision (France, USA). (i) photovoltaic pixels for preclinical studies under microscopy (Lorach et al., 2015) (ii) eye fundus of an AMD patient implanted with the PRIMA chip (Palanker et al., 2020). **E.** EPIRET-3 implant by RWTH Aachen University. (i) implant with coil and transmitter (ii) eye fundus of a RP patient implanted with EPIRET-3 (Roessler et al., 2009). **F.** Bionics Technologies Generation 2 device produced at Melbourne University (Petoe et al., 2021)

In Germany, around the same times, research on subretinal implants at the University of Tübingen led to the creation of **Retina Implant AG** company. Their second product, the alpha-AMS, was commercialised and implanted in 72 RP patients with again mixed results but up to word reading

(Zrenner et al., 2011). Inspired by the ASR chip, the alpha-AMS prosthesis was composed of micro-photodiodes on silicon substrate with iridium oxide (IrOx) electrodes (Fig. 14.C). However, an additional circuit to amplify currents generated by the photodiodes was added to reach levels activating neurons, and thus a battery supply had to be connected through a wire extending beyond the ear. Unfortunately, both companies which reached the market, Second Sight and Retina Implant, ceased their activity in 2019. In September 2022, Second Sight Medical Products merged with Nano Precision Medical to become Vivani medical company, while resuming activity only on their cortical implant, Orion.

In Aachen (Germany), the **EPIRET-3** wireless epiretinal prosthesis was tested in 6 RP patients for surgery feasibility (Fig. 14.E). As the German law forbids clinical studies longer than 28 days for academic research, functionality of the prosthesis was not tested (Roessler et al., 2009). The team is currently optimising its epiretinal array with a wider field of view (VLARS prosthesis, (Lohmann et al., 2019)) with integration of photosensors in their new OPTO-EPIRET wireless prosthesis (Schaffrath et al., 2021) while improving their surgery technique.

Several other projects are also close to clinical trial stages. The subretinal chip of the **Boston Retinal Project** has been implanted in rabbits and tested for biocompatibility in minipigs with satisfactory outcomes (Rizzo, 2011). The team launched the Bionic Eye Technologies start-up, who microfabricated a 256-electrodes arrays with gold wires and IrOx-coated electrodes (D. Shire et al., 2020).

The French company **Pixium Vision** is undergoing a phase III clinical trial (NCT04676854) in 38 AMD patients from 6 different European countries implanted with the wireless **PRIMA** subretinal prosthesis containing 378 electrodes, each with a diameter of 100 µm (Fig. 14.D). Its previous epiretinal Intelligent Retinal Implant System (IRIS) II prosthesis with 150 platinum (Pt) electrodes has been discontinued because of implant lifespan issues upon 2016-2017 6-months clinical trials in 10 RP patients (Muqit et al., 2019). The new PRIMA implant relies on photovoltaic hexagonal IrOx shaped-pixels which converts infrared light into electrical currents sent to the remaining retinal neurons (Mathieson et al., 2012). Like the first ASR, this subretinal prosthesis is totally wireless but stimulated by googles in the infrared range to enhance the light intensity. Patients have reached a visual acuity between 20/460 to 20/560 allowing word reading (Palanker et al., 2020) and fusion of the natural peripheral vision and the artificial central vision (Palanker et al., 2022). Daniel Palanker, who produced the initial PRIMA prototype, has recently proposed an advanced design of the implant to enhance further the patient visual acuity (Wang et al., 2022).

Among promising future devices, the **POLYRETINA** epiretinal soft and wireless implant manufactured in Switzerland at EPFL also proved functionality in minipigs with the perspective to generate a very wide field retinal prosthesis (Chenais et al., 2021). Intraretinal stimulation strategies with a 3D electrode array are also explored to improve neural interfacing and hence current delivery. The NR600 device designed by Nano Retina company and Tel Aviv University (Israel) is composed of needle-like silicon electrodes with titanium nitride (TiN) tips. Visual perception tests of 9 implanted patients in a preliminary clinical feasibility study showed improvements of daily tasks performance (Yanovitch et al., 2022).

The - less common - suprachoroidal approach is being investigated by the Australian team behind the Bionics Vision Technologies implants. After a conclusive clinical phase I, 44-Pt-electrode arrays have been implanted in 4 RP patients without any serious adverse effects (Petoe et al., 2021).

c. Cortical prostheses

For diseases in which the optic nerve is damaged such as glaucoma or diabetes, electrical stimulation for restoring vision can only occur with electrode arrays placed in higher visual areas such as at the surface of the visual cortex V1 (subdural) or within the brain tissue itself (intracortical). After early observations on blind war-wounded patients, the development of cortical prosthesis really started in the 1960s with the implantation of subdural electrodes in the occipital lobe by Button and Puttnam (Button & Putnam, 1962), and subsequently when in the 60s, Brindley and Lewin implanted a 80 electrode array on the visual cortex (Brindley & Lewin, 1968). The patient described seeing small spots of white light or cloudy phosphenes upon electrical stimulation of a single electrodes at several volts (>8V). They could even discriminate patterns when several electrodes were simultaneously activated. Dobelle followed on a similar path to demonstrate braille reading or form perception in patients, yet the

stability of this restored vision remained problematic (Dobelle et al., 1976; Dobelle & Mladejovsky, 1974; Dobelle, 2000).

These pioneering works were recently reproduced with a superficial cortical prosthesis. **Orion**, a subdural prosthesis developed by 2nd Sight company (USA) showed form vision by the sequential stimulation of different points with an expected poor dynamics vision (Beauchamp et al., 2020). Studies on non-human primates (Tehovnik & Slocum, 2007) showed that intracortical electrodes required lower currents (1-100 µA) with respect to superficial electrodes needing several mA (Beauchamp et al., 2020). The Fernandez's team at the Universidad Miguel Hernandez (Spain) confirmed these results in blind patients with the **CORTIVIS** brain-computer interface based on a Utah intracortical array (Fernández et al., 2021). In this ongoing clinical trial, a second patient was included again for a limited 6-month period after the promising results shown by the first one. These penetrating electrodes were shown to elicit form perception in a much more dynamic mode by the direct stimulation pattern presentation. Unfortunately, Utah electrode arrays also generates major fibrotic reactions around the array in non-human primates (NHPs) excluding thereby long-term applications in patients in current state (X. Chen et al., 2023).

Different approaches with novel electrode materials are developing to avoid these fibrotic reactions. *In vivo* chronic assessment on canine subjects of the Wireless Floating Microelectrode Array (WFMA) developed at the Illinois Institute of Technology (Chicago, USA) showed no delamination nor degradation of the activated iridium oxide films electrodes (AIROF) (Frederick et al., 2022). Meanwhile, the Gennaris Bionic vision wireless intracortical system created by the Monash Vision Group in Australia have recently gathered funding to go into clinical stage, after *in vivo* tests in sheep (Rosenfeld et al., 2020).

I.B.3. Retinal electrical stimulation strategies

There is no strict convention among the neuroprosthetics community regarding electrical stimulation protocols, although the choice of stimulation parameters plays on the stimulation efficiency and might hence influence the design of the visual prosthesis. Usually, continuous biphasic pulsatile waves are sent to the targeted organ. The first phase depolarizes the nearby neurons while the second phase balances the charges sent during the first phase, in order to avoid charge accumulation on the electrodes (Merrill et al., 2005). Sometimes, a short interphase time is added to avoid reversing completely the effect of the first pulse. Key parameters playing on stimulation efficiency are the location of the electrodes (and therefore, the stimulated cells), the pulse polarity, amplitudes and pulse duration.

a. Pulse polarity

Cathodic- or **anodic-**first stimulation induce a different polarity on the targeted cell membrane (Fig. 15.A-B). When anodic electrical pulses are sent, the membrane underneath the electrode becomes more positive, attracting in the intracellular space the negative charges. This results in strong hyperpolarisation close to the electrode and depolarisation more far away. The contrary occurs in cathodic stimulation, and explains why traditionally cathodic stimulation are preferred, being more efficient with less current injection than anodic ones to depolarise the cells (Merrill et al., 2005). We will discuss hereafter the different strategies, with a focus on retinal stimulation only.

b. Pulse location and targeted cells

In the retina, electrical stimulation patterns sent from the artificial chips should resemble as much as possible natural pattern so that the brain process them accordingly. The subretinal electrical stimulation paradigm is in this sense more advantageous as it is network-mediated (Fig. 15.C, bottom): it lets the bipolar cells modulate the stimulation so that the afferent activity sent by the to the higher orders are more natural. In the epiretinal location, implants can directly depolarize RGCs and trigger action potentials. Epiretinal stimulation is a "direct" stimulation which also activates axons bundles lying between electrodes and RGCs (Fig. 15.C, top) whose soma are more distant from the target soma, creating unattended elongated visual percepts. This axonal stimulation plays in favour of subretinal stimulation, believed to create more "natural" signals. This is nonetheless not entirely true because

current technologies do not allow selective activation of ON and OFF bipolar cells. When the subretinal electrical stimulation is repeated too much, desensitization of the RGCs happens and is most likely at play in percept fading (Freeman & Fried, 2011; Jensen & Rizzo, 2007).

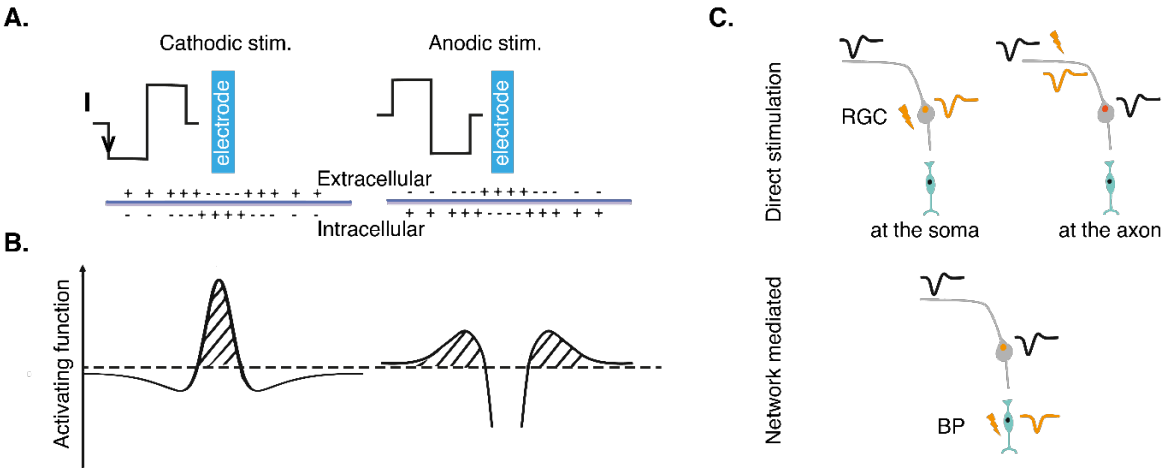

Fig. 15 Retinal stimulation strategies. Modified from (Yue et al., 2016). **A.** Cathodic- or anodic-first biphasic pulses and respective cellular membrane polarity. **B.** Corresponding activating function with activated membrane locations (stripped areas).

c. Relation between pulse amplitude, duration, polarity and location

RGCs usually fire around tens of milliseconds in normal visual processing and around 5 ms in artificial direct activation paradigm (Jensen et al., 2005). The stimulation thresholds (lowest amplitude to trigger an action potential) are lower using cathodic-first pulses (Boinagrov et al., 2014; Fried et al., 2006). Short pulses usually around 10 to 100 µs are more favourable for direct RGCs activation and longer pulses of above 0.1 ms aim at indirect activation mediated by the BPs and horizontal cells. Sinusoidal signals with frequencies below 25 Hz were also found to be effective in indirect RGCs activation (Freeman et al., 2010). Additionally, there is a dependence between the current amplitude and duration. For shorter pulses, a higher amplitude is needed in order to trigger an action potential from RGCs (Boinagrov et al., 2014; Sekirnjak et al., 2006).

In the inner plexiform layer, bipolar cell neurons are not firing axon potentials in a digital mode but undergo sustained graded depolarizations according to the light level in an analogue circuit mode. As a consequence, anodic-first stimulation with longer pulses demonstrated *in vitro* more efficient activation of the bipolar cells (Boinagrov et al., 2014; Lorach et al., 2015; Paknahad et al., 2021). Anodic-first symmetric biphasic pulse of more than 8 ms lowered the stimulation threshold compared to cathodic-first biphasic pulses of same intensity (Paknahad et al., 2021). This is because sodium and calcium channels are respectively located on the RGC and the BPs facing the epiretinal side (Palanker et al., 2020).

d. Counter electrode configuration

The counter electrode configuration is also a key feature in the design of retinal prostheses, as the injected current through the electrode travels in retinal tissues back to the return electrode as in the Argus II implant or the Alpha AMS implant. Joucla et Yvert showed an expected better focalisation of electrical current in the case of ground electrodes as compared to monopolar stimulation using computational models (Joucla & Yvert, 2012; Bendali et al., 2015). Local return electrodes strategies have been explored, as well as using multiple electrodes of the array as one large return electrode (Matteucci et al., 2016). It is also possible to modify electrode size and shape to reduce distance to neurons and avoid cross-talk. Pillar-shaped electrodes are one example among others (Bendali et al., 2015; Butterwick et al., 2009; Djilas et al., 2011; Flores et al., 2018; Ho et al., 2019). The PRIMA implants include such a return common grid electrode allowing a high resolution with RGCs sensitive to a single electrode (Prévot et al., 2019).

I.B.4. Current challenges

Past and current visual prostheses which reached the clinical stage were all composed of metal-based electrodes, and most of them with silicon substrates. Despite encouraging clinical results, the prostheses still do not meet the end-user's needs, hastening the collapse of previously mentioned companies.

Indeed, there is a constant gap between patients' expectations and clinical trials results. Overall, there is always a significant difference during prosthesis evaluation tests (objects recognition tasks, high-contrast letters reading, standardised screen tasks) between prothesis switched ON and OFF (Muqit et al., 2019; Stingl et al., 2013). In the first stages of the clinical trial of the alpha-IMS (Stingl et al., 2013), only 5 out of 9 implanted patients declared the implant useful for daily tasks. In some cases, disappointments can be associated with the limited spatial resolution and image fading. Spatial resolution can be improved from a technical point of view by downsizing the electrodes, in order to stimulate one neuron at a time and reduce cross-talks. However, with classical metal-based electrodes, decreasing the diameter of the electrodes goes in pair with increased impedance and reduction of electrochemical surface available for charge injection.

Although the Alpha AMS contained 1500 electrodes, the spatial resolution was only slightly better than the one of SecondSight, which suggest other factors influencing stimulation efficiency, such as the return-electrode configuration but also the distance between targeted neurons and the implant which enlarge with time and gliosis. Indeed, the two prototypes from Retina Implant AG respectively lasted in average 0.6 and 3.3 years implanted in patients. Explantations were mostly due to failures (Daschner et al., 2017). Metal-based electrodes and silicon substrates also show important mismatch in terms of stiffness with neural tissues, causing large fibrotic reactions when chronically implanted, as mentioned previously. Moreover, they are subject to degradation and corrosion if the implant packaging shows defect.

In consideration of past clinical results, new innovative materials for the electrodes and substrates could be a solution to tackle biocompatibility issues while improving stimulation efficiency. In this thesis, we took advantage of the promising electrochemical and chemical-physical properties of reduced graphene oxide electrodes on flexible arrays to explore its stimulation capabilities, as a part of the research on next-generation prostheses (see §III).

I.C. Reading for Epilepsy

Besides electrical stimulation functionality exploited for neural rehabilitation such as vision restoration, BCIs also grant the possibility to **record** neural signals and decipher neural mechanisms still partially or totally non-understood. Seizures (fast abnormal brain oscillations) and cortical spreading depolarizations (infraslow waves of near-complete depolarisation of neurons and glial cells) which occur during epilepsy diseases fall into that category.

In the scope of the Graphene Flagship, a European Commission funded innovation project, we explored the potential of a graphene-based electrophysiology tool for measuring both high and infraslow frequencies, particularly suited for epilepsy studies. Our work described in section §II.B provides insights into the advantage of simultaneous DC-coupled recordings with functional ultrasound imaging (fUS) of the brain in a preclinical rodent model of acute seizures, as a unique platform to investigate the neurovascular coupling during seizures and CSDs. One could think that similar technological platform could one day be used clinically to monitor patients and help their diagnosis or treatment by providing a 4D picture of the whole brain with accurate temporal and spatial resolution.

The next section gives an overview of the state of the art from a physiological, cellular and clinical point of view with a particular emphasis on the electrophysiology tools used to investigate their link in the context of neurovascular coupling research.

I.C.1. Epilepsy disease

a. Definition

Epilepsy is a chronic neurological disorder which affects more than fifty million people worldwide. Beneath this generic term hides a family of diseases with various causes and symptoms, all characterised by **seizures**, and more recently sometimes associated with the occurrence of **cortical spreading depolarisations** (CSDs). The International League Against Epilepsy (ILAE) refined the definition of epilepsy in 2014 as a brain disorder characterised by either “At least two unprovoked/reflex seizures occurring more than 24 h apart, a single unprovoked/reflex seizure with a probability of further seizures similar to the general recurrence risk (at least 60%) after two unprovoked seizures, occurring over the next 10 years; diagnosis of an epilepsy syndrome” (Fisher et al., 2014). Because of the detrimental neuronal consequences of epileptic seizures, the comorbidities represent a significant societal burden (Stafstrom & Carmant, 2015).

b. Diagnosis

Diagnosis of epilepsy syndromes relies on the patient’s history and neurological examinations. Seizures are not always associated with visible motor manifestations hence the utility in recording brain signals in presumably epileptic patients with electrophysiology tools.

Electroencephalography (EEG) and electrocorticography (ECoG) measure the local superposed extracellular potentials from neurons in the brain. Electrophysiological events which can be recorded during seizures are interictal spikes and fast oscillations of around hundreds of Hertz. Typical oscillations are shown on Fig. 16.A. EEGs are measured generally on the scalp with gold cup electrodes (Fig. 16.B) and usually serve as a confirmation of the diagnosis and help to classify the epilepsy type. A significant change in EEG signals usually correlate with a change of consciousness and/or behaviour.

EEG represents the most common clinical non-invasive electrophysiology method to record brain signals. However, EEGs suffer from signal attenuation because of the skull isolation. On the contrary, electrocorticography arrays (**ECoGs**) are placed directly on the dura matter or directly on the cortex surface, and their proximity to the brain offer better quality signals. This is why in preclinical research, ECoGs are preferred despite the necessity to expose the brain by craniotomy.

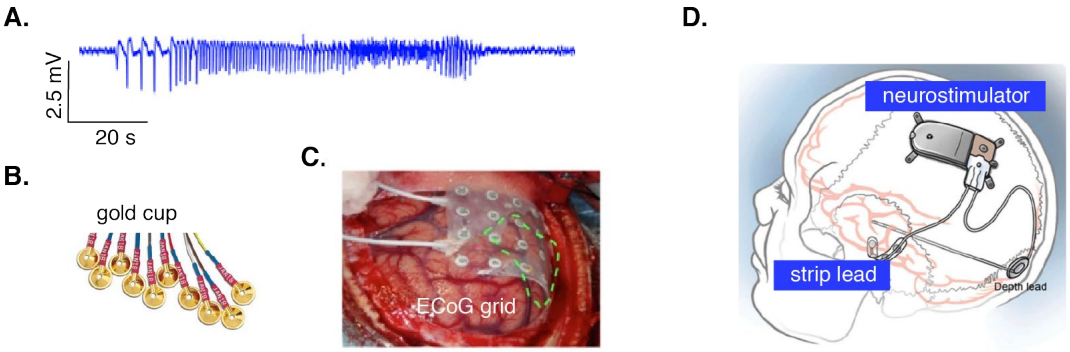

Fig. 16 Epilepsy diagnosis and treatments. **A.** Typical seizures (ictal activities) measured with ECoGs after high-pass filter (>0.1 Hz) from (Wykes et al., 2022). **B.** Electroencephalography (EEGs) gold cup electrodes used in clinical diagnosis of epilepsy. **C.** Clinical use of electrocorticography (ECoG) grids to localize epilepsy onset foci prior to brain resection surgeries (Demuru et al., 2020) **D.** Neuropace RNS® system for chronic closed-loop stimulation of the seizures onset zones for surgery refractory patients. Modified from (Jarosiewicz & Morrell, 2021).

c. Treatment

Current treatments aim at improving the life of epileptic patients, and vary depending on epilepsy type, etiology and patient history.

Commercialized antiseizures drugs are used to prevent or control the seizures in most of the cases. They can act for instance on inhibition of Na-channels pumps (carbamazepine) or voltage-gated Ca2+ channels (ethoxuximide) in order to prevent depolarization, or blocking of glutamate receptor (perampanel) (Vera-González, 2022). Despite their relatively proven efficacy, they do come with side effects such as sleepiness and still allow for occasional seizures. - The mechanism of action is still

poorly understood so that most patient will need months to years of trial and error with combinations of anti-epileptic drugs (usually three) until seizures are controlled. If the patient is resistant to antiseizure drugs (~30% of the cases), alternative options need to be considered, which range from ketogenic diet to more invasive methods such as partial brain tissue removal in open skull surgeries, vagus nerve or cortical electrical stimulation. Even though more than 30 new anti-epileptic drugs were approved over the last 40 years the number of people with drug-refractory epilepsy has not changed.

In clinical set-ups, ECoGs such as the strips on Fig. 16.C are already widely used by neurosurgeons for epilepsy resection surgery to locate the seizures foci and are evaluated for chronic stimulation of the detected seizures foci (Nune et al., 2019; Pellegrino et al., 2016; Ren et al., 2019), with often the help of prior functional neuroimaging methods (fMRI, PET, CT). Even then, surgery cannot ensure definite eradication of epilepsy symptoms, as 30 to 40% of the patients who undergo temporal lobe removal surgery will experience again seizures in the year after surgery (Engel et al., 2003). In some medically-intractable epilepsy cases, surgery is not even possible because the seizures onset zones are multiple and located in not accessible deeper zones.

Clinical ECoGs for long-term recording and/or stimulation purposes which could match the requirements for biocompatible, mechanically stable, and electrically efficient prostheses design are taking a new turn with the development of the **RNS®** system from NeuroPace®, shown on Fig. 16.D. This commercial FDA-approved neurostimulator is an appealing solution for patients resistant to drug treatments which is implanted chronically intracranially near or at the epilepsy foci. The system can predict onset of seizures based on algorithms to launch stimulation at early times, thereby reducing the frequency of seizures (Jarosiewicz & Morrell, 2021). Even though the commercial implant is showing encouraging results for refractory epilepsy patients, 10% of the patients had site infection and bone flap osteomyelitis, associated with multiple replacement of the pulse generator yearly (Wei et al., 2016).

Chronic stimulation of the brain with the commercialised Neuropace RNS® closed-loop stereo-EEG-based system has been proven to be efficient to decrease seizures rates in such patients, up to 75% after 9 years of implantation and stimulation (Skarpaas et al., 2019). Such system is implanted in subdural near the epilepsy foci, chronically records ECoGs signals and sends electrical pulses when abnormal signals are detected (Nune et al., 2019).

However even these treatments do not control entirely the seizure patterns. There is still a gap to close before finding a definite cure to epilepsy due to poorly understood disease mechanisms.

I.C.2. Seizures

Seizures happen when neurons from the central nervous system (CNS) fire synchronously and abnormally in a large brain region, propagating sometimes to more distant regions. The period between two seizure events is called the interictal period, by contrast with the discharge period called ictal events. The period following seizures is the postictal period. Seizures are not specific to epilepsy, and can occur for example after primary brain injury, tumours, or infections.

Seizures can be classified as partial/focal or generalized. The most common partial seizures are the complex partial seizures, or psychomotor seizures. The patient can manifest impairments, hyperactivation of sensory systems (e.g. visual hallucinations if located in the occipital lobe) to loss of consciousness. Such seizures can spread to the whole cortex and become generalized seizures which episodes last 1 to 2 minutes. However, prolongation of generalised seizures can become status epilepticus condition which can lead to detrimental neuronal loss and death (book neurosciences). Generalised seizures can be clonic-tonic seizures, triggering convulsions or on the contrary absence seizures where the patient is unresponsive for a brief (few seconds) period. In those cases, the EEG usually shows 3 Hz oscillations.

Sometimes, epileptic spikes can trigger cortical spreading depolarizations. The association between the two cerebral perturbations have been recorded and demonstrated in rodents (Bonaccini Calia et al., 2022) and in humans (Fabricius et al., 2008) yet the exact neurovascular mechanisms linking the two remains unclear (Kramer et al., 2017). There is evidence for seizures occurring prior to CSD and vice versa. The spatiotemporal interactions between the two phenomena is poorly understood, but is now being actively investigated by numerous international laboratories.

I.C.3. Cortical spreading depolarisations (CSDs)

In the last few decades, **CSDs** have been associated with many neurological disorders, and among them, epilepsy. These slow waves of near-complete depolarisation of neurons and glial cells happen at infraslow frequencies (<0.1 Hz) and cannot be detected using classical alternative-current-based electrophysiology tools which high-pass filter the recorded signals between ~1-300 Hz in order to recover local field potentials (LFPs) with low noise. Therefore, clinically, it is impossible to measure CSDs on patients with classical EEG electrodes on the scalp. Moreover, during epilepsy events, seizures happen at high frequencies hence the difficulty to monitor both phenomena at the same time. The research around CSDs in the context of epilepsy is very recent but stimulates the development of more reliable electrophysiology tools to improve the real time monitoring of cortical signals in order to find the exact epileptic foci during resection surgeries, all the more as multi-modal monitoring has a non-neglectable plus-value for patients in neurocritical care (Dreier et al., 2018). Investigation of CSDs and seizures have provided insights into the understanding of epilepsy and could help potential therapeutic interventions aimed at modulating these phenomena (Dreier, 2011).

a. Definition

CSDs are propagating waves of near-complete depolarization of neurons and glial cells. They have been discovered first by Aristides Leao at Harvard Medical School back in 1944 by sending electrical discharges to the brain of anaesthetised rabbits and measuring neural activity using silver chloride electrodes (Leao, 1944). Often misused, the term “spreading depression” first described by Leao refers to the suppression of neural activity in electrode channels and is implicit during CSDs. CSDs have been associated with different pathologies such in stroke, migraine, ischaemia, traumatic brain injury (TBI), epilepsy, which explains why research on CSDs gained considerable interest over the last decades even though detailed physio-pathological mechanisms remain obscure.

CSDs are characterized by a slow potential change (SPC) with 3 distinct phases (Smith et al., 2006; Somjen et al., 1992), clearly visible using DC-coupling technologies (Fig. 17.A-B):

1. a fast-negative shift of 5 to 20 mV lasting 30 to 50 s corresponding to the drastic rise of extracellular $[K^+]_o$,
2. up to another local more negative maximum
3. and a slow shift back to baseline

CSDs propagate at a speed of around 2-6 mm/min in rabbits, rats, cats (S. Chen et al., 2008; Leao, 1944; Piper et al., 1991; Zhang et al., 2011; Nasretdinov et al., 2017). In humans with traumatic brain injury or intracranial haemorrhage CSD speeds were reported to be around 0.6 to 5.0 mm/min (Strong et al., 2002).

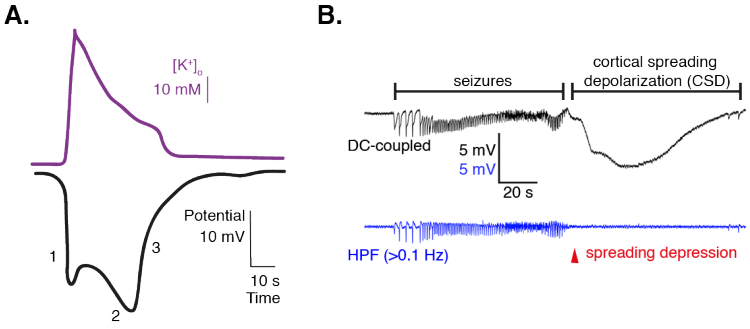

Fig. 17 Recordings of typical electrophysiology, ionic and metabolic signals during epilepsy-related events. **A.** Usual cortical spreading depolarisation (CSD) signal measured with DC-coupled technology and corresponding extracellular potassium monitoring [K+]o. Phase (1) corresponds to a fast negative shift of potential, followed by a slower but more negative shift (2) before a slow increase back to normal potentials (3). Modified from (Somjen et al., 1992). **B.** DC-coupled signals and high-pass filtered

(HPF) signals recorded using graphene-based transistors ECoG, showing seizures and seizures-associated CSDs. CSD in DC-channels is associated with spreading depression on HPF signals. Modified from (Wykes et al., 2022).

b. Electrophysiology measures of CSDs

Usual alternating current (AC) electrodes are set to only record signals above ~10^{-1} Hz, in order to prevent recording amplifier saturation. The **local field potentials (LFPs)** recorded this way consists in extracellular potentials around the intracortical electrodes, strictly speaking differing with ECoGs signals which are recorded usually under the dura (yet, the misappropriation between the two is common (Buzsáki et al., 2012)). Both LFPs and ECoGs signals have low amplitude signals (~10 µV) so after acquisition (sampling rate >10^3 Hz), they are amplified (~500 times) and filtered (~0.1-300 Hz) before analysis.

In contrast, CSDs are by definition **infraslow potential shifts** which can only be recorded with high fidelity using **direct current** (DC) coupled electrophysiology technologies. Such DC-coupled recordings represent a technical challenge as they necessitate stable electrodes and adequate amplifiers.

i. State-of-the-art

CSDs were first measured on anaesthetised rabbits using silver chloride wires (Leao, 1944), and **micropipettes** filled with saline is currently the gold standard for DC-recordings (Piper et al., 1991). However, they only allow recordings at few locations and are complicated to handle, whereas CSD necessitate multiple measure points (at least two) to be able to see the propagation from one point to another.

Ten mm diameter silver chloride (AgCl) disk electrodes were reported to record with reasonable stability low-frequency brain signals on patients' scalp (0.015 – 40 Hz) revealing CSDs in that frequency bandwidth (Bastany et al., 2020). Nonetheless, silver chloride wires have been shown to be chronically toxic for brain tissue (Li et al., 2016). Classical metallic electrodes in Pt or Au can also record infraslow frequency activity but their polarization induces potential shifts superposed onto actual physiological slow shift which hinders quality recordings.

As transistors can also record neuronal activities (Offenhäusser et al., 1997; Vassanelli & Fromherz, 1998), they were progressively incorporated into electrophysiology tools. In contrast with micropipettes, transistor-based technologies benefit from industrial-scale production methods and yield large signal-to-noise ratios because of the intrinsic signal amplification of the semiconductor device. Furthermore, multiple transistors can be assembled on a same array for brain mapping.

ii. Field-effect transistors (FETs)

Field effect transistors (FETs) are nowadays produced in mass and found in almost all electronic devices. A metal-oxide-semiconductor field effect transistor (MOSFET) is made of three parts: an insulator (dielectric layer), a thin semi-conducting layer and three metal electrodes. Classical MOSFETs are made with silicon (Si) as semiconductor material and SiO_2 as dielectric layer which separates the gate electrode from the semiconducting layer (Fig. 18.A). The FET amplifier operates as an electronic capacitor in which the voltage V_{GS} input at the gate electrode modulates the free carriers' density in the semiconductor channel and hence controls the current I_{DS} flowing between the drain and source electrodes. The output current I_{out} can hence be controlled by the applied voltage V_{GS} which sets the number of charge carriers in the channel.

In field effect transistors, there is an additional gate electrode which modulates the conductivity of the channel material. In other words, during operating mode, the semiconductor layer couples to the gate which allows conduction through the channel upon application of a source-drain voltage V_{DS}. The transconductance of the transistor corresponds to the efficiency of I_{DS} modulation by the gate. It depends on both the charge carrier mobility of the channel material and the interfacial capacitance (combining quantum capacitance and double-layer capacitance) (Hébert et al., 2018). FETs are particularly interesting for neural recording because the signal amplification is intrinsic to the system. This way, external noises are not amplified along with the signal of interest, resulting in higher signal to noise ratio (SNR).

As the performance of the transistor highly depends on the fabrication process, FETs have to be fully characterized beforehand. Critical parameters such as the mobility µ presumed constant and

intrinsic noise can be calculated from measured I_{ds}-V_{gs} and I_{ds} vs time characteristics. More importantly, characterization of the FETs helps to choose a constant V_{GS} for optimal recording.

iii. Graphene-based FETs (gFETs)

Miniaturisation of the transistors comes with reduction in size and thickness of the dielectric layer, creating current leakage issues and reduction in carrier mobility density and speed (Burghard et al., 2009; Sokolov et al., 2009). For the past decades, carbon-based materials were investigated as promising materials with higher carrier mobility but with also better biocompatibility and chemical stability for incorporation in new generations of brain-computer interfaces. Graphene is one of those materials, but its electronic configuration is such that there is no gap between its valence and conduction band hence the difficulties to “switch off” the material (Burghard et al., 2009; Reddy et al., 2011).

Recently, new technological advances contributed to the development of **graphene solution-gated field effect transistors (gSGFETs or gFETs)** using CVD monolayer graphene as channel material with a reference electrode in an electrolyte as the gate as schematised on Fig. 18.B (Hébert et al., 2018; Hess et al., 2013). gFETs are even more attractive because of their flexibility: CVD graphene can be transferred on soft substrate such as polyimide, parylene C to fabricate arrays allowing brain mapping (Fig. 18.C). Therefore, gFETs arrays suit better the conformability of the brain and can be placed underneath fUS probes for scientific studies, which can not be achieved with micropipettes. The mobility of charge carriers in CVD graphene are 2 order of magnitude higher than Si, traditionally used in FETs as channel semiconductor. As a consequence, the transconductance of graphene is high and benefits a high sensitivity recording, especially suited for infraslow recording. CVD graphene is also valuable on neural implants since it does not oxidise easily in aqueous media.

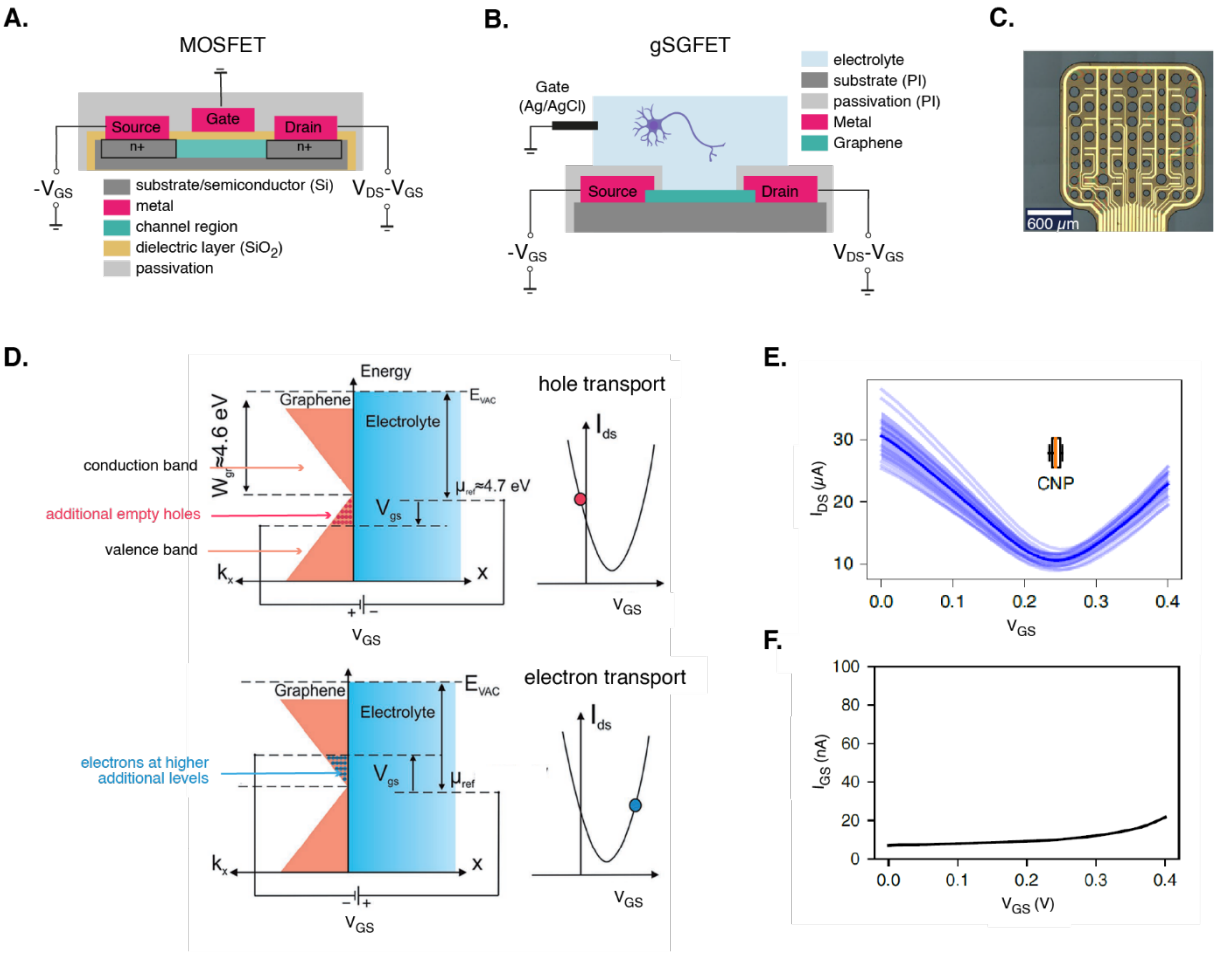

Fig. 18 Principles and characteristics of graphene-based transistors. **A.** Simplified schematics of metal-oxide-semiconductor field-effect transistor (MOSFET). The electrical field at the gate modulates the charge carriers (n+) from the source to the drain through the channel region. **B.** Schematics of a flexible graphene solution-gated field effect transistor (gSGFET). The substrate is polyimide,

and graphene serves as channel material. The gate is usually an Ag/AgCl electrode in contact with the transistor body through an electrolyte or the extracellular medium. **C.** The gSGFETs used in this doctoral study are made with 16 transistors on polyimide substrate. (from Masvidal-Codina et al., 2019) **D.** Simplified momentum-energy diagram explaining the conductivity modulation in graphene by application of a gate voltage (from Hébert et al., 2018) The electrochemical potential at the gate corresponds to 4.7 eV, and the working function of the graphene is around Wgr = 4.6 eV. **E-F.** Characteristic curves of gSGFETs in 10 mM PBS with a drain–source voltage bias (VDS) of 50 mV. **E.** Transfer curves of a gSGFET. Average characteristic curve is in dark blue. The charge neutrality point (CNP) corresponds to the minimum conductivity state of the (from Masvidal-Codina et al., 2019). **F.** Leakage current of the gSGFET at the source IGS for different values of VGS.

How does a gFSGFET function? When a voltage is applied at the gate, the last energy level of electrons occupation known as the Fermi level is shifted in the transistor channel made of CVD graphene. The lowering of Fermi level is lowered creates empty levels on top of the valence band (Fig. 18.D, top panel). The positive holes formed becomes the charge carriers and the graphene electrode becomes positively biased. When the Fermi level is increased (Fig. 18.D, bottom panel), electrons are populating an extra level of energy close to the conduction band. The charge carriers are the negative electrons; the graphene electrode is negatively biased. The graphene material can be therefore polarised both ways. If the Fermi level reaches the point at which the conduction and valence band meet, also called the Dirac point, the conductivity drops and charge carriers' mobility is at its lowest. The corresponding gate voltage V_{GS} to reach this point is called the **charge neutrality point** (CNP). It can be estimated by measuring the transfer curve of the transistor (Fig. 18.E) which corresponds to the relation between I_{DS} and V_{GS} for a set V_{DS} value. The CNP is reached at the minimum of the $I_{DS} = f(V_{GS})$ plot.

Several studies already operated the gFET technology and proved its high signal fidelity recovery as compared to a classical micropipette for DC signals (Masvidal-Codina et al., 2019) and its superiority in terms of SNR ratio but also stability in comparison to passive electrodes (Pt black or Au standard electrodes) for infraslow frequency. Moreover, gFETs have comparable characteristics for higher frequency brain signals on both anaesthetised (Masvidal-Codina et al., 2019) or awake animals (Masvidal-Codina et al., 2021). Such technology does not work only for ECoGs but can also be made into intracortical arrays to probe the deeper layers of the brain (Bonaccini Calia et al., 2022).

c. Cellular mechanisms

From a cellular point of view, CSDs can arise from different triggers. In normal healthy brain, high concentration of KCl can induce CSDs. In diseases, CSDs trigger an increase of extracellular potassium concentration $[K^+]_o$ which can reach a very high threshold of around 12 mM, hindering the usual $[K^+]_o$ clearance mechanisms (Somjen et al., 1992; Ayata & Lauritzen, 2015). The membrane resistance then drops, causing opening of cations channels, drastic increase of $[K^+]_o$ concentration up to 60 mM as seen on the purple plot of fig. 5.A and rapid intracellular intake of sodium $[Na^+]_i$, chloride ions $[Cl^-]_i$, $[Ca^{2+}]_i$ and water. All the ionic movements result in cell swelling so reduction of extracellular space and even more concentrated $[K^+]_O$. Release of many neurotransmitters such as aspartate, GABA, taurine, glutamate, the latter which facilitates spreading of CSD to neighbouring regions) have been reported in literature (Mody et al., 1987; Nasretdinov et al., 2017). This hyperexcitability phase is followed by a "depression" or silencing of neural signals.

d. Seizures-associated CSDs

Seizures and CSDs can co-occur in humans (Fabricius et al., 2008) and animal models (Masvidal-Codina et al., 2019; Zakharov et al., 2019). However, the dynamic interplay between seizures and CSDs is not clearly understood, as well as the relationship between high-frequencies local field potentials (LFPs), DC potentials and blood flow. Nonetheless, some aspects are consistent across studies. For instance, LFP silencing has been observed a few seconds after CSD onsets in both animals and humans (Bahari et al., 2018; Masvidal-Codina et al., 2019; Bastany et al., 2020). Then, the activity progressively recovers at the end of the CSD. Active and passive DC-shifts can be respectively observed at the onset and end of seizures (Ikeda, 1999; Bonaccini Calia et al., 2022). CSDs can complicate into sudden unexpected death in epilepsy (SUDEP) and have always been associated with pathophysiological mechanisms. Recently, spontaneous CSDs have been found to occur more easily when seizures spread out or generalize. The proof of CSD as playing an antiseizure role (Tamim et al., 2021) in models of

focal neocortical seizures even questions the essence of the mechanism: could CSD be physiological instead of pathophysiological? The topic remains controversial as there is no tangible demonstration of CSDs terminating the seizures and no proof on awake animals.

I.C.4. Neurovascular coupling during seizures and CSDs

Research interest for neurovascular coupling (NVC) has been growing for the past few decades. As in many other neurodegenerative diseases, the normal NVC is perturbed in epilepsy yet the exact underlying mechanism during seizures and CSDs remains unclear. Both seizures and CSDs are known to profoundly affect CBF. A better understanding of the neurovascular coupling impairment after CSDs and seizures (Chang et al., 2010; Dreier, 2011) may allow development of novel disease-modifying drugs. The advent of novel functional imaging techniques such as functional ultrasound imaging (fUS) granted access to information of vascular changes with high spatial resolution (~100 µm), in deeper brain structures and with a larger spatial spread compared to local ECoG mappings. Details on fUS and NVC are given in §I.D.1, while the following section presents the state-of-the-art on NVC studies during ictal events.

a. Vascular changes during seizures

Vascular and metabolic mechanisms during seizures are not entirely elucidated, but what is known is the consequent energy demand during epilepsy states caused by the neuron hyperexcitability. The most popular hypothesis favours the hypoxia and blood hypoperfusion, which, on the long run, cause neural damage and physiological changes (Simon, 1985). However, using Opto-microwave radar imaging systems (ORIS) (Bahar et al., 2006; Zhao et al., 2007) and Positron-emission tomography (PET) (Franck et al., 1986), studies in rats and humans show rapid decrease of blood oxygenation named the “epileptic dip” (Bahar et al., 2006) concurrent with an increase in cerebral blood volume (CBV) for the duration of the seizure. In epileptic patients, CBV variations seem to precede electrophysiology changes by 20 s (Zhao et al., 2007). To date, there is no consensus about whether local CBV increases or decreases during seizures. More recently, functional imaging techniques were exploited to decipher the neurovascular mechanisms at play during seizures. Sieu et al. recorded spontaneous epileptic seizures in the rat model, generic absence epilepsy rat from Strasbourg (GAERS), with fUS and EEG electrodes and found inverse electrographic-hemodynamic coupling between the caudate putamen (CPu) and somatosensory cortex plus thalamus (Fig. 19.A). These findings substantiate existing EEG-fMRI results (Mishra et al., 2011). However, fUS has only been coupled so far with AC electrophysiology tools, and other studies have used rarely DC-coupled electrophysiology, which explains perhaps the diversity of findings.

i. Vascular changes during CSDs

In normal tissue, depolarisation of the cells calls for an increased metabolic activity and hence an increase in blood flow to supply oxygen and nutrients to neurons, allowing repolarization. During CSDs, the haemodynamic response resembles the one of normal neuronal activation, but the rCBF increases more drastically, becoming a spreading hyperaemia reaching levels of more than 100%. This is due to the more acidic blood pH and drastic increased $[K^+]_o$ which helps vasodilation. After hyperaemia follows a prolonged period of oligemia (Lauritzen et al., 1982; Dreier, 2011).

This biphasic pattern has been confirmed across literature yet the shape of the waves varies depending on the animal model and the technique used. Piper et al. have reported this hyperaemic activity followed by prolonged oligemia in the gyroencephalic cortex of anesthetised cats using laser-doppler velocimetry upon pinprick (Piper et al., 1991), while Chen et al. recorded the biphasic change in anaesthetised rats using optical intrinsic signal imaging (OISI) upon pinprick (S. Chen et al., 2008). In humans, Mayevski et al. measured the biphasic change in severe traumatic brain injury patients (Mayevsky et al., 1996).

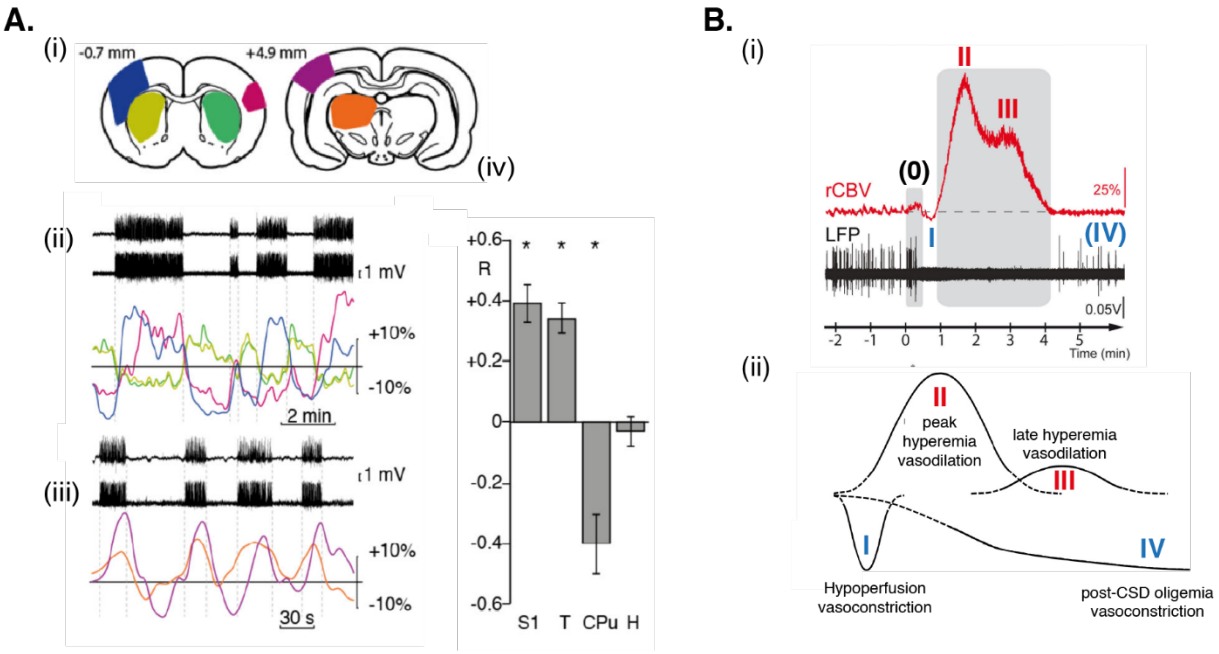

Fig. 19 Simultaneous fUS and electrophysiology measurements in literature. **A.** Recordings of spontaneous epileptic seizures in Genetic Absence Epilepsy Rats in both brain hemisphere. (i) brain areas where rCBV is averaged. (ii) bilateral seizures and bilateral fluctuations in CPu (greens). (iii) Synchronisation of oscillations in Thalamus (orange) and cortex (purple) (iv) Pearson correlation coefficient R between EEG and fUS average rCBV over somatosensory cotex (S1), thalamus (T), caudate putamen (CPu) and hippocampus (H). Modified from (Sieu et al., 2015). **B.** (i) (red) average rCBV in somatosensory cortex (S1) and (black) local field potentials recorded during CSD. 4 distinct phases were extracted (0, I,II, III, IV). (modified from (Bourgeais-Rambur et al., 2022) (ii) conceptual interpretation of vasomotor response to CSD. 4 phases have been identified. Modified from (Ayata & Lauritzen, 2015).

More recently, progress in **fUS** allowed visualisation of cerebral blood flow (CBF) propagation during 4-aminopyridine-induced acute CSDs in rats (Macé et al., 2011). Using the same technology but in the context of a migraine study, Bourgeais-Rambur et al. decomposed the CBF signals recorded using fUS in anaesthetised rats upon KCl drops on V1 cortex. LFP recordings using electrophysiology tools confirmed the spreading depression (brain silencing) during the occurrence of CSD. The four distinct phases found (Fig. 19.B.(i)) match the conceptual framework of vasomotor components described by Ayata & Lauritzen (Ayata & Lauritzen, 2015) who collected CBV response to CSD from different laboratories, animal models (rats, cats, mice), techniques (laser Doppler or speckle flowmetry) and different gaseous anaesthesia (isoflurane, halothane, urethane) (see figure 4 of Ayata & Lauritzen, 2015). Fig. 19.B.(ii) illustrates that four distinct phases can be monitored in blood signals in response to CSDs. Phase I, not always seen, is concomitant with the start of the DC-shift in electrophysiology and corresponds to a small amplitude vasoconstriction. Phase II is usually the most striking, characterized by a peak in blood volume increase (hyperaemia). Sometimes another hyperaemia component (phase III) is found in between phase II and IV. Then vasoconstriction/oligemia occurs very slowly and lasts for 1 or 2 hours (phase IV).

Despite all those findings, many interrogations still remain around the metabolism and vascular mechanisms during CSDs, and around the idea of an impaired neurovascular coupling or even neurovascular uncoupling occurring after the CSD (Lauritzen & Henrik Diemer, 1986; Chang et al., 2010).

ii. Animal models of seizures and CSDs

The many unknown and high stakes behind the research in neurovascular coupling dysfunction and the need of novel treatments for neurological disorders call for the implementation of relevant animal models. There exist different ways to replicate seizures and CSDs in preclinical research in order to investigate neurovascular coupling dysfunction.

The most common and easiest method to induce multiple CSDs in normal animals is the topical application of a saturated **KCl** solution (> 1M) to raise the extracellular potential. Other CSD-inducing chemicals involve metabolic inhibitors (NaCN for example) which poison oxidative metabolism, NaF and iodoacetate which interfere with glycolysis. Mechanical local stimulation or “**pinprick**” can trigger an isolated CSD. Some chemo-convulsant drugs are known to generate focal seizures. For instance, 4-

aminopyridine (**4-AP**) is a non-selective potassium channel blocker which limits extracellular potassium $[K^+]_o$, hence longer action potentials and increased excitability of neurons.

Genetically modified rodents also exist, such as the Genetic Absence Epilepsy Rats (GAERS) characterized by spontaneous seizures (Sieu et al., 2015). Acute stroke models are also often used to trigger CSDs and seizures. In swine, the middle cerebral artery occlusion model (MCAO) blocks the blood intake in the brain: the hypoxia triggers CSDs.

Studies on terminal CSDs usually monitor electrophysiological and physiological signals before, during and after cardiac arrest. In rats, the most common and easy model to implement is the injection of concentrated KCl (1 M) in the body. Injection of rose-bengal and activation of photothrombosis with green laser (Watson et al., 1985) is an acute stroke model.

Overall, research on CSDs is not only critical to provide better treatments and perhaps find a biomarker or neurovascular signature for epilepsy to tailor such treatments, but also to understand better the mechanisms involved in many more pathophysiological brain states. Indeed, recent scientific evidence of implication of CSD not only in epilepsy but also in migraine, traumatic brain injury, stroke and many neurodegenerative diseases such as Alzheimer's disease highlights the importance of this research field.

I.D. Functional ultrasound imaging of the brain

Functional ultrasound imaging (fUS) is a novel imaging technique developed intensively first by the French research group Physics for Medicine led by Michael Tanter. The development of the technique fastened in the 90s notably with the advent of faster graphical processing units, and spreads in a growing community worldwide, seduced by its easy handling, low-invasiveness and competitive price compared to classical (pre)clinical imaging technologies (fMRI, PET, CT), making it a technology of choice to investigate in rodents the cerebral activity with high spatial resolution in easier implementation of experimental protocols. We took advantage of these features and used it to prove the functionality of our custom rGO subretinal implant by visualising neural activation of the visual pathway (see §III). Its weak temporal resolution can be compensated by simultaneous electrophysiology recordings. This is precisely what we designed for exploration of neurovascular coupling during CSDs and seizures, in an attempt to better understand both the brain connectivity and the correlation between blood flow, LFPs and infraslow signals in epilepsy (see §II.B).

The fUS technology relies on the concept of neurovascular coupling (NVC). Imaging cerebral blood flow (CBF) changes provides an indirect measure of the neural activity. We first describe briefly the cellular mechanisms at play in order to justify the validity of using such technology for our experiments (§I.D.1), then explain the physics principle (§I.D.2) and data pre-processing behind the technology (§I.D.3).

I.D.1. Neurovascular coupling

Neurovascular coupling (NVC) refers to the link between neuronal activity and blood flow. In this section, we attempt to describe briefly the hypothetic cellular mechanisms at the origin of NVC. To do so, we star with a rapid overview on brain vasculature.

a. Brain vasculature

The brain vasculature is made of different types of vessels surrounded by different types of cells (Fig. 20.A). The vascular tree at the surface of the brain within the subarachnoid space consists in pial arteries and arterioles which are enveloped by arteriolar smooth muscle cells (SMCs) which control blood flow through constriction or dilation. On those SMCs, perivascular nerve fibres from the peripheral autonomic and sensory ganglia are branched (Fig. 20.B). The pial arteries and arterioles give rise to penetrating arterioles who run deeper down the brain. These penetrating arterioles have a different

structure: they are surrounded by a perivascular space filled with various cells (macrophages, pial cells etc.) and nerve fibres. This space is itself enveloped in astrocytes endfeet in deeper brain regions. In those deeper regions, intraparenchydermal arterioles and capillaries are also enclosed in astrocytes or neurons processes from neurons nearby. The proximity of neurons with the cerebral vascular system explains in part the neurovascular coupling.

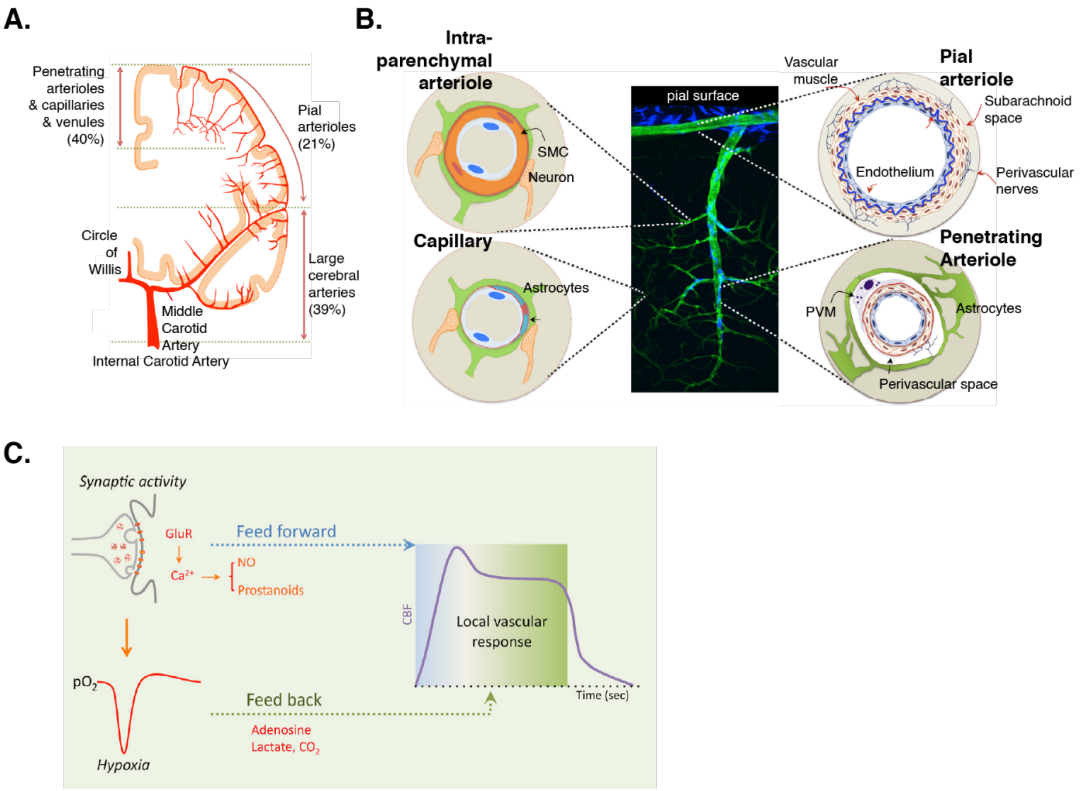

Fig. 20 Neurovascular coupling in the brain. Modified from (Iadecola, 2017). **A.** Brain vasculature. **B.** Description of the 4 types of vessels: intraparenchymal arterioles, capillaries, pial arterioles and penetrating arterioles. SMC = smooth muscle cell. PVM = Perivascular macrophage. **C.** Feed forward and feedback models to describe the local increase of cerebral blood flow (CBF) upon neuron activation.

b. Cellular mechanism

As the brain needs energy to maintain its homeostasis, blood flow increases (hyperaemia) and contributes to irrigating the organ in metabolites and cleanses it from overload of toxic elements such as lactate or CO_2. Although two distinct models have been proposed to explain the origin of NVC, it is arguable that the truth is not solely black nor white and might be a mix of both hypotheses (Fig. 20.C), depending on the region of the brain (Iadecola, 2017). There might be first a feedforward mechanism by which neurons release vasodilators by-products such as potassium, nitric oxide (NO), prostanoids, through signalling pathways prior to neural activation. After what, a second metabolism-driven feedback mechanism brings back the blood flow to a high value. The sudden peak of CBF is modulated by metabolic by-products such as adenosine, CO_2, H^+, lactate, released because of glucose and O_2 consumption/need.

Three cellular pathways account for most of the released calcium Ca^{2+} influx is favoured by glutamate-related post synaptic activity and activates neuronal NO synthase (nNOS) and cyclooxygenase 2 (COX-2) which are calcium-depend enzymes, leading to respective release of NO and prostanoids. Glutamate also activates astrocytes leading to increase of calcium influx and production of adenosis which contributes to the vasodilation. Many unknowns remain in the equation, such as the contribution of astrocytes the chicken-and-egg question about the link between neurovascular coupling dysfunction and several neurovascular diseases. As already noted for cortical spreading depolarisations in section §I.C.3, neurovascular coupling perturbation during pathological events is still poorly understood.

When neurons are activated in a certain area of the brain, there is a dwell-time and rapid response of the vascular system in the same region because of the neurovascular coupling. This property made it possible to quantify CBF by mapping brain functions, and hence to do functional imaging of the brain.

I.D.2. fUS principles

Nowadays, fUS technology is in full expansion in *in vivo* experiments involving rodents, lagomorphs or NHPs. It is mainly used to draw functional connectivity maps through evoked activity or to investigate effects of pharmalogical drugs on brain connectomics. We retrace in the following section the advantages and limits of fUS and detail its working principles and key pre-processing steps.

a. Advantages and drawbacks of fUS

Fig. 17 replaces fUS in comparison with more classical brain imaging technologies. The spatial resolution can therefore go down to **100 µm**, which is slightly better than fMRI and PET (Logothetis, 2008; Lancelot & Zimmer, 2010). This was until the advent of functional Ultrasound localization microscopy (**fULM**) with which details down to few micrometres can now be seen thanks to the tracking of microbubbles injected intravenously (Renaudin et al., 2022). In terms of temporal resolution, fUS is less performant than electrophysiology but not far from optical imaging methods such as optical intrinsic signal (OIS) imaging.

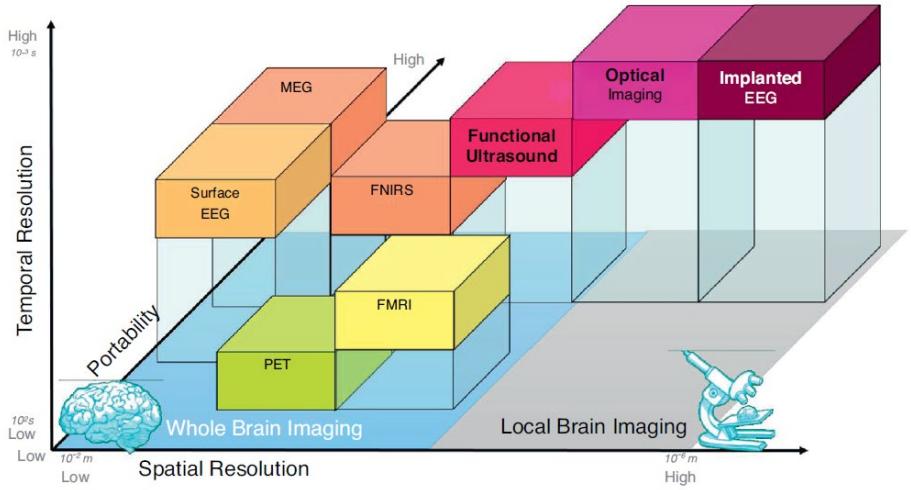

Fig. 21 Comparison between different brain imaging techniques in terms of temporal resolution, spatial resolution and portability. EEG = Electroencephalography, MEG = magnetoencephalography, PET = positron emission tomography, FMRI = functional magnetic resonance imaging. Retrieved from (Deffieux et al., 2018).

fUS is also less costly and more practical because the machinery is portable, compared to functional magnetic resonance imaging (fMRI). It can be combined easily with electrophysiology tools and implant monitoring, while it is not the case for fMRI. As the probe is small and easy to handle, fUS is particularly interesting for *in vivo* studies with awake animals.

A major disadvantage was the necessity to remove or thin the skull for imaging because ultrasounds are attenuated and distorted by the bones. Craniotomies are necessary for *in vivo* studies on rodents. Thinning the skull instead reduces the surgery severity yet comes at the expense of image quality. This issue is at the center of current research. Nowadays, with fULM, transcranial imaging in humans at high resolution is becoming a reality (Demené et al., 2021).

As it is easier to handle the machine, preclinical studies in awake animals (Bimbard et al., 2018; Brunner et al., 2021; Provansal et al., 2021; Sieu et al., 2015) and even clinical human studies (Imbault et al., 2017; Soloukey et al., 2020; Demené et al., 2021) have been made possible, reinforcing the high potential of fUS for preclinical research and clinical diagnosis.

b. Conventional fUS

Fig. 22 describes the physics principle behind conventional focused ultrasound (Fig. 22.A-D) and ultrafast ultrasound imaging (Fig. 22.E-H).

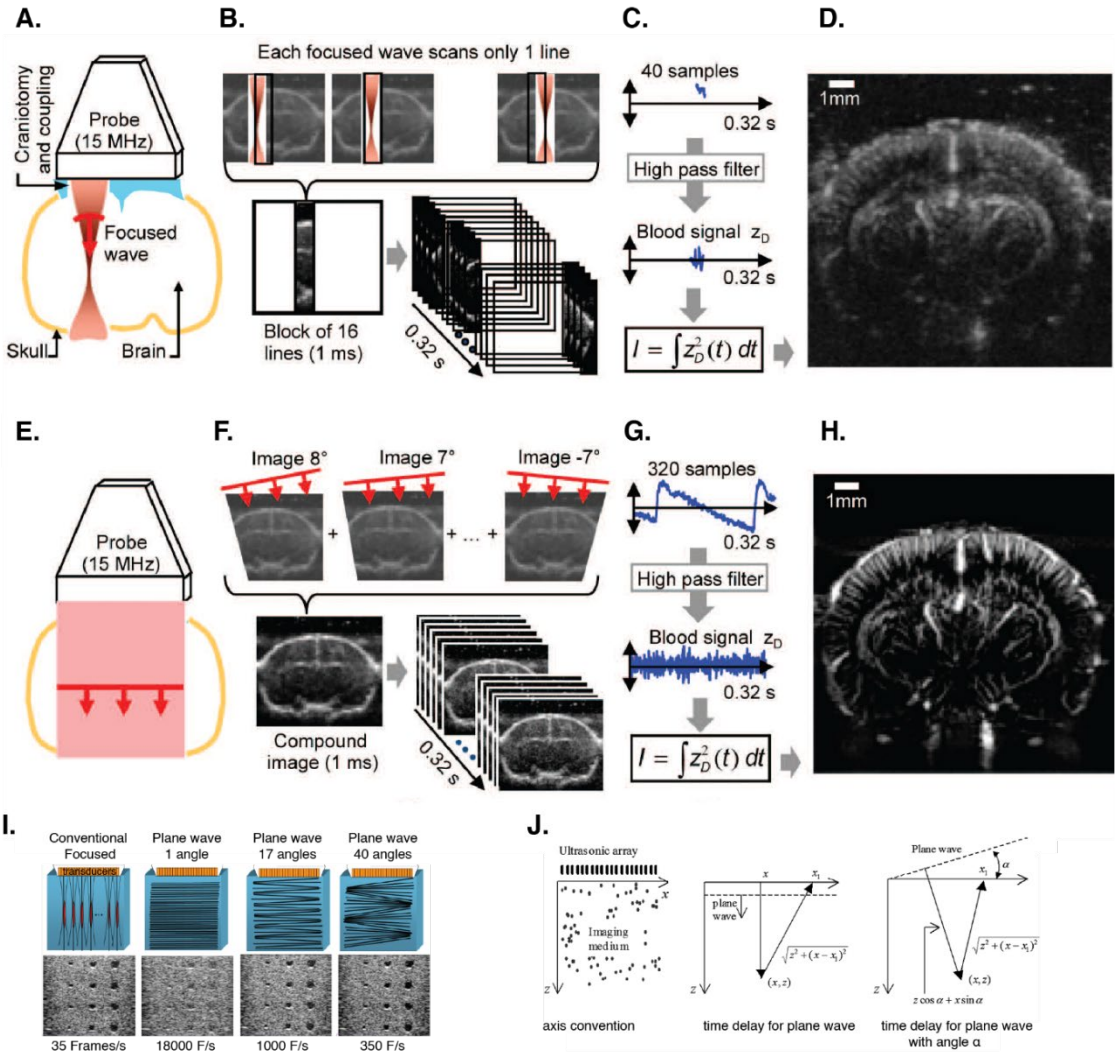

Fig. 22 Principles of conventional **(A-D)** and ultrafast **(E-H)** ultrasound imaging. **A. & E**. fUS set-up. **B.& F**. Image acquisition process. The waves emitted are either pulsed focused waves and consequent to one another (B.) or tilted plane waves with an angle processed in parallel **(F.)** (Macé et al., 2013) **C.& G**. Signal filtering and calculation of the mean intensity of blood signal. **D.& H.** Reconstructed power doppler image in both methods. **I.** Comparison of the trade-off between time cost to generate the image and image quality (Tanter & Fink, 2014). **J.** Comparison of time delay between plane wave and tilted plane wave. (Montaldo et al., 2009)

The fUS probe is usually made of 128 or 256 piezoelectric transducer elements, and is placed on top of the imaged tissue, typically the brain (Fig. 22.A, E). The array both transmits the incident wave and receives the echo wave, scattered back by the red blood cells with a time $\tau = \frac{2z}{c}$, z being the distance and c the speed in blood, c~1500 m/s. In the conventional fUS method, a focused beam is sent sequentially line after line in order to map the whole area (Fig. 22.B) (Mace et al., 2013), and at different focal depths (usually 4) because there is energy dissipating when focalizing on one point only. This means that for a 128-piezoelectric transducer, 4*128=512 ultrasonic shots are necessary to obtain one image. As the total time of flight for the waves to go in the tissue and back to the transducer costs around 60 µs for a 5 cm depth scan, the imaging time is hence 512*60 = 0.032 s, corresponding to a frame rate of 1/0.032 = 35 Frames/s (F/s). This method generates what is called a “B-mode” image.

c. Ultrafast ultrasound imaging

It is nonetheless possible to increase the frame rate by using the **coherent plane wave compounding method.** In this upgrade technology qualified as “ultrafast” ultrasound, plane waves are

sent. If multiple plane non-tilted waves would be sent, the separation of the source in the time-reversed signal would pose an issue. Tilting the waves with different angles (Fig. 22.F,I) (Montaldo et al., 2009; Tanter & Fink, 2014) allows to bypass this problem, as each received signal will have a distinct shape. This could be seen as artificially adding a delay to the sent waves (Fig. 22.J).

While each wave gives a low-quality image ("**IQ**" image), the coherent summation of each pixel reconstructs the image with better resolution compared to direct summation of the waves. At this step, a physical time-reversal operation called "**beamforming**" is performed on the phase of each waves in order to reconstruct the transmitted information. This beamforming consists in realigning the waves depending on their reception time by the transducers. While using one single angle reconstructs fast the image (18000 F/s), the contrast is low (Fig. 22.I). Using 17 angles gives a frame rate of 1000 F/s at a fair resolution with reasonable cost in time (Tanter & Fink, 2014). The choice of the number of angles is standard trade-off between time cost and image quality.

d. Our set-up

At the Institut de la Vision, two different types of functional ultrasound scanner were used during this doctoral work. The first one is an experimental version ("Aixplorer", Vermon, FR) modified for animal experiments and was used for all acute *in vivo* experiments on rodents. The second is a commercialized system ("Iconeus One", Iconeus, FR) with four-axis motorized platform to hold the probe and an integrated software for data acquisition. Only data for chronic subretinally-implanted rats were acquired with the Iconeus One. For both of them, the probe is made of 128 piezoelectric elements emitting planar waves at 15 MHz from 2 to 12 mm in depth (subject to change), with 15 different angles (subject to change) at a frame rate of 500 F/s. This results in 200 compounding images. The acquisition frequency is 1 Hz. The pitch between piezoelectric elements is 110 µm and pixels are spaced by 100 µm in depth.

I.D.3. fUS data pre-processing

a. high-pass clutter filter

The goal of fUS in neuroscience is to retrieve information on blood flow in small cerebral vessels. However, coherent signal stemming from the brain tissue which also scatters the radio frequency signals hampers the proper analysis of hemodynamic changes. Historically, a **clutter filter** consisting in a high-pass filter around 70 Hz was first applied to the reconstructed signal s(x,z,t) for each pixel (x,z) after beamforming (Macé et al., 2011; Mace et al., 2013) in order to get rid of this noise. The idea was that tissue motion was slower than the blood one. By doing so, only information on blood with a velocity higher than 4 mm/s would be preserved. However, as the frequency domains of tissue data and blood data overlap with each other, the 70 Hz high-pass filter also removes information on blood volume.

b. Spatiotemporal singular value decomposition clutter filter

Another method known as **spatiotemporal singular value decomposition (SVD) clutter filtering** (Demene et al., 2015; Baranger et al., 2018) replaced the 70 Hz filter and is still valid today for anaesthetised animals. The method relies on the spatial coherence of the data and mimics data processing in fMRI: instead of filtering in the frequency space, data are taken in a new base from the decomposition of the IQ images.

From a theoretical point of view, the IQ images containing a signal s of size (n_x,n,n_t) are reshaped into a linear 2D space-time matrix **S** of size (X*Z, T) called Casorati matrix (Fig. 23.A). Performing SVD filtering consists in decomposing **S** into 3 matrices U, Δ and V* such as **S** = U Δ V* where U is the spatial singular vector, V* is the temporal singular vector and Δ the singular value λ diagonal matrix of size (X*Z, T). Therefore, **S** is the sum of separable matrices with weight/singular value λ such that **S** = $\sum \lambda i \, . \, U_i \otimes V_i$.The singular values λ are ranked from the highest value (large coherence) to the smallest. Interestingly, the tissue pixels behave in a similar way: they are highly coherent hence are explained by the first singular values. Blood information is contained in the lowest rank singular values. By "cutting" the singular values corresponding to tissue data in the covariance matrix |S.S*| (Fig. 23.B), a better-quality image is obtained with no/less loss of blood information compared to high-pass

filter method. In our laboratory, the Aixplorer machine is set to filter out the 60 first modes bearing the “tissue space”.

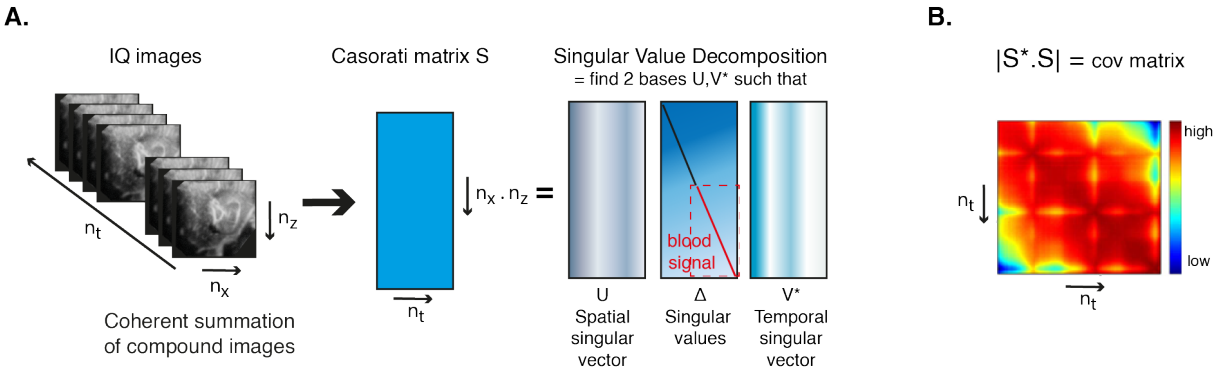

Fig. 23 Singular Value Decomposition (SVD) principles applied for beamformed signal s(x,z,t). S is the Casorati matrix. **A.** Decomposition of the casorati matrix in a new (U,V*) base. **B.** covariance matrix for clutter filtering. Modified from (Déméné et al. 2018).

Once data is clutter-filtered, power doppler data are retrieved under a 3D matrix of size X*Z*T. The intensity of the final doppler signal $I = \int s^2(x,z,t)dt$ is proportional to blood volume in the imaged region, under the hypothesis that the red blood cells do not deform (Shung et al., 1976).

c. Offline analysis

For stimulation experiments, the analysis relies either on **Pearson correlation** or **Global Linear Model** (GLM). For GLM, the *spm* matlab toolbox (Friston, 2007) compares for each pixel the expected theoretical response X with the experimental response Y using the linear model Y = AX + B. X is usually the stimulation pattern sent, but research has shown that it is better to convolute it with the hemodynamic response function (**HRF**) either determined experimentally with the shortest stimulation length to give a neural response, or using the canonical one (Aydin et al., 2020). For our work, we rely on the HRF determined experimentally in (Claron et al., 2021).

II. Recording with carbon-based implants

II.A. A full diamond-based ECoG

The following work falls within the scope of the **NEURODIAM** European Research Council starting grant (ERC-STG) which consists in engineering new thin ECoG arrays based on diamond nanostructuration combined with micro technology, backed by the team of Lionel Rousseau at ESIEE Paris. The project aims at developing a reliable long-lasting neural implant with a hermetic and inert packaging, in order to avoid water migration inside the implant architecture and degradation/corrosion of the conductive elements. As diamond is at the same time chemically inert and conductive if doped with boron, the idea was to exploit both properties into a flexible micro-electrode array.

The article presented in the following section summarises first the original microfabrication process of boron-doped diamond electrodes, packaged in a hermetic intrinsic diamond (C*) coating, developed by our collaborators at ESIEE Paris. Then, it demonstrates the “reading” abilities of such ECoG implant *in vivo*. For this purpose, the eye of the animal was stimulated with light flashes and visually evoked potentials (VEPs) were successfully recorded on the surface of the visual cortex in rodents. The animal experiments were performed both at the Vision Institute and at the EPFL during a two-month academic secondment in the Neuroengineering Lab (LNE, Dr. Ghezzi) in the scope of the Marie Skłodowska-Curie enTRAINVision network.

The article was submitted.

Personal contribution: *in vitro* characterisation, *in vivo* experiments, data analysis, manuscript writing and figures drawing (fig. 3,4,5). Microfabrication was performed by C. Wilfinger and L. Rousseau.

Article

In vivo recording of Visually Evoked Potentials with novel full diamond ECoG implant.

F C Wilfinger[1], J M. Zhang[2], D Nguyen[2], J Dégardin[2], P Bergonzo[3], S Picaud[2], E Borda[4], D Ghezzi[4], E Scorsone[5], G Lissorgues[1] and L Rousseau[1]

[1] ESYCOM, Université Gustave Eiffel, CNRS, CNAM, ESIEE Paris, F-77454 Marne-la-Vallée, France; e-mail: gaelle.lissorgues@esiee.fr
[2] Sorbonne Université, INSERM, CNRS, Institut de la Vision, 17 rue Moreau, F-75012 Paris, France; e-mail: serge.picaud@inserm.fr
[3] Department of Electronic and Electrical Engineering University College London, 17-19 Gordon Street, London, WC1H0AH, United Kingdom ; e-mail: pbergonzo@sekidiamond.com
[4] Center for Neuroprosthetics and Institute of Bioengineering, École Polytechnique Fédérale de Lausanne, Chemin des Mines 9, 1202 Geneva, Switzerland ; e-mail: diego.ghezzi@epfl.ch
[5] Université Paris-Saclay, CEA, List, F-91120 Palaiseau, France ; e-mail: emmanuel.scorsone@cea.fr

* Correspondence: gaelle.lissorgues@esiee.fr

Abstract: *Objective.* Implantable neuroprosthetic devices such as electrocorticography (ECoG) and intracortical microelectrodes have the potential to restore neurological functions in disabled individuals. They constitute the direct interface with the body and require long term efficiency. We propose an ultra-thin diamond-based implant to tackle challenges related with long term implantation, and demonstrate its functionality on rodents. *Approach*. We take advantage of thin-film diamond to generate not only the electrodes but also the thin passivation foil, leading to a full thin film diamond EcoG. *Results*. We manufactured implants with boron-doped diamond (BDD) electrodes connected through titanium nitride (TiN) conductive tracks, all being encapsulated in intrinsic diamond. A complete electrochemical characterization proved that the TiN tracks were well embedded inside diamond and the efficiency of the BDD electrodes. Functionality of the ECoG device was also provided by the recording of classic visual evoked potentials (VEPs) on wild-type mice and rats. *Significance*. This thin film diamond technology successfully responds to long term issues (linked with electrode material or device packaging) and holds the potential to inspire and pave the way for future generations of various electrode arrays.

Keywords: Thin film technology, neural implants, boron-doped diamond, microfabrication, microelectrodes, brain-computer interface, visually evoked potential

1. Introduction

Wearable neuroprosthetic devices offer the promise of restoring neurological functions for disabled individuals. For instance, recent developments in the field of brain-computer interfaces (BCIs) implanted in the central nervous system demonstrated the possibility of controlling prosthetic limbs through electrocorticography (ECoG) recordings of the brain activity [3], [17]. Electrical stimulation through penetrating microelectrodes also enables the recovery of some visual perceptions [16]. Despite encouraging research results [2], [50], chronic intracortical or subdural implants are still not available on the market due to several issues linked to the electrode material or the device packaging. Electrode efficiency can for instance be limited by the tissue responses or gliosis at the interface to the foreign and rigid device [39], [22]. Indeed, the reaction is likely enhanced by the mechanical mismatch between the electrode material and the neural tissue. Besides the host body responses, electrical stimulation usage can lead to dissolution of the metallic

layers [8]. Failure can also occur at the level of the polymer coating: delamination and peeling off the passivation layer have been reported in literature [30], [12], [43]. For instance, migrating water a few months post-implantation induced electromigration of the metal, which progressively degraded the performance of the implant, during the clinical study testing Retina Implant AG subretinal prosthesis [13]. In order to solve this issue and create water-tight structures, several research teams have proposed innovative approaches such as stacked layers of inorganic and organic materials [1].

Implants fabricated by conventional technology are usually composed of metal tracks and electrodes embedded in a biocompatible polymer insulation layer. Recent advances in the field of material bioengineering showed that the immune response of tissues can be reduced by selecting biocompatible and soft materials which better follow the tissue topology [21], [7]. Among the novel materials being investigated, diamond is a carbon-based material, which has received consequent attention in the neuroengineering field. The high stability of the covalent bonds between carbon atoms confers both structural stability and chemical inertness [28]. Its use as an encapsulation material in fully hermetic devices is consistent with hermiticity to small molecules like water, reducing thereby the risk of implant swelling [18], [35].

Intrinsic diamond provides electrical insulator, while doped diamond possesses attractive electrochemical properties for neural interfacing due to its semi-conductor properties. Ultra-nanocrystalline diamond with nitrogen inclusion (N-UNCD) grown in polycrystalline diamond substrate mills were introduced in diamond-based subretinal implants [23], [42], but the different chips remained within 100 to 250μm thick embedded into polymer, limiting the global flexibility to conformally follow the tissues. However, these solutions demonstrated doped diamond recording capacity [49]. Similarly, Boron-doped diamond (BDD) electrodes feature excellent electrochemical characteristics with a large potential window (3V) in aqueous media [38] showing a material stability adequate for neural stimulation. With the evolution of diamond production technologies, very thin diamond layers of a few hundred nanometers in its nanocrystalline form can be obtained using specific plasma reactors [20]. So BDD electrodes have been used for neural recordings [38], [27], and neurotransmitters sensing |15], and finally the material biocompatibility was demonstrated on neural cells and tissues in vitro and in vivo with both CVD diamond N-UNCD electrodes and BDD electrodes [44], [41], [45], [4], [5].

Convinced that these diamond properties, in its intrinsic or doped forms, provide the material of choice to manufacture a long-term biocompatible and hermetic neural implant, we have developed the process flow for the fabrication of a full-diamond-based electrocorticography electrode array, and assessed its characteristics and functionality for recording purposes. The major achievement relies in the design and fabrication of the nanocrystalline BDD electrodes embedded in an intrinsic ultra-thin diamond matrix. The resulting thin and flexible full-diamond ECoG implant is, to our knowledge, the first to combine BDD electrodes in an intrinsic diamond flexible structure. Although hermetic full diamond feedthrough arrays with UNCD electrodes had been investigated by Bionic Vision Australia, we have here developed a complete novel process better compatible with standard micro-technological processes and resulting into a fully flexible thin implant.

2. Materials and Methods

A. Intrinsic and boron-doped diamond growth process

Nanocrystalline diamond coatings were grown on 4-inch wafers using microwave assisted plasma chemical vapour deposition (MPCVD) in a SEKI SDS6K reactor with hydrogen plasma containing methane as the source of carbon [34]. Trimethylboron (TMB) was added to the gas phase for doping in the case of BDD electrode preparation. The boron concentration in the crystal was in the range of 2.1021 at.cm3. Diamond films were grown at a pressure of 30 Torr. The typical power used was 3000 W. The substrate temperature

was kept between 650 °C and 780°C and the growth durations were respectively of 4.5 hours and 12 hours for intrinsic diamond and BDD coatings. Prior to growth, the substrates were seeded according to a process described in literature [20], using 5-nm-negatively-charged Detonation Nanodiamond Suspensions in de-ionised (DI) water (1wt. %) from Adámas.

Diamond grown layer may be patterned either by reactive-ion etching (RIE) using a mixture of O2/CF4 plasmas ("top-down") or by performing a local diamond growth while protecting nanoparticles from the plasma with a specific layer to prevent their growth in the masked areas ("bottom-up"). During the whole process described below, we switched between these two methods depending on the diamond layer (intrinsic or boron doped) and the fabrication needs.

B. Full-diamond implant microfabrication

The entire process was developed on standard 550 µm-thick Silicon substrates with a 1.5 µm-thick thermal SiO2 layer. The wafer was pre-activated in Ar/O2 plasma (with pressure 110 mTorr, power 90 W, flow rates 50 sccm O2 and 40 sccm Ar, during 5 minutes) prior to diamond nanoparticle electrostatic seeding. After the seeding step, the wafer was then placed inside the MPCVD reactor in order to grow the diamond seeds slightly for a few minutes to obtain a good adhesion of the nanoparticles over the whole surface of the wafer.

To restrict the diamond growth to a specific pattern, localised growth was carried out as follows. After the initial diamond nanoparticle seeding (step 1 in figure 1(A)), a thin layer of aluminium nitride (AlN: yellow in figure 1(A)) was sputtered over the diamond nanoparticles (MP500S, PLASSYS) under the following conditions: pressure 0.53.10-2 mbar, power 500 W, flow rates 14 sccm for Ar and 27 sccm for N2, and deposition time 30 minutes. AlN, which can withstand plasma conditions in the diamond growth reactor, was used here as a masking layer during the growth of non-doped diamond (C* light blue in figure 1(A)). The AlN layer was then patterned by photolithography and wet etched in order to open the areas where diamond had to grow (step 2 in figure 1(A)). The wafer was then introduced inside the chamber of the SEKI diamond reactor (3000 W, 30 Torr, 500 sccm H2 and 7.5 sccm CH4, during 4h30). These conditions resulted in a 1 µm-thick intrinsic diamond film measured by a mechanical profilometer (Dektak XT, Bruker). The AlN mask was then removed using an alkaline etchant (photoresist developer PRD 238, CMC Materials) (step 3 in figure 1(A)).

The next step consisted in growing a BDD layer directly on the whole substrate, to obtain the conductive parts of the implants. The wafer was again seeded with diamond nanoparticles and then introduced in another SEKI diamond reactor dedicated to doping, with TMB added in the gas mixture to grow a 600-nm-thick BDD layer, under the reported growth conditions [24]. At this stage, the wafer was completely covered with the BDD layer. Patterning of BDD tracks and electrodes was achieved through the top-down approach, by depositing an aluminium (Al) masking layer of 500 nm patterned by photolithography and etching the unwanted BDD in a RIE equipment (NE110, Nextral) with the following parameters: power 100 W, pressure 37.5 mTorr, flow rates 40.6 sccm O2, 2.2 sccm CF4, during 900 s. After this localised BDD etching, the remaining Al masking layer was completely removed in the Al chemical etchant bath (TechniEtch Al80, TECHNIC) (step 5 in figure 1(A)).

As the resistivity of BDD is too high (> 10-2 Ohm.cm) to be used alone as conductive material under the electrode pads and over the tracks, additional conductive tracks were produced to decrease the serial resistance of the implant alongside its foil. Titanium nitride

(TiN) was used to guarantee stability and compatibility under the harsh conditions of diamond growth, especially the high temperatures around 600°C inside the reactor, as previously reported [36]. TiN deposition was carried out with the following parameters in the sputtering equipment: a pressure controlled at 0.5.10-2 mbar, a power of 150 W, balanced gas flow rates of 20 sccm Ar and 20 sccm N2. TiN tracks were defined using standard photolithography, then etched in hydrogen peroxide (H2O2), creating an annular contact around the BDD electrode along with tracks and pads (TiN: brown, step 6 in figure 1(A)). To finalise our full-diamond implant, a second layer of intrinsic diamond was seeded to encapsulate the conductive layer (step 7 in figure 1(A)). Here, the etching process could not be used to open the diamond layer because there is low selectivity between BDD and intrinsic diamond layers. We used another AlN mask to protect the electrodes and the contact pads during the diamond growth (step 8 in figure 1(A)). At this stage, we successfully developed a full hermetic diamond structure with individual tracks composed of TiN tracks embedded inside protective non-doped diamond with opened BDD electrodes (step 9 in figure 1(A)). The SEM image (Neon 40, Carl Zeiss) shows the finished electrode diamond structure (figure 2(B)).

The diamond implant was finally embedded in parylene (pink in figure 1(A)) to ease its manipulation (from 1.5 µm with diamond only to 15 µm thickness with additional parylene packaging). A 7 µm-thick film was deposited on the top side of the wafer to obtain the first polymer encapsulating layer. A thin layer of Al was then deposited to protect the parylene film. Lithography was performed to open the parylene layer locally on the electrodes and contact pads (step 10 in figure 1(A)). The openings of these contact pads and electrodes were made with dry-etching using O2/CF4 plasma (conditions of the plasma : pressure 125 mTorr, power 100 W, O2 50 sccm, CF4 10 sccm). The wafer was then cleaned and 500 nm of Al layer was deposited on its back side. A back-side lithography step was done to localise openings in the Al layer below the implant. Next, the SiO2 layer was dry-etched and the silicon was etched by Deep Reactive Ion Etching (DRIE) (A160E, ALCATEL) (Step 11 in figure 1(A)).

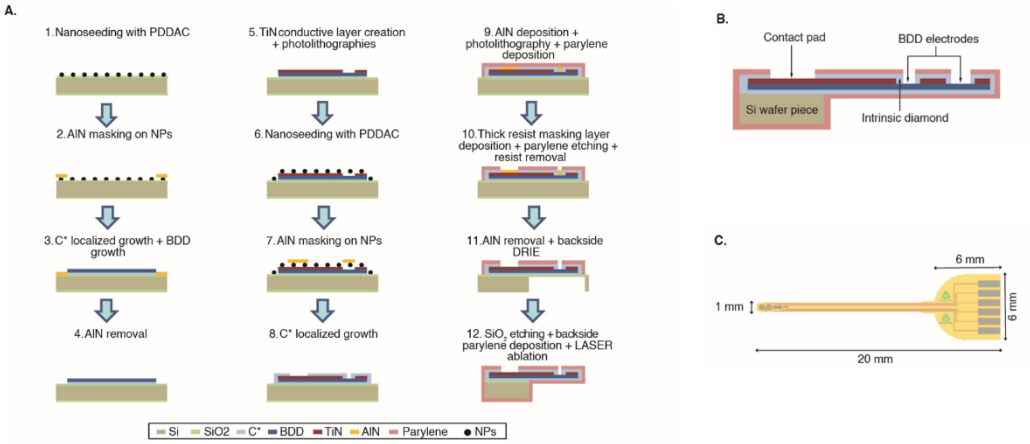

Figure 1. Design and microfabrication of the full diamond ECoG. (A) Description of the fabrication steps for a full diamond implant.Si = Silicon, SiO2 = Silicon Dioxide, AlN = Aluminium nitride, NPs = Nanoparticles, C* = intrinsic diamond, BDD = Boron-Doped Diamond, TiN = Titanium Nitride, DRIE = Deep Reactive Ion Etching. (B) Cross-section schematic view of the implant; (C) schematic drawing of the implant –top view.

In practice, a piece of silicon wafer underneath the contact pads area was left during the final steps of the process for better handling purposes. Subsequently, the SiO2 layer under the implant was removed in buffered HF solution. Hence, the second 7 -µm-thick parylene layer was deposited on the backside of the implants (Step 12 in figure 1(A)).

Finally, the implants were ready to be released from the wafer after LASER ablation (UP-213, New Wave Research). Each 4 inches wafer can produce up to 30 implants.

C. Assembly of the implants

A connector was soldered to a specific PCB board (RS) which was mounted onto the implants. The welding was performed using a stencil to spread the conductive paste over the pieces to be soldered. Then, a pick-and-place machine (Tresky AG) was used to join the pieces and the implant together. Finally, the mounted devices were put inside an oven at 150°C for 5 min so that the conductive paste could glue. The resulting assembly was stiffened with UV glue to ensure its robustness. The piece of Si wafer left from the process reinforces the connection between the contact pads and the PCB board.

D. Electrode characterization

Before in vivo experiments, the electrochemical characteristics of the implants were measured by standard electrochemical techniques. Cyclic Voltammetry (CV) and Electrochemical Impedance Spectroscopy (EIS) were performed using a SP-200 potentiostat from Biologic, interfaced by the EC-lab Express software. The 3-electrode electrochemical cell was composed of the tested BDD electrodes (surface area: 0.031, 0.126 or 0.283 cm^2) as the working electrode, a platinum wire as the counter electrode, and an Ag/AgCl pellet as the reference electrode. Each electrode was cycled 3 times between -1.5 to 1.5 V at a sweep rate of 100 mV.s-1. EIS was carried out in a 0.01 M Phosphate-Buffered Saline (PBS) solution (Sigma-Aldrich). The signal was swept across the system at frequencies ranging from 1 MHz to 1 Hz. CV was performed in the presence of 0.5 M lithium perchlorate ($LiClO_4$, Sigma-Aldrich), a conductive electrolyte.

E. Animal surgery

Visually evoked potentials were recorded in two laboratories on rodents, on adult (>1-month-old) C57BL/6J mice (Charles River Laboratories) at Ecole Polytechnique Fédérale de Lausanne – EPFL (Lausanne, Switzerland) and on Long Evans (Janvier Labs) 9-week-old rats at the Vision Institute – IDV (Paris, France). In Switzerland, experiments were conducted according to the animal authorisation GE/193/19 approved by the Département de l'emploi, des affaires sociales et de la santé (DEAS), Direction générale de la santé de la République et Canton de Genève. In Paris at the Vision Institute – IDV, the experiments and procedures were all approved by the Local Animal Ethics Committee N°005 (registration number APAFIS #15258-2018052811521506 v1). The rodents were kept in a 12 h day/night cycle with access to food and water ad libitum. White light (300 ± 50 lux) was present from 8 a.m. to 8 p.m at IDV with no light during night, while from 7 a.m. to 7 p.m. at EPFL with red light (650–720 nm, 80–100 lux) during night from 7 p.m. to 7 a.m.

At EPFL, the mice were all anaesthetized with an intraperitoneal injection of ketamine (87.5 mg.kg-1) and xylazine (12.5 mg.kg-1). Analgesia was performed by subcutaneous injection of buprenorphine (0.1 mg.kg-1) and lidocaine (6 mg.kg-1). Artificial tears were used to prevent the eyes from drying. The depth of anaesthesia was assessed with the pedal reflex. The skin of the head was shaved and cleaned with betadine. Mice were placed on a stereotaxic frame, and the skin was opened to expose the skull. A craniotomy was performed to expose the visual cortex. At IDV, the rats were anesthetized with an intraperitoneal injection of ketamine (40mg/Kg, Axience, France) and medetomidine (0.14 mg/kg, Domitor®, Vétoquinol, France) diluted in sodium chloride. Buprenomorphine (0.05 mg/kg, Buprecare®, Med'Vet, France) and Dexamethasone solution (Dexazone®, Virbac, France) were injected subcutaneously to reduce any inflammation and pain. After

being shaved, a local analgesic, Lidocaine (4 mg/kg, Laocaïne, MSD, France) was administered subcutaneously under the scalp skin and Xylocaine gel (2%) was applied in the ears. Similarly to EPFL, a surgical craniotomy was performed under anesthesia, after disinfection with iodopovidone solution with a sagittal incision revealing the skull.

The remaining periosteum was removed and the skull was cleaned with H2O2. A rectangular piece of bone was removed in the presence of cortex buffer by drilling with 0.07 and 0.05 mm diameter drill bits, revealing the visual cortex. In both cases, the temperature of the animals was maintained at 37 °C with a heating pad.

F. Visually Evoked Potentials (VEPs) recordings

In both cases, Visually-evoked potentials (VEPs) were recorded in a dark room at ambient temperature. Our diamond implant was placed in contact with the dura and tested with different set-ups.

At EPFL, a Ganzfeld light stimulator was used to send light flashes (20 ms, 1 Hz, repeated 20 times). Signals were pre-amplified (Biomedica Mangoni, BM 623 HC4) and band-passed on-line between 0.1 - 200 Hz. Data was acquired at a frequency of 1.0 kHz. Visual acuity tests were also performed on the anaesthetised normal adult mice. A custom matlab program was used to control chessboard patterns on a screen 50 cm apart from the eyes of the mice. Visual acuities under 0.1, 0.2, and 0.3 cycles per degrees conditions repeated 30 times were assessed while brain signals were recorded using the same pre-amplifier. VEPs data were analysed on Matlab. Raw data were first filtered with a Butterworth second order filter, to remove electromagnetic interferences at 50 Hz, and then band passed between 1 to 100 Hz. Signals from the electrodes were averaged in alignment with the trigger onset provided by the Ganzfeld stimulator. Mean amplitudes and latencies were calculated. Results are expressed in terms of mean ± error of the mean. Comparison between mean peak-to-peak amplitude was achieved by one-way ANOVA with Dunn-Sidak multi-comparison correction tests. P-values are symbolised as follows: *$p < 0.05$, **$p < 0.01$, ***$p < 0.001$. Signal-to-noise ratio (SNR) was calculated as the ratio between P1-N1 peak-to-peak amplitude and twice the root mean square of the baseline taken as 90 ms before the light onset.

At IDV, a collimated white LED (MWWHLP1, ThorLabs, USA) controlled by a stimulus generator (STG 4002, Multi-Channel Systems, Germany) was used to send light flashes, placed at 15 cm from the left eye of the animal, the other eye being covered with a dark cloth. It was calibrated such that the eye was illuminated with an intensity of 2 cd/cm². Signals from the diamond implant were first pre-amplified with a miniature amplifier (MPA 8I , Multi-Channel Systems, Germany) via a custom adapter stacked on another adapter for 16-electrode NeuroNexus Probe and two MPA8I Amplifiers (ADPT-NN-16, Multi Channel Systems, Germany). A return electrode was positioned in the contralateral muscle of the craniotomy. Signals recorded with the 16-channel amplifier (Portable ME16-System, Multi-Channel Systems, Germany) were digitally transmitted to a US-connected computer with a 10 kHz sampling rate. VEPs data were also analysed on Matlab following the same data processing as at EPFL**3.**

3. Results

A. Full-diamond implant microfabrication

The different fabrication steps described in the material and methods section (figure 1(A)) led us to the production of full-diamond implants. Figure 1(B) cross-section illustrates the different doped and undoped diamond layers in contact with the TiN conductive layer (brown). The non-doped diamond (light blue) covers all the BDD (dark blue)

except at the electrode openings. The total thickness of these layers (intrinsic, BDD and TiN) is below 20 μm leading to a fragile but flexible device. A silicon piece was kept from the initial wafer at the pad extremity for a better manipulation of the implant, and a 7-μm-thick parylene layer (figure 1(B) pink) surrounds the whole implant except around the electrodes and contact pads in order to improve the global mechanical robustness for handling purposes. The schematic drawing in figure 1(C) provides a top view of the tracks which start at the contact pads and extend to the electrodes. The detached implant after laser cutting is shown on figure 2(A) with the contact pads above the remaining piece of wafer and the six electrodes on the other end of the implant. The BDD electrodes surrounded by the intrinsic diamond layer as well as the tracks are visible on the SEM image of the implant tail (figure 2(B)). The polycrystalline shape of the diamond films can be seen (figure 2(C)), providing evidence for the appropriate growth of the diamond layers. Moreover, the picture shows the thin, almost transparent, border representing the desired insulation of the electrode by diamond (indicated as "C*" in figure 2(C)).

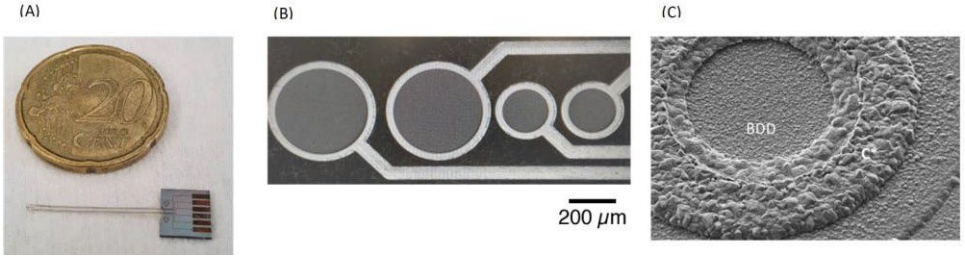

Figure 2. Fabricated implants. (A) Photography of an implant at the end of the process after laser cutting, (B) Scanning electron microscope (SEM) image of fabricated BDD electrodes composed of a TiN track on top connected via an annular contact – the whole being packaged inside intrinsic diamond layers. Scale bar represents 200 μm. (C) Magnification view of a 400 μm-electrode (Neon 40, Carl Zeiss).

B. Electrochemical characterization

Electrochemical characterization was performed for the three sizes of BDD electrodes (600-, 400- and 200-μm-diameter electrodes). The Bode spectrum (modulus and phase) shown in figure 3(A) spanned from 1 Hz to 1 MHz (sine wave, 10 mV). The values of the impedance at 1 kHz for the electrodes with diameter 600 μm, 400 μm and 200 μm are respectively 7.9 kΩ, 10.3 kΩ and 48.5 kΩ, showing values much lower than results from [29]. From 1 to 103 Hz, the impedance increases with decreasing electrode diameter. This is consistent with the fact that larger electrode surfaces allow more easily the same flow of charge to be interfaced. From 103 Hz to 1 MHz, the 400 μm electrode becomes less resistive than the 600 μm one, probably due to some surface roughness increasing the effective surface area on the tested samples. The linearity of the impedance modulus curve over the broad frequency range and its phase remaining around -90° indicate the capacitive behaviour of the BDD electrodes. At low frequencies (1 to 102 Hz), the 600 and 400 μm-electrodes are more capacitive than the 200 μm ones, but the 600-μm electrode shifts towards a more resistive behaviour first from 102 Hz to 5·104 Hz.

The cyclic voltammograms (CV) performed at a scan rate v=100 mV/s displayed in figure 3(B) exhibit a wide potential window of around 3 V consistent with the presence of BDD on the characterised electrodes. For the three electrode diameters, the onset of the oxidation/reduction of water happens around ±1.1V. And the low background currents indicate that the conductive electrode is carbon-based, consistent with its boron-doped diamond nature (Sun et al 2012). The absence of oxido-reduction peaks and the large width of the electrochemical potential windows (>2.8 V) suggest the absence of defects on the passivation layers. Indeed, the parylene etching step (step 10 on figure 1(A)) requires an energetic plasma and could create defects on the BDD electrode sites. The TiN tracks

underneath, exposed to the electrolyte due to these supposed defects, could generate an electrochemical window inferior to 1.8 V (Meijs et al 2018), which is not the case here. Our electrochemical results demonstrate that the TiN tracks are well embedded inside intrinsic diamond and that the BDD electrodes are made of a continuous layer.

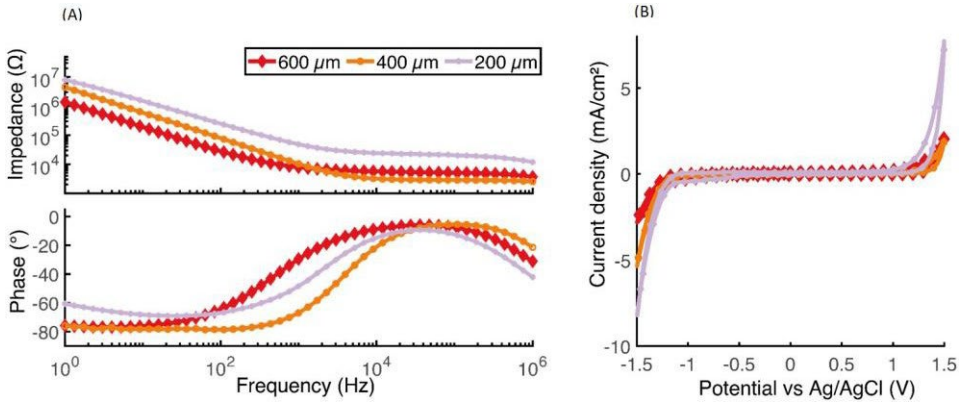

Figure 3. Electrochemical characterization of 3 sizes of BDD electrode on full diamond implant – averaged values (A) EIS in PBS 0.01 M. (B) CV in LiClO4 0.5 M with a scan rate of 100 mV/s. The counter electrode is a platinum wire, the reference electrode is a Ag/AgCl pellet.

C. In vivo VEPs recording

We tested the same 600 and 400 μm electrodes during in vivo experiments in the above mentioned laboratories.

The full-diamond custom implants were placed over the right visual cortex of the animal. The implant tail displaying the BDD electrodes was layered above the dura mater to record local neural activities.

At EPFL, to elicit a response, the eyes were stimulated with 20 consecutive white flashes in a Ganzfeld stimulator box at a rate of 1 Hz. Figure 4(A) illustrates the recorded responses after filtration and averaging for a 600-μm-diameter electrode. The recorded signals show the classic positive and negative peaks of VEPs [33] with amplitudes increasing with the light intensity. According to the International Society for Clinical Electrophysiology of Vision (ISCEV) standards [37], positive peaks (P1) are marked upwards. P1-N1 peak-to-peak average amplitudes measured for the 600 μm-diameter electrode increased respectively from 144.1± 9.0, 145.9± 6.8, 222.0±12.6 μV, to 233.7±19.6 μV for light intensities varying from 0.05, 0.1, 0.5 and 1 cd.s/m² (Figure 4(B)). A similar increase in response amplitudes when increasing the light intensities were observed for both 600 and 400 diameter BDD electrodes. Figure 4(B) illustrates that these P1-N1 peak-to-peak amplitude increases showed statistically significant differences for the 600-μm electrode when light intensity increased from 0.1 to 0.5 cd.s/m² (***p=0.00049), and for the 400-μm electrode when light intensity was raised from 0.5 to 1 cd.s/m² (*p=0.035). Amplitudes of signals recorded with the 600-μm electrode were also higher than the ones recorded with the 400 μm one. Figure 4(C) displays time latencies defined as the time to reach the first peak P1. One-way ANOVA and pairwise comparison demonstrate no significant differences between all intensities and between all intensity pairs. Figure 4(D) shows cortical recordings using a 600-μm-diameter electrode upon a black and white alternating chessboard of pattern visual stimulation at 1 Hz, which is a classic test to assess visual acuity (Odom et al 2016).

In this test, visual evoked potentials become flat when the size of alternating white and black squares matrix or when the number of cycles/degree are no longer detectable by the visual cortex. Figures 4(D/E) elicit clear visual evoked potentials with similar am-

plitudes at 0.1 or 0.2 cycles/degree (62.11±5.62 µV and 72.15±7.44 µV respectively). By contrast, the mean peak amplitude is reduced to 46.34±7.05 µV at 0.3 cycles/degree, which generated a statistically significant difference than the measurement at 0.2 cycles/degree (*p=0.025 at a 5% alpha level). These signals recorded with our full-diamond implant indicate a visual function threshold between 0.2 and 0.3 cycles/degree for wild-type mice in agreement with previous study indicating a value of 0.5 cycles/degree for C57BU6 [40] or C57BL/6J mice [46]. Our difference could result from the greater distance of the eye to the checkerboard screen in our study (50 cm versus 16 cm in [46]), but also to the progressive eye cloudiness due to the anesthetic state.

Finally, the signal-to-noise ratio (SNR) was calculated for the 600 and 400 µm-electrode recordings at different light intensities (figure 4(F)). The signal quality is higher for the largest electrode diameter and when the highest light intensity is used (1 cd.s/m²), reaching 7.7±1.5.

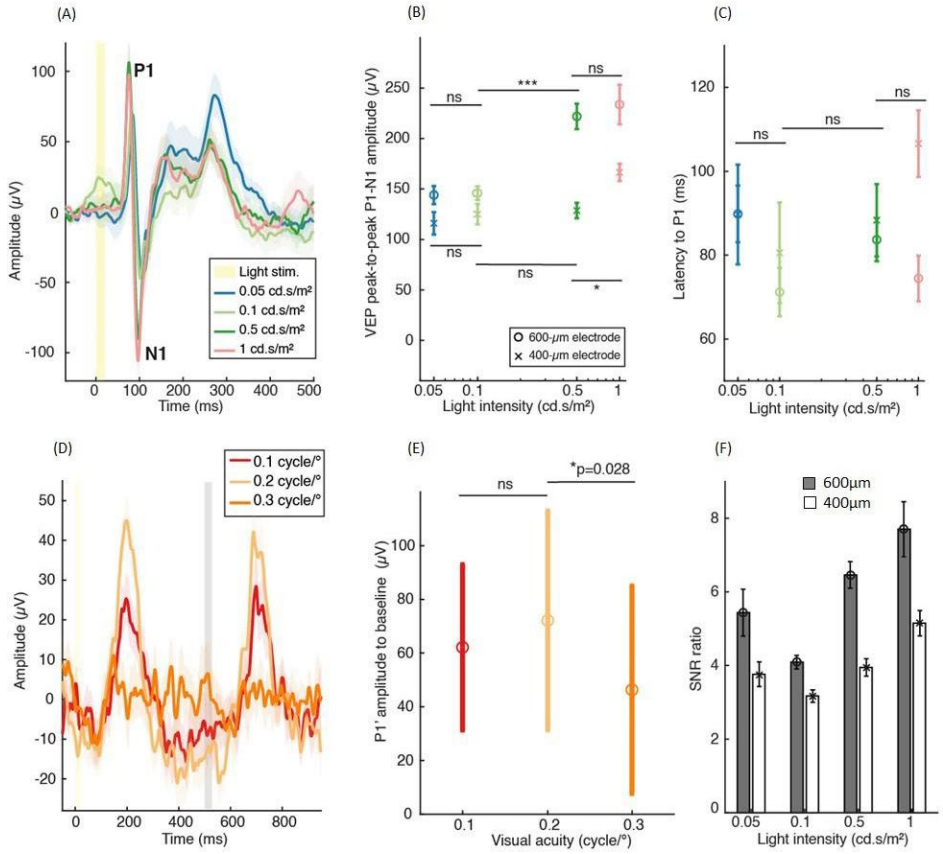

Figure 4. VEPs recording on wild-type adult mice with 600- or 400-µm-diameter BDD custom electrodes. (A) VEP response to light stimulation at different intensities (1 Hz, range from 0.05 to 1 cd.s/m², Ganzfeld stimulator). Mean signals (n=20) are shown and errors of the mean are in light shades. VEPs traces are presented with positive peak P1 upwards according to clinical conventions (Odom et al 2016), (B) P1-N1 peak-to-peak amplitudes (µV) as a function of light intensity for 600 and 400-µm-diameter electrodes. (C) Latency (ms) to reach peak P1 as a function of light intensity. (D) VEPs recorded during checkerboard pattern visual stimulation (cycles/degree). (E) P1' peak amplitude (µV) as a function of visual acuity value (cycles/degree), as mean and standard deviations, (F) Signal-to-noise ratio (SNR) of recorded VEPs at different light intensities. All results are presented as mean ± error of the mean. One-way ANOVA with Dunn-Sidak multi-comparison test: ns = non-significative, *p<0.05, **p<0.01, ***p<0.001.

Additionally, at IDV, we used a collimated white LED controlled by a stimulus generator to send light flashes towards the left eye of the rat. The average amplitude of P1 recorded was around 100 µV (figure 5). The presence of a second positive peak (P2) shortly

after the first one (P1) resembles the overall shape of VEPs described in literature. Through these experiments, we demonstrated the successful recording of VEPs using the fabricated full-diamond implants.

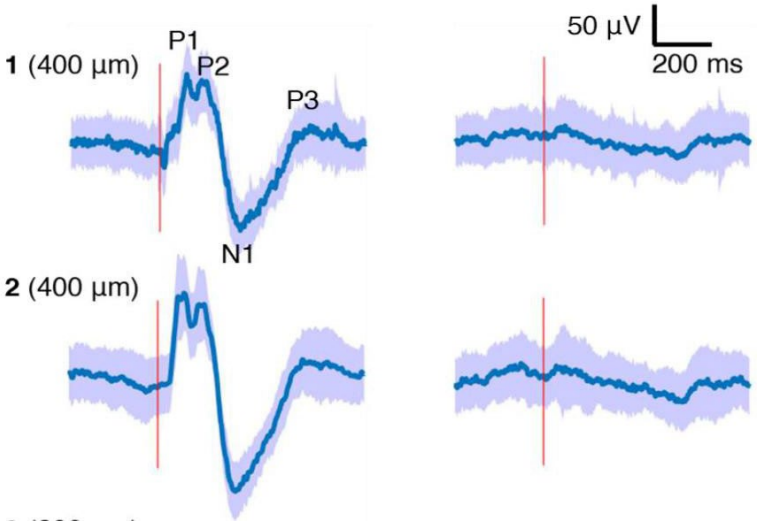

Figure 5. VEPs recording on Long Evans rats with 400-µm-diameter BDD custom electrodes. Mean signals averaged over 100 repetitions and standard deviations (light blue shades) in response to light stimulation (first column) and to hidden light stimulation (second column. Red line indicates the trigger from the light stimulus. VEPs traces are presented with positive peaks (P1, P2, P3) upwards.

4. Discussion

It is the first time, to our knowledge, that a manufacturing process is described to successfully build a full-diamond neural implant with BDD electrodes and intrinsic diamond passivation in an ultra-thin flexible technology (below 20 µm) compatible with standard microfabrication processes.

Most neural flexible implants for brain-machine interfaces are currently made of biocompatible polymers with various electrode materials (metals, semiconductors, organic polymers). Lately, interest has grown for carbon-based materials because of their high stability and biocompatibility, and promising electro-chemical properties for neural interfacing applications [[26], [14], [5]. BDD material has been previously applied on such polymer implants to generate biocompatible electrodes [9] and to record neurons in vitro when deposited on rigid substrates [38], [15]. In parallel, intrinsic diamond was used to fabricate biocompatible and hermetic cases [18], [35]. Here we combined these results and developed a new process to fabricate neural implants with BDD electrodes and TiN tracks embedded in intrinsic diamond layers using localised growth of intrinsic diamond in a cleanroom environment. The solution of using adequate masking capacity of Aluminium nitride (AlN) helps the localised growth inside the diamond reactor. Indeed AlN appears resilient to the high CVD diamond plasma conditions allowing the well-defined shape of the electrodes (figure 2(B) and (C)).

The intrinsic diamond encapsulating the conductive layers and the presence of BDD electrodes offer a strong protection against biological reactions that can occur post-implantation [25]. The high stability of diamond precludes water penetration and conse-

quent delamination. The choice of TiN material to define the conductive tracks was motivated by its natural ability to withstand diamond growth conditions and a reliable adhesion surface for diamond. Long-lasting ageing experiments are on-going to confirm the absence of delamination of such diamond implants and their ability to endure harsh biological environments. The fabricated flexible device also had to be slightly rigidified for better manipulation during surgery by parylene encapsulation, a class IV material that can be legally used for clinical applications [48], [31]. A remaining silicon piece facilitates handling and connection during animal experimentations. Overall it seems that the device could easily comply with legal standards for future clinical translations.

The 3V wide potential window in the CV measurement demonstrates that our electrodes are clearly made of BDD. Although the electrochemical window of our BDD electrodes is lower than the 4V window of the 3-mm-diameter N-UNCD electrodes [19], it is still twice wider compared to classical metals such as platinum (1.3 V, [10]), or novel materials such as Poly(3,4-ethylenedioxythiophene)-poly(styrenesulfonate) (PEDOT-PSS) coated electrodes (1.7 V in 0.9% NaCl, [47]) or sputtered iridium oxide films (SIROFs) electrodes (1.4 V in PBS, [11]).

The hypothesis of a rough BDD electrode surface is further supported by the low impedance values measured at 1 kHz along with the satisfactory conductivity of the fabricated TiN. Compared to the previously mentioned materials, the impedance of our BDD electrodes is in the same order of magnitude as 200-µm-diameter SIROFs electrodes [11].

This first technological success in terms of BDD-electrode-based implant fabrication validates the future production of a next generation device with far more electrodes per device, enabling better statistics and recording performances over a larger total surface. The thin total thickness allows its flexibility and the intrinsic diamond coating its longevity, proposing such a device could even be suitable for neural stimulation purposes.

For brain-machine interfaces, signal-to-noise ratio (SNR) is a sine qua non condition for quality restitution of neural signals. Although the electrodes here have a relatively large diameter compared to standard BCIs (≈ 30 µm), they are nonetheless suitable for neural recording on the brain surface considering that the diameter of micro ECoG implants can reach up to 1 mm diameter.

The flash VEPs recorded here demonstrate the functionality of the full-diamond implant and its BDD electrodes in a recording mode, as it was performed with two different experimental setups on rodents (Long Evans rats and C57BL mice). In both cases, the presence of a large second positive peak after the first positive P1 and negative N1 ones resembles the overall shape of VEPs described in literature [52]. In another study from [6] where VEPs were recorded on rabbits with printed platinum electrodes, mean amplitudes at 1 cd.s/m² were reported to be around 300 µV. Such differences with our measured values in amplitudes could be imputed to animal species differences and placement of the electrode on the brain. The SNR was measured to be similar to 50x50 µm² gold electrodes used for spiking activity recordings even though doped graphene ones were 6 times higher [32]. One could argue that our electrodes are larger in size and hence will pick up more noise in proportion to the smaller graphene ones, which was not observed.

Diamond was already shown to be highly biocompatible both ex vivo and in vivo [51]. In addition, the low impedance value of the fabricated full diamond implants is unprecedented for diamond-based electrodes. These in vivo results constitute the first step towards the microfabrication of a denser full-diamond electrodes array which could serve clinically as a chronic neuroprosthesis. Complementary works are under process to certify the stability and hermeticity of the full-diamond structure through ageing experiments. Future studies will have to explore how to generate smaller electrodes with a higher developed surface. However, we here provide the first proof of concept that a full thin film diamond electrode array implant is feasible for recording. More technological developments will be required to obtain a full-diamond implant for bi-directional stimulation-recording abilities.

5. Conclusions

In summary, we designed, fabricated, and validated a novel flexible thin film full-diamond implant for neural interfacing applications focussing ECoG, and we tested them through in vivo experiments to validate their functionality.

We reported the methodology of manufacturing and characterizing these implants. Diamond was mainly selected for its biocompatibility and inertness leading to little tissue reaction and long term capabilities. These thin implants composed of BDD electrodes in contact with neural tissues are also embedded into intrinsic diamond and seem resistant enough to external mechanical forces as a result of the remarkable properties of diamond.

These characteristics promote the long-term stability of such novel BCI. Besides these results, electrodes were tested in multiple animal facilities under different conditions, and VEPs were recorded at the surface of the cortex of rodents, proving that the new implants are capable of recording cortical signals. Both the in vitro characterization and the successful in vivo recordings confirm the suitable use of diamond as a material of choice for neuronal recordings, opening new pathways in the ECoG field towards long-lasting chronic electrodes tests.

In the future, we will extend this study to obtain smaller electrodes with 3D texturing to cover a larger surface of the visual cortex. Therefore this work serves as a proof-of-concept for further design of a 32-channel whole-diamond ECoG.

Author Contributions: LR, GL, SP conceptualised the project. CW and LR fabricated the implants, JZ, DN, JD, EB, DG performed the in vivo experiments. GL, CW and JZ wrote the manuscript.

Funding: "This work has been funded by the European Research Council (ERC) established by the European Commission. Lionel Rousseau has received support of an ERC starting grant 2017 (758700 — NEURODIAM). This project also received funding from the European Union's Horizon 2020 research and innovation program under the Marie Skłodowska-Curie grant agreement No 861423 (enTRAIN Vision). Additionally, we acknowledge the support of LabEx LIFESENSES (ANR-10-LABX-65) and IHU FOReSIGHT (ANR-18-IAHU-01)."

Institutional Review Board Statement: "The animal study protocol was approved by the following Institutional Review Boards: 1. according to the animal authorisation GE/193/19 approved by the Département de l'emploi, des affaires sociales et de la santé (DEAS), Direction générale de la santé de la République et Canton de Genève, 2. approved by the Local Animal Ethics Committee N°005 (registra-tion number APAFIS #15258-2018052811521506 v1), for the Institute of Vision, Paris, France.

Informed Consent Statement: "Not applicable."

Data Availability Statement: The raw/processed data required to reproduce these findings cannot be shared at this time due to technical limitations.

Conflicts of Interest: "The authors declare no conflict of interest, and declare that the research was conducted in the absence of any commercial or financial relationships that could be construed as a potential conflict of interest."

References

1. Ahnood A, Meffin H, Garrett DJ, Fox K, Ganesan K, Stacey A, Apollo NV, Wong YT, Lichter SG, Kentler W, Kavehei O, Greferath U, Vessey KA, Ibbotson MR, Fletcher EL, Burkitt AN, Prawer S (2017) Diamond Devices for High Acuity Prosthetic Vision. Advanced Biosystems 1:1600003.
2. Alahi MEE, Liu Y, Xu Z, Wang H, Wu T, Mukhopadhyay SC (2021) Recent advancement of electrocorticography (ECoG) electrodes for chronic neural recording/stimulation. Materials Today Communications 29:102853.
3. Benabid AL et al. (2019) An exoskeleton controlled by an epidural wireless brain–machine interface in a tetraplegic patient: a proof-of-concept demonstration. The Lancet Neurology 18:1112–1122.
4. Bendali A, Agnès C, Meffert S, Forster V, Bongrain A, Arnault J-C, Sahel J-A, Offenhäusser A, Bergonzo P, Picaud S (2014) Distinctive Glial and Neuronal Interfacing on Nanocrystalline Diamond Egles C, ed. PLoS ONE 9:e92562.
5. Bendali A, Rousseau L, Lissorgues G, Scorsone E, Djilas M, Dégardin J, Dubus E, Fouquet S, Benosman R, Bergonzo P, Sahel J-A, Picaud S (2015) Synthetic 3D diamond-based electrodes for flexible retinal neuroprostheses: Model, production and in vivo biocompatibility. Biomaterials 67:73–83.
6. Borda E, Ferlauto L, Schleuniger J, Mustaccio A, Lütolf F, Lücke A, Fricke S, Marjanović N, Ghezzi D (2020) All-Printed Electrocorticography Array for In Vivo Neural Recordings. Advanced Engineering Materials 22:1901403.
7. Cho Y, Park S, Lee J, Yu KJ (2021) Emerging Materials and Technologies with Applications in Flexible Neural Implants: A Comprehensive Review of Current Issues with Neural Devices. Adv Mater 33:2005786.
8. Chow AY, Pardue MT, Chow VY, Peyman GA, Chanping Liang, Perlman JI, Peachey NS (2001) Implantation of silicon chip microphotodiode arrays into the cat subretinal space. IEEE Trans Neural Syst Rehabil Eng 9:86–95.
9. Cobb SJ, Ayres ZJ, Macpherson JV (2018) Boron Doped Diamond: A Designer Electrode Material for the Twenty-First Century. Annual Rev Anal Chem 11:463–484.
10. Cogan SF (2008) Neural Stimulation and Recording Electrodes. Annu Rev Biomed Eng 10:275–309.
11. Cogan SF, Plante TD, Ehrlich J (2004) Sputtered iridium oxide films (SIROFs) for low-impedance neural stimulation and recording electrodes. In: The 26th Annual International Conference of the IEEE Engineering in Medicine and Biology Society, pp 4153–4156. San Francisco, CA, USA: IEEE. Available at: http://ieeexplore.ieee.org/document/1404158/ [Accessed January 3, 2023].
12. Čvančara P, Boretius T, López-Álvarez VM, Maciejasz P, Andreu D, Raspopovic S, Petrini F, Micera S, Granata G, Fernandez E, Rossini PM, Yoshida K, Jensen W, Divoux J-L, Guiraud D, Navarro X, Stieglitz T (2020) Stability of flexible thin-film metallization stimulation electrodes: analysis of explants after first-in-human study and improvement of in vivo performance. J Neural Eng 17:046006.
13. Daschner R, Greppmaier U, Kokelmann M, Rudorf S, Rudorf R, Schleehauf S, Wrobel WG (2017) Laboratory and clinical reliability of conformally coated subretinal implants. Biomed Microdevices 19:7.
14. Devi M, Vomero M, Fuhrer E, Castagnola E, Gueli C, Nimbalkar S, Hirabayashi M, Kassegne S, Stieglitz T, Sharma S (2021) Carbon-based neural electrodes: promises and challenges. J Neural Eng 18:041007.
15. Fan B, Rusinek CA, Thompson CH, Setien M, Guo Y, Rechenberg R, Gong Y, Weber AJ, Becker MF, Purcell E, Li W (2020) Flexible, diamond-based microelectrodes fabricated using the diamond growth side for neural sensing. Microsyst Nanoeng 6:42.
16. Fernández E, Alfaro A, Soto-Sánchez C, Gonzalez-Lopez P, Lozano AM, Peña S, Grima MD, Rodil A, Gómez B, Chen X, Roelfsema PR, Rolston JD, Davis TS, Normann RA (2021) Visual percepts evoked with an intracortical 96-channel microelectrode array inserted in human occipital cortex. Journal of Clinical Investigation 131:e151331.
17. Flesher SN, Downey JE, Weiss JM, Hughes CL, Herrera AJ, Tyler-Kabara EC, Boninger ML, Collinger JL, Gaunt RA (2021) A brain-computer interface that evokes tactile sensations improves robotic arm control. Science 372:831–836.
18. Ganesan K, Garrett DJ, Ahnood A, Shivdasani MN, Tong W, Turnley AM, Fox K, Meffin H, Prawer S (2014) An all-diamond, hermetic electrical feedthrough array for a retinal prosthesis. Biomaterials 35:908–915.

19. Garrett DJ, Ganesan K, Stacey A, Fox K, Meffin H, Prawer S (2011) Ultra-nanocrystalline diamond electrodes: optimization towards neural stimulation applications. J Neural Eng 9:016002.
20. Girard HA, Perruchas S, Gesset C, Chaigneau M, Vieille L, Arnault J-C, Bergonzo P, Boilot J-P, Gacoin T (2009) Electrostatic Grafting of Diamond Nanoparticles: A Versatile Route to Nanocrystalline Diamond Thin Films. ACS Appl Mater Interfaces 1:2738–2746.
21. Gori M, Vadalà G, Giannitelli SM, Denaro V, Di Pino G (2021) Biomedical and Tissue Engineering Strategies to Control Foreign Body Reaction to Invasive Neural Electrodes. Front Bioeng Biotechnol 9:659033.
22. Grani F, Soto-Sanchez C, Farfan FD, Alfaro A, Grima MD, Rodil Doblado A, Fernández E (2022) Time stability and connectivity analysis with an intracortical 96-channel microelectrode array inserted in human visual cortex. J Neural Eng 19:045001.
23. Hadjinicolaou AE, Leung RT, Garrett DJ, Ganesan K, Fox K, Nayagam DAX, Shivdasani MN, Meffin H, Ibbotson MR, Prawer S, O'Brien BJ (2012) Electrical stimulation of retinal ganglion cells with diamond and the development of an all diamond retinal prosthesis. Biomaterials 33:5812–5820.
24. Hébert C, Mazellier JP, Scorsone E, Mermoux M, Bergonzo P (2014a) Boosting the electrochemical properties of diamond electrodes using carbon nanotube scaffolds. Carbon 71:27–33.
25. Hébert C, Scorsone E, Bendali A, Kiran R, Cottance M, Girard HA, Degardin J, Dubus E, Lissorgues G, Rousseau L, Mailley P, Picaud S, Bergonzo P (2014b) Boron doped diamond biotechnology: from sensors to neurointerfaces. Faraday Discuss 172:47–59.
26. Hejazi M, Tong W, Ibbotson MR, Prawer S, Garrett DJ (2021) Advances in Carbon-Based Microfiber Electrodes for Neural Interfacing. Front Neurosci 15:658703.
27. Hejazi MA, Tong W, Stacey A, Sun SH, Yunzab M, Almasi A, Jung YJ, Meffin H, Fox K, Edalati K, Nadarajah A, Prawer S, Ibbotson MR, Garrett DavidJ (2020) High Fidelity Bidirectional Neural Interfacing with Carbon Fiber Microelectrodes Coated with Boron-Doped Carbon Nanowalls: An Acute Study. Adv Funct Mater 30:2006101.
28. Hess P (2012) The mechanical properties of various chemical vapor deposition diamond structures compared to the ideal single crystal. Journal of Applied Physics 111:051101.
29. Hess AE, Sabens DM, Martin HB and Zorman CA (2011), "Diamond-on-Polymer Microelectrode Arrays Fabricated Using a Chemical Release Transfer Process," in Journal of Microelectromechanical Systems, vol. 20, no. 4, pp. 867-875.
30. Kozai TDY, Catt K, Li X, Gugel ZV, Olafsson VT, Vazquez AL, Cui XT (2015) Mechanical failure modes of chronically implanted planar silicon-based neural probes for laminar recording. Biomaterials 37:25–39.
31. Kuppusami S, Oskouei RH (2015) Parylene Coatings in Medical Devices and Implants: A Review. ujbe 3:9–14.
32. Kuzum D, Takano H, Shim E, Reed JC, Juul H, Richardson AG, de Vries J, Bink H, Dichter MA, Lucas TH, Coulter DA, Cubukcu E, Litt B (2014) Transparent and flexible low noise graphene electrodes for simultaneous electrophysiology and neuroimaging. Nat Commun 5:5259.
33. Levin KH, Chauvel P eds. (2019) Clinical neurophysiology: basis and technical aspects. Amsterdam: Elsevier.
34. Li X, Perkins J, Collazo R, Nemanich RJ, Sitar Z (2006) Investigation of the effect of the total pressure and methane concentration on the growth rate and quality of diamond thin films grown by MPCVD. Diamond and Related Materials 15:1784–1788.
35. Lichter SG, Escudié MC, Stacey AD, Ganesan K, Fox K, Ahnood A, Apollo NV, Kua DC, Lee AZ, McGowan C, Saunders AL, Burns O, Nayagam DAX, Williams RA, Garrett DJ, Meffin H, Prawer S (2015) Hermetic diamond capsules for biomedical implants enabled by gold active braze alloys. Biomaterials 53:464–474.
36. Meijs S, McDonald M, Sørensen S, Rechendorff K, Fekete L, Klimša L, Petrák V, Rijkhoff N, Taylor A, Nesládek M, Pennisi CP (2018) Diamond/Porous Titanium Nitride Electrodes With Superior Electrochemical Performance for Neural Interfacing. Front Bioeng Biotechnol 6:171.
37. Odom JV, Bach M, Brigell M, Holder GE, McCulloch DL, Mizota A, Tormene AP, International Society for Clinical Electrophysiology of Vision (2016) ISCEV standard for clinical visual evoked potentials: (2016 update). Doc Ophthalmol 133:1–9.

38. Piret G, Hébert C, Mazellier J-P, Rousseau L, Scorsone E, Cottance M, Lissorgues G, Heuschkel MO, Picaud S, Bergonzo P, Yvert B (2015) 3D-nanostructured boron-doped diamond for microelectrode array neural interfacing. Biomaterials 53:173–183.
39. Polikov VS, Tresco PA, Reichert WM (2005) Response of brain tissue to chronically implanted neural electrodes. Journal of Neuroscience Methods 148:1–18.
40. Prusky GT, West Paul WR, Douglas RM (2000) Behavioral assessment of visual acuity in mice and rats. Vision Research, 40(16), pp. 2201–2209.
41. Specht CG, Williams OA, Jackman RB, Schoepfer R (2004) Ordered growth of neurons on diamond. Biomaterials 25:4073–4078.
42. Stamp MEM, Tong W, Ganesan K, Prawer S, Ibbotson MR, Garrett DJ (2020) 3D Diamond Electrode Array for High-Acuity Stimulation in Neural Tissue. ACS Appl Bio Mater 3:1544–1552.
43. Takmakov P, Ruda K, Scott Phillips K, Isayeva IS, Krauthamer V, Welle CG (2015) Rapid evaluation of the durability of cortical neural implants using accelerated aging with reactive oxygen species. J Neural Eng 12:026003.
44. Tang L, Tsai C, Gerberich WW, Kruckeberg L, Kania DR (1995) Biocompatibility of chemical-vapour-deposited diamond. Biomaterials 16:483–488.
45. Thalhammer A, Edgington RJ, Cingolani LA, Schoepfer R, Jackman RB (2010) The use of nanodiamond monolayer coatings to promote the formation of functional neuronal networks. Biomaterials 31:2097–2104.
46. Tokashiki N, Nishiguchi KM, Fujita K, Sato K, Nakagawa Y, Nakazawa T (2018) Reliable detection of low visual acuity in mice with pattern visually evoked potentials. Sci Rep 8:15948.
47. Vomero M, Castagnola E, Maggiolini E, Ciarpella F, Rembado I, Goshi N, Fadiga L, Kassegne S, Ricci D (2016) A Direct Comparison of Glassy Carbon and PEDOT-PSS Electrodes for High Charge Injection and Low Impedance Neural Interfaces. In, pp 68–76 Available at: https://www.scientific.net/AST.102.68 [Accessed January 3, 2023].
48. Wolgemuth L (2000) Assessing the Performance and Suitability of Parylene Coating. mddionline.com Available at: https://www.mddionline.com/news/assessing-performance-and-suitability-parylene-coating [Accessed December 6, 2022].
49. Wong YT, Ahnood A, Maturana MI, Kentler W, Ganesan K, Grayden DB, Meffin H, Prawer S, Ibbotson MR, Burkitt AN (2018) Feasibility of Nitrogen Doped Ultrananocrystalline Diamond Microelectrodes for Electrophysiological Recording From Neural Tissue. Front Bioeng Biotechnol 6:85.
50. Wu N, Wan S, Su S, Huang H, Dou G, Sun L (2021) Electrode materials for brain–machine interface: A review. InfoMat 3:1174–1194.
51. Yang K-H, Narayan RJ (2019) Biocompatibility and functionalization of diamond for neural applications. Current Opinion in Biomedical Engineering 10:60–68.
52. You Y, Klistorner A, Thie J, Graham SL (2011) Improving reproducibility of VEP recording in rats: electrodes, stimulus source and peak analysis. Doc Ophthalmol 123:109.

II.B. Graphene-based transistors

Chemical Vapor Deposited (CVD) graphene is a semi-metal with high charge carrier mobility. Its application in gated-field effect transistors for DC recordings was successfully reported by our collaborators of the Graphene Flagship, a European Commission funded innovation program (Blaschke et al. 2017, Hébert et al. 2018, Masvidal-Codina et al. 2019, Wykes et al. 2022). In the continuation of the project to demonstrate the many technological advantages of such graphene-based transistors, we combined it with fUS to investigate NVC.

The following paper was submitted.

Personal contribution: *in vivo* experiments (except light stimulation experiments), data analysis (fUS, gFET), manuscript writing, figures drawing (graphical abstract, fig. 1 & 2), brainstorming for fig. 3-5.

Concurrent functional ultrasound imaging with graphene-based DC-coupled electrophysiology as a platform to study neurovascular coupling under physiological and pathophysiological brain states.

Julie Meng Zhang*[a], Eduard Masvidal-Codina*[b], Diep Nguyen[a], Xavi Illa[c,d], Julie Dégardin[a], Ruben Goulet[a], Elisabet Prats-Alfonso[b,c] Stratis Matsoukis[e], Christoph Guger[e], Jose Antonio Garrido[#b,f], Serge Picaud[#a], Anton Guimerà-Brunet[#d], Rob C Wykes[#g,h]

a. Sorbonne Université, INSERM, CNRS, Institute de la Vision, F75012 Paris, France.
b. Catalan Institute of Nanoscience and Nanotechnology (ICN2), CSIC and BIST, Campus UAB, Bellaterra, Barcelona, Spain
c. Centro de Investigación Biomédica en Red en Bioingeniería, Biomateriales y Nanomedicina (CIBER-BBN), Madrid, Spain
d. Institute of Microelectronics of Barcelona, (IMB-CNM), CSIC, Spain.
e. g-tec medical engineering GmbH Austria
f ICREA, Barcelona, Spain
g University College London Queen Square Institute of Neurology, London, United Kingdom
h Nanomedicine Lab, Division of Neuroscience, University of Manchester, United Kingdom
* Authors contributed equally
# Corresponding authors: anton.guimera@imb-cnm.csic.es r.wykes@ucl.ac.uk

Abstract (308 words)

Neurovascular coupling (NVC) is a fundamental mechanism by which the brain regulates blood flow in response to neuronal activity. Traditional methods for studying NVC, such as fMRI, are indirect and have limitations in terms of temporal and spatial resolution; and AC-coupled electrographic recordings fail to accurately capture slow brain signals <0.1Hz. In this study, we demonstrate a new method for concurrent cerebral blood volume (CBV) and wide bandwidth electrophysiological mapping using simultaneous functional ultrasound imaging (fUS) and graphene-based DC-coupled recordings (gFETs). This approach allows recordings of both fast and infraslow brain signals, which is important for understanding the role of NVC in both normal and pathological brain function. To validate the feasibility of this methodology visually evoked NVC responses were examined. gFET recordings were not affected by concurrent fUS imaging, and vice versa. To examine directly the influence of infraslow potential shifts to NVC, cortical spreading depolarisations (CSDs) were induced. A biphasic pattern of first decreased and then increased CBV throughout the contralateral cortex, and a delayed decrease in deeper subcortical brain regions was detected. In a model of acute seizures CBV oscillations could be observed prior to seizure initiation. In the seconds before the electrographic onset of seizure CBV dropped before increasing beyond baseline levels during ictal discharge. This pattern of CBV was restricted to cortical regions. Seizures were associated with infraslow oscillations (ISO) <0.1Hz. Tight coupling between ISO, blood flow, and seizure onset were observed. NVC responses when seizures co-occurred with CSDs were larger in amplitude and also resulted in delayed CBV decreases in subcortical structures including the contralateral hippocampus. Our data demonstrate that gFETs are highly compatible with fUS and allow examination of NVC in a more comprehensive way than traditional methods. This technological advance has the potential to improve our understanding of how NVC works, and how it is affected by disease.

Graphical summary

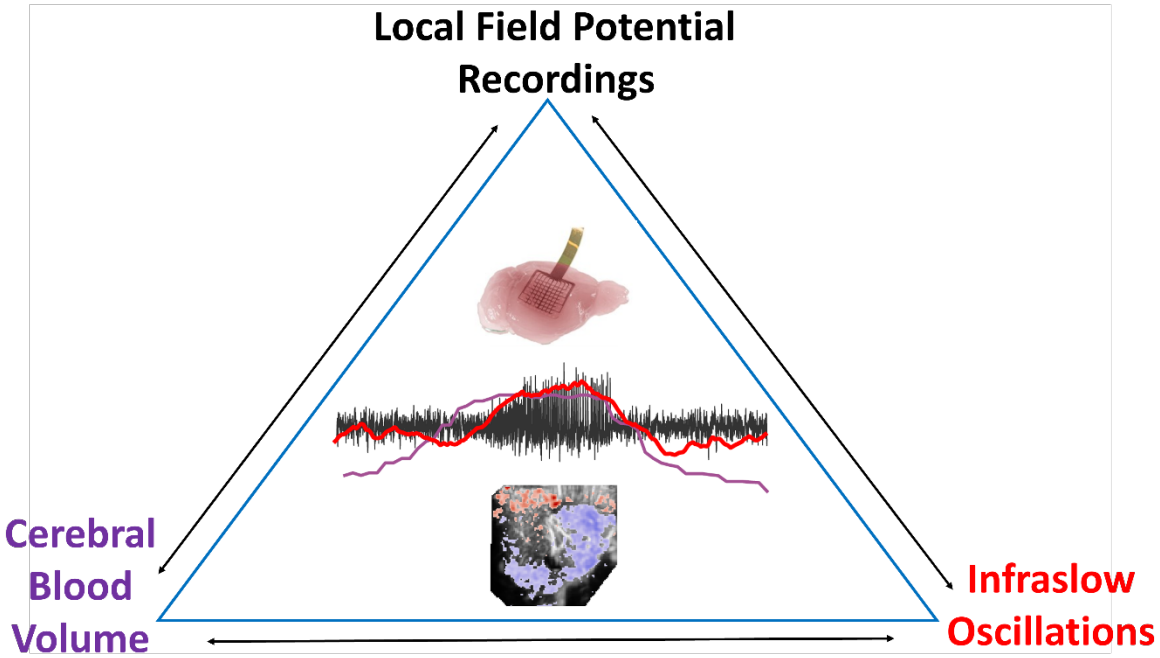

New concepts statement (197 words)

Neurovascular coupling (NVC) is a complex process that regulates relative cerebral blood volume (rCBV) to meet the dynamic energy needs of the brain, and involves the coordinated activity of neurons, astrocytes, and blood vessels. It is widely reported that dysfunction of NVC occurs and contributes to a number of neurological disorders. Application of functional ultrasound (fUS) imaging of rCBV, with traditional electrophysiology are the current state-of-art methodology. However, this approach is only able to report 2-sides of a 3-sided story. Metal-based electrodes are poorly suited to record infraslow brain oscillations (ISO) and DC potential shifts, which likely influence both local field potential (LFP) recordings and rCBV; particularly in disease-relevant settings. Graphene micro-transistor (gFET) arrays overcome limitations of metal-based electrodes and can faithfully map DC-coupled electrographic responses and LFP with high fidelity. In this technical report, we demonstrate that flexible gFET arrays are compatible with fUS and can be used to investigate NVC under both physiological and pathophysiological conditions. This technological approach is based on graphene-enabled electrophysiological probes, which can provide unparalleled insight into how ISOs, LFP and rCBV are inherently coupled. This has the potential to revolutionize our understanding of NVC and its role in neurological disorders.

Introduction (373 words)

Neurovascular coupling (NVC) is a complex process that ensures that the brain receives the blood flow it needs to function properly. It involves the coordinated activity of neurons, astrocytes, and blood vessels. NVC is essential for normal brain function, and its dysfunction is linked to a number of neurological disorders[1]. Conventional methods to study NVC at the mesoscale are limited by both the technology used to detect electrophysiological signals and the imaging approaches used to study blood flow. Electrophysiological methods typically acquire only AC-coupled signals with frequencies >0.1Hz, due in part to the poor performance of traditional metal-based electrodes in recording slow brain potentials[2,3]. However, functional magnetic resonance imaging (fMRI) studies suggest that signals 0.1Hz and below, called infraslow brain oscillations (ISO) contribute to NVC[4]. fMRI itself is an indirect

measure based on changes in blood oxygenation, and uses strong magnetic fields complicating concurrent electrophysiological applications. To understand the contribution of DC potential shifts and ISO to NVC, novel approaches combining wide bandwidth DC-coupled electrophysiology with more direct methods for imaging cerebral blood volume (CBV) are warranted. Graphene, a 2D material with exceptional electrical conductivity, is ideal for integration into electrographic devices[5]. Graphene microtransistor arrays (gFETs) demonstrate excellent recording stability and a high signal-to-noise ratio for DC-coupled measurements[6]. Flexible arrays of gFETs can be used to map with high fidelity both fast and slow brain signals including seizures and spreading depolarisations[7,8]. Functional Ultrasound (fUS) is a method for identifying regions of brain activation by imaging transient changes in blood volume. fUS is based on backscattered echoes from red blood cells, allowing imaging of whole brain NVC[9]. It allows higher temporal and spatial resolution compared to fMRI and permits imaging of deeper brain regions in contrast to other methods such as laser speckle contrast imaging. In this study, we investigated the compatibility of surface DC-coupled electrophysiology recordings enabled by gFETs simultaneously with fUS imaging of CBV. This approach permits recording both fast and infraslow brain signals, which is important for understanding the role of NVC in both normal and pathological brain function. We demonstrate our approach to study NVC in response to visual stimulation, cortical spreading depolarisations, and seizures. Our data determine that this new approach is a valuable tool for studying NVC.

Results and Discussion

To demonstrate the power of our experimental paradigm, we performed concurrent fUS imaging with graphene-based DC-coupled electrophysiology in anesthetized rats subjected to both physiological and pathological stimuli.

Compatibility of concurrent acquisition of CBV and DC-coupled electrophysiology

The experimental setup is shown in Fig. 1a. The principles of fUS are presented in Fig.1a, right box. In contrast to passive electrodes, gFETs are active devices. The recording mechanism of gFETs is shown in the bottom box of Fig. 1a. Briefly, a bias Vds voltage is applied across the graphene channel to promote current flow that fluctuates based on the signals at the graphene surface which is in contact with the neural tissue. To set an appropriate operating point a Ids-Vgs curve is performed to convert the obtained current (Ids) signals into voltage. Due to the excellent electrochemical stability of graphene and the FET-based acquisition mechanism, signals are acquired in DC-coupled mode with excellent signal fidelity[6]. Potential crosstalk effects between both modalities were examined. Activation of fUS acquisition (which exerts 15 MHz ultrasound waves) did not affect the recorded signal quality from gFETs (Fig. 1b). No detectable artifacts or changes in LFP power were observed by switching on and off fUS acquisition (Fig. 1b). The presence of gFETs embedded in a thin, flexible polyimide substrate did not result in imaging artefacts on fUS acquired images (Fig. 1c), demonstrating the compatibility of these two distinct methodologies. To validate the feasibility of this approach we first examined visually evoked NVC. Light stimulation (2Hz, 50% duty cycle) to the contralateral eye induced on/off potentials recorded from the gFETs observed temporal and spectral analysis (Fig. 1f), and an increase in CBV in areas related to visual processing such as the superior colliculus (SC), lateral geniculate nucleus (LGN) and primary visual cortex (V1) (Fig. 1d-e, n=3 animals) in accordance with literature[10].

NVC response to Cortical Spreading Depolarisations.

Spreading depolarisation is the most severe disruption of brain homeostasis that can occur in living neural tissue. It is characterized by a sudden, near-complete collapse of the transmembrane ion gradients and a large-amplitude (tens of millivolts) negative shift in extracellular potential that lasts for tens of seconds[11].To demonstrate the ability to record slow pathological brain signals, we induced cortical spreading depolarisations (CSD) by either mechanical (pinprick), or pharmacological (high extracellular potassium) administration via a small bur hole close to the imaging window (Fig. 2a). We were able to map the propagation of the CSD across the cortex using both electrographic and haemodynamic recordings. Pinprick induced a cortical propagating wave of depolarisation (depolarisation duration 80±33s, 9 CSDs from 5 rats), with a sustained period of cortical spreading depression, Fig. 2b. Full recovery of neuronal activity assessed by local field potential power took approximately 7 minutes. The haemodynamic response to CSD was biphasic in cortical regions. An initial decrease in CBV was subsequently followed by an increase in CBV. A peak decrease (P1) of CBV -53.32±3.58%, in both regions close to the site of induction (visual areas V1/V2), as well as cortical

regions further away from onset (motor area, M1) were observed. This was followed by a peak hyperaemia, P2 40.92±13.21%, delayed by 47.17±7.09s (n=9 pinprick CSDs from n=5 animals). CSD propagation speed calculated from CBV changes was calculated at 6.05±1.28mm/min (Fig. 2d) were similar to previously reported ranges[12]. Similar results were obtained when CSD was induced via localised administration of potassium chloride to the burr hole. CSD duration 46±34s, propagation speed 5.2±1.57mm/min (5 CSDs from 4 rats). Interestingly we observed delayed subcortical blood flow changes indicating that neurovascular responses to a CSD are not restricted to the cortex. Although haemodynamic response to CSD in the cortex have been well studied and reported, the technical approaches taken usually only detect blood flow changes in the cortex, resulting in an assumption that changes in blood flow are limited to the cortex. Recently a fUS imaging study reported that CSD can induce complex subcortical CBV changes[13]. Indeed, we observe delayed reductions in CBV in subcortical regions including the hippocampus, amygdala and piriform cortex (Fig. 2 b-d). Functional hyperaemia was however confined to cortical regions (Fig. 2e). The combination of DC-coupled electrophysiology, surface arrays, or in future studies penetrating probes8 with fUS imaging of both cortical and deep brain structures will permit more advanced studies into the impact of CSD to brain function.

NVC response to Seizures and Seizure-associated Spreading Depolarisations.
Seizures can be generated by a coupled dynamical system in which there are both fast and slow processes[14] and induce large haemodynamic responses. Active pre-seizure DC potential shifts and ISO's <0.1Hz can open seizure susceptibility windows[8], but the role of blood flow in the transition to seizure is poorly understood. It has been reported that preictal blood flow changes can occur several seconds before seizure onset[15]. To investigate the temporal relationship between CBV changes, ISO and seizure onset we induced acute seizures by focal administration of a chemoconvulsant (4-AP) to the visual cortex. Several minutes after injection recurrent seizures arise (fig. 3a). Of interest we observed oscillations in cortical CBV which preceded the onset of seizure (n = 5 animals) (Fig 3.b). These oscillations grew in amplitude with the onset of seizures, with one cycle per seizure. The peak trough of CBV occurred before seizure onset. The crest of the oscillation had peak CBV, which occurred during the ictal discharge (Fig. 3c).

DC-coupled electrophysiology revealed an ISO with one cycle per seizure (Fig. 4 a,b).
Although the time course of the ISO and CBV cycles were similar, there was heterogeneity in the order of events, with ISO sometimes fractionally preceding CBV and in other instances CBV occurring prior to ISO (Fig 4. e). We attribute this to the relatively small gFET arrays used in this study (1.6 x 1.6 mm). We have previously reported that 'active' DC shifts and ISO are temporally and spatially restricted[8]. It is possible that in some instances seizures arise directly underneath the array, whereas others may start further away which could explain the slight variability in ISO/CBV order. Future studies employing larger arrays will be able to investigate this possibility. Our results do demonstrate a tight correlation, with phase-amplitude coupling between ISO's and LFP in addition to CBV (Fig. 4. c,d). It is probable that the generator(s) for seizure-associated ISOs and CBV oscillations share a common mechanism. In this regard our technological approach will allow future dissection of pathways which result in this form of activity and provide insight into seizure genesis with important therapeutic implications.

Seizures have been reported to co-occur with spreading depolarisations[8,16], but due to the prominence of AC-coupled electrophysiology used by the epilepsy community this is a largely overlooked phenomenon even though it has important clinical implications[17,18.] When seizures were associated with CSD we observed larger and more sustained increases in CBV post-seizure in cortical regions and delayed and prolonged decreased CBV in subcortical regions including the hippocampus (Fig. 5.).

By using a model of chemoconvulsant-induced seizures we report a tight phase coupling between infraslow brain signals, blood flow, and seizure onset. Consistent with recent findings, we observed a decrease in blood flow to the brain in the seconds before transition to seizure, and an increase during the seizure[19,20]. Seizures that occurred with CSDs showed more complex NVC responses, with a delayed reduction of CBF in subcortical regions including the hippocampus.

Conclusion (250 words)

Our findings demonstrate that gFETs are compatible with fUS, enabling us to study how both fast and infraslow brain signals contribute to NVC. This technological breakthrough will improve our understanding of NVC and its role in disease.

Experimental Section

NVC was examined under three experimental approaches; visual stimulation via full-field LED illumination of the contralateral eye; induction of CSD by either mechanical (pinprick), or chemical (high potassium 1µl of 100mM injected into the superficial cortex) approaches; and initiation of seizures via injection of 1µl of 50mM 4-aminopyridine (4-AP) to the visual cortex. For each stimulus, epidural DC-coupled electrographic signals from the visual/somatosensory cortex of a single hemisphere were recorded using polyimide-based flexible graphene field-effect microtransistor arrays. These are 1.6 x 1.6 mm in size, with a 4x4 arrangement of 50x50 or 100x100 μm^2 channel sizes. The fabrication was performed at the clean-room of the Institut de Microelectrònica de Barcelona (IMB-CNM,CSIC) following the process described in previous studies[6,7]. Concurrent to the electrographic recordings, functional ultrasound imaging (fUS) of the brain was used to explore neural activation in the cortex and deeper subcortical structures.

Animal experiments and surgical details

A total of 14 Long Evans (LE) wild-type rats were used for this study. Rats were co-housed in ventilated cages with food and water ad libidum with enrichment. The temperature in the animal facility was maintained at 22°C +/- 2 and light cycle was reversed every 12 hours. All animal experiments were completed in accordance with the Charles Darwin No5 Ethics Committee in Animal Experimentation in the approved animal facilities associated to the Vision Institute (registration number APAFIS#24563-2020030614031084 v6). Half an hour before the surgical intervention, the rats were injected subcutaneously with Buprenorphine (0.05 mg/kg, Buprecare®, Axience, France) and Dexamethasone (0,7 mg/kg, Dexazone®, Virbac, France) to reduce any pain and inflammation. After being shaved, a local analgesic, Lidocaine (4 mg/kg, Laocaïne®, MSD, France) was administered subcutaneously under the scalp skin and Xylocaine gel (2%) was applied in the ears. Anaesthesia was provided by 5% gaseous induction of isoflurane (Isorane®, Axience, France) and maintained at 2-3 %. Animals were placed in a stereotaxic frame. The temperature of the body was maintained at 37°C with a heating plate. Drops of ocular gel (Lubrithal®, Dechra, France) were delivered on the eyes of the rats to avoid drying out and were then covered with a black cloth for dark adaptation. The skin was disinfected with iodopovidone solution (Vetedine®, Vetoquinol, France) and incised. Remaining skin parts were removed, and the skull was cleaned with oxygenated water. A unilateral craniotomy was performed to expose the dura from motor to visual cortical regions (left hemisphere). A burr hole was drilled next to the cranial window in the same brain hemisphere, at Bregma –7 mm (visual cortex), to enable access to the brain for CSD induction (pinprick or KCL) and injection of chemoconvulsant in the cortex for initiation of epileptiform and seizure activity. The array was placed over the visual/somatosensory cortical area. A piece of plastic (TPX® polymethylpentene, GoodFellow Cambridge, UK) was cut to fit the craniotomy and placed on top of the array. The fUS probe was placed on top of this, after applying generous drops of ultrasound gel. The probe was positioned coronally at bregma -5.5 mm for light stimulation experiments, and between midline (ML) +3.75 and 4.3 mm sagittally for other stimuli. The animals were kept under isoflurane anaesthesia for up to 4 hours and euthanized at the end of the experiment by intracardiac injection overdose of euthanasian (200 mg/kg, Exagon®, Axience, France).

Light stimulation

Light stimulation with a white full-field LED (MWWHLP1, ThorLabs, USA) controlled by a stimulus generator (STG 4002, Multi-Channel Systems, Germany) was used on 3 LE rats. The protocol consisted of 2Hz light stimulus (50% duty cycle) during 10s followed by 20s without light stimulation repeated for 10 times, i.e., a total protocol duration of 5 min. The LED amplitude was set at high intensity (2.0 mW/cm^2) or low intensity (0.3 mW/cm^2) in compliance with animal safety rules.

Induction of CSDs and seizures.
CSDs were induced by either pricking the surface of the brain with a needle (31G), n = 5 animals, or injection of a high potassium solution directly into the superficial cortex via the pre-drilled bur hole (1µl of 100mM, n= 4 animals). To elicit seizures 0.5-1µl of 50mM 4-aminopyridine (4-AP) was injected through the bur hole close to the edge of the gFET array (n= 4 animals).

gFET calibration and analysis
Signal acquisition.
Electrophysiological recordings were performed using flexible gFETs arrays. The transistor arrays were carefully connected to a PCB and lowered onto the cortical surface. Whereas most currently available electrodes are passive, gSGFETs are active devices that transduce local voltage changes to current and permit a wide recording bandwidth6. The experimental setup used to perform the *in vivo* recordings provides Vs and Vd bias control and current-to-voltage conversion for up to 16 gFET channels, custom g.HIamp biosignal amplifier, (g.RAPHENE, g.tec medical engineering GmbH Austria). The instrumentation splits the recorded signals into two bands with different gains: low-pass filtered (LPF, < 0.16 Hz, 104 gain) and bandpass filtered (BPF, 0.16 Hz < f < 160 kHz, 106 gain), preventing amplifier saturation. Prior to recording, Ids − Vgs curves were obtained at the start and end of each experiment to allow determination of the performance of the gFET and custom code was used to calculate the optimal bias point (average across the arrays of the maximum of the mean absolute transconductance left from charge neutrality point). Two custom Simulink models were used: i) to perform the transfer curve of the microtransistors once inserted and at the end of the experiment; ii) to set the Vs and Vd bias and acquire the recorded signals. Signals were sampled at 9.6 kHz.

Data Calibration
All electrophysiological data were calibrated using Python 3.9 packages (Matplotlib, Numpy, Neo) and the custom library PhyREC (https://github.com/aguimera/PhyREC). The conversion of the recorded current signals (LPF and BPF) to a voltage signal was performed by summation of the two signals and inverse interpolation in the *in vivo*/chronic measured transfer curve of the corresponding gSGFET when possible, and by applying the transconductance factor at the bias point (gm(Vgs)) otherwise. The transfer curves were always measured at the beginning and end of every recording to ensure that no significant variations were present and to detect any malfunctioning transistor.

Data analysis
All electrophysiological data were calibrated using Python 3.9 packages (Matplotlib 3.2.0, Numpy 1.17.4, Pandas 0.25.3, Seaborn 0.9.0 and Neo 0.8.0) and the custom library PhyREC (https://github.com/aguimera/PhyREC). CSD analysis methods have previously been reported[7]. No high pass filtering is applied to the recorded extracellular potentials for the analysis of CSD waveforms, extraction of CSD parameters or plotting to avoid any signal distortion. Briefly, for each CSD extracellular voltage shift the peak amplitude and duration were extracted. Raw signals were down sampled to 3 Hz and zero voltage was set to the average value of the 5 s before the light stimulus. We defined the onset of the CSD as the onset of the negative shift with a threshold at −4 mV. Peak amplitude was defined as the minimum value of the wave and reported as an absolute value. CSD duration was defined as the time that the extracellular voltage remained below −4 mV; it was determined using below and above thresholds.

fUS acquisition and analysis
The fUS probe is composed of a linear ultrasound probe (128 piezoelectric elements, 15 MHz, 110 µm pitch and 8 mm elevation focus, Vermon, France), connected to an ultrafast ultrasound scanner (Aixplorer, Verasonics, France) controlled through Matlab. Detailed physics principles behind fUS can be found in previous literature[9,21], and are illustrated in Fig.1a. Briefly, a sequence of tilted plane waves (11, angles from –10° to +10° with a 2° step) are simultaneously emitted by the transducers and their backscattered echoes are recorded. To obtain a high-resolution image, the sequence is repeated 200 times at 500 Hz which takes 0.4 s in total per image. Beamforming of the echoed signal enables reconstruction of the imaged brain slice and takes less than 0.6 s. The final image sampling rate is 1 Hz, resulting in a compound image (IQ) created per second. After acquisition, the compound images are filtered to remove background noise and the resulting power doppler signals (proportional to the cerebral blood volume (CBV)) are obtained. Pre-processing of acquired images consisted of using singular value

decomposition (SVD) with a clutter filter at λ=60 to filter out singular values linked to the tissue space[22]. The power doppler signals retrieved (PwD) is proportional to blood volume. The signals PwD were then smoothed (gaussian 3x3 filter) and analysed offline using Matlab. Baseline signal (BL) was calculated by averaging PwD during the first 30 s of acquisitions for light stimulation experiments and during the time before pinprick for other stimuli. The cerebral blood flow (CBV) was normalised into a relative steady-state value (rCBV) and calculated as the following:

$$rCBV = \frac{(PwD - BL)}{BL} * 100\ (\%)$$

Images were manually registered.

For light stimulation experiments, correlation heatmaps between stimulation pattern and doppler data were calculated using a global linear model[23] with Benjamini correction ($q<0.1$). Lateral geniculate nucleus (LGN), superior colliculus (SC) and visual cortex (V1/V2) ROIs were identified according to the Paxinos & Watson rat brain atlas[24]. In these ROIs, rCBV was averaged over successive repetitions.
For pinprick experiments, KCl and 4-AP injection experiments, rectangle ROIs (15x10 voxels) were selected in the visual cortex (V1), somatosensory cortex (S1), and other subcortical regions such as Hippocampus (Hip), Thalamus (Thal) or Amygdala (Amygd). For pinprick and KCl experiments, global minimum (P1) and global maximum (P2) peaks were identified on rCBV plots during the CSD events (n=9 experiments for 5 animals). Peaks rCBV percentage and time from onset stimulus were quantified across subjects. CSD propagation heatmaps were represented for P1, P2 in terms of rCBV amplitude and time from stimulus onset. Voxels for which rCBV amplitude at P1 was below three times the baseline standard deviation were discarded. Additionally, for voxels in cortical regions, the time at which P1 occurs from onset time versus distance of the voxels from onset point was calculated. CSD speed (mm/min) was obtained by calculating the slope of the linear fit to this plot.

Author Contributions

Conceptualization: S.P., A. G-B., R. W. Investigation: D.N., J.Z., E.M-C., A. G-B., R. W., Resources: J.D., R.G., X.I., S.M., C.G., Visualization and writing: J.Z., E.M-C., A. G-B., R. W.

Conflicts of Interest

Stratis Matsoukis & Christoph Guger work for g-tec medical engineering, GmbH Austria.

Acknowledgements

This research was funded by the European Union's Horizon 2020 research and innovation programme under grant agreement n°881603 (Graphene flagship Core 3). This project has also received funding from the European Union's Horizon 2020 research and innovation programme under the Marie Skłodowska-Curie grant agreement No 861423 (enTRAIN Vision). We acknowledge the LabEx LIFESENSES (ANR-10-LABX-65) and IHU FOReSIGHT (ANR-18-IAHU-01). RW holds a Senior Research Fellowship funded by the Worshipful Company of Pewterers. ICN2 is supported by the Severo Ochoa Centres of Excellence programme (Grant CEX2021-001214-S), funded by MCIN/AEI/10.13039.501100011033, and by the CERCA Programme of Generalitat de Catalunya. E.M.C. acknowledges grant FJC2021-046601-I funded by Agencia Estatal de Investigación of Spain and the European Union NextGenerationEU/PRTR.

References

1 Stackhouse, T. L. & Mishra, A. Neurovascular Coupling in Development and Disease: Focus on Astrocytes. Frontiers in Cell and Developmental Biology 9 (2021). https://doi.org:10.3389/fcell.2021.702832

2 Li, C. et al. Evaluation of microelectrode materials for direct-current electrocorticography. Journal of neural engineering 13, 016008 (2016). https://doi.org:10.1088/1741-2560/13/1/016008

3 Hartings, J. A. How slow can you go? Nature materials 18, 194-196 (2019). https://doi.org:10.1038/s41563-018-0272-5

4 Drew, P. J., Mateo, C., Turner, K. L., Yu, X. & Kleinfeld, D. Ultra-slow Oscillations in fMRI and Resting-State Connectivity: Neuronal and Vascular Contributions and Technical Confounds. Neuron 107, 782-804 (2020). https://doi.org:10.1016/j.neuron.2020.07.020

5 Kostarelos, K., Vincent, M., Hebert, C. & Garrido, J. A. Graphene in the Design and Engineering of Next-Generation Neural Interfaces. Advanced materials (Deerfield Beach, Fla.) 29 (2017). https://doi.org:10.1002/adma.201700909

6 Masvidal-Codina, E. et al. High-resolution mapping of infraslow cortical brain activity enabled by graphene microtransistors. Nature materials 18, 280-288 (2019). https://doi.org:10.1038/s41563-018-0249-4

7 Masvidal-Codina, E. et al. Characterization of optogenetically-induced cortical spreading depression in awake mice using graphene micro-transistor arrays. Journal of neural engineering 18 (2021). https://doi.org:10.1088/1741-2552/abecf3

8 Bonaccini Calia, A. et al. Full-bandwidth electrophysiology of seizures and epileptiform activity enabled by flexible graphene microtransistor depth neural probes. Nat Nanotechnol 17, 301-309 (2022). https://doi.org:10.1038/s41565-021-01041-9

9 Macé, E. et al. Functional ultrasound imaging of the brain. Nature methods 8, 662-664 (2011). https://doi.org:10.1038/nmeth.1641

10 Gesnik, M. et al. 3D functional ultrasound imaging of the cerebral visual system in rodents. NeuroImage 149, 267-274 (2017). https://doi.org:10.1016/j.neuroimage.2017.01.071

11 Dreier, J. P. The role of spreading depression, spreading depolarization and spreading ischemia in neurological disease. Nat Med 17, 439-447 (2011). https://doi.org:10.1038/nm.2333

12 Pietrobon, D. & Moskowitz, M. A. Chaos and commotion in the wake of cortical spreading depression and spreading depolarizations. Nature reviews. Neuroscience 15, 379-393 (2014). https://doi.org:10.1038/nrn3770

13 Bourgeais-Rambur, L. et al. Altered Cortical Trigeminal Fields Excitability by Spreading Depolarization Revealed with *in vivo* Functional Ultrasound Imaging Combined with Electrophysiology. The Journal of Neuroscience 42, 6295-6308 (2022). https://doi.org:10.1523/jneurosci.1825-21.2022

14 Jirsa, V. K., Stacey, W. C., Quilichini, P. P., Ivanov, A. I. & Bernard, C. On the nature of seizure dynamics. Brain 137, 2210-2230 (2014). https://doi.org:10.1093/brain/awu133

15 Chaudhary, U. J. et al. Mapping preictal and ictal haemodynamic networks using video-electroencephalography and functional imaging. Brain 135, 3645-3663 (2012). https://doi.org:10.1093/brain/aws302

16 Aiba, I., Ning, Y. & Noebels, J. L. A hyperthermic seizure unleashes a surge of spreading depolarizations in Scn1a-deficient mice. JCI Insight 8 (2023). https://doi.org:10.1172/jci.insight.170399

17 Loonen, I. C. M. et al. Brainstem spreading depolarization and cortical dynamics during fatal seizures in Cacna1a S218L mice. Brain 142, 412-425 (2019). https://doi.org:10.1093/brain/awy325

18 Aiba, I. & Noebels, J. L. Spreading depolarization in the brainstem mediates sudden cardiorespiratory arrest in mouse SUDEP models. Science Translational Medicine 7 (2015). https://doi.org:ARTN 282ra46/10.1126/scitranslmed.aaa4050

19 Nourhashemi, M., Mahmoudzadeh, M., Heberle, C. & Wallois, F. Preictal neuronal and vascular activity precedes the onset of childhood absence seizure: direct current potential shifts and their correlation with hemodynamic activity. Neurophotonics 10, 025005 (2023). https://doi.org:10.1117/1.NPh.10.2.025005

20 Lim, H. K. et al. Differential contribution of excitatory and inhibitory neurons in shaping neurovascular coupling in different epileptic neural states. Journal of cerebral blood flow and metabolism : official journal of the International Society of Cerebral Blood Flow and Metabolism 41, 1145-1161 (2021). https://doi.org:10.1177/0271678x20934071

21 Tanter, M. & Fink, M. Ultrafast imaging in biomedical ultrasound. IEEE Trans Ultrason Ferroelectr Freq Control 61, 102-119 (2014). https://doi.org:10.1109/tuffc.2014.6689779

22 Demené, C. et al. Spatiotemporal Clutter Filtering of Ultrafast Ultrasound Data Highly Increases Doppler and fUltrasound Sensitivity. IEEE Trans Med Imaging 34, 2271-2285 (2015). https://doi.org:10.1109/tmi.2015.2428634

23 Friston, K. J. in Neuroscience Databases: A Practical Guide (ed Rolf Kötter) 237-250 (Springer US, 2003).

24 Paxinos, G., and Watson, C. The rat brain in stereotaxic coordinates. Compact seventh edition. edn, (Elsevier, Academic Press, 2018).

Figures

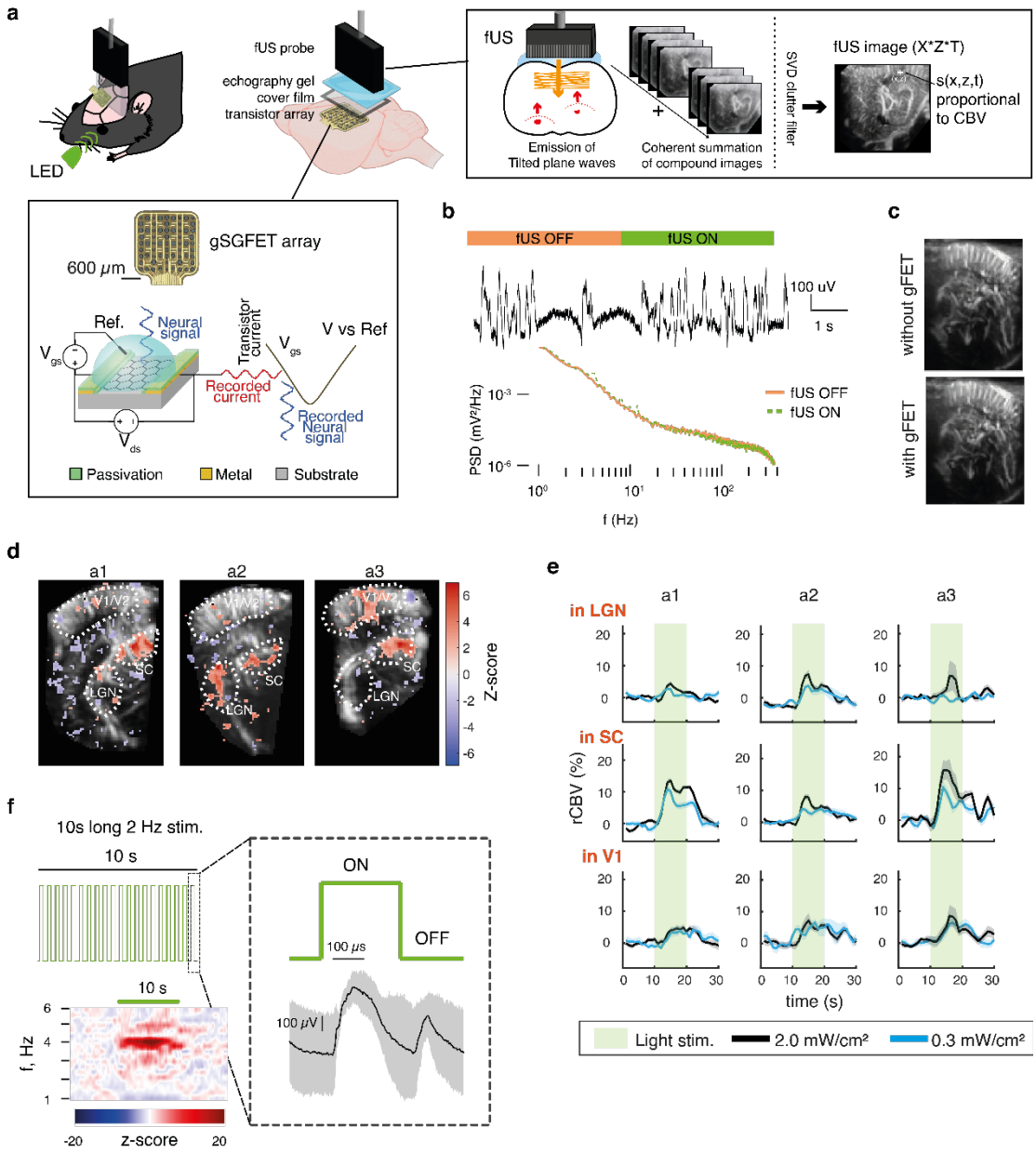

Figure 1. Electrophysiological and functional ultrasound imaging compatibility. **a.** Schematic of the experimental paradigm. An LED was used to visually stimulate the eye contralateral to electrographic and imaging recordings. Over the left hemisphere cortex of a rat a large (3 x 9 mm) craniotomy was performed to be used as fUS imaging window (AP +1 to -8 mm, ML 0.5-3.5 mm). A 16 channel gSGFET array was positioned in the dura over visual/somatosensory cortex and the craniotomy sealed with a piece of cover film before application of transduction gel and placement of the fUS probe. Schematic cross-section of a graphene micro-transistor, with the driving voltage (Vds) and the operation point selector voltage (Vgs) labelled. Current fluctuations in the drain-source current (Ids) are then converted back to voltage using the transfer characteristics of the transistor (Ids-Vgs curve)[6]. The principles of fUS imaging are shown in schematic form (right box). **b.** Representative gFET-acquired raw electrophysiological signal and power spectrum density during times when fUS-acquisition was switched ON or OFF. **c.** Representative fUS-acquired image with or without gFET placement over the cortex underneath the fUS probe. **d.** Z-score of correlation between stimulation pattern and CBV for 3 different animals (a1, a2, a3). Region of Interests ROIs are the visual cortex (V1), the superior colliculus (SC) and the lateral geniculate nucleus (LGN). **e.** Averaged CBV increase during the 10s visual stimulation at the 3 selected regions. **f.** Visual stimulation protocol consisted of 2Hz light stimulus (50% duty cycle) during 10s followed by 20s without light stimulation repeated 10 times, i.e. total protocol duration of 5

min. Averaged z-scored power spectrogram during the 10s light stimulation shows an increase in power at double of the LED stimulation frequency (4Hz) as expected. Right: Median and median absolute deviation of the electrophysiological response recorded using a gFET in response to the visual stimulation. ON and OFF visually evoked potentials are observed.

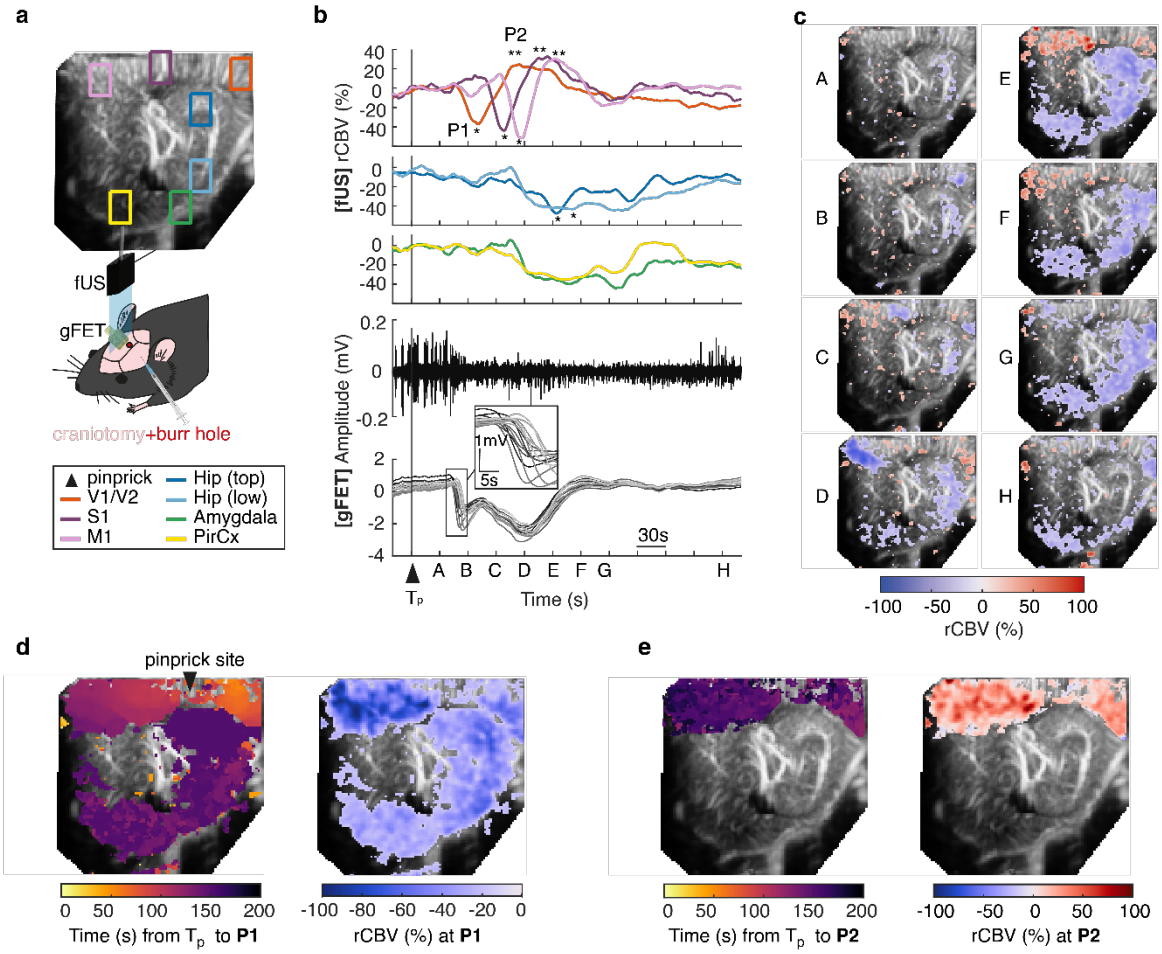

Figure 2 Characterisation of cortical spreading depolarisations (CSDs) using simultaneous gFET epidural recordings and fUS. **a.** Schematic of the experimental protocol. The fUS probe was placed on top of the array in sagittal orientation. Either pinprick or KCl stimulus was applied via a burr hole next to the craniotomy at bregma – 7 mm. The colour code for CBV changes in different brain regions is shown below. **b-f.** A CSD event occurring upon mechanical pinprick. **b.** in visual cortical areas. The time course of cerebral blood volume (CBV) changes in visual areas (V1/V2, orange), somatosensory cortex (S1, brown), motor cortex (M1, pink), hippocampus (blue), and amygdala (green) and piriform cortex (yellow). Below show the electrographic response recorded using the graphene transistor array (gFET); AC signal from a single transistor (top), and DC signals from multiple transistors, with blow up to illustrate propagation (below). T_p represents pinprick onset. Description of the CSD wave recorded in fUS by 2 distinct peaks: P1 (first global minimum), P2 (global maximum). **c.** Time course of CSD changes in CBV through the sagittal plane of the brain. **d.** (left) Propagation of P1 over time across the cortical and subcortical regions of the brain and (right) corresponding rCBV at P1. **e.** Propagation of P2 over time across the cortical and subcortical regions of the brain (left) and corresponding rCBV at P2 (right).

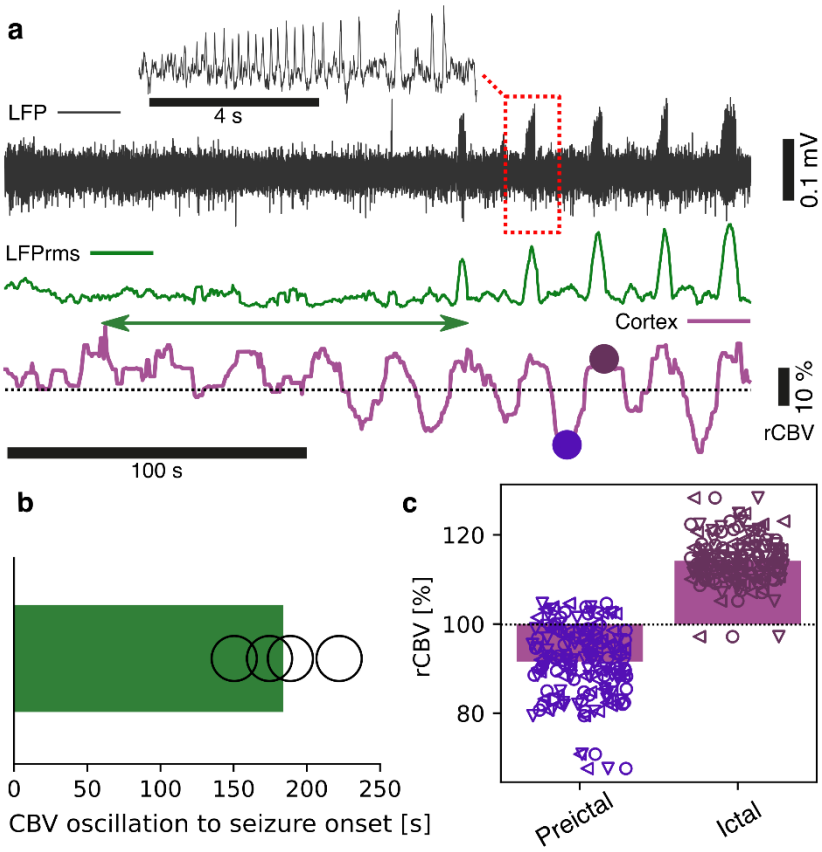

Figure 3. Blood flow changes precede the onset of chemoconvulsant-induced seizures. a. Representative high-pass filtered (>0.3Hz) recording (black trace), with corresponding rms signal (green trace) from a single transistor of the period post-injection of chemoconvulsant (4-AP) until the onset of seizures. Red box indicates a seizure with blow up above. Concurrent cortical CBV imaging (purple trace) is shown below. **b.** Oscillations in CBV occur prior to the electrographic onset of seizure, Bar and scatter plot of the time CBV oscillation start preceding seizure onset n=4 animals. **c.** A biphasic response to CBV is observed with a decrease in rCBV occurring prior to seizure, and an increase peaking during ictal activity, bar and scatter plot of the change in rCBV during preictal and ictal states as defined by the electrographic onset of seizure (n=4 animals)

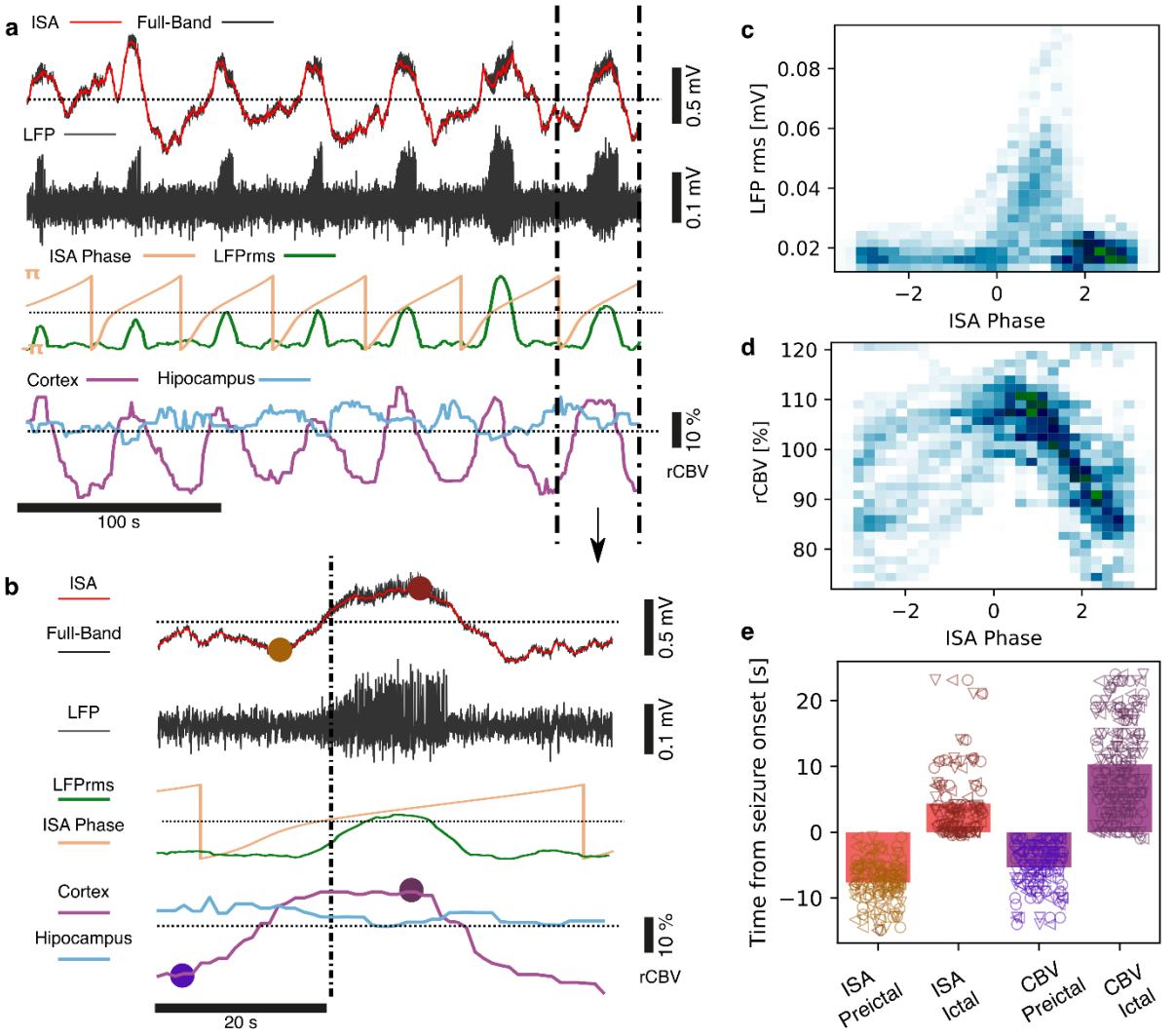

Figure 4. Correlations between rCBV, ISA and seizures. a. Raw DC-coupled recording of 7 seizures (black), with the DC potential (<0.1Hz) displayed in red. The signal filtered above 0.5Hz is shown below (black), with the LFP rms displayed in green, and the ISO phase (yellow, 0.01-0.1Hz). rCBV from a region of interest in the cortex (purple) and hippocampus (blue) are shown at the bottom. **b.** Blow up of a single seizure event illustrating the amplitude-phase correlation between ISO, seizure and cortical CBV. The brown and purple dots mark the trough and peaks of the ISO and CBV respectively **c.** Density distributions of the ISO phase and seizure LFP rms. **d**. Density distributions of the ISO phase and rCBV, **e**. Barplots with scatter of the time of ISO and CBV increase prior to seizure onset and its peak time during the ictal state. The rise of the ISO and CBV occurred prior to seizure onset, peaking towards the end of ictus, before dropping again (n=3 animals).

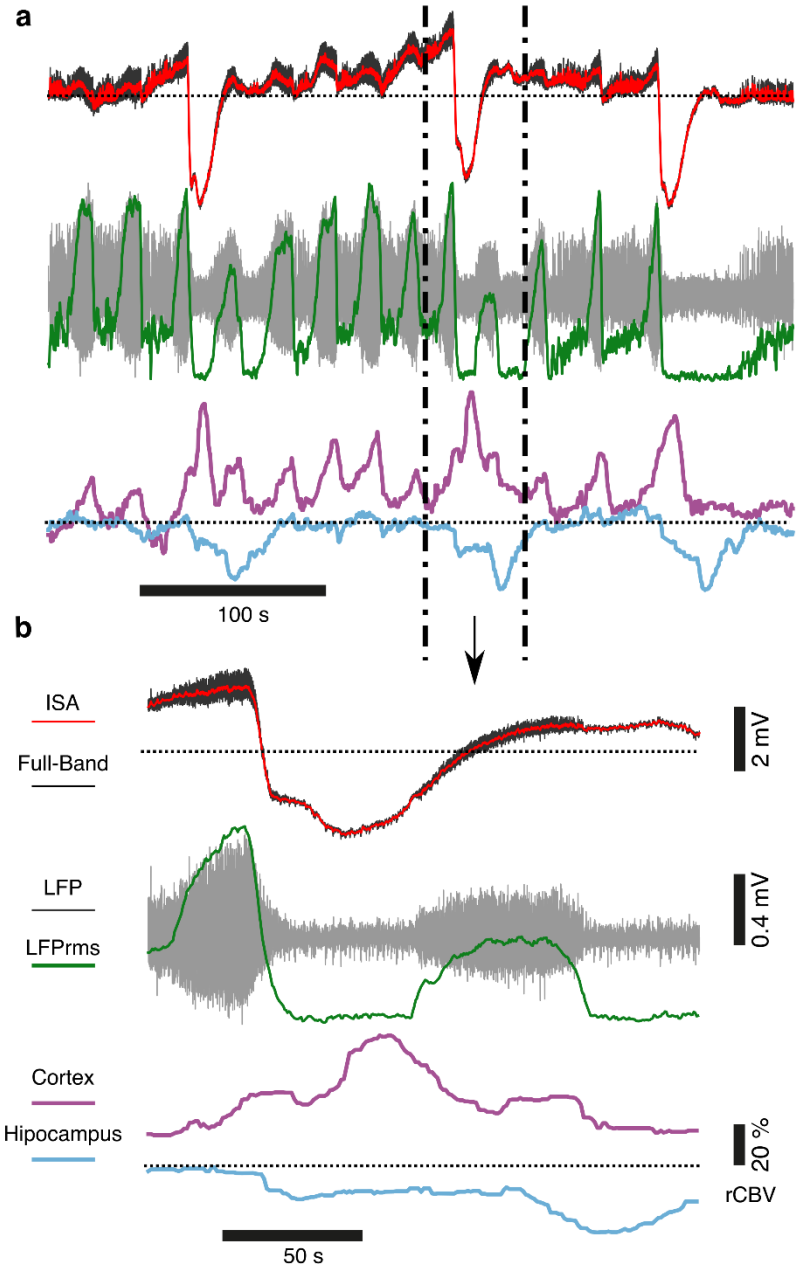

Figure 5. Seizures associated with spreading depolarisation result in hyperaemia in cortical regions and decreased blood flow in subcortical regions. a. DC-coupled recording (black) of multiple seizures and 3 CSDs, with the DC potential (<0.1Hz) displayed in red. The signal filtered above 0.5Hz is shown below (grey), with the LFP rms displayed in green. rCBF from a region of interest in the cortex (purple) and hippocampus (blue) are shown at the bottom. **b.** Blow up of an individual seizure and associated spreading depolarisation event. Note, in response to the seizure and SD there is a large increase in CBV in the cortex, with a delayed decrease in CBV in the hippocampus, n=3 seizure-SD events, n=1 animal.

III. Stimulating with graphene-based subretinal implant

The following article manuscript is still in preparation. It describes the *in vivo* proof of concept of the long-term biocompatibility of reduced Graphene Oxide (rGO) -based implants in the subretinal space and the functionality of such implants as subretinal electrodes for vision restoration.

Personal contribution: Experiments conceptualisation, *in vitro* characterisation, *in vivo* experiments (craniotomy sometimes, fUS and electrical stimulation, micron/OCT), immune-histology and confocal imaging, IMARIS quantification, data analysis, manuscript writing, figures drawing (all except fig.1).

Title

In vivo validation of reduced graphene oxide-based subretinal implant for vision restoration

Author

Julie M. Zhang*[1], F. Taygun Duvan[2], Steven Walston[2], Vi Anh Nguyen[1], Diep Nguyen[1], Julie Dégardin[1], Ruben Goulet[1], Quénol César[1], Jose A. Garrido[2#], Serge Picaud[1#]

1 Sorbonne Université, INSERM, CNRS, Institut de la Vision, F-75012 Paris, France

2 Catalan Institute of Nanoscience and Nanotechnologies (ICN2), Barcelona, Spain

Corresponding authors

Jose A. Garrido, joseantonio.garrido@icn2.cat

Serge Picaud, serge.picaud@inserm.fr

Conflict of Interest

None

Abstract

Brain-machine interface have to solve various challenges in terms of electrode size and biocompatibility to reach the great expectations and hopes in treating handicaps and neurological diseases. Taking retinal prostheses as a model system, we here explored a reduced graphene-oxide-based microelectrode technology with electrodes down to 25 µm to stimulate a neuronal circuit. We established first the *in vivo* long-term biocompatibility of such material in the subretinal space by quantifying the microglial cells 3 months post-implantation. The electrode efficacy was demonstrated by imaging visual areas with functional Ultrasound imaging. We show that the activation is dependent on the electrode size and the stimulation amplitude. The graphene electrode sustained the stimulation paradigms as characterized before by measuring impedance spectroscopy, cyclic voltammetry and voltage transients in response to long pulses (10 ms) in PBS. These results provide the first demonstration of the *in vivo* biocompatibility and *in vivo* efficacy in stimulating a neuronal circuit for the small reduced graphene oxide electrodes paving the way for future chronic long-lasting implantation.

Keywords

Graphene, microelectrode, ultrasound imaging, retinal electrophysiology, biocompatibility

Introduction

Blindness resulting from the loss of photoreceptors can occur in different diseases including retinal dystrophies like, retinitis pigmentosa (RP), or age-related macular degeneration (AMD). AMD is the leading cause of blindness in developed countries with no treatment to fully prevent the development of the atrophic form of the disease. Following photoreceptor degeneration, most bipolar cells (BCs) and retinal ganglion cells (RGCs) within the inner retina survive (Kim et al., 2002, Santos et al., 1997). These surviving neurons can be electrically stimulated with an array of electrodes in a spatiotemporal pattern to produce a signal that is transmitted through the visual pathway to the visual cortex and interpreted as a visual percept (Freeman et al., 2011). Retinal prostheses have been developed over the past few decades in order to restore some useful vision and improve the daily life of blind patients (Humayun et al., 2012; Luo & Da Cruz, 2016; Stingl et al., 2015).

The state of the art, retinal prosthesis represented by the Argus II device from the 2nd Sight company, is composed of a multi-electrode array (MEA), a head-mounted camera, a visual processing unit, and a power and data telemetry modules (Lovell et al., 2010; Weiland & Humayun, 2014). Recently, better visual acuity was achieved with subretinal implants (Palanker et al., 2020). However, these subretinal electrical stimulation paradigms require more charge to inject current pulses with longer pulse duration in order to target non-spiking graded bipolar cells (Lorach et al., 2015) The resolution of the device is highly related to the electrode pitch, their individual size and thus to the electrode material which has to be biocompatible (Wellman et al., 2018; Schiavone et al., 2020; Vomero et al., 2022).

Each material is characterized by its electrochemical performance, which defines the amount of charge that can be safely delivered through an electrode of a given size. Electrochemical stability refers to the inertness of the material while operating in the biological environment while its biocompatibility refers to its non-toxicity on the tissue and the absence of a deleterious immune response over time. Electrodes are classically manufactured from biocompatible metals with high conductivity such as gold (Au), platinum (Pt), or their alloys such as iridium oxide (IrOx) or titanium nitride (TiN). An important aspect for optimizing the delivered charge density reside in the deconvoluted surface of an electrode resulting in the production of porous materials to enlarge this surface as in platinum black. Despite their high conductivity, noble metals have modest electrochemical performance, which worsen upon miniaturisation of the electrode size and all are subject to corrosion if the implant packaging is not hermetic or if the coating delaminates over time. Although IrOx is characterised by a high charge injection capacity up to 4 mC/cm² (Negi et al., 2010), it delaminates rapidly *in vitro* at charge injections above 3 mC/cm² (Cogan et al., 2004) and degrades over time *in vivo* (Weiland & Anderson, 2000; Chen et al., 2023). For the packaging issue, recent technological advances propelled flexible substrate such as polyimide, parylene or PDMS as the new standard for flexible arrays matching better the mechanical properties of neural tissues and causing less tissue scaring and minimal foreign-body reaction upon implantation (Walton et al., 2022).

Graphene has been proposed as an adequate material to generate electrodes due to its semi-metal properties conferring it a high conductivity and its compatibility with clean room microfabrication techniques. Furthermore, we recently demonstrated the *in vitro* and *in vivo* biocompatibility of single layer chemical vapor deposited (CVD) graphene (Bendali et al., 2013; Nguyen, Valet, Dégardin, Boucherit, Illa, De La Cruz, et al., 2021). Electrodes were recently made from reduced graphene oxide (rGO), which harbours a three-dimensional porous architecture with pore sizes below 100 µm (Viana et al., 2022). This porous Engineered Graphene for Neural Interface microelectrode TEchnology (EGNITE) features promising electrochemical characteristics such as a charge injection limit of 4-8 mC/cm2 for 1-ms pulses, a low impedance at 1kHz (~27 kΩ for a 25-µm diameter electrode) and long-term electrochemical stability (Viana et al., 2022). This high electrode performance could enable stimulation with micrometre-scale electrodes allowing more focal activation, higher density of electrodes and in the end, better spatial resolution.

In the present study, we investigated the biocompatibility, the inertness of the electrodes and their *in vivo* efficacy using the eye as an accessible model system with the prospective of improving retinal prostheses.

Results

Microfabrication results

A manufacturing process was developed to deposit the reduced-graphene oxide (rGO) at the electrode position in different sizes. Figure 1 illustrates the schematic design of the reduced graphene oxide-based (rGO) subretinal implant (**Figure 1.a**) and a final assembled device (**Figure 1**.**b**). The implant possesses 12 rGO-electrodes of 3 different sizes (100, 50 and 25 µm) on top of gold (Au) and titanium (Ti) metal tracks on the polyimide (PI) flexible substrate. The whole structure is embedded in a PI coating to isolate tracks. Overall, the implant thickness is 15 µm and was tailored for studies with rats. After the lift-off step from the wafer, detached implants are mounted on a rigid PCB allowing easy anchoring and an Omnetics connector for interfacing with the digital world. The implant head was designed with a circular shape (diameter 1 mm) to comply with the constraints of the *in vivo* subretinal surgery. We first examined visually the correct microfabrication of the implant under optical microscope. On the image, the porous graphene appears black to the naked eye (**Figure 1.c**).

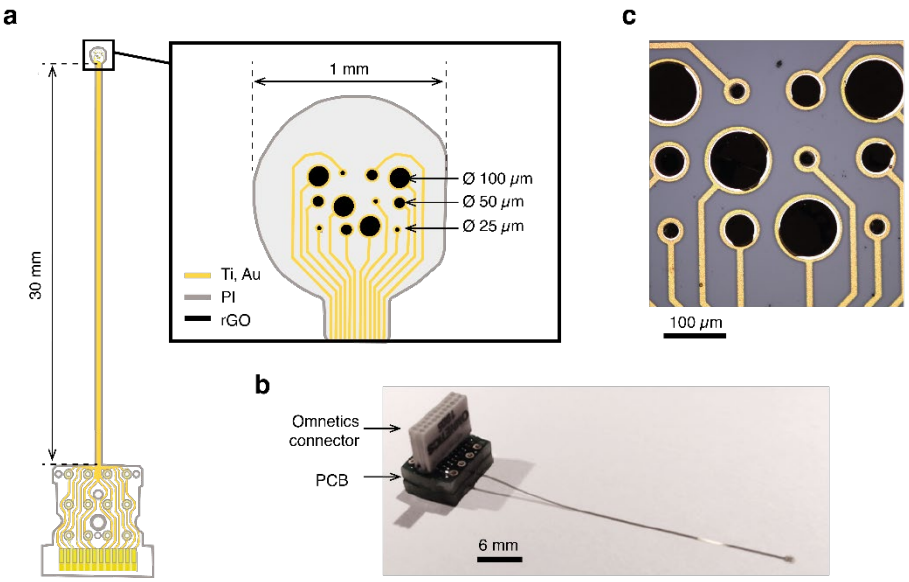

Figure 1 Reduced graphene oxide-based (rGO) subretinal implant design. **a.** device schematics. The implant is composed of gold (Au) and titanium (Ti) tracks embedded in a polyimide (PI) substrate and coating, and 12 rGO electrodes of 3 different sizes (25, 50 and 100 µm). **b.** Photography of microfabricated and mounted implant. An Omnetics connector linked to a PCB on the implant connector pads allow current injection in the electrodes using an external stimulator. **c.** Microscope view of electrodes.

In vitro characterisation

To further assess the proper graphene deposition on the electrodes, we measured the *in vitro* electrochemical performance. **Figure 2** illustrates these electrochemical performances for the different electrodes' sizes: 100-µm-,50-µm- and 25-µm-diameter. At 1 kHz, the electrodes have respectively an impedance Z_{1kHz} of 12.70±0.76 kΩ, 9.96±0.93 kΩ, 24.87±0.02 kΩ and a phase φ_{1kHz} of -55.55±0.81°, -44.03±1.63°, -46.59±1.41°, consistent with previous data (Viana et al., 2022). Overall, the average impedance plot of 25-µm-diameter electrodes is always higher than the two others. The average cut-off frequency $f_{cut\text{-}off}$ was respectively found equal to 3.363±0.270 kHz, 1.202±0.219 kHz and 1.831±0.476 kHz, corresponding to the average impedance $Z_{cut\text{-}off}$ of 6.196±0.319 kΩ, 10.128±0.719 kΩ and 22.981±1.739 kΩ. They yield an anodic charge storage capacity (CSC_a) of respectively 0.252±0.009 mC/cm², 0.481±0.0339 mC/cm² and 1.107±0.136 mC/cm², and a cathodic charge storage capacity (CSC_c) of respectively 0.343± 0.027 mC/cm², 0.806± 0.088 mC/cm² and 1.882±0.236 mC/cm². These measurements are in complete agreement with the graphene composition of the electrodes as it is in the range previously described for this material (Viana et al., 2022).

However, in microelectrodes, the charge storage capacity usually overestimates the actual charge which can be injected because not all charges are available for release. As a consequence, to obtain a more

precise measurement, we measured the charge injection capacities (CIC) by pulsing voltage transients at different current amplitudes. The cathodic charge injection capacity CIC_c was around 0.455, 0.629 and 2.7752 mC/cm^2 for biphasic pulses of 1 ms for electrodes with 100, 50, 25 µm diameter, respectively. By contrast, the anodic charge injection capacity CIC_a was estimated to be around 1.361, 5.847 mC/cm² for the 50 and 25 µm electrode diameter (**supplementary figure 1.b**) and no CIC_a limits was measured for the 100 µm diameter electrodes. To compare the initial electrode characteristics to the *in vivo* conditions, we applied our *in vivo* experimental paradigm in a medium more representative of the *in vivo* conditions. When biphasic anodic-first pulses of 10 ms were applied in series at 8, 10 and 12 µA (**Figure 2.d**), the resulting polarisation of the electrode (~1.2 V) did not exceed water window (1.7 V), which we therefore assumed safe for the electrode inertness.

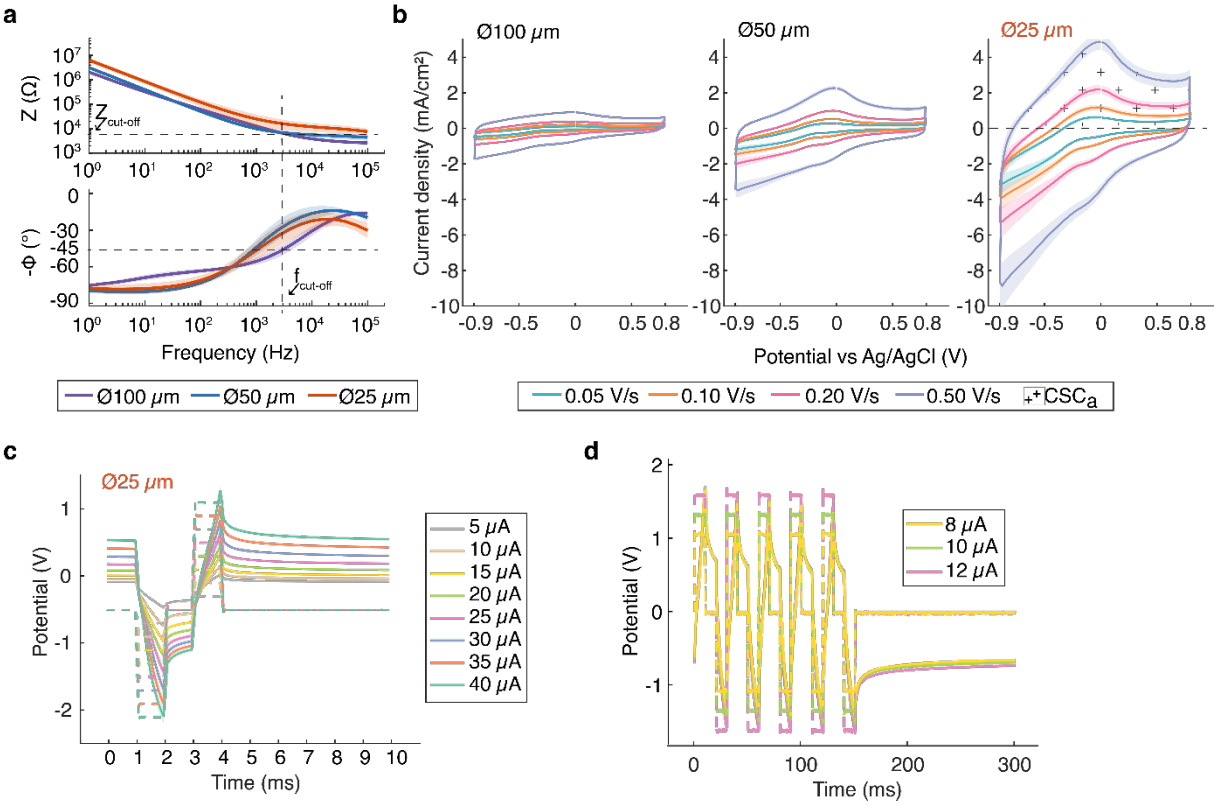

Figure 2 *In vitro* electrochemical characterisation of rGO electrodes of diameter 100, 50 and 25 µm in a 3-electrode electrochemical cell composed of a platinum counter electrode and an Ag/AgCl reference electrode all bathed in a PBS solution (10X). **a.** Electrochemical impedance spectroscopy (EIS) Bode plots for electrodes of diameter 100, 50 and 25 µm. Impedance (Z) and phase (φ) were averaged over N=27, 17 and 11 electrodes respectively. The cut-off frequency $f_{cut\text{-}off}$ and the corresponding $Z_{cut\text{-}off}$ were estimated when -φ = -45. **b.** Cyclic voltammetry for same electrodes, at different sweep rates. Charge storage capacities for anode (CSC_a) and cathode (CSC_c) are calculated using area under the curve. **c.** Voltage transients for 25-µm electrodes with 1 ms cathodic-first biphasic pulses. **d.** Voltage transients for 25-µm electrodes with 10 ms anodic-first biphasic pulses

Biocompatibility

Biocompatibility of the rGO material was evaluated by examining *in vivo* the tissue and then quantifying the inflammation in the *post-mortem* retina of blind P23H rats implanted during 90 days post implantation (dpi). Specific non-connected implants were manufactured following the same process to generate passive electrodes (**Figure 3.a**). For comparison, control implants were generated with Pt-electrodes not covered by rGO and a sham implant was produced from PI only with a similar substrate thickness (~16 µm). Because animals with a photoreceptor degeneration have already a reactive retina, we compared the implanted tissue with non-implanted eyes of the same age considered as a true control (ctrl).

All implants were individually followed over 90 days *in vivo* at different time points, 7, 14, 30, 60 and 90 days-post-implantations (dpi) (**Figure 3.b**). This follow up was achieved in the blind P23H rats by eye fundus and optical coherence tomography (OCT) imaging. These examinations confirmed the correct implantation in the subretinal space as retinal blood vessels were seen above the implant in eye fundus

observations and the thin retinal tissue was observed above the implant in OCT exams at 7 days (**Figure 3.c, d, e**). No monitoring was performed before this date in order to allow the animal to recover entirely from the surgery. Generally speaking, when light or mild inflammation was observed at 7 dpi, it easily resorbed at 14 dpi no matter the implant material. Although some internal haemorrhage could happen due to the surgery as seen for the example given for the PI-based (**Figure 3.c**) or the rGO-based implants (**Figure 3.e**), it usually disappeared by 14 dpi. Overall, until 90 dpi, there was no displacement of the implants in the eye nor delamination.
After isolating the eyes after 90 dpi for histological examination, the retina was isolated with extra care to preserve the contact between the implant and the tissue (**Figure 3.f**). The samples were immunolabeled with an antibody directed against Iba-1 (488 nm) to visualize microglial cells. We verified integrity of the retina and the implant at a low magnification (10X) under the confocal microscopes (**Figure 3.g, h, i, j**). All implants appeared totally normal and the tissue did not show any abnormality. Then, to examine the tissue at a cellular resolution, we used a higher magnification (40X) to acquire a 3D image of 317x317µm² squares on all the implants (**Figure 3.k, l, m, n**), which were randomly selected above the implant. The polyimide material used as substrate appears green because it fluoresces under the excitation wavelength used to image Iba-1-immunopositive cells (**Figure 3.h**).
Thanks to the confocal imaging, the implant layers were eliminated to achieve the quantification of microglial cells with the Imaris software (**Figure 3.l**). The platinum material appears orange because it fluoresces when using a 594 nm excitation wavelength (**Figure 3.i,m**), and the gold tracks were similarly detected underneath the graphene layer (fig. 3j). These observations under different wavelengths enabled us to define the electrode position and the gold tracks. In the control P23H retina, microglia cells displayed stellate shapes with long and ramified processed (**Supplementary Figure 2.a**). However, in one of these ctrl samples (n=9), we also observed round ameboid microglia distributed among ramified microglia. PI samples (**Supplementary Figure 2.b**) and half of the Pt samples (**Supplementary Figure 2.c**) had ameboid microglia. Surprisingly, some microglia were lying on the surface of the Pt electrodes (**Figure 3.q**). In rGO samples, the microglia seemed to display shorter processes than in the ctrl samples although they appeared less ameboid than in the Pt samples. Densities of microglia appeared slightly lower in PI or some Pt and rGO samples compared to the negative controls.
To quantify the microglia cells, they were modelled in a semi-automated way with Imaris software (**Figure 3.o, p, q, r**). The boxplots on **Figure 3.s** and **Figure 3.t** compare the total number of microglia cells per 0.1 mm² and the total volume of microglia cells per 0.1 mm² for the different implanted materials. Although no statistical difference was found between all categories' distribution nor pairwise (Kruskall-Wallis with multiple comparison test, α=0.05), the number of microglia for PI, Pt, rGO are slightly higher than for ctrl samples, which could result from the surgery.

In vivo recording during retinal electrical stimulation

In a previous study, we showed that functional ultrasound (fUS) imaging can provide a general view of different visual areas with a sensitivity equivalent to electrical recording of the visual cortex (Provansal *et al.*, 2021). We therefore used fUS imaging to assess the performances of our custom rGO-based electrodes on connected subretinal implants in electrically stimulating on the retina of wild-type rats. Before such electrical stimulations, the correct subretinal insertion was verified by eye fundus examination (**Figure 4.a)** showing the retinal blood vessels passing above the implant. We intended to insert the implant close to the optic nerve for its easier visual perception and lower retinal detachment. To perform electrical subretinal stimulation, we applied anodic-first biphasic pulses lasting 10ms per phase and repeated 5 times over 300ms onto one electrode at a time (**Figure 4.b**) at a 3.33 Hz stimulation rate for 6 s. Such a sequence was repeated 10 times with 30s interleave periods. A light stimulation test with 300ms flash at a same frequency for 6s served as a control to visualize brain visual areas. The fUS probe, which measures a change in the cerebral blood flow (CBF) due to the neurovascular coupling, was placed on top of a craniotomy, located at around bregma-6.5mm so that both the superior colliculus contralateral to the implanted eye (SCc) and ipsilateral (Sci) were visible. The visual and electrical stimulations generated inverse Gaussian shapes at different voxels for the calculated relative cerebral blood volume (rCBV) in various regions of interests (ROIs) witnessing thereby the local and transient increase in neural activity.

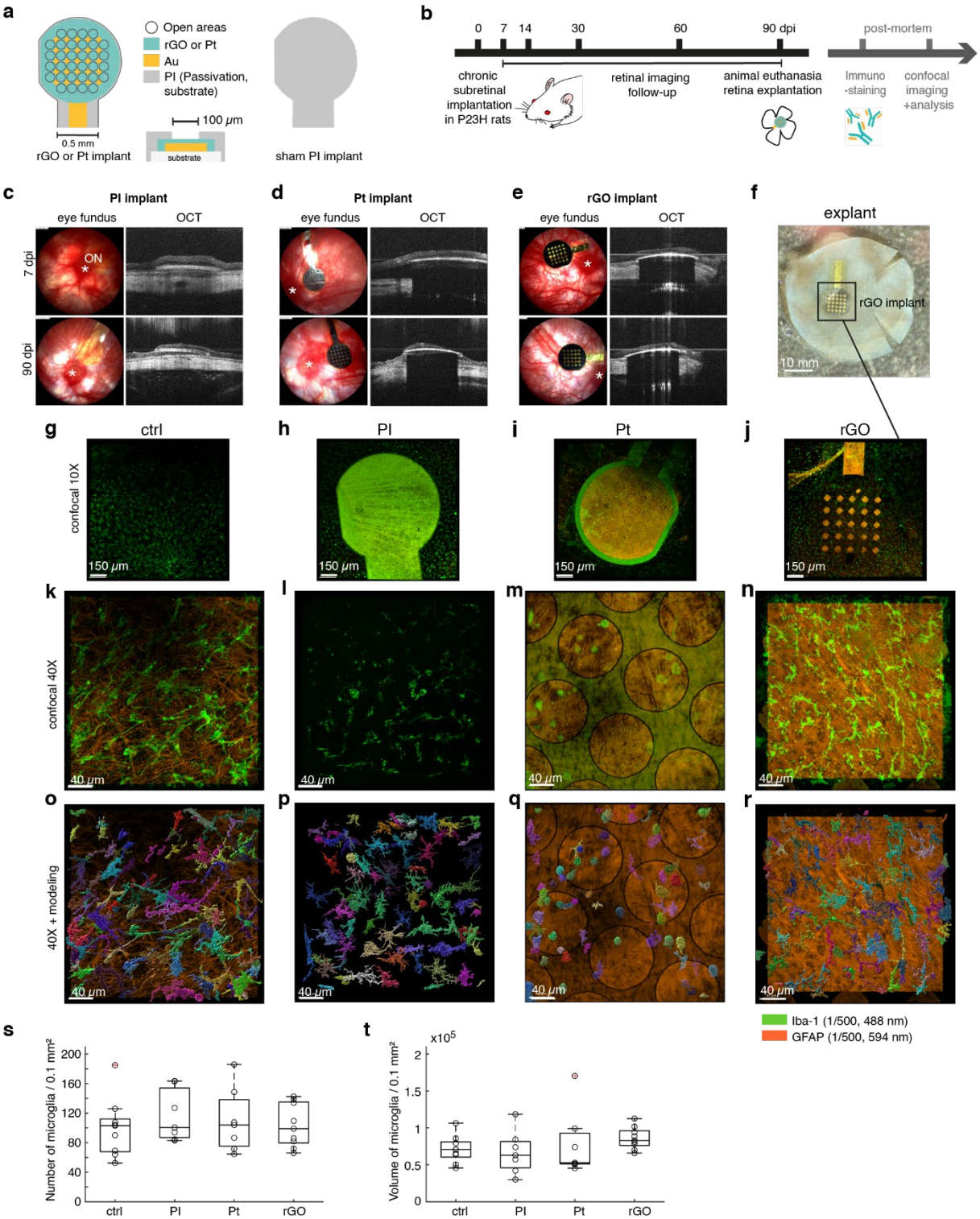

Figure 3 Biocompatibility study of reduced graphene oxide (rGO) electrodes versus sham polyimide (PI) device and platinum (Pt) electrodes. **(a)** Schematics of the implants. Electrodes are either rGO or Pt. **(b)** Design of experiment and corresponding timeline. After chronic subretinal implantation of the devices in blind P23H rats, the retina is examined *in vivo* at 7, 14, 30, 60, 90 days post-implantation (dpi) using eye fundus imaging and optical coherence tomography (oct). At 90 dpi, the rat is euthanised and the retinal tissue with the implant is processed for immunolabeling. **(c,d,e)** *In vivo* retinal follow-up by eye fundus and OCT imaging at 7 or 90 dpi on rats implanted with a sham PI device (c), a Pt device (d) or a rGO device(e). **(f).** Post-mortem fixed tissue showing the implant below the retina. **(g-n)** Immunostaining against Iba-1 to visualize microglial cells (green) at a 10X (g-j) and 40X magnification (k-n) in control a P23H retina (g,k), above a PI sham implant (h, l), a Pt-electrode implant (i, m), a rGO electrode implant (j, n). **(o-r)** Microglial cells reconstruction using Imaris software to extract individual retinal microglial cells from the above

confocal images (k-n). **(s-t)** Quantification of the microglial cell density (s) and their individual volume (t) in the different experimental conditions (N_{ctrl} = 9, N_{Pl}=7, N_{Pt}=7, N_{rGO}=9) No pairs display a significantly different distribution from one another (Kruskal-Wallis with multiple comparison tests, α=0.05)

The fUS heatmaps (**Figure 4.c, d**) illustrate the activation of the superior colliculi in both hemispheres for light stimulation and in the contralateral superior colliculus (SCc) for the electrical stimulations in the implanted eye for one animal. In the heatmaps, the activated voxels are displayed in red for a significant increase in cerebral flow for light control (**Figure 4.c)** and for a 100 µm-rGO electrode with different amounts of injected current (**Figure 4.d**) (Global linear model fitting, Benjamini-Hochberg correction with a 90% confidence). At 0.25 mC/cm², there is only a weak activation in the region around the lateral geniculate nucleus (LGN), whereas starting from 0.51 mC/cm² the activated area in the SCc keeps growing spatially and with stronger correlation as the charge density increases. However, compared to the light control paradigm for which the SCc, the SCi and the ipsilateral visual cortex (V1i) were all found to be highly correlated to the stimulus (**Figure 4.c**), electrical stimulation resulted in no clear activation of the visual cortex and the SCi. For the visual cortex activation, it remains very moderate even with light stimulation as indicated previously in other studies (Gesnik et al., 2017; Provansal et al., 2021), likely due to the anaesthesia. The absence of activation in the SCi in this example is consistent with the implantation in an area not related to bilateral vision. For the light stimulation with a full-field white LED (2 mW/cm²) illuminating the whole eye, part of the eye devoted to bilateral vision was stimulated. The corresponding CBV time courses averaged over 10 repetitions are shown in **Figure 4.e.** There is a CBV peak in SCc at already 0.25 mC/cm² (2 µA), and a clear increase in the peak amplitude with increasing charge density.

The number of activated voxels in SCc was correlated significantly with the injected current and thus with the injected charges in n=11 animals (**Figure 4.f-g**). For the negative control and the light control, the blood flow was found to be positively correlated with stimulation pattern in respectively 5.6±1.9 voxels and 98.5±13.5 voxels. For 100 µm-electrodes, the positive correlation was found for respectively 9.0±5.8, 9.4±3.2, 13.5±4.8, 32.0±9.8, 61.0±26.5 for 0.07, 0.13, 0.25, 0.51, and 1.02 mC/cm² (**Figure 4.f**). For 25 µm-diameter rGO electrodes, mean numbers of positively correlated voxels are 3.9±2.4, 8.3±2.8, 5.2± 3.1, 17.9±8.5, 48.1±14.7 (**Figure 4.g**). This correlation was dependent upon the size of the electrode. Kruskal-Wallis test with multiple comparison for 100 µm-diameter-electrodes reveals that from 0.07 to 0.51 mC/cm² the number of correlated voxels in SCc is significantly lower than for light control while starting from 0.51 mC/cm², there is no significant difference anymore between light and electrical stimulation in terms of number of activated voxels in SCc (**Figure 4.f**). On the other hand, for the 25-µm-diameter electrodes, number of activated voxels with the highest tested current density (16.3 mC/cm²) remained significantly different than the light control (**Figure 4.g**). Therefore, at equivalent injected total current between the two electrodes, the voxel number was significant for the 100µm (0.51mC/cm2) but not for the 25µm electrode (16.3 mC/cm²) (**Figure 4.j**). To further assess this distinction between the two electrode sizes and thus the spatial resolution of the stimulation, we quantified the change in cerebral blood flow amplitudes. For this parameter, the significant changes were also observed at the highest charge density for both the 100-µm-electrode (1.02 mC/cm², **Figure 4.h**) and the 25-µm-electrode (16.3 mC/cm², **Figure 4.i**). Therefore, both electrode sizes reached an amplitude of activation non-significantly different than light stimulation, at the same injected charge (8 µA) but the highest cerebral blood flow appeared to be reach by the smallest electrode sizes (**Figure 4.k**). Overall, although no significant difference was found between each pair of injected charge (**Figure 4.f-i**), the boxplots and heatmaps highlight an overall larger number of activated voxels starting from 0.51 mC/cm².

These results demonstrate the ability to activate with rGO-based electrodes the retinal circuit with an efficiency dependent upon the electrode size at high current amplitudes.

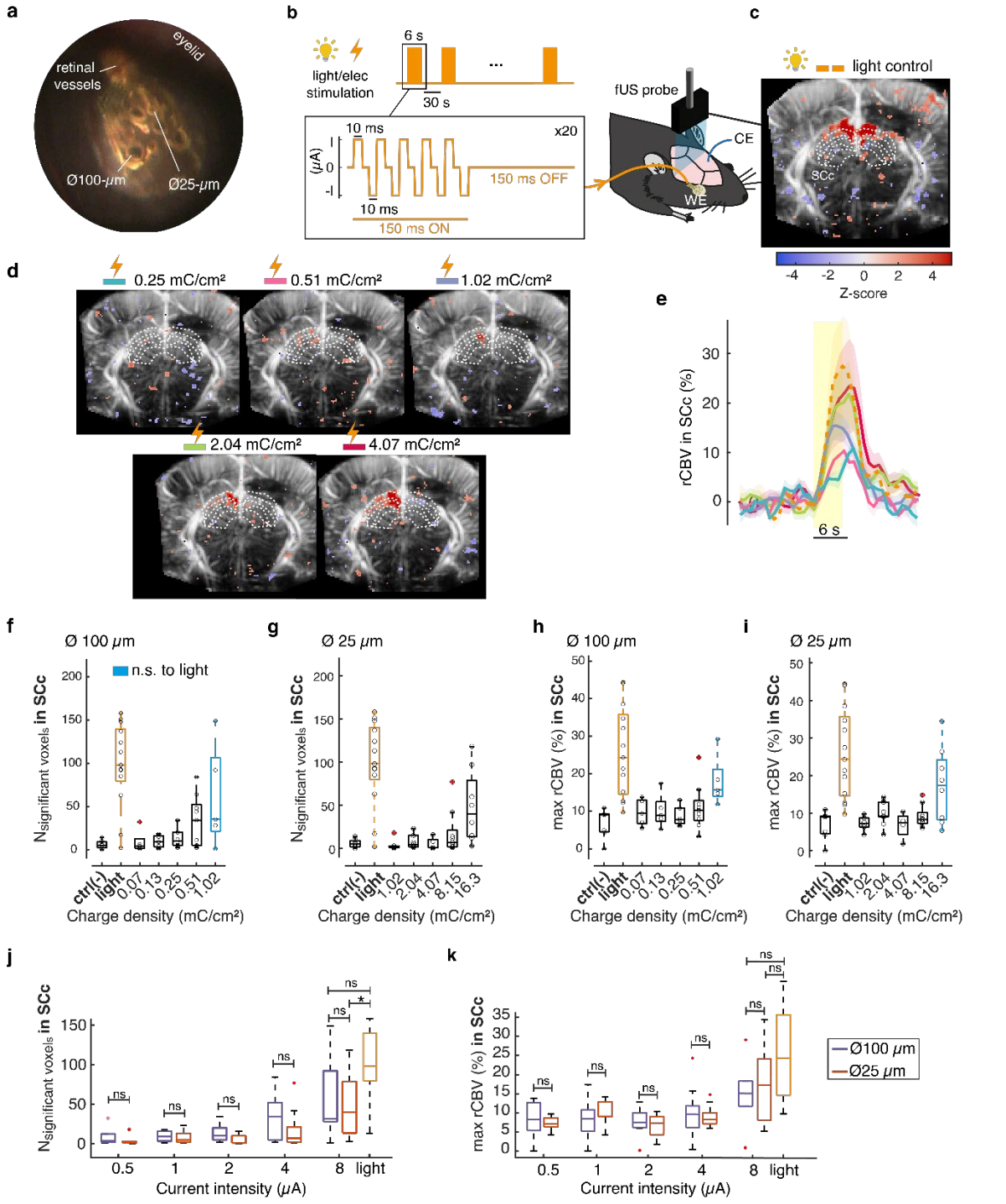

Figure 4 Functionality of reduced graphene oxide (rGO) electrodes, by functional ultrasound imaging (fUS) of the brain during subretinal electrical stimulation. **(a)** eye fundus of a normal rat implanted with rGO-based implant. **(b)** Electrical stimulation protocol and surgery. A biphasic anodic-first 10ms-pulse-based current was injected into rGO working electrodes (WE) in 300ms sequences repeated at a 3,33Hz for 6s, such stimulation protocol was reproduced 10 times with 30 s interleave periods. The implant was inserted acutely in the subretinal space of the normal rat, while the return electrode (CE) was introduced in the contralateral muscle on the brain. Full field LED light stimulation were applied to locate visual areas with the probe for functional ultrasound imaging (fUS) placed on a brain craniotomy. **(c, d)** fUS activation heatmap (global linear model between power doppler and stimulation pattern with Benjamini-Hochberg correction) with light (c) or electrical stimulation using a 100 µm-diameter rGO electrode (d). **(e)** Cerebral blood volume relative to baseline (rCBV) in the superior colliculus contralateral to stimulated eye (SCc) for each charge density in (d), n=1. rCBV are averaged over 10 repetitions. **(f-g)** Number of activated voxels in the SCc for different amount of charge injected. **(h-i)** Cerebral blood Volume relative to baseline (rCBV) in SCc at maximum peak for different amount of charge injected in (g) 100 µm- and (h) 25 µm-diameter rGO electrodes. **(f,g,h,i)** Only non-significant pairs with light stimulation are indicated, in blue (Kruskal-Wallis with pairwise comparison, 5%). **(j)** Number of activated voxels in the SCc at different amount of total current for the 25 µm- and 100 µm- electrodes. **(k)** rCBV in SCc at maximum peak at different amount of total current for the 25 µm- and 100 µm- electrodes. (Mann-Whitney test, 5%, *p<0.05)

Discussion

We successfully fabricated a rGO-based subretinal flexible electronic implant customised for rodent preclinical studies of subretinal electrical stimulation for vision restoration (**fig.1**). Such a device was already produced for short-term investigation in animals to then enter in clinical trials during intraoperative procedures (Viana et al., 2022). Here, our objective was to investigate the long-term safety on implanting the material on a device and its ability to generate electrical stimulation in an *in vivo* biological environment. The flexibility of neural probes is highly desired in order to decrease effects of foreign body reaction upon chronic implantation, which is well exemplified by the fibrotic reaction reported around Utah arrays in the visual cortex (X. Chen et al., 2023). However, some rigidity was also required to facilitate the implant insertion into the subretinal space through the sclera. We therefore took advantage of Polyimide, a biocompatible polymer, which played the role of both substrate and coating and was used previously with great success in different studies (Bendali et al., 2015; Linderholm et al., 2013). Moreover, the polarisation of rGO electrodes during pulses injection was stable and within the range of the water window for both 1 ms and 10 ms pulses, although charge density becomes relatively high for smaller electrodes. This inertness of electrode provided a major and highly scrutinized result because we applied long stimulation durations required to activate selectively the non-spiking bipolar cells at a high charge density (sometimes above theorical safety charge injection limit) and thus generate a network-mediated responses (Boinagrov et al., 2014; Ho et al., 2018). Our study therefore confirms the high quality of the EGNITE electrodes for recording and stimulation of neuronal circuits.

The toxicity of carbon-based nanomaterial on human health is a common fear since the major scarce in 2008 engendered by long needle-like carbon nanotubes asbestos-like pathogenicity (Poland et al., 2008). Graphene derivatives make no exception and present contrasting cytotoxicity results, depending on dosage, time of exposure, and application. However, in EGNITE electrodes, the rGO material is not released in the body but remains attached to the device. The biocompatibility of the rGO-based implant had already been reported to be safe after 2 months of interfacing with the rat tibial nerve (Viana et al., 2022). We here investigated its safety in a neuronal and retinal tissue, which provides a model system for brain structures. We examined microglial cells because their transformation in an amoeboid shape provides a clear indicator of a chronic foreign body reaction (Polikov et al., 2005). Because inserting a subretinal implant triggers a retinal degeneration in rats (Lorach *et al.*, 2015), we used P23H rats, a model of retinal degeneration at an age when photoreceptors have already disappeared to study the effect of the implant on the residual tissue and not that of a local degenerative process. Our quantification provides no evidence of a reactive gliosis toward any of the implant as the number and shape of the microglial cells did not change statistically significantly. These results with 3D rGO material are in good agreement to our previous study on for the chemical vapor deposited (CVD) graphene-based subretinal implants (Nguyen et al., 2021). Future studies will have to investigate the biocompatibility of the rGO material when used for electrical stimulation in chronic implantation. However, such cable-tethered implants will include high risks for implant displacement during eye movements. Our study has excluded this risk with a non-connected device to specifically investigate the biocompatibility of the rGO material.

The material rGO was previously used to record the cortical activity especially as an electrocorticography (ECoG) array (Viana et al., 2022). In this article, we investigate the use of similar electrodes but for neuronal stimulation. Indeed, electrical stimulations are applied in prostheses, to depolarise neurons in the vicinity of electrodes. In retinal prosthesis, electrical stimulation of the retina was shown previously to generate perception in blind patients by either epiretinal or subretinal implants. In our study, we demonstrated retinal activation by measuring the activation of the superior colliculus (SC) by fUS imaging. This imaging technology enabled us to examine the elicited activity in an entire brain slices even as deep as the SC by light or rGO electrical activation of the retina. The visual cortex V1 was only weakly responsive during light stimulation and almost not at all during electrical ones, while high correlation between blood flow and stimulus pattern was located in the contralateral SC region. The absence of measured activity in V1 was reported in different visual studies and it was imputed to the influence of anaesthesia on blood flow dynamics (Provansal et al., 2021). The preferred SC activation is also related to its high retinal innervation from RGCs by contrast to V1 in rodents (Ellis et al., 2016). Overall, electrical stimulation with both 25- and 100-µm electrodes trigger a significant increase of blood flow in the SC, which translates into neural activation. In terms of total charge conveyed, there was no significant difference in spatial activation with either electrodes, although their charge injection capacity

differs. However, at maximum current tested (8 µA), the neural activation triggered by the 25-µm electrode was more focal (less correlated voxels) but higher in average in amplitude than the 100-µm electrode. One interpretation is that in acute studies, the retina remains detached and not in tight contact to the implant so that the current is injected in this subretinal space preventing a more local activation by the smaller electrodes at low current injected. The gap between the electrode and the tissue elevate the required current to activate the neurons and thus trigger a response in visual areas. As a consequence, our applied current densities exceeded by far the legal recommendations for tissue safety (30 µC/cm² in the brain for instance) but the stimulation was likely distributed onto a larger retinal surface than the electrode surface in most cases. Furthermore, the monopolar stimulation protocol (with a distant ground in the contralateral brain muscle) may also concur to enlarge the stimulated retinal area. For future chronic evaluation, local return electrodes introduced in photovoltaic prosthesis would restrain the current diffusion (Flores et al., 2018; Ho et al., 2019). Moreover, our *in vitro* characterization of the electrodes also indicates a low impedance and large water window. In accordance with past investigations (Viana et al., 2022), this study suggests that the rGO electrodes could serve for both recording and stimulation modes in a bimodal therapeutic application.

Conclusion

In summary, we report in this article the successful implementation of long-term biocompatible rGO electrodes on a customised flexible subretinal implant coated with PI and tailored for rodent surgery. These electrodes display *in vitro* high charge injection capacities higher than 3 mC/cm² for 25 µm-diameter sizes and stable voltage transients' profiles within safe stimulation window. Moreover, the material does not induce harsh inflammation compared to PI probes or Pt-based electrodes nor degrade over 3 months post-implantation in the subretinal space of blind rats. Following the biocompatibility study, neural electrical stimulation functionality was also demonstrated for 25- and 100-µm-diameter electrodes in wild type rats using fUS technology. After an acute surgery with cranial window and subretinal implantation, electrical stimulation of retinal neurons in the subretinal space with slow pulses (10 ms) activated neurons in the SC contralateral to stimulated eye, one of the main relays of the visual pathway for optic nerve axonal inputs. While much more charge density was necessary for 25-µm electrodes to achieve comparable activation with full field light control stimulation in contrast to 100-µm electrodes, the smaller electrode size did trigger a more focal neural activation only at high total charge injected, highlighting a limit in monopolar stimulation with distant ground. Overall, the present work contributes to better assessment of the chronic functionality study of rGO electrodes using wild-type subretinally-implanted rats with cranial window for fUS, currently ongoing in our team. Above all, this proof-of-concept study confirms the possibility to switch from metal-based electrodes subject to corrosion and limited in charge injection capacity, to rGO-based electrodes which are long-lasting, efficient for subretinal stimulation but also operable in neural recording mode for bimodal or even closed-loop neuroprosthetics.

Material and methods

Microfabrication

The electrodes were fabricated in the cleanroom at the Catalan Institute of Nanoscience and Nanotechnologies (ICN2), following a process previously described (Viana et al., 2022). Briefly, graphene oxide flakes in an aqueous media are filtered into a thin film which is then transferred onto a gold substrate. Next, thermal reduction creates a porous film which will be the active electrode material adhering on top of gold tracks.

In vitro characterisation

After microfabrication, graphene electrodes were characterised *in vitro* at ICN2 with a 3-electrode electrochemical cell in a 10X PBS bath (Sigma-Aldrich) using a Metrohm potentiostat (Autolab PGSTAT128N). The counter electrode (CE) was a Pt wire (Alfa Aesar, 45093) and the reference electrode (RE) was an Ag/AgCl electrode (FlexRef, WPI). Prior to electrochemical characterisation, the electrodes were pulsed with 10,000 charge-balanced pulses (1 ms, 15 µA). For electrochemical

impedance spectroscopy (EIS), frequencies were swept from 100 kHz to 1 Hz. Impedance and phases were averaged over respectively 27, 17 and 11 electrodes of diameter 100 µm, 50 µm and 25 µm. For cyclic voltammetry (CV), electrodes were cycled twice between [-0.9 0.8] V with increasing sweeping rates **v** (0.05, 0.1, 0.2 and 0.5 V/s). Sampling frequency was set at 50 Hz. Anodic and cathodic charge storage capacity (CSCa and CSCc, respectively) were calculated as followed (**supplementary Figure 2.a**) (Gong et al., 2016; Slavcheva et al., 2004) :

$$CSC = \frac{1}{\nu A}\int_{U_c}^{U_a}|i|dU \text{ (Eq. 1)}$$

For chronopotentiometry, biphasic cathodic-first pulses of 1 ms/phase with a 1 ms interphase and with an amplitude of 5, 10, 15, 20, 25, 30, 35 and 40 µA were sent in increasing amplitude order. Potential responses (U) were averaged over the 10 repetitions. Charge injection capacity (CIC) was calculated as the intersection of the water window plots (U_c = -0.9 V and U_a = +0.8 V) with the affine fit function U=f(ΔEp), ΔEp being the maximum (for anodic CIC) or minimum (for cathodic CIC) electrode polarisation. Additionally, 5 biphasic anodic-first pulses of 10 ms/phase were sent every 150 ms 10 times at 6, 8, 10 and 12 µA to verify the safety of the electrode in the experimental design which will be used *in vivo*.

Animal experiments

The *in vivo* experiments were all carried out at the Institut de la Vision (France). The procedures were all approved by the Local Animal Ethics Committee N°005 (registration number APAFIS #15219-2018052410447053 v2). 10 adult Long Evans rats (Janvier-Labs®, France) were used to verify acute functionality of the EGNITE implants. 24 blind male 9-month-old homozygous P23H rats were used to investigate the biocompatibility of rGO-based electrodes as compared with Pt standard, PI sham device and control eye. The rats were housed per pairs in ventilated cages with food and water ad libidum with enrichment. The temperature in the animal facility was maintained at 22°C +/- 2 and light cycle was reversed every 12 hours. For all surgeries, the temperature of the animals was maintained at 37 °C with a heating pad throughout the whole surgery, and heart rate monitored with (PhysioSuite, Kent Scientific Corporation). The non-operated eye was also protected with ocular gel (Lubrithal®, Dechra, USA) and covered with a dark cloth.

Biocompatibility study

Chronic subretinal implantation surgery: For the biocompatibility study, Pt, rGO and PI arrays were implanted into the right eye of anaesthetised P23H rats (isoflurane 2%) as described above for the acute functionality study. The anaesthesia and micro-surgery were performed as described previously (Salzmann, 2006; Nguyen et al., 2021). Buprenorphine (0.05 mg/kg, Buprecare®, Axience, France) was administered as analgesics. Briefly, the eyelid was lifted with clamped suture wires and a small sclerotomy was performed on the dorsal sclera of the anaesthetised eye. A gel of sodium chondroitin sulfate – sodium hyaluronate (Viscoat, Alcon, France) was injected to generate a retinal detachment. The implant was then inserted in the subretinal space targeting an adjacent location to the optic disk. The correct placement was observed with a plastic coverslip gently pressed on ophthalmic gel on the implanted eye with the microscope (**Figure 3.b**).

Chronic follow-up: Eye fundus imaging (MICRON® IV, Phoenix, USA) and optical coherence tomography (Bioptigen® OCT system, Leica microsystems, Germany) data were collected at 7-, 14-, 30-, 60- and 90-days post-implantation (dpi) to monitor inflammation state and correct implantation. Prior to the session, the eye of interest was dilated with a tropicamide-based eye drop solution (Mydriaticum®, Théa, France). For eye fundus imaging only, a generous amount of ocular gel (Lubrithal®, Dechra, USA) was applied on the eye of interest. If the implant is found to be incorrectly implanted, or if after one month, the inflammation in the eye did not resorb and worsen or if there is severe bleeding in the eye all associated with distress behavior, the animal was immediately euthanized. After the 90 dpi time-point, the animals were euthanized by intracardiac injection of overdose of euthanasian (200 mg/kg, Exagon®, Axience, France) and the implanted eye was dissected to retrieve samples containing both the retina and the implanted chip.

Immunohistology: The immune-histology procedure is similar to previous study (Nguyen et al., 2021). Briefly, after overnight fixation in paraformaldehyde (4% in PBS) and washing in PBS, the samples were permeabilised and saturated with a blocking solution (10% bovine serum albumin (Sigma, France), 2% Triton X-100 (Sigma, France), 0.5% Tween 20 (Sigma, France) in PBS for 1 h. A 3-day incubation at 4°C with slow stirring of primary antibodies: rabbit anti Glial Fibrillary Acidic Protein GFAP (1/150), mouse anti-G0alpha (1/200), and goat anti-Iba-1 (1/500) (Sigma, France). The fragments were rinsed throroughly with PBS and then incubated with secondary antibodies: donkey anti-rabbit IgG AlexaFluor®-594 nm (1/500), donkey anti-mouse IgG AlexaFluor®-647 nm, donkey anti-goat IgG AlexaFluor®-488 (1/500), and nuclear stain, 4',6-diamidino-2-phenylindole (DAPI, 1/750). The stained samples were finally rinsed thoroughly in PBS, mounted with Permafluor (Epredia, France) on microscope slide with Secure-Seal spacers™ (Invitrogen, USA) and were covered with 40-mm glass lamellae. They were imaged under an upright confocal microscope (FV1000, Olympus, Numerical aperture NA=1.30, 10X and 40X magnification, 8 µs/pixel). DAPI counterstaining, AlexaFluor®-488, AlexaFluor®-594 and AlexaFluor®-647 were respectively detected by excitation with a 405 nm laser diode, a 488 nm argon ion laser, 559 nm and 635 nm laser diode lines.
Microglia analysis: Confocal data was imported into Bitplane Imaris software for visualisation of microglia cells. The samples were sorted and discarded if the dissection damaged the retina around the implant, if staining was insufficient or if post-analysis of retinal images showed mild inflammation associated with abnormal eye fundus which remained until 90 dpi. The semi-automated quantification of microglial cells in the randomly selected zones on the implant surface was achieved using a protocol for 3D cell surface rendering of microglia described previously in literature (Nemes-Baran & DeSilva, 2021). Briefly, using the surface render tool, surfaces details were first automatically smoothed with 0.1 µm resolution and thresholded at 180 absolute intensity for all samples. Surfaces were filtered to only keep volumes above 100 μm^3 and voxels above 10 to screen noise. For PI implants, a Z-position filter was added to screen the auto-fluorescence of polyimide at 488 nm. The microglia modelled by the software were then manually compared to the microglia imaged and were either deleted if not corresponding to actual microglia or cut into several microglia if the modelling fused real microglia together. The non-automated part of the protocol was reviewed by two experimenters to decrease subject-linked bias.

Acute functionality study

Acute surgery (subretinal implantation and acute craniotomy): For the acute functionality study, acute craniotomies took around 30 min for acute experiments and subretinal implantation took less than 15 min.
Prior to the surgery, Buprenorphine (0.05 mg/kg, Buprecare®, Axience, France) and Dexamethasone solution (Dexazone®, Virbac, France) were injected subcutaneously to reduce any pain and inflammation. The animals were anesthetized with an intraperitoneal injection of ketamine (40mg/Kg, Ketamidor®, Axience, France) mixed with medetomidine (0.14 mg/kg, Domitor®, Vétoquinol, France) diluted in sodium chloride. A local analgesic, Lidocaine (4 mg/kg, Laocaïne®, MSD, France) was also administered subcutaneously under the scalp skin and Xylocaine gel (2%) was applied in the ears before placing the animal and the stereotaxic frame.
After application of antiseptic solution (Vétédine®, Vétoquinol, France), the skin was incised, the remaining periosteum removed and the skull cleaned with H_2O_2. A rectangular piece of bone was removed in the presence of cortex buffer by drilling with 0.07 and 0.05 mm-diameter drill bits in both hemispheres, from bregma -3 to -9 mm. The right eye was implanted with microsurgical procedure as described for the biocompatibility study. The implant was interfaced with an adapter (Neuronexus, USA).

Electrical stimulation and brain imaging: The return electrode was placed in the brain muscle contralateral to the implanted eye. Ultrasonic gel was applied on the dura to allow functional ultrasonic imaging of the brain (fUS). Electrical stimuli were sent via a current generator system (STG4004, Multichannel system, Harvard Bioscience, USA) grounded to the Earth and wired to a custom adapter plugged on the Omnetics connector on the implant. The light stimulation control was performed with a full-field white LED (Thorlabs, Germany). It lasted for 6 s ('ON') at a pulse train rate of 3.33 Hz (150 ms pulse train, with 150 ms pause), repeated 10 times with a 30 s pause ('OFF') between each repetition. Biphasic, anodic-first pulses with a pulse of 10 ms/phase with a 10 ms interphase, were repeated 5 times, making-up a 150 ms-pulse train repeated 20 times also at a rate of 3.33 Hz. The electrical

simulation “ON” time also lasted (150+150)x20 = 6000 ms = 6s, and was repeated 10 times with a 30 s pause (stimulation “OFF”) between each repetition.
Visual cortical areas were imaged concomitantly during the light or electrical stimulation thanks to an ultrasonic scanner (Aixplorer®, Supersonic Imagine, France) complexed with an array of 128 linear ultrasonic transducers (Vermon, France). The ultrasonic probe (15 MHz, 110 µm pitch) was placed at -6.5 mm from Bregma after applying generously ultrasonic gel on the craniotomy. fUS principles can be found in previous literature (Gesnik et al., 2017; Macé et al., 2011). Briefly, tilted plane waves were sent simultaneously by the 128 transducers and their back-scattered echo aligned temporally and summed by coherent compounding to recreate the imaged brain slice in depth (Tanter & Fink, 2014). Acquired data is proportional to the cerebral blood flow (CBF). On-line pre-processing consists in filtering noise stemming from the brain tissue using a singular-value decomposition clutter-filter (Demene et al., 2015; Baranger et al., 2018). Data is then smoothed with a Gaussian 3x3 kernel.
At the end of the experiment, the rats are euthanised by intracardiac injection of euthanasian (200 mg/kg, Exagon®, Axience, France).

fUS data analysis: Power doppler data power doppler data are retrieved under a 3D matrix of size X*Z*T and imported into Matlab for further analysis. Relative cerebral blood volume (rCBV) was calculated by dividing with the first baseline. The spm matlab toolkit for global linear model analysis (Friston, 2007) was uploaded to compare for each pixel the expected theoretical response X with the experimental response Y using the linear model Y = AX + B. The theoretical response used was the stimulation pattern convoluted with an experimentally determined haemodynamic function response function (HRF) described in previous literature (Claron et al., 2021).

Acknowledgements

This work has been funded by the European Union 2020 Horizon Research and innovation programme under grant agreement N°881603 (Graphene Flagship Core 3) and by the Marie Sklowdoska-Curie interactive network under grant agreement N°861423 (entrain Vision). We acknowledge the LabEx LIFESENSES (ANR-10-LABX-65) and IHU FOReSIGHT (ANR-18-IAHU-01).

Supplementary information

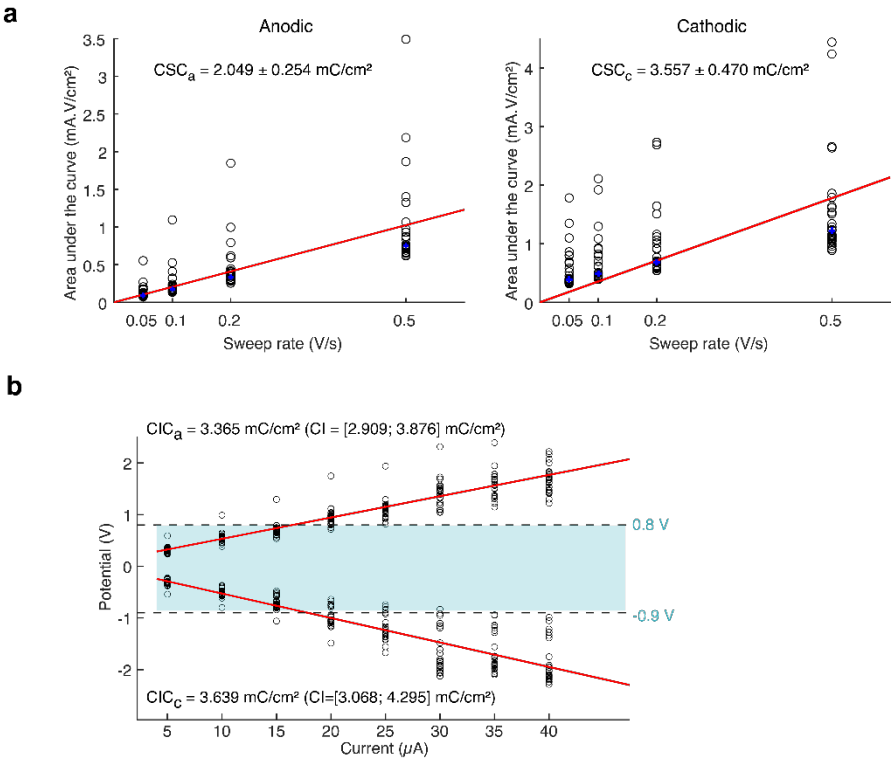

Supplementary Figure 1 Electrochemical variables calculation process. **(a)** Calculation of anodic and cathodic charge storage capacity (CSC) based on Cyclic voltammetry area under the curve. **(b)** Calculation of anodic and cathodic charge injection capacity (CIC) based on electrode polarisation measured on voltage transients.

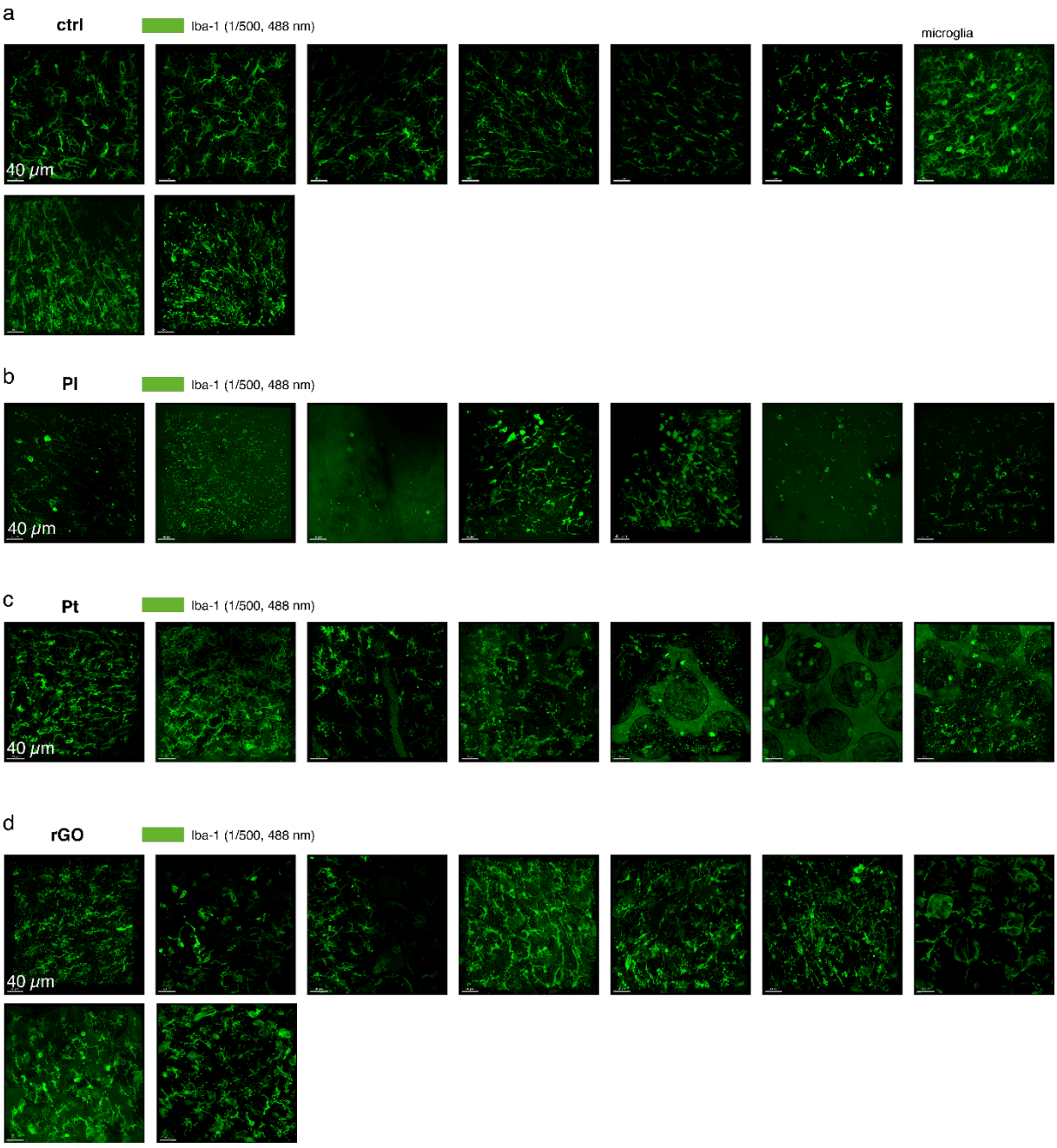

Supplementary Figure 2 Confocal imaging (40X) of all explanted retina/implant samples after 90 days *in vivo*. Quantification of these microglia are shown in fig. 3 (s) and (t). Each sample comes from a different P23H rat eye with a different implant. Microglia are stained with Iba-1 (1/500, 488 nm). **(a)** control (ctrl) non-implanted eyes (N=9) **(b)** polyimide (PI) implants (N=7) **(c)** platinum (Pt) implants (N=7) **(d)** reduced-graphene oxide (rGO) implants (N=9).

References

Baranger, J., Arnal, B., Perren, F., Baud, O., Tanter, M., & Demene, C. (2018). Adaptive Spatiotemporal SVD Clutter Filtering for Ultrafast Doppler Imaging Using Similarity of Spatial Singular Vectors. IEEE Transactions on Medical Imaging, 37(7), 1574–1586. https://doi.org/10.1109/TMI.2018.2789499

Bendali, A., Hess, L.H., Seifert, M., Forster, V., Stephan, A.F., Garrido, J.A. & Picaud, S. (2013) Purified neurons can survive on peptide-free graphene layers. Adv Healthc Mater, 2, 929-933.

Boinagrov, D., Pangratz-Fuehrer, S., Goetz, G., & Palanker, D. (2014). Selectivity of direct and network-mediated stimulation of the retinal ganglion cells with epi-, sub- and intraretinal electrodes. Journal of Neural Engineering, 11(2), 026008. https://doi.org/10.1088/1741-2560/11/2/026008

Claron, J., Hingot, V., Rivals, I., Rahal, L., Couture, O., Deffieux, T., Tanter, M., & Pezet, S. (2021). Large-scale functional ultrasound imaging of the spinal cord reveals in-depth spatiotemporal responses of spinal nociceptive circuits in both normal and inflammatory states. Pain, 162(4), 1047–1059. https://doi.org/10.1097/j.pain.0000000000002078

Demene, C., Deffieux, T., Pernot, M., Osmanski, B.-F., Biran, V., Gennisson, J.-L., Sieu, L.-A., Bergel, A., Franqui, S., Correas, J.-M., Cohen, I., Baud, O., & Tanter, M. (2015). Spatiotemporal Clutter Filtering of Ultrafast Ultrasound Data Highly Increases Doppler and fUltrasound Sensitivity. IEEE Transactions on Medical Imaging, 34(11), 2271–2285. https://doi.org/10.1109/TMI.2015.2428634

Ellis, E. M., Gauvain, G., Sivyer, B., & Murphy, G. J. (2016). Shared and distinct retinal input to the mouse superior colliculus and dorsal lateral geniculate nucleus. Journal of Neurophysiology, 116(2), 602–610. https://doi.org/10.1152/jn.00227.2016

Flores, T., Lei, X., Huang, T., Lorach, H., Dalal, R., Galambos, L., Kamins, T., Mathieson, K., & Palanker, D. (2018). Optimization of pillar electrodes in subretinal prosthesis for enhanced proximity to target neurons. Journal of Neural Engineering, 15(3), 036011. https://doi.org/10.1088/1741-2552/aaac39

Freeman, D. K., Rizzo, J. F., & Fried, S. I. (2011). Encoding visual information in retinal ganglion cells with prosthetic stimulation. Journal of Neural Engineering, 8(3), 035005. https://doi.org/10.1088/1741-2560/8/3/035005

Friston, K. J. (2007). Statistical parametric mapping: The analysis of functional brain images (1st ed). Elsevier / Academic Press.

Gesnik, M., Blaize, K., Deffieux, T., Gennisson, J.-L., Sahel, J.-A., Fink, M., Picaud, S., & Tanter, M. (2017). 3D functional ultrasound imaging of the cerebral visual system in rodents. NeuroImage, 149, 267–274. https://doi.org/10.1016/j.neuroimage.2017.01.071

Gong, C.-S., Syu, W.-J., Lei, K., & Hwang, Y.-S. (2016). Development of a Flexible Non-Metal Electrode for Cell Stimulation and Recording. Sensors, 16(10), 1613. https://doi.org/10.3390/s16101613

Ho, E., Lei, X., Flores, T., Lorach, H., Huang, T., Galambos, L., Kamins, T., Harris, J., Mathieson, K., & Palanker, D. (2019). Characteristics of prosthetic vision in rats with subretinal flat and pillar electrode arrays. Journal of Neural Engineering, 16(6), 066027. https://doi.org/10.1088/1741-2552/ab34b3

Ho, E., Smith, R., Goetz, G., Lei, X., Galambos, L., Kamins, T. I., Harris, J., Mathieson, K., Palanker, D., & Sher, A. (2018). Spatiotemporal characteristics of retinal response to network-mediated photovoltaic stimulation. Journal of Neurophysiology, 119(2), 389–400. https://doi.org/10.1152/jn.00872.2016

Humayun, M. S., Dorn, J. D., da Cruz, L., Dagnelie, G., Sahel, J.-A., Stanga, P. E., Cideciyan, A. V., Duncan, J. L., Eliott, D., Filley, E., Ho, A. C., Santos, A., Safran, A. B., Arditi, A., Del Priore, L. V., Greenberg, R. J., & Argus II Study Group. (2012). Interim results from the international trial of Second Sight's visual prosthesis. Ophthalmology, 119(4), 779–788. https://doi.org/10.1016/j.ophtha.2011.09.028

Kim, S.Y., Sadda, S., Humayun, M.S., de Juan, E., Jr., Melia, B.M. & Green, W.R. (2002) Morphometric analysis of the macula in eyes with geographic atrophy due to age-related macular degeneration. Retina, 22, 464-470.

Lorach, H., Goetz, G., Mandel, Y., Lei, X., Kamins, T. I., Mathieson, K., Huie, P., Dalal, R., Harris, J. S., & Palanker, D. (2015). Performance of photovoltaic arrays in-vivo and characteristics of prosthetic vision in animals with retinal degeneration. Vision Research, 111, 142–148. https://doi.org/10.1016/j.visres.2014.09.007

Lorach, H., Kung, J., Beier, C., Mandel, Y., Dalal, R., Huie, P., Wang, J., Lee, S., Sher, A., Jones, B.W. & Palanker, D. (2015) Development of Animal Models of Local Retinal Degeneration. Invest Ophthalmol Vis Sci, 56, 4644-4652.

Lovell, N. H., Morley, J. W., Chen, S. C., Hallum, L. E., & Suaning, G. J. (2010). BiologicalMachine systems integration: Engineering the neural interface. Proceedings of the IEEE, 98(3), 418–431. https://doi.org/10.1109/JPROC.2009.2039030

Luo, Y. H.-L., & Da Cruz, L. (2016). The Argus® II Retinal Prosthesis System. Progress in Retinal and Eye Research, 50, 89–107. https://doi.org/10.1016/j.preteyeres.2015.09.003

Macé, E., Montaldo, G., Cohen, I., Baulac, M., Fink, M., & Tanter, M. (2011). Functional ultrasound imaging of the brain. Nature Methods, 8(8), Article 8. https://doi.org/10.1038/nmeth.1641

Nemes-Baran, A. D., & DeSilva, T. M. (2021). Quantification of microglial contact and engulfment of oligodendrocyte progenitor cells in the rodent brain. STAR Protocols, 2(2), 100403. https://doi.org/10.1016/j.xpro.2021.100403

Nguyen, D., Valet, M., Dégardin, J., Boucherit, L., Illa, X., de la Cruz, J., del Corro, E., Bousquet, J., Garrido, J. A., Hébert, C., & Picaud, S. (2021). Novel Graphene Electrode for Retinal Implants: An in vivo Biocompatibility Study. Frontiers in Neuroscience, 15, 615256. https://doi.org/10.3389/fnins.2021.615256

Nguyen, D., Valet, M., Dégardin, J., Boucherit, L., Illa, X., De La Cruz, J., Del Corro, E., Bousquet, J., Garrido, J. A., Hébert, C., & Picaud, S. (2021). Novel Graphene Electrode for Retinal Implants: An in vivo Biocompatibility Study. Frontiers in Neuroscience, 15, 615256. https://doi.org/10.3389/fnins.2021.615256

Palanker, D., Le Mer, Y., Mohand-Said, S., Muqit, M. & Sahel, J.A. (2020) Photovoltaic Restoration of Central Vision in Atrophic Age-Related Macular Degeneration. Ophthalmology, 127, 1097-1104.

Poland, C. A., Duffin, R., Kinloch, I., Maynard, A., Wallace, W. A. H., Seaton, A., Stone, V., Brown, S., MacNee, W., & Donaldson, K. (2008). Carbon nanotubes introduced into the abdominal cavity of mice show asbestos-like pathogenicity in a pilot study. Nature Nanotechnology, 3(7), 423–428. https://doi.org/10.1038/nnano.2008.111

Polikov, V. S., Tresco, P. A., & Reichert, W. M. (2005). Response of brain tissue to chronically implanted neural electrodes. Journal of Neuroscience Methods, 148(1), 1–18. https://doi.org/10.1016/j.jneumeth.2005.08.015

Provansal, M., Labernède, G., Joffrois, C., Rizkallah, A., Goulet, R., Valet, M., Deschamps, W., Ferrari, U., Chaffiol, A., Dalkara, D., Sahel, J. A., Tanter, M., Picaud, S., Gauvain, G., & Arcizet, F. (2021). Functional ultrasound imaging of the spreading activity following optogenetic stimulation of the rat visual cortex. Scientific Reports, 11(1), 12603. https://doi.org/10.1038/s41598-021-91972-z

Salzmann, J. (2006). Subretinal electrode implantation in the P23H rat for chronic stimulations. British Journal of Ophthalmology, 90(9), 1183–1187. https://doi.org/10.1136/bjo.2005.089110

Santos, A., Humayun, M. S., Juan, E. De, Marsh, M. J., Klock, I. B., & Milam, A. H. (1997). Preservation of the Inner Retina in Retinitis Pigmentosa: A Morphometric Analysis. Archives of Ophthalmology, 115, 511–515.
Schiavone, G., Kang, X., Fallegger, F., Gandar, J., Courtine, G., & Lacour, S. P. (2020). Guidelines to Study and Develop Soft Electrode Systems for Neural Stimulation. Neuron, 108(2), 238–258. https://doi.org/10.1016/j.neuron.2020.10.010

Slavcheva, E., Vitushinsky, R., Mokwa, W., & Schnakenberg, U. (2004). Sputtered Iridium Oxide Films as Charge Injection Material for Functional Electrostimulation. Journal of The Electrochemical Society, 151(7), E226. https://doi.org/10.1149/1.1747881

Stingl, K., Bartz-Schmidt, K. U., Besch, D., Chee, C. K., Cottriall, C. L., Gekeler, F., Groppe, M., Jackson, T. L., MacLaren, R. E., Koitschev, A., Kusnyerik, A., Neffendorf, J., Nemeth, J., Naeem, M. A. N., Peters, T., Ramsden, J. D., Sachs, H., Simpson, A., Singh, M. S., … Zrenner, E. (2015). Subretinal Visual Implant Alpha IMS – Clinical trial interim report. Vision Research, 111, 149–160. https://doi.org/10.1016/j.visres.2015.03.001

Tanter, M., & Fink, M. (2014). Ultrafast imaging in biomedical ultrasound. IEEE Transactions on Ultrasonics, Ferroelectrics, and Frequency Control, 61(1), 102–119. https://doi.org/10.1109/TUFFC.2014.2882

Viana, D., Walston, S. T., Illa, X., Valle, J. del, Hayward, A., Dodd, A., Loret, T., Prats-Alfonso, E., Oliva, N. de la, Palma, M., Corro, E. del, Rodríguez-Meana, B., Bernicola, M. del P., Rodríguez-Lucas, E., Gener, T. A., Cruz, J. M. de la, Torres-Miranda, M., Duvan, F. T., Ria, N., … Garrido, J. A. (2022). Graphene-based thin film microelectrode technology for in vivo high resolution neural recording and stimulation (p. 2022.11.16.515761). bioRxiv. https://doi.org/10.1101/2022.11.16.515761

Vomero, M., Ciarpella, F., Zucchini, E., Kirsch, M., Fadiga, L., Stieglitz, T., & Asplund, M. (2022). On the longevity of flexible neural interfaces: Establishing biostability of polyimide-based intracortical implants. Biomaterials, 281, 121372. https://doi.org/10.1016/j.biomaterials.2022.121372

Walton, F., Cerezo-Sanchez, M., McGlynn, E., Das, R., & Heidari, H. (2022). Cleanroom strategies for micro- and nano-fabricating flexible implantable neural electronics. Philosophical Transactions of the Royal Society A: Mathematical, Physical and Engineering Sciences, 380(2228), 20210009. https://doi.org/10.1098/rsta.2021.0009
Weiland, J. D., & Humayun, M. S. (2014). Retinal prosthesis. IEEE Transactions on Biomedical Engineering, 61(5), 1412–1424. https://doi.org/10.1109/TBME.2014.2314733

Wellman, S. M., Eles, J. R., Ludwig, K. A., Seymour, J. P., Michelson, N. J., McFadden, W. E., Vazquez, A. L., & Kozai, T. D. Y. (2018). A Materials Roadmap to Functional Neural Interface Design. Advanced Functional Materials, 28(12), 1701269. https://doi.org/10.1002/adfm.201701269

IV. Discussion and Conclusion

In this final section, we first place back the results of the 3 different research project around carbon-based neural implants in the context of neural recording or neural electrical stimulation (§IV.A). We then discuss about carbon nanomaterials in comparison to classical materials or novel conductive polymers (§IV.B) and we finally reflect about electrical stimulation protocols for subretinal prostheses (§IV.C)

IV.A. Achievements

A major challenge in BCI is to generate flexible implants with small electrodes to read with high spatiotemporal resolution the brain activity or to stimulate neuronal circuit efficiently. In this search, scientists have recently turned towards **carbon-based nanomaterials** which are thought to be more biocompatible because of the prevalence of carbon in the human body, and which are attractive by their semi-conductor properties. In this phD thesis, we proved how 3 different carbon-based neural interfaces can be operated for different neurological applications in either the READ or WRITE mode.

In section §II.A, we described the microfabrication of a recording ECoG implant designed at ESIEE Paris by our collaborators. The implants were made with BDD electrodes and C* coating, featuring tracks in BDD and TiN, a conductive ceramic material able to withstand the harsh temperature and pressure conditions for diamond growth in the reactor. Their electrochemical characterization *in vitro* confirmed the expected large water window (3 V) and low impedance for diamond-doped electrodes (10 kΩ for a 400-µm diameter). To confirm the electrode functionality, we recorded visually evoked potentials upon light stimulation in both Long Evans rats and C57 mice. We even recovered the normal mouse visual acuity between 0.2 and 0.3 cpd showing thereby the decent electrode sensitivity. These results open a new path towards the fabrication of more complex implants with such full diamond technology.

In section §II.B, we explored the potential of combining graphene-based transistors (gFET) as a DC-coupled ECoG implant (fabricated at ICN2 in Barcelona), with the simultaneous ultrasound imaging of brain activity within voxel (110x100x400 μm^3) to unravel cortical spreading activity during physiological and pathophysiological events. This study demonstrates the compatibility between the 2 technologies showing that the gFET implants do not impede the ultrasound measurements. Furthermore, by generating CSDs using mechanical pinprick or KCl drops, our measurements illustrate nicely how we can correlate the DC currents related to the neuronal activity to the cerebral blood flow measures modified by the neurovascular coupling. Modelling epileptic seizures in rats up to status epilepticus by injection of a chemoconvulsant, 4-AP, our study provides evidence of the positive correlation between LFP and ISA phase and CBV and ISA phase for seizures. Our platform also revealed an increase of both CBF and LFP signal at the onset of the seizure oscillations, the CBV starting to oscillate shortly before the first seizures occur. The combined fUS and gFET strategy could become an exceptional one when defining the epileptic focus for brain resection surgery in pharmaco-resistant patients. However, its potential extends beyond epilepsy research as CSDs have been associated with many neurological disorders such as Alzheimer's disease or stroke.

In section §III, we tested *in vivo* for the first time the rGO electrodes, fabricated at ICN2, in the stimulation mode in the retina. As carbon materials were often criticized for biocompatibility, we first examined the tissue reaction to the *in vivo* long-term insertion of rGO electrodes in the subretinal space of blind rats through quantification of microglia cells and bi-weekly/monthly follow-up of the retina. This confirmed the lack of toxicity and we can interpret this positive result by the fact the rGO material is not freely released in the tissue for cell phagocytosis. Then, when applying high charge injections and at a pulse width of 1 or 10 ms/phase, the electrochemical characterization of the electrodes provides

evidence of their inertness. The neuronal stimulation was demonstrated by CBV variations in the SC of LE rats using fUS during electrical stimulation with the rGO electrodes in the subretinal space. Further studies are therefore needed now to investigate the long-term stability of these electrodes in chronic implantation with regular neuronal stimulations.

IV.B. Carbon nanomaterials versus classical materials

In the present study, we have used different electrodes: BDD, gFET and rGO. The two first materials are made with diamond or graphene having a very low surface ratio preventing their use for stimulation but showing a great potential for recording the neuronal activity. By contrast, rGO electrodes display a high surface ratio allowing reading and stimulation. Following our studies, it is important to compare the electrical characteristics of these different electrode material with respect to electrodes classically used in clinical trials such as Pt, TiN or IrOx and novel polymeric materials such as PEDOT in terms of structure (§IV.B.1.a), of electrochemical properties and biocompatibility (§IV.B.1.b). Finally, we will discuss clinical applications of graphene- and diamond-based electrodes (§IV.B.2).

IV.B.1. Comparison

a. Structure

Large surface areas promote larger charge storage capacity, beneficial for electrical stimulation. Fig. 24 displays examples of microscopy structures (SEM) for previously mentioned materials, keeping in mind that for coatings, the exact morphology depends also on the layers below it. Pt (Fig. 24.A) is rather flat and homogenous, explaining its low charge injection capacity of 0.3 – 0.4 mC/cm² (Table 2) (Negi et al., 2010) by contrast to other materials displaying a 3D bulky morphology. For instance, TiN has a column structure (Weiland et al., 2002) (Fig. 24.B), while IrOx is more granular (Negi et al., 2010) (Fig. 24.C). PEDOT-CNT electrodes also display granular surface (not shown) (Castagnola et al., 2015). Conversely, the originality of rGO lies in its porosity created by the nanometric distance separating the graphene sheets (Viana et al., 2022) (Fig. 24.D).

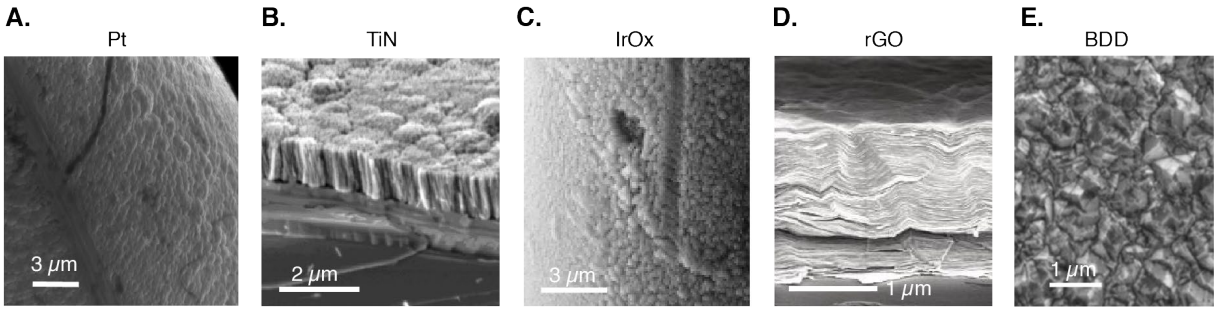

Fig. 24 Scanning electron Microscope images of different neural stimulation/recording electrodes **A.** Pt coating on Utah array electrodes from (Negi et al., 2010). **B.** TiN electrode from (Weiland et al., 2002). **C.** IrOx electrode from (Negi et al., 2010). **D.** reduced graphene oxide (rGO) electrodes on Ti/Au, from (Viana et al., 2022). **E.** Boron-doped diamond (BDD) growth side from (Fan et al., 2020).

b. Electrochemical characteristics

Table 2 summarises the electrochemical characteristics for examples of Pt, sputtered IrOx (SIROF), TiN, PEDOT, diamond and graphene-based electrodes in different preclinical applications in either the READ or WRITE mode. Table 3 presents their biocompatibility status.

All the materials previously presented can also be used for neural recording. In the READ mode, the porosity is less critical than a low impedance, a high cut-off frequency above electrophysiology recording frequency ranges and a low thermal noise. In particular, the very flat CV of flat BDD and its planar morphology (Fig. 24.E) are unfit for efficient charge storage and injection. However, a rougher surface is often synonym of a higher specific surface area and hence a lower impedance. In the example given in Fig. 24.E, the BDD growth side used for biosensing still displays grains of ~0.5 µm size in average (Fan et al., 2020). 3D diamond such as BDD coated vertical CNTS electrodes can in contrast be exploited for electrical stimulation applications (Piret et al., 2015).

The conductive and electrochemical properties of flat BDD makes them particularly interesting for neural recording. The challenge with diamond technology lies first in the microfabrication, as the harsh growth conditions of diamond seeds is only sustained by few other materials. Recent advances made it possible to obtain micrometric thick layers of diamond around 1.5 µm with low impedance (10 kΩ for a 400 µm-electrode) and acceptable SNR (although not the best), as reported in §II.A for our full-diamond ECoG. When used in its stimulation mode, diamond-based electrodes display larger water window (up to 3 V, Table 2) which allow larger stimulation excursions without generating harmful oxydo-reductant *in vivo*. Finally, perhaps diamond electrodes draw their main strength from their chemical inertness and the material biocompatibility, extensively studied and promising for long-lasting neural interfaces.

Table 2. Comparison of electrochemical characteristics of classical and novel materials for neural stimulation (WRITE mode) or recording (READ mode)

electrode material	R/W	GSA	Z (kΩ)	fcutoff (kHz)	CV window (V)	length (V)	Q_{inj}	CICc (mC/cm²)	Ref.
Pt	(R/W)	2000 µm² (50 µm tip)	125	~8	-0.6; +0.8	1,4	F,C	0.3 – 0.4	Negi et al.,2010
IrOx (SIROF)	(W)	1960–125,600 µm² (various thickness)	~1	~0.05	-0.6; +0.8	1.4	F	up to 8.9 mC/cm² for 1 ms pulse	Cogan et al., 2009
	(R/W)	2000 µm² (50 µm tip)	6	~0.5				2, up to 5 if positive bias for 0.2 ms pulse	Negi et al.,2010
	(W)	4000 µm² (ø~70 µm)	~10	~0.5	-0.6; +0.7	1.3		4 mC/cm² for 0.2 ms pulse	Weiland et al., 2002
TiN	(W)	4000 µm² (ø~70 µm)	~20	~4	-0.6; +0.7	1.4	C	0.95 mC/cm² for 0.2 ms	Weiland et al., 2002
PEDOT:PSS	(R)	~70700 µm² (ø=300 µm)	~1	/	/	1.7	C	1.5 – 15 mC/cm²	Vomer et al., 2016
BDD	(R)	125667 µm² (ø=400 µm)	10	~8	-1.5; +1.5	3	C	/	Wilfinger et al., in prep.
BDD	(R)	7900 µm² (ø~60 µm)	~207.9		-1.8; +1.8	3.6		/	Fan et al., 2020
N-UNCD	(W)	12600 µm² (ø=80 µm, pillar height=150 µm)	20	>10	-1.8; +1.3	3.1		0.68 mC/cm²	Stamp et al., 2020
rGO	(W)	156 µm² (25 µm)	30	~1.8	-0.9 +0.8	1.7	C	1.5 – 6 mC/cm²	Zhang et al., in prep.

For neural recording, Pt electrodes, although the standard commercialised tools in the electrophysiology field, yield a high thermal noise *in vitro* (1.2 µV at 1 kHz bandwidth) which is rather non-optimal compared to SIROF for instance (0.2 µV) (Negi et al., 2010). Recently, poly(3,4-ethylenedioxythiophene):poly(styrenesulfonate) (PEDOT:PSS)-based **NeuroGrid** demonstrated a very low noise of 5 dB at 1 kHz *in vivo*, sensitive to both LFPs and spikes (Khodagholy et al., 2015) while CVD graphene-based transistors were characterised with a 25-30 µV gate noise between 1 to 2 kHz (Bonaccini Calia et al., 2022), showing higher recording amplitudes of infraslow signals than gold and platinum arrays (Masvidal-Codina et al., 2019). Both PEDOT:PSS and CVD graphene open a new window of possibilities in the electrophysiology field, by allowing simultaneous coupling with calcium imaging for PEDOT:PSS probes (Donahue et al., 2018), and with optogenetics (Masvidal-Codina et al., 2021) or with functional ultrasound imaging (Zhang, Masvidal-Codina et al., in prep, §II.B) for CVD-graphene-based transistors. In addition, gFETs are particularly suited for DC recordings which only few have looked at, allowing investigations of infraslow oscillations and CSDs in this new range of frequencies below 0.1 Hz, which are relevant in many neurological disorders.

The poor CIC of Pt (0.3 – 0.4 mC/cm², (Negi et al. 2010)), followed closely by TiN (0.95 mC/cm², (Weiland et al., 2002)) make them unfit for efficient electrical stimulation in neurorehabilitation. In contrast, SIROF, PEDOT and rGO have larger CICs.

PEDOT, rGO, and BDD have been proven to be biocompatible *in vivo* for specific applications (Table 3). As PEDOT is usually associated with anions to increase its conductivity, their biocompatibility has to be (and have been) verified in diverse cases (association with polypyrole (PPy) or with dexamethasone release for instance). In the end, both PEDOT and rGO show promising CIC and large window (1.7 V) for neural stimulation, but also adequate properties for neural recording or even biosensing.

Table 3. Biocompatibility of classical and novel electrode materials for neural stimulation or neural recording.

electrode material	Applications (W/R)	Biocompatibility	Ref
Pt	Cortical stimulation (W)	Dissolution upon elecStim (cats)	(Roblee et al., 1983)
IrOx (SIROF)	Utah array-based intracortical visual prostheses	Delamination, degraded tips (NHPs, 3 years)	(Chen et al. 2023)
IrOx (SIROF)	TIME rat sciatic nerve	distant damage and axonal degeneration, attributed to stiffness	(Badia et al., 2011)
TiN	Pacemaker electrodes (W)	increased cell death (*in vitro*)	(Weiland et al., 2002)
PEDOT	NeuroGrid (R)	Yes (with PPy, Dexamethasone, Nafion)	(Bianchi et al., 2022)
PEDOT:PSS	POLYRETINA (W)	Yes (blind minipigs, 2 weeks)	(Vagni et al. 2022)
BDD pillars	retinal prostheses (W)	Yes (blind rats, subretinal)	(Bendali et al., 2016)
BDD	retinal prostheses (W)	guinea pigs (back muscle)	(Garrett et al., 2016)
N-UNCD			
rGO	retinal prostheses (W)	Yes (blind rats, 3 months)	(Zhang et al., in prep.)

IV.B.2. Clinical applications

In our preclinical study, graphene transistors have been coupled with fUS technology thanks to the optical properties of graphene, “transparent” to US. gFETs compensate the low temporal resolution of fUS at both infraslow and high frequencies, while fUS can image a whole brain slice at high spatial resolution (110x100x400 μm^3). Consequently, the coupled platform is a tool of choice for neurovascular coupling research. Meanwhile, clinical studies with both technologies separately are already a reality. On one hand, fUS has been used to image tumor vasculature during awake brain surgery in 10 patients, showing high potential for vascular mapping and hence applications in brain resection surgeries (Soloukey et al., 2020). On the other hand, the graphene EGNITE technology is already mature enough to reach clinical stage, driven by the spin-off company INBRAIN Neuroelectronics S.L from the Graphene Flagship. Moreover, the various studies around gFETs (Bonaccini Calia et al., 2022; Masvidal-Codina et al., 2019, 2021) in addition to our new study (§II.B) are bringing them nearer to the clinical stage. Indeed, their great advantage in recording DC signals should speak for the clinical development of the technology. Future prospects will therefore lie in the clinical combination of both gFETs and fUS as a powerful surgery monitoring aid or clinical research tool to follow brain states at the surface with electrodes and in the depth with fUS.

Moreover, vision restoration strategies are not limited to electrical stimulation. Two years ago, an optogenetic-based prosthesis have shown the possibility to partially restore vision in a blind RP patient (Sahel et al., 2021). The patient was injected intravitreally with chrimsonR-tdTomato to target RGCs, and just as for electrical stimulation, images are converted by goggles into infrared light pulses sent to the eye. During visual tasks experiments, neural activity in the visual cortex is recorded using EEGs. Meanwhile, sonogenetics-based visual restoration strategies are also being actively investigated. The artificial overexpression of mechanosensitive ion-channels to functional ultrasound stimulation revealed activation of both retinal and cortical neurons (Cadoni et al., 2023). We could envision that in order to build a closed-loop cortical optogenetic/sonogenetic BCI, optically transparent graphene electrodes could be used to record from the cortex while still enabling IR light/ultrasound to penetrate in the brain.

IV.C. Subretinal prostheses and remaining challenges

As discussed above, our study confirms the great interest for carbon-based electrodes with different applications for the read and write potentials. In the case of rGO-based electrodes, their properties allowed their transfer to clinical trials (Viana et al., 2022) . No difference was observed upon stimulations with the 25 and 100µm electrode diameter. Although this result might sound awkward, it is important to remind that the experiments were carried out in the acute mode. The retina was detached by fluid injection and the implant was introduced in the subretinal pocket with no chance of the tissue to adhere to the implant in the short experimental time. As a consequence, the charges are released in the fluid below the retina losing the spatial confinement of the electrode. Resorption of the subretinal fluid in a chronic implantation would be needed to investigate the respective resolutions of the 25 and 100µm diameter electrodes, Furthermore, ground grid electrodes may also be required to confine the current in a very restricted area (§IV.C.1). As the state of the art in currently, the photovoltaic implant (ref Palanker), an ideal test bench would be to compare current photovoltaic with rGO-based photovoltaic implants to compare the light intensity requirement for the retinal activation. Finally, we will discuss briefly the other factors which have to be taken into account for subretinal prostheses clinical trials and commercialisation (§IV.B.3).

IV.C.1. Spatial resolution

If we consider that a perfect 20/20 visual acuity corresponds to two points separated by α=1 min of arc (') and that the distance between the retina and the eye lens is f≃1.6 cm, then using trigonometry the corresponding distance d separating two photoreceptors in the retina is d = 2*f*tan(α). This makes d≃10 µm, and D=1/d=100 lines/mm in terms of spatial frequency. Based on Shannon's law, the sampling frequency for the electronic device should at least twice higher, so 200 lines/mm or a distance of 5 µm separating 2 artificial pixels. So far, retinal prostheses which reached the clinical stage all had electrodes of large sizes (for ex. 200 µm for the Argus II, 100 µm for the PRIMA). The best visual acuity, 20/460 was obtained by the PRIMA subretinal implant from Pixium Vision on AMD patients using Landolt ring tests (Palanker 2020). In the best case of Alpha-IMS, a similar visual acuity was achieved with 2 patients. Despite smaller pixel size (70 µm), the visual acuity is surprisingly not better than PRIMA., contradicting the mathematical demonstrations above: reducing the size of pixels should improve spatial resolution if the prosthesis provides a focal and selective activation of individual cells. Theoretically, a pixel size of 50 µm could ideally achieve a visual acuity of 20/20 (Palanker et al., 2005). This suggests that the electrical stimulation with smaller size of electrodes could not avoid cross-talk hence limiting visual contrast perception (Loudin et al., 2007).

Another issue is that downsizing electrodes diameter increases the stimulation threshold, increases the impedance at the interface and limits their capacitance and penetrating electrical field. Although IrOx electrodes can comply with the requirements, they are nonetheless limited to a minimum size of 55 µm to be able to match retinal stimulation thresholds (Flores et al., 2019). In contrast, we showed that rGO-based electrodes down to 25 µm have enough charge injection capacity to activate the visual pathway without degradation of the material. In addition, lower charge injection would be required for the tissue activation if the retina was reattached to the implant in chronic conditions.

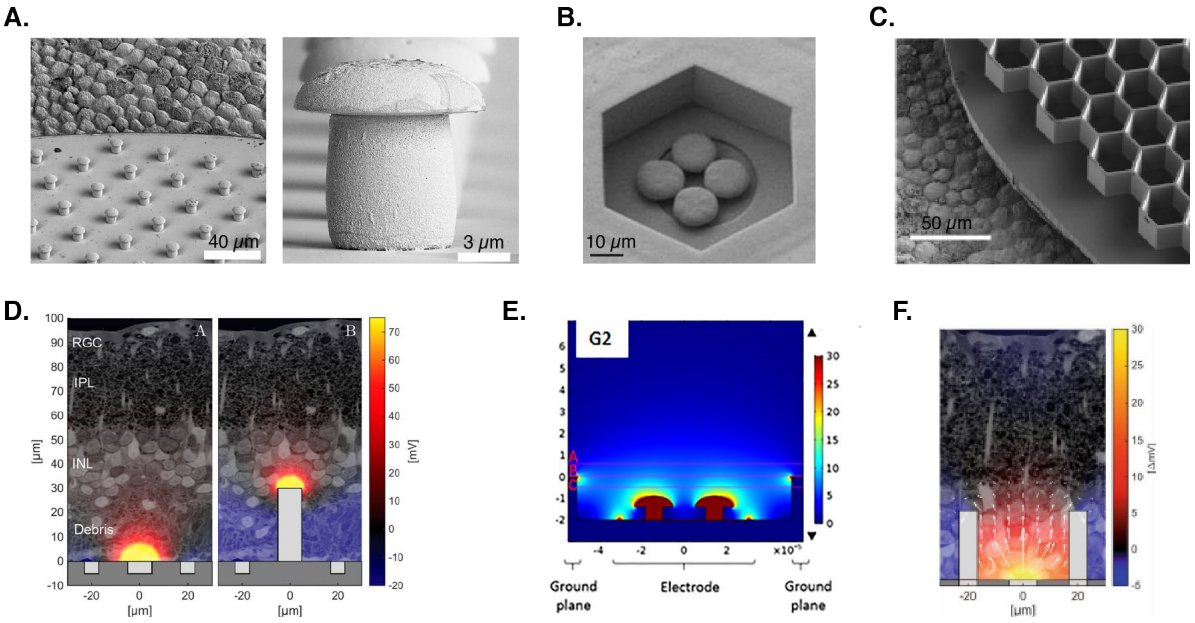

Fig. 25 Examples of novel stimulating electrode and return electrode configurations for subretinal implants. Electrical field model is shown below each SEM images of the implant. **A,D.** Retrieved from (Flores et al., 2018). **B,D.** Retrieved from (Losada et al., 2018). **C,F.** Retrieved from (Flores et al., 2019).

An important limitation in reducing the electrode size with a local return electrode is the likelihood of not having any current entering the tissue to be stimulated. This limitation led to develop novel 3D configuration of the stimulating electrode and return electrode. For example, pillar 3D electrodes (Fig. 25.A, D) could bypass debris of degenerated photoreceptor cells and target more efficiently bipolar cells (Flores et al., 2018). Protuberant mushroom-shaped subretinal electrodes in a cavity with plane ground (Fig. 25.B, E) were also found to increase cortical response in visual areas compared to planar

electrodes (Losada et al., 2019). Recently, honey-comb shaped pillar electrodes with return electrode at the vertical edge of the stimulating electrode were designed in Stanford University (Fig. 25.C, F). In this configuration, neurons from the inner retina layers migrated into the well (with no biocompatibility difference compared to planar configuration), reducing the distance between the stimulating electrodes and stimulated neurons. Such ideas could inspire a new design of subretinal implants with rGO electrodes instead of IrOx, in order to increase penetration of electrical field and hence both the efficiency and precision of the stimulation. Perhaps the easier way to start in the near future would be to choose neighbouring electrodes to constitute a ring of return electrodes as suggested in (Flores et al., 2019).

Nowadays, the PRIMA photovoltaic implant under feasibility trial in France (NCT03333954) could restore a prosthetic acuity above 20/100 = 0.2 for 4 patients with x8 electronic magnification of the image projected on the implant during Landolt ring tests (Palanker et al., 2022). This value corresponds to the legal limit of blindness in the USA, and is slightly below the 0.3 value attributed for legal definition of mild visual impairment in Europe. Moreover, the whole PRIMA system allows the combination of prosthetic and natural remaining vision thanks to its transparent goggles, translating the images from the real world onto LED patterns shone onto the subretinal photovoltaic implant. However, the spatial in prosthetic vision is not only influenced by the number and size of pixels but also by the visual angles rescued. Indeed, larger visual coverage in prosthetic vision does make a significant difference in object recognition tasks and letter reading as simulated with virtual reality (Thorn et al., 2020). However, the PRIMA implant previously mentioned only covers ~7° visual angle with 378 hexagonal pixels of 100 µm width, not even one tenth of the ~130° in natural vision. Implanted RP patients have to constantly scan their surroundings in order to benefit fully from the prosthetic vision. In contrast, the lens-alike epiretinal POLYRETINA photovoltaic prosthesis contains 10,498 pixels, improving both comfort and visual coverage (~43°) (Chenais et al., 2021).

IV.C.2. Image fading and temporal resolution

One example of another major challenge for retinal prostheses is **image fading**. As eyes naturally move around quickly, scanning surroundings, each small movement acts as an image refreshing procedure. However, with prosthetic vision, the repetitive stimulation of one electrode which makes the captured image fade away in the brain because of RGCs desensitization. This fading can be frustrating and was one of the major causes for one alpha-IMS implanted patient inferior appreciation in daily-life tasks (Stingl et al., 2013). Electrical stimulation protocol can be tuned to counter image fading, by sending for instance pulses with randomised duration (Thorn et al., 2022).

IV.C.3. Other considerations

One might still also wonder why there is still no (more) commercially available visual prostheses, despite fast-paced research to solve biocompatibility, spatial resolution and temporal resolution challenges. We see 2 more non-scientific factors at play.

In the case of subretinal implants, the surgery is the first key step as for clinical trials than for preclinical studies. Its success respectively reduces the risk of complications for the patient but also impacts the acquired data quality. During clinical retinal implant trials, serious adverse events (SAE) either life-threatening or necessitating surgery/hospitalization (ISO 14155) can unfortunately happen, such as conjunctival erosions, hypotony, vitreous haemorrhage, endophthalmitis. For Argus II (Second Sight Medical Devices), 13 SAE were reported for a one-year study on 47 patients (Schaffrath et al., 2021), 4 being linked to the implantation procedure. Similarly, for the epiretinal IRIS 2 implant (Pixium Vision), 6 SAE were reported for 4 patients (Muqit et al., 2019), 4 SAE being imputed to the surgical

procedure itself (tack fixation for instance). Non-serious adverse events (choroidal detachment, conjunctivitis, ocular pain, dry eye, and phlebitis) are less traumatic yet still unpleasant.

While there is still a gap to close between patients' expectations and clinical trials results, the failure of the retinal prostheses is also plunged by financial reasons. For example, criticised overtly for "leaving their patients in the dark" (Strickland & Harris, 2022), 2nd Sight company (USA) had to face financial difficulties exacerbated by the COVID19 which led to its merge with another company. Additionally, large investments have to be secured as it usually takes over a decade to achieve commercialisation. Legally speaking, non-wireless versions of implants require an active implantable medical part (stimulator and its power supply for instance) which is one of the most strictly regulated human product in the world. Waiting time for ethical approval of clinical trials added to preclinical research time lengthen even more the path to commercialisation. Last but not least, low and country-specific health-care system coverage fees for the patient and regulatory might become a nightmare to comply with (Faber et al., 2020).

Work perspectives

Next steps of the subretinal prosthesis project involve chronic testing. We first plan on following-up with retinal imaging techniques the implanted retina for a period up to 2 months. As our tethered design allows the connection to a potentiostat, we will measure weekly the evolution of electrochemical characteristics (while it is not possible for photovoltaic interfaces) to understand better the changes of the electrode/tissue interface. We will also investigate thresholds of neural activation in fUS upon chronic electrical stimulation on anaesthetised rats for a period up to 2 months. Indeed, we expect a decrease of thresholds compared to acute set-ups as over time the retina re-attaches itself on the electrode. Few teams explored the chronic *in vivo* evolution of impedance, cyclic voltammetry and voltage transients of retinal implants. We expect a correlation between tissue damage/gliosis and increase of impedance (Linderholm et al., 2013; Pham et al., 2013; Hébert et al., 2016; Schiavone et al., 2020) at a perhaps lower range because of the higher biocompatibility of graphene electrodes.

The technology platform combining fUS and gFET could be applied to multiple preclinical and clinical research questions. We choose to continue the preclinical investigation of CSDs in epilepsy but also in stroke, this time in awake animals. Another point to explore is terminal CSDs, which can help to investigate treatments reviving blood circulation after cardiac arrest, to time better artificial ventilation for survival, to perhaps change current organ donation rules which are regulated with strict timing after blood circulation stops (Dreier et al., 2018), and finally to gain knowledge about brain death. Those data were gathered during our epilepsy experiments but not yet analysed.

The NEURODIAM project with the BDD electrodes encapsulated in intrinsic diamond is also going towards the chronic stage, with a larger 32-electrode ECoG array. We envision a biocompatibility study with chronic subdural implantation and measures to investigate electrochemical characteristics and SNR stability over time. As enhancing the BDD surface ratio was also achieved in different conditions, transferring this technology on an implant would allow its use for both read and write technology in the brain, to build a cortical prosthesis for visual restoration for instance.

Although there is still a long way to go for reliable visual prostheses, exponential advances in BCIs the past decade made neurorehabilitation hopes come closer to reality. For instance, just this year 2023, a tetraplegic patient with spinal cord injury was able to walk again thanks to a close-loop brain-spine interface developed at the EPFL (Switzerland) (Lorach et al., 2023). Prosthetic arms enabling amputee or tetraplegic patients to grasp objects are being improved thanks to sensory feedback (Flesher et al., 2021). We believe that the future generation of BCIs can rely on carbon nanomaterials for improved long-term biocompatibility and efficient mutimodal neural reading or/and writing.

References

Ahnood, A., Escudie, M. C., Cicione, R., Abeyrathne, C. D., Ganesan, K., Fox, K. E., Garrett, D. J., Stacey, A., Apollo, N. V., Lichter, S. G., Thomas, C. D. L., Tran, N., Meffin, H., & Prawer, S. (2015). Ultrananocrystalline diamond-CMOS device integration route for high acuity retinal prostheses. *Biomedical Microdevices*, *17*(3), 50. https://doi.org/10.1007/s10544-015-9952-y

Alcaide, M., Taylor, A., Fjorback, M., Zachar, V., & Pennisi, C. P. (2016). Boron-Doped Nanocrystalline Diamond Electrodes for Neural Interfaces: In vivo Biocompatibility Evaluation. *Frontiers in Neuroscience*, *10*. https://doi.org/10.3389/fnins.2016.00087

An, W., Zhang, Y., Zhang, X., Li, K., Kang, Y., Akhtar, S., Sha, X., & Gao, L. (2018). Ocular toxicity of reduced graphene oxide or graphene oxide exposure in mouse eyes. *Experimental Eye Research*, *174*, 59–69. https://doi.org/10.1016/j.exer.2018.05.024

Apollo, N. V., Maturana, M. I., Tong, W., Nayagam, D. A. X., Shivdasani, M. N., Foroughi, J., Wallace, G. G., Prawer, S., Ibbotson, M. R., & Garrett, D. J. (2015). Soft, Flexible Freestanding Neural Stimulation and Recording Electrodes Fabricated from Reduced Graphene Oxide. *Advanced Functional Materials*, *25*(23), 3551–3559. https://doi.org/10.1002/adfm.201500110

Ariano, P., Lo Giudice, A., Marcantoni, A., Vittone, E., Carbone, E., & Lovisolo, D. (2009). A diamond-based biosensor for the recording of neuronal activity. *Biosensors and Bioelectronics*, *24*(7), 2046–2050. https://doi.org/10.1016/j.bios.2008.10.017

Ayata, C., & Lauritzen, M. (2015). Spreading Depression, Spreading Depolarizations, and the Cerebral Vasculature. *Physiological Reviews*, *95*(3), 953–993. https://doi.org/10.1152/physrev.00027.2014

Aydin, A.-K., Haselden, W. D., Goulam Houssen, Y., Pouzat, C., Rungta, R. L., Demené, C., Tanter, M., Drew, P. J., Charpak, S., & Boido, D. (2020). Transfer functions linking neural calcium to single voxel functional ultrasound signal. *Nature Communications*, *11*(1), 2954. https://doi.org/10.1038/s41467-020-16774-9

Bahar, S., Suh, M., Zhao, M., & Schwartz, T. H. (2006). Intrinsic optical signal imaging of neocortical seizures: The 'epileptic dip'. *NeuroReport*, *17*(5), 499–503. https://doi.org/10.1097/01.wnr.0000209010.78599.f5

Bahari, F., Ssentongo, P., Liu, J., Kimbugwe, J., Curay, C., Schiff, S. J., & Gluckman, B. J. (2018). *Seizure-associated spreading depression is a major feature of ictal events in two animal models of chronic epilepsy* [Preprint]. Neuroscience. https://doi.org/10.1101/455519

Bajaj, P., Akin, D., Gupta, A., Sherman, D., Shi, B., Auciello, O., & Bashir, R. (2007). Ultrananocrystalline diamond film as an optimal cell interface for biomedical applications. *Biomedical Microdevices*, *9*(6), 787–794. https://doi.org/10.1007/s10544-007-9090-2

Baranger, J., Arnal, B., Perren, F., Baud, O., Tanter, M., & Demene, C. (2018). Adaptive Spatiotemporal SVD Clutter Filtering for Ultrafast Doppler Imaging Using Similarity of Spatial Singular Vectors. *IEEE Transactions on Medical Imaging*, *37*(7), 1574–1586. https://doi.org/10.1109/TMI.2018.2789499

Bastany, Z. J. R., Askari, S., Dumont, G. A., Kellinghaus, C., Kazemi, A., & Gorji, A. (2020). Association of cortical spreading depression and seizures in patients with medically intractable epilepsy. *Clinical Neurophysiology*, *131*(12), 2861–2874. https://doi.org/10.1016/j.clinph.2020.09.016

Beauchamp, M. S., Oswalt, D., Sun, P., Foster, B. L., Magnotti, J. F., Niketeghad, S., Pouratian, N., Bosking, W. H., & Yoshor, D. (2020). Dynamic Stimulation of Visual Cortex Produces Form Vision in Sighted and Blind Humans. *Cell*, *181*(4), 774-783.e5. https://doi.org/10.1016/j.cell.2020.04.033

Bendali, A., Agnès, C., Meffert, S., Forster, V., Bongrain, A., Arnault, J.-C., Sahel, J.-A., Offenhäusser, A., Bergonzo, P., & Picaud, S. (2014). Distinctive Glial and Neuronal Interfacing on Nanocrystalline Diamond. *PLoS ONE*, *9*(3), e92562. https://doi.org/10.1371/journal.pone.0092562

Bendali, A., Hess, L. H., Seifert, M., Forster, V., Stephan, A.-F., Garrido, J. A., & Picaud, S. (2013). Purified Neurons can Survive on Peptide-Free Graphene Layers. *Advanced Healthcare Materials*, *2*(7), 929–933. https://doi.org/10.1002/adhm.201200347

Bendali, A., Rousseau, L., Lissorgues, G., Scorsone, E., Djilas, M., Dégardin, J., Dubus, E., Fouquet, S., Benosman, R., Bergonzo, P., Sahel, J.-A., & Picaud, S. (2015). Synthetic 3D diamond-based electrodes for flexible retinal neuroprostheses: Model, production and in vivo biocompatibility. *Biomaterials*, *67*, 73–83. https://doi.org/10.1016/j.biomaterials.2015.07.018

Beynon, S. B., & Walker, F. R. (2012). Microglial activation in the injured and healthy brain: What are we really talking about? Practical and theoretical issues associated with the measurement of changes in microglial morphology. *Neuroscience*, *225*, 162–171. https://doi.org/10.1016/j.neuroscience.2012.07.029

Bimbard, C., Demene, C., Girard, C., Radtke-Schuller, S., Shamma, S., Tanter, M., & Boubenec, Y. (2018). Multi-scale mapping along the auditory hierarchy using high-resolution functional UltraSound in the awake ferret. *eLife*, *7*, e35028. https://doi.org/10.7554/eLife.35028

Black, J., & Black, J. (2005). *Biological Performance of Materials: Fundamentals of Biocompatibility, Fourth Edition* (0 ed.). CRC Press. https://doi.org/10.1201/9781420057843

Boehler, C., Carli, S., Fadiga, L., Stieglitz, T., & Asplund, M. (2020). Tutorial: Guidelines for standardized performance tests for electrodes intended for neural interfaces and bioelectronics. *Nature Protocols*, *15*(11), 3557–3578. https://doi.org/10.1038/s41596-020-0389-2

Boinagrov, D., Pangratz-Fuehrer, S., Goetz, G., & Palanker, D. (2014). Selectivity of direct and network-mediated stimulation of the retinal ganglion cells with epi-, sub- and intraretinal electrodes. *Journal of Neural Engineering*, *11*(2), 026008. https://doi.org/10.1088/1741-2560/11/2/026008

Bonaccini Calia, A., Masvidal-Codina, E., Smith, T. M., Schäfer, N., Rathore, D., Rodríguez-Lucas, E., Illa, X., De la Cruz, J. M., Del Corro, E., Prats-Alfonso, E., Viana, D., Bousquet, J., Hébert, C., Martínez-Aguilar, J., Sperling, J. R., Drummond, M., Halder, A., Dodd, A., Barr, K., … Garrido, J. A. (2022). Full-bandwidth electrophysiology of seizures and epileptiform activity enabled by flexible graphene microtransistor depth neural probes. *Nature Nanotechnology*, *17*(3), Article 3. https://doi.org/10.1038/s41565-021-01041-9

Borda, E., Ferlauto, L., Schleuniger, J., Mustaccio, A., Lütolf, F., Lücke, A., Fricke, S., Marjanović, N., & Ghezzi, D. (2020). All-Printed Electrocorticography Array for In Vivo Neural Recordings. *Advanced Engineering Materials*, *22*(3), 1901403. https://doi.org/10.1002/adem.201901403

Borda, E., Gaillet, V., Airaghi Leccardi, M. J. I., Zollinger, E. G., Moreira, R. C., & Ghezzi, D. (2022). Three-dimensional multilayer concentric bipolar electrodes restrict spatial activation in optic nerve stimulation. *Journal of Neural Engineering*, *19*(3), 036016. https://doi.org/10.1088/1741-2552/ac6d7e

Bourgeais-Rambur, L., Beynac, L., Mariani, J.-C., Tanter, M., Deffieux, T., Lenkei, Z., & Villanueva, L. (2022). Altered Cortical Trigeminal Fields Excitability by Spreading Depolarization Revealed with *in Vivo* Functional Ultrasound Imaging Combined with Electrophysiology. *The Journal of Neuroscience*, *42*(32), 6295–6308. https://doi.org/10.1523/JNEUROSCI.1825-21.2022

Bourrier, A., Shkorbatova, P., Bonizzato, M., Rey, E., Barraud, Q., Courtine, G., Othmen, R., Reita, V., Bouchiat, V., & Delacour, C. (2019). Monolayer Graphene Coating of Intracortical Probes for Long-Lasting Neural Activity Monitoring. *Advanced Healthcare Materials*, *8*(18), 1801331. https://doi.org/10.1002/adhm.201801331

Brindley, G. S., & Lewin, W. S. (1968). The sensations produced by electrical stimulation of the visual cortex. *The Journal of Physiology*, *196*(2), 479–493. https://doi.org/10.1113/jphysiol.1968.sp008519

Brunner, C., Grillet, M., Urban, A., Roska, B., Montaldo, G., & Macé, E. (2021). Whole-brain functional ultrasound imaging in awake head-fixed mice. *Nature Protocols*, *16*(7), 3547–3571. https://doi.org/10.1038/s41596-021-00548-8

Burghard, M., Klauk, H., & Kern, K. (2009). Carbon-Based Field-Effect Transistors for Nanoelectronics. *Advanced Materials*, *21*(25–26), 2586–2600. https://doi.org/10.1002/adma.200803582

Butterwick, A., Huie, P., Jones, B. W., Marc, R. E., Marmor, M., & Palanker, D. (2009). Effect of shape and coating of a subretinal prosthesis on its integration with the retina. *Experimental Eye Research*, *88*(1), 22–29. https://doi.org/10.1016/j.exer.2008.09.018

Button, J., & Putnam, T. (1962). *Visual responses to cortical stimulation in the blind*.

Buzsáki, G., Anastassiou, C. A., & Koch, C. (2012). The origin of extracellular fields and currents—EEG, ECoG, LFP and spikes. *Nature Reviews Neuroscience*, *13*(6), 407–420. https://doi.org/10.1038/nrn3241

Cadoni, S., Demené, C., Alcala, I., Provansal, M., Nguyen, D., Nelidova, D., Labernède, G., Lubetzki, J., Goulet, R., Burban, E., Dégardin, J., Simonutti, M., Gauvain, G., Arcizet, F., Marre, O., Dalkara, D., Roska, B., Sahel, J. A., Tanter, M., & Picaud, S. (2023). Ectopic expression of a mechanosensitive channel confers spatiotemporal resolution to ultrasound stimulations of neurons for visual restoration. *Nature Nanotechnology*, *18*(6), 667–676. https://doi.org/10.1038/s41565-023-01359-6

Castagnola, E., Maiolo, L., Maggiolini, E., Minotti, A., Marrani, M., Maita, F., Pecora, A., Angotzi, G. N., Ansaldo, A., Boffini, M., Fadiga, L., Fortunato, G., & Ricci, D. (2015). PEDOT-CNT-Coated Low-Impedance, Ultra-Flexible, and Brain-Conformable Micro-ECoG Arrays. *IEEE Transactions on Neural Systems and Rehabilitation Engineering*, *23*(3), 342–350. https://doi.org/10.1109/TNSRE.2014.2342880

Chang, J. C., Shook, L. L., Biag, J., Nguyen, E. N., Toga, A. W., Charles, A. C., & Brennan, K. C. (2010). Biphasic direct current shift, haemoglobin desaturation and neurovascular uncoupling in cortical spreading depression. *Brain*, *133*(4), 996–1012. https://doi.org/10.1093/brain/awp338

Charvet, G., Sauter-Starace, F., Foerster, M., Ratel, D., Chabrol, C., Porcherot, J., Robinet, S., Reverdy, J., D'Errico, R., Mestais, C., & Benabid, A. L. (2013). WIMAGINE®: 64-channel ECoG recording implant for human applications. *2013 35th Annual International Conference of the IEEE Engineering in Medicine and Biology Society (EMBC)*, 2756–2759. https://doi.org/10.1109/EMBC.2013.6610111

Chen, J., Yao, B., Li, C., & Shi, G. (2013). An improved Hummers method for eco-friendly synthesis of graphene oxide. *Carbon*, *64*, 225–229. https://doi.org/10.1016/j.carbon.2013.07.055

Chen, S., Li, P., Gong, H., Luo, W., Zeng, S., & Luo, Q. (2008). Cortical Spreading Depression in Rats. *IEEE Engineering in Medicine and Biology Magazine*, *27*(5), 29–35. https://doi.org/10.1109/MEMB.2008.929418

Chen, X., Wang, F., Fernandez, E., & Roelfsema, P. R. (2020). Shape perception via a high-channel-count neuroprosthesis in monkey visual cortex. *Science*, *370*(6521), 1191–1196. https://doi.org/10.1126/science.abd7435

Chen, X., Wang, F., Kooijmans, R., Klink, P. C., Boehler, C., Asplund, M., & Roelfsema, P. R. (2023). Chronic stability of a neuroprosthesis comprising multiple adjacent Utah arrays in monkeys. *Journal of Neural Engineering*, *20*(3), 036039. https://doi.org/10.1088/1741-2552/ace07e

Chenais, N. A. L., Airaghi Leccardi, M. J. I., & Ghezzi, D. (2021). Photovoltaic retinal prosthesis restores high-resolution responses to single-pixel stimulation in blind retinas. *Communications Materials*, *2*(1), 28. https://doi.org/10.1038/s43246-021-00133-2

Chow, A. Y., Bittner, A. K., & Pardue, M. T. (2010). The artificial silicon retina in retinitis pigmentosa patients (an American Ophthalmological Association thesis). *Transactions of the American Ophthalmological Society*, *108*, 120–154.

Chow, A. Y., Pardue, M. T., Chow, V. Y., Peyman, G. A., Chanping Liang, Perlman, J. I., & Peachey, N. S. (2001). Implantation of silicon chip microphotodiode arrays into the cat subretinal space. *IEEE Transactions on Neural Systems and Rehabilitation Engineering*, *9*(1), 86–95. https://doi.org/10.1109/7333.918281

Claron, J., Hingot, V., Rivals, I., Rahal, L., Couture, O., Deffieux, T., Tanter, M., & Pezet, S. (2021). Large-scale functional ultrasound imaging of the spinal cord reveals in-depth spatiotemporal responses of spinal nociceptive circuits in both normal and inflammatory states. *Pain*, *162*(4), 1047–1059. https://doi.org/10.1097/j.pain.0000000000002078

Cogan, S. F. (2008). Neural Stimulation and Recording Electrodes. *Annual Review of Biomedical Engineering*, *10*(1), 275–309. https://doi.org/10.1146/annurev.bioeng.10.061807.160518

Cogan, S. F., Guzelian, A. A., Agnew, W. F., Yuen, T. G. H., & McCreery, D. B. (2004). Over-pulsing degrades activated iridium oxide films used for intracortical neural stimulation. *Journal of Neuroscience Methods*, *137*(2), 141–150. https://doi.org/10.1016/j.jneumeth.2004.02.019

Creel, D. J. (2019). Visually evoked potentials. In *Handbook of Clinical Neurology* (Vol. 160, pp. 501–522). Elsevier. https://doi.org/10.1016/B978-0-444-64032-1.00034-5

Daschner, R., Greppmaier, U., Kokelmann, M., Rudorf, S., Rudorf, R., Schleehauf, S., & Wrobel, W. G. (2017). Laboratory and clinical reliability of conformally coated subretinal implants. *Biomedical Microdevices*, *19*(1), 7. https://doi.org/10.1007/s10544-017-0147-6

Davalos, D., Grutzendler, J., Yang, G., Kim, J. V., Zuo, Y., Jung, S., Littman, D. R., Dustin, M. L., & Gan, W.-B. (2005). ATP mediates rapid microglial response to local brain injury in vivo. *Nature Neuroscience*, *8*(6), 752–758. https://doi.org/10.1038/nn1472

Deffieux, T., Demene, C., Pernot, M., & Tanter, M. (2018). Functional ultrasound neuroimaging: A review of the preclinical and clinical state of the art. *Current Opinion in Neurobiology*, *50*, 128–135. https://doi.org/10.1016/j.conb.2018.02.001

Delbeke, J., Pins, D., Michaux, G., Wanet-Defalque, M. C., Parrini, S., & Veraart, C. (2001). Electrical stimulation of anterior visual pathways in retinitis pigmentosa. *Investigative Ophthalmology & Visual Science*, *42*(1), 291–297.

Demene, C., Deffieux, T., Pernot, M., Osmanski, B.-F., Biran, V., Gennisson, J.-L., Sieu, L.-A., Bergel, A., Franqui, S., Correas, J.-M., Cohen, I., Baud, O., & Tanter, M. (2015). Spatiotemporal Clutter Filtering of Ultrafast Ultrasound Data Highly Increases Doppler and fUltrasound Sensitivity. *IEEE Transactions on Medical Imaging*, *34*(11), 2271–2285. https://doi.org/10.1109/TMI.2015.2428634

Demené, C., Robin, J., Dizeux, A., Heiles, B., Pernot, M., Tanter, M., & Perren, F. (2021). Transcranial ultrafast ultrasound localization microscopy of brain vasculature in patients. *Nature Biomedical Engineering*, *5*(3), 219–228. https://doi.org/10.1038/s41551-021-00697-x

Demuru, M., Kalitzin, S., Zweiphenning, W., Van Blooijs, D., Van'T Klooster, M., Van Eijsden, P., Leijten, F., Zijlmans, M., RESPect Group, Braun, K., Ferrier, C., Gebbink, T., Gosselaar, P., Huiskamp, G., Van Klink, N., Ophorst, J., Van Rijen, P., Van Der Salm, S., & Winter, A. V. (2020). The value of intra-operative electrographic biomarkers for tailoring during epilepsy surgery: From group-level to patient-level analysis. *Scientific Reports*, *10*(1), 14654. https://doi.org/10.1038/s41598-020-71359-2

Di Paolo, M., & Ghezzi, D. (2015). Inflammatory and morphological characterisation of a foreign body retinal response. *European Journal of Neurodegenerative Diseases*.

Di Russo, F., Martínez, A., Sereno, M. I., Pitzalis, S., & Hillyard, S. A. (2002). Cortical sources of the early components of the visual evoked potential: Cortical Sources of VEP. *Human Brain Mapping*, *15*(2), 95–111. https://doi.org/10.1002/hbm.10010

Djilas, M., Olès, C., Lorach, H., Bendali, A., Dégardin, J., Dubus, E., Lissorgues-Bazin, G., Rousseau, L., Benosman, R., Ieng, S.-H., Joucla, S., Yvert, B., Bergonzo, P., Sahel, J., & Picaud, S. (2011). Three-dimensional electrode arrays for retinal prostheses: Modeling, geometry optimization and experimental validation. *Journal of Neural Engineering*, *8*(4), 046020. https://doi.org/10.1088/1741-2560/8/4/046020

Dobelle, W. H., & Mladejovsky, M. G. (1974). Phosphenes produced by electrical stimulation of human occipital cortex, and their application to the development of a prosthesis for the blind. *The Journal of Physiology*, *243*(2), 553–576. https://doi.org/10.1113/jphysiol.1974.sp010766

Dobelle, W. H., Mladejovsky, M. G., Evans, J. R., Roberts, T. S., & Girvin, J. P. (1976). 'Braille' reading by a blind volunteer by visual cortex stimulation. *Nature*, *259*(5539), 111–112. https://doi.org/10.1038/259111a0

Dobelle, Wm. H. (2000). Artificial Vision for the Blind by Connecting a Television Camera to the Visual Cortex: *ASAIO Journal*, *46*(1), 3–9. https://doi.org/10.1097/00002480-200001000-00002

Donahue, M. J., Kaszas, A., Turi, G. F., Rózsa, B., Slézia, A., Vanzetta, I., Katona, G., Bernard, C., Malliaras, G. G., & Williamson, A. (2018). Multimodal Characterization of Neural Networks Using Highly Transparent Electrode Arrays. *Eneuro*, *5*(6), ENEURO.0187-18.2018. https://doi.org/10.1523/ENEURO.0187-18.2018

Dreier, J. P. (2011). The role of spreading depression, spreading depolarization and spreading ischemia in neurological disease. *Nature Medicine*, *17*(4), 439–447. https://doi.org/10.1038/nm.2333

Dreier, J. P., Major, S., Foreman, B., Winkler, M. K. L., Kang, E.-J., Milakara, D., Lemale, C. L., DiNapoli, V., Hinzman, J. M., Woitzik, J., Andaluz, N., Carlson, A., & Hartings, J. A. (2018). Terminal spreading depolarization and electrical silence in death of human cerebral cortex: Terminal SD. *Annals of Neurology*, *83*(2), 295–310. https://doi.org/10.1002/ana.25147

Ellis, E. M., Gauvain, G., Sivyer, B., & Murphy, G. J. (2016). Shared and distinct retinal input to the mouse superior colliculus and dorsal lateral geniculate nucleus. *Journal of Neurophysiology*, *116*(2), 602–610. https://doi.org/10.1152/jn.00227.2016

Engel, J., Wiebe, S., French, J., Sperling, M., Williamson, P., Spencer, D., Gumnit, R., Zahn, C., Westbrook, E., & Enos, B. (2003). Practice parameter: Temporal lobe and localized neocortical resections for epilepsy: Report of the Quality Standards Subcommittee of the American Academy of Neurology, in Association with the American Epilepsy Society and the American Association of Neurological Surgeons. *Neurology*, *60*(4), 538–547. https://doi.org/10.1212/01.WNL.0000055086.35806.2D

Evariste, L., Mottier, A., Lagier, L., Cadarsi, S., Barret, M., Sarrieu, C., Soula, B., Mouchet, F., Flahaut, E., Pinelli, E., & Gauthier, L. (2020). Assessment of graphene oxide ecotoxicity at several trophic levels using aquatic microcosms. *Carbon*, *156*, 261–271. https://doi.org/10.1016/j.carbon.2019.09.051

Faber, H., Bartz-Schmidt, K. U., Stett, A., Zrenner, E., & Stingl, K. (2020). Elektronische Netzhautimplantate – ein aufgegebener Traum? *Klinische Monatsblätter für Augenheilkunde*, *237*(03), 288–293. https://doi.org/10.1055/a-1021-5040

Fabricius, M., Fuhr, S., Willumsen, L., Dreier, J. P., Bhatia, R., Boutelle, M. G., Hartings, J. A., Bullock, R., Strong, A. J., & Lauritzen, M. (2008). Association of seizures with cortical spreading depression and peri-infarct depolarisations in the acutely injured human brain. *Clinical Neurophysiology*, *119*(9), 1973–1984. https://doi.org/10.1016/j.clinph.2008.05.025

Fadeel, B., Bussy, C., Merino, S., Vázquez, E., Flahaut, E., Mouchet, F., Evariste, L., Gauthier, L., Koivisto, A. J., Vogel, U., Martín, C., Delogu, L. G., Buerki-Thurnherr, T., Wick, P., Beloin-Saint-Pierre, D., Hischier, R., Pelin, M., Candotto Carniel, F., Tretiach, M., … Bianco, A. (2018). Safety Assessment of Graphene-Based Materials: Focus on Human Health and the Environment. *ACS Nano*, *12*(11), 10582–10620. https://doi.org/10.1021/acsnano.8b04758

Fallegger, F., Schiavone, G., Pirondini, E., Wagner, F. B., Vachicouras, N., Serex, L., Zegarek, G., May, A., Constanthin, P., Palma, M., Khoshnevis, M., Van Roost, D., Yvert, B., Courtine, G., Schaller, K., Bloch, J., & Lacour, S. P. (2021). MRI-Compatible and Conformal Electrocorticography Grids for Translational Research. *Advanced Science*, *8*(9), 2003761. https://doi.org/10.1002/advs.202003761

Fan, B., Rusinek, C. A., Thompson, C. H., Setien, M., Guo, Y., Rechenberg, R., Gong, Y., Weber, A. J., Becker, M. F., Purcell, E., & Li, W. (2020). Flexible, diamond-based microelectrodes fabricated using the diamond growth side for neural sensing. *Microsystems & Nanoengineering*, *6*(1), 42. https://doi.org/10.1038/s41378-020-0155-1

Fariss, R. N., Li, Z.-Y., & Milam, A. H. (2000). Abnormalities in rod photoreceptors, amacrine cells, and horizontal cells in human retinas with retinitis pigmentosa. *American Journal of Ophthalmology*, *129*(2), 215–223. https://doi.org/10.1016/S0002-9394(99)00401-8

Faulkner, L. L., & Bard, A. J. (2001). *Electrochemical methods and applications* (2nd ed). Wiley.

Fernández, E., Alfaro, A., Soto-Sánchez, C., Gonzalez-Lopez, P., Lozano, A. M., Peña, S., Grima, M. D., Rodil, A., Gómez, B., Chen, X., Roelfsema, P. R., Rolston, J. D., Davis, T. S., & Normann, R. A. (2021). Visual percepts evoked with an intracortical 96-channel microelectrode array inserted in human occipital cortex. *Journal of Clinical Investigation*, *131*(23), e151331. https://doi.org/10.1172/JCI151331

Fisher, R. S., Acevedo, C., Arzimanoglou, A., Bogacz, A., Cross, J. H., Elger, C. E., Engel, J., Forsgren, L., French, J. A., Glynn, M., Hesdorffer, D. C., Lee, B. I., Mathern, G. W., Moshé, S. L., Perucca, E., Scheffer, I. E., Tomson, T., Watanabe, M., & Wiebe, S. (2014). ILAE Official Report: A practical clinical definition of epilepsy. *Epilepsia*, *55*(4), 475–482. https://doi.org/10.1111/epi.12550

Flesher, S. N., Downey, J. E., Weiss, J. M., Hughes, C. L., Herrera, A. J., Tyler-Kabara, E. C., Boninger, M. L., Collinger, J. L., & Gaunt, R. A. (2021). A brain-computer interface that evokes tactile sensations improves robotic arm control. *Science*, *372*(6544), 831–836. https://doi.org/10.1126/science.abd0380

Flores, T., Huang, T., Bhuckory, M., Ho, E., Chen, Z., Dalal, R., Galambos, L., Kamins, T., Mathieson, K., & Palanker, D. (2019). Honeycomb-shaped electro-neural interface enables cellular-scale pixels in subretinal prosthesis. *Scientific Reports*, *9*(1), 10657. https://doi.org/10.1038/s41598-019-47082-y

Flores, T., Lei, X., Huang, T., Lorach, H., Dalal, R., Galambos, L., Kamins, T., Mathieson, K., & Palanker, D. (2018). Optimization of pillar electrodes in subretinal prosthesis for enhanced proximity to target neurons. *Journal of Neural Engineering*, *15*(3), 036011. https://doi.org/10.1088/1741-2552/aaac39

Franck, G., Sadzot, B., Salmon, E., Maquet, P., Peter, J., Quaglia, L., Delfiore, G., & Lamotte, D. (1986). Etude chez l'homme, par tomographie a emission de positons, du metabolisme et du debit sanguin cerebral dans les epilepsies partielles complexes et dans differents etats de mal. *Revue D&'apos;Electroencéphalographie et de Neurophysiologie Clinique*, *16*(3), 199–216. https://doi.org/10.1016/S0370-4475(86)80048-X

Frederick, R. A., Shih, E., Towle, V. L., Joshi-Imre, A., Troyk, P. R., & Cogan, S. F. (2022). Chronic stability of activated iridium oxide film voltage transients from wireless floating microelectrode arrays. *Frontiers in Neuroscience*, *16*, 876032. https://doi.org/10.3389/fnins.2022.876032

Freeman, D. K., Eddington, D. K., Rizzo, J. F., & Fried, S. I. (2010). Selective Activation of Neuronal Targets With Sinusoidal Electric Stimulation. *Journal of Neurophysiology*, *104*(5), 2778–2791. https://doi.org/10.1152/jn.00551.2010

Freeman, D. K., & Fried, S. I. (2011). Multiple components of ganglion cell desensitization in response to prosthetic stimulation. *Journal of Neural Engineering*, *8*(1), 016008. https://doi.org/10.1088/1741-2560/8/1/016008

Fried, S. I., Hsueh, H. A., & Werblin, F. S. (2006). A method for generating precise temporal patterns of retinal spiking using prosthetic stimulation. *Journal of Neurophysiology*, *95*(2), 970–978. https://doi.org/10.1152/jn.00849.2005

Friston, K. J. (2007). *Statistical parametric mapping: The analysis of functional brain images* (1st ed). Elsevier / Academic Press.

Fritsch, G., & Hitzig, E. (2009). Electric excitability of the cerebrum (Über die elektrische Erregbarkeit des Grosshirns). *Epilepsy & Behavior*, *15*(2), 123–130. https://doi.org/10.1016/j.yebeh.2009.03.001
Garrett, D. J., Ganesan, K., Stacey, A., Fox, K., Meffin, H., & Prawer, S. (2011). Ultra-nanocrystalline diamond electrodes: Optimization towards neural stimulation applications. *Journal of Neural Engineering*, *9*(1), 016002. https://doi.org/10.1088/1741-2560/9/1/016002
Garrett, D. J., Saunders, A. L., McGowan, C., Specks, J., Ganesan, K., Meffin, H., Williams, R. A., & Nayagam, D. A. X. (2016). *In vivo* biocompatibility of boron doped and nitrogen included conductive-diamond for use in medical implants. *Journal of Biomedical Materials Research Part B: Applied Biomaterials*, *104*(1), 19–26. https://doi.org/10.1002/jbm.b.33331
Garrett, D. J., Tong, W., Simpson, D. A., & Meffin, H. (2016). Diamond for neural interfacing: A review. *Carbon*, *102*, 437–454. https://doi.org/10.1016/j.carbon.2016.02.059
Geim, A. K., & Novoselov, K. S. (2007). The rise of graphene. *Nature Materials*, *6*(3), 183–191. https://doi.org/10.1038/nmat1849
Gesnik, M., Blaize, K., Deffieux, T., Gennisson, J.-L., Sahel, J.-A., Fink, M., Picaud, S., & Tanter, M. (2017). 3D functional ultrasound imaging of the cerebral visual system in rodents. *NeuroImage*, *149*, 267–274. https://doi.org/10.1016/j.neuroimage.2017.01.071
Goetz, G. A., & Palanker, D. V. (2016). Electronic approaches to restoration of sight. *Reports on Progress in Physics*, *79*(9), 096701. https://doi.org/10.1088/0034-4885/79/9/096701
Golda-Cepa, M., Engvall, K., Hakkarainen, M., & Kotarba, A. (2020). Recent progress on parylene C polymer for biomedical applications: A review. *Progress in Organic Coatings*, *140*, 105493. https://doi.org/10.1016/j.porgcoat.2019.105493
Gong, C.-S., Syu, W.-J., Lei, K., & Hwang, Y.-S. (2016). Development of a Flexible Non-Metal Electrode for Cell Stimulation and Recording. *Sensors*, *16*(10), 1613. https://doi.org/10.3390/s16101613
Grani, F., Soto-Sanchez, C., Farfan, F. D., Alfaro, A., Grima, M. D., Rodil Doblado, A., & Fernández, E. (2022). Time stability and connectivity analysis with an intracortical 96-channel microelectrode array inserted in human visual cortex. *Journal of Neural Engineering*, *19*(4), 045001. https://doi.org/10.1088/1741-2552/ac801d
Hadjinicolaou, A. E., Leung, R. T., Garrett, D. J., Ganesan, K., Fox, K., Nayagam, D. A. X., Shivdasani, M. N., Meffin, H., Ibbotson, M. R., Prawer, S., & O'Brien, B. J. (2012). Electrical stimulation of retinal ganglion cells with diamond and the development of an all diamond retinal prosthesis. *Biomaterials*, *33*(24), 5812–5820. https://doi.org/10.1016/j.biomaterials.2012.04.063
Hassler, C., Von Metzen, R. P., Ruther, P., & Stieglitz, T. (2010). Characterization of parylene C as an encapsulation material for implanted neural prostheses. *Journal of Biomedical Materials Research Part B: Applied Biomaterials*, *9999B*, NA-NA. https://doi.org/10.1002/jbm.b.31584
Hébert, C., Cottance, M., Degardin, J., Scorsone, E., Rousseau, L., Lissorgues, G., Bergonzo, P., & Picaud, S. (2016). Monitoring the evolution of boron doped porous diamond electrode on flexible retinal implant by OCT and in vivo impedance spectroscopy. *Materials Science and Engineering: C*, *69*, 77–84. https://doi.org/10.1016/j.msec.2016.06.032
Hébert, C., Masvidal-Codina, E., Suarez-Perez, A., Calia, A. B., Piret, G., Garcia-Cortadella, R., Illa, X., Del Corro Garcia, E., De La Cruz Sanchez, J. M., Casals, D. V., Prats-Alfonso, E., Bousquet, J., Godignon, P., Yvert, B., Villa, R., Sanchez-Vives, M. V., Guimerà-Brunet, A., & Garrido, J. A. (2018). Flexible Graphene Solution-Gated Field-Effect Transistors: Efficient Transducers for Micro-Electrocorticography. *Advanced Functional Materials*, *28*(12), 1703976. https://doi.org/10.1002/adfm.201703976
Hébert, C., Mazellier, J. P., Scorsone, E., Mermoux, M., & Bergonzo, P. (2014). Boosting the electrochemical properties of diamond electrodes using carbon nanotube scaffolds. *Carbon*, *71*, 27–33. https://doi.org/10.1016/j.carbon.2013.12.083
Hess, L. H., Seifert, M., & Garrido, J. A. (2013). Graphene Transistors for Bioelectronics. *Proceedings of the IEEE*, *101*(7), 1780–1792. https://doi.org/10.1109/JPROC.2013.2261031
Ho, E., Lei, X., Flores, T., Lorach, H., Huang, T., Galambos, L., Kamins, T., Harris, J., Mathieson, K., & Palanker, D. (2019). Characteristics of prosthetic vision in rats with subretinal flat and pillar electrode arrays. *Journal of Neural Engineering*, *16*(6), 066027. https://doi.org/10.1088/1741-2552/ab34b3
Ho, E., Smith, R., Goetz, G., Lei, X., Galambos, L., Kamins, T. I., Harris, J., Mathieson, K., Palanker, D., & Sher, A. (2018). Spatiotemporal characteristics of retinal response to network-mediated photovoltaic stimulation. *Journal of Neurophysiology*, *119*(2), 389–400. https://doi.org/10.1152/jn.00872.2016
Huang, X., Zeng, Z., Fan, Z., Liu, J., & Zhang, H. (2012). Graphene-Based Electrodes. *Advanced Materials*, *24*(45), 5979–6004. https://doi.org/10.1002/adma.201201587
Hubel, D. H. (1957). Tungsten Microelectrode for Recording from Single Units. *Science*, *125*(3247), 549–550. https://doi.org/10.1126/science.125.3247.549
Humayun, M. S., Dorn, J. D., da Cruz, L., Dagnelie, G., Sahel, J.-A., Stanga, P. E., Cideciyan, A. V., Duncan, J. L., Eliott, D., Filley, E., Ho, A. C., Santos, A., Safran, A. B., Arditi, A., Del Priore, L. V., Greenberg, R. J., & Argus II Study Group. (2012). Interim results from the international trial of Second Sight's visual prosthesis. *Ophthalmology*, *119*(4), 779–788. https://doi.org/10.1016/j.ophtha.2011.09.028
Humayun, M. S., Prince, M., de Juan, E., Barron, Y., Moskowitz, M., Klock, I. B., & Milam, A. H. (1999). Morphometric analysis of the extramacular retina from postmortem eyes with retinitis pigmentosa. *Investigative Ophthalmology & Visual Science*, *40*(1), 143–148.
Humayun, M. S., Weiland, J. D., Fujii, G. Y., Greenberg, R., Williamson, R., Little, J., Mech, B., Cimmarusti, V., Van Boemel, G., Dagnelie, G., & de Juan, E. (2003). Visual perception in a blind subject with a chronic

microelectronic retinal prosthesis. *Vision Research*, *43*(24), 2573–2581. https://doi.org/10.1016/s0042-6989(03)00457-7
Hummers, W. S., & Offeman, R. E. (1958). Preparation of Graphitic Oxide. *Journal of the American Chemical Society*, *80*(6), 1339–1339. https://doi.org/10.1021/ja01539a017
Iadecola, C. (2017). The Neurovascular Unit Coming of Age: A Journey through Neurovascular Coupling in Health and Disease. *Neuron*, *96*(1), 17–42. https://doi.org/10.1016/j.neuron.2017.07.030
Ikeda, A. (1999). Focal ictal direct current shifts in humanepilepsy as studied by subdural and scalp recording. *Brain*, *122*(5), 827–838. https://doi.org/10.1093/brain/122.5.827
Imbault, M., Chauvet, D., Gennisson, J.-L., Capelle, L., & Tanter, M. (2017). Intraoperative Functional Ultrasound Imaging of Human Brain Activity. *Scientific Reports*, *7*(1), 7304. https://doi.org/10.1038/s41598-017-06474-8
Jarosiewicz, B., & Morrell, M. (2021). The RNS System: Brain-responsive neurostimulation for the treatment of epilepsy. *Expert Review of Medical Devices*, *18*(2), 129–138. https://doi.org/10.1080/17434440.2019.1683445
Jensen, R. J., & Rizzo, J. F. (2007). Responses of ganglion cells to repetitive electrical stimulation of the retina. *Journal of Neural Engineering*, *4*(1), S1–S6. https://doi.org/10.1088/1741-2560/4/1/S01
Jensen, R. J., Ziv, O. R., & Rizzo, J. F. (2005). Responses of rabbit retinal ganglion cells to electrical stimulation with an epiretinal electrode. *Journal of Neural Engineering*, *2*(1), S16-21. https://doi.org/10.1088/1741-2560/2/1/003
Jinno, S., Fleischer, F., Eckel, S., Schmidt, V., & Kosaka, T. (2007). Spatial arrangement of microglia in the mouse hippocampus: A stereological study in comparison with astrocytes. *Glia*, *55*(13), 1334–1347. https://doi.org/10.1002/glia.20552
Joucla, S., & Yvert, B. (2012). Modeling extracellular electrical neural stimulation: From basic understanding to MEA-based applications. *Journal of Physiology-Paris*, *106*(3–4), 146–158. https://doi.org/10.1016/j.jphysparis.2011.10.003
Khodagholy, D., Gelinas, J. N., Thesen, T., Doyle, W., Devinsky, O., Malliaras, G. G., & Buzsáki, G. (2015). NeuroGrid: Recording action potentials from the surface of the brain. *Nature Neuroscience*, *18*(2), 310–315. https://doi.org/10.1038/nn.3905
Kiew, S. F., Kiew, L. V., Lee, H. B., Imae, T., & Chung, L. Y. (2016). Assessing biocompatibility of graphene oxide-based nanocarriers: A review. *Journal of Controlled Release*, *226*, 217–228. https://doi.org/10.1016/j.jconrel.2016.02.015
Kigure, C., Naganuma, H., Sasaki, Y., Kino, H., Tomita, H., & Tanaka, T. (2013). Fabrication and In vivo Evaluation of Poly(3,4-ethylenedioxythiophene) Stimulus Electrodes for Fully Implantable Retinal Prosthesis. *Japanese Journal of Applied Physics*, *52*(4S), 04CL03. https://doi.org/10.7567/JJAP.52.04CL03
Kim, S. Y., Sadda, S., Humayun, M. S., De Juan, E., Melia, B. M., & Green, W. R. (2002). MORPHOMETRIC ANALYSIS OF THE MACULA IN EYES WITH GEOGRAPHIC ATROPHY DUE TO AGE-RELATED MACULAR DEGENERATION: *Retina*, *22*(4), 464–470. https://doi.org/10.1097/00006982-200208000-00011
Kozai, T. D. Y., Jaquins-Gerstl, A. S., Vazquez, A. L., Michael, A. C., & Cui, X. T. (2015). Brain Tissue Responses to Neural Implants Impact Signal Sensitivity and Intervention Strategies. *ACS Chemical Neuroscience*, *6*(1), 48–67. https://doi.org/10.1021/cn500256e
Kramer, D. R., Fujii, T., Ohiorhenuan, I., & Liu, C. Y. (2017). Interplay between Cortical Spreading Depolarization and Seizures. *Stereotactic and Functional Neurosurgery*, *95*(1), 1–5. https://doi.org/10.1159/000452841
Krętowski, R., Jabłońska-Trypuć, A., & Cechowska-Pasko, M. (2021). The Preliminary Study on the Proapoptotic Effect of Reduced Graphene Oxide in Breast Cancer Cell Lines. *International Journal of Molecular Sciences*, *22*(22), 12593. https://doi.org/10.3390/ijms222212593
Kumar, C. V., & Pattammattel, A. (2017). Discovery of graphene and beyond. In *Introduction to Graphene* (pp. 1–15). Elsevier. https://doi.org/10.1016/B978-0-12-813182-4.00001-5
Kwak, Y. H., Choi, D. S., Kim, Y. N., Kim, H., Yoon, D. H., Ahn, S.-S., Yang, J.-W., Yang, W. S., & Seo, S. (2012). Flexible glucose sensor using CVD-grown graphene-based field effect transistor. *Biosensors and Bioelectronics*, *37*(1), 82–87. https://doi.org/10.1016/j.bios.2012.04.042
Lacour, S. P., Benmerah, S., Tarte, E., FitzGerald, J., Serra, J., McMahon, S., Fawcett, J., Graudejus, O., Yu, Z., & Morrison, B. (2010). Flexible and stretchable micro-electrodes for in vitro and in vivo neural interfaces. *Medical & Biological Engineering & Computing*, *48*(10), 945–954. https://doi.org/10.1007/s11517-010-0644-8
Lancelot, S., & Zimmer, L. (2010). Small-animal positron emission tomography as a tool for neuropharmacology. *Trends in Pharmacological Sciences*, *31*(9), 411–417. https://doi.org/10.1016/j.tips.2010.06.002
Lauritzen, M., & Henrik Diemer, N. (1986). Uncoupling of cerebral blood flow and metabolism after single episode of cortical spreading depression in the rat brain. *Brain Research*, *370*(2), 405–408. https://doi.org/10.1016/0006-8993(86)90504-4
Lauritzen, M., Jøsrgensen, M. B., Diemer, N. H., Gjedde, A., & Hansen, A. J. (1982). Persistent oligemia of rat cerebral cortex in the wake of spreading depression: Oligemia after Spreading Depression. *Annals of Neurology*, *12*(5), 469–474. https://doi.org/10.1002/ana.410120510
Leao, A. A. P. (1944). SPREADING DEPRESSION OF ACTIVITY IN THE CEREBRAL CORTEX. *Journal of Neurophysiology*, *7*(6), 359–390. https://doi.org/10.1152/jn.1944.7.6.359
Lee, K. Y., Moon, H., Kim, B., Kang, Y. N., Jang, J., Choe, H. K., & Kim, S. (2020). Development of a Polydimethylsiloxane-Based Electrode Array for Electrocorticography. *Advanced Materials Interfaces*, *7*(24), 2001152. https://doi.org/10.1002/admi.202001152

Lee, M., Lee, S., Kim, J., Lim, J., Lee, J., Masri, S., Bao, S., Yang, S., Ahn, J.-H., & Yang, S. (2021). Graphene-electrode array for brain map remodeling of the cortical surface. *NPG Asia Materials*, *13*(1), 65. https://doi.org/10.1038/s41427-021-00334-8

Lewis, P. M., Ackland, H. M., Lowery, A. J., & Rosenfeld, J. V. (2015). Restoration of vision in blind individuals using bionic devices: A review with a focus on cortical visual prostheses. *Brain Research*, *1595*, 51–73. https://doi.org/10.1016/j.brainres.2014.11.020

Li, C., Narayan, R. K., Wu, P.-M., Rajan, N., Wu, Z., Mehan, N., Golanov, E. V., Ahn, C. H., & Hartings, J. A. (2016). Evaluation of microelectrode materials for direct-current electrocorticography. *Journal of Neural Engineering*, *13*(1), 016008. https://doi.org/10.1088/1741-2560/13/1/016008

Lim, J., Lee, S., Kim, J., Hong, J., Lim, S., Kim, K., Kim, J., Yang, S., Yang, S., & Ahn, J.-H. (2023). Hybrid graphene electrode for the diagnosis and treatment of epilepsy in free-moving animal models. *NPG Asia Materials*, *15*(1), 7. https://doi.org/10.1038/s41427-023-00464-1

Linderholm, P., Guyomard, J.-L., Djilas, M., Salzmann, J., Simonutti, M., Sahel, J. A., Safran, A. B., Renaud, P., & Picaud, S. (2013). Long-Term *in vivo* Impedance Changes of Subretinal Microelectrodes Implanted in Dystrophic P23H Rats. *The International Journal of Artificial Organs*, *36*(9), 612–619. https://doi.org/10.5301/ijao.5000213

Logothetis, N. K. (2008). What we can do and what we cannot do with fMRI. *Nature*, *453*(7197), 869–878. https://doi.org/10.1038/nature06976

Lohmann, T. K., Haiss, F., Schaffrath, K., Schnitzler, A.-C., Waschkowski, F., Barz, C., Van Der Meer, A.-M., Werner, C., Johnen, S., Laube, T., Bornfeld, N., Mazinani, B. E., Rößler, G., Mokwa, W., & Walter, P. (2019). The very large electrode array for retinal stimulation (VLARS)—A concept study. *Journal of Neural Engineering*, *16*(6), 066031. https://doi.org/10.1088/1741-2552/ab4113

Lorach, H., Galvez, A., Spagnolo, V., Martel, F., Karakas, S., Intering, N., Vat, M., Faivre, O., Harte, C., Komi, S., Ravier, J., Collin, T., Coquoz, L., Sakr, I., Baaklini, E., Hernandez-Charpak, S. D., Dumont, G., Buschman, R., Buse, N., … Courtine, G. (2023). Walking naturally after spinal cord injury using a brain–spine interface. *Nature*. https://doi.org/10.1038/s41586-023-06094-5

Lorach, H., Goetz, G., Mandel, Y., Lei, X., Kamins, T. I., Mathieson, K., Huie, P., Dalal, R., Harris, J. S., & Palanker, D. (2015). Performance of photovoltaic arrays in-vivo and characteristics of prosthetic vision in animals with retinal degeneration. *Vision Research*, *111*, 142–148. https://doi.org/10.1016/j.visres.2014.09.007

Lorach, H., Marre, O., Sahel, J.-A., Benosman, R., & Picaud, S. (2013). Neural stimulation for visual rehabilitation: Advances and challenges. *Journal of Physiology-Paris*, *107*(5), 421–431. https://doi.org/10.1016/j.jphysparis.2012.10.003

Loudin, J. D., Simanovskii, D. M., Vijayraghavan, K., Sramek, C. K., Butterwick, A. F., Huie, P., McLean, G. Y., & Palanker, D. V. (2007). Optoelectronic retinal prosthesis: System design and performance. *Journal of Neural Engineering*, *4*(1), S72–S84. https://doi.org/10.1088/1741-2560/4/1/S09

Löwenstein, K., & Borchardt, M. (1918). Symptomatologie und elektrische Reizung bei einer Schußverletzung des Hinterhauptlappens. *Deutsche Zeitschrift für Nervenheilkunde*, *58*(3–6), 264–292. https://doi.org/10.1007/BF01629694

Luo, Y. H.-L., & Da Cruz, L. (2016). The Argus® II Retinal Prosthesis System. *Progress in Retinal and Eye Research*, *50*, 89–107. https://doi.org/10.1016/j.preteyeres.2015.09.003

Macé, E., Montaldo, G., Cohen, I., Baulac, M., Fink, M., & Tanter, M. (2011). Functional ultrasound imaging of the brain. *Nature Methods*, *8*(8), Article 8. https://doi.org/10.1038/nmeth.1641

Mace, E., Montaldo, G., Osmanski, B.-F., Cohen, I., Fink, M., & Tanter, M. (2013). Functional ultrasound imaging of the brain: Theory and basic principles. *IEEE Transactions on Ultrasonics, Ferroelectrics and Frequency Control*, *60*(3), 492–506. https://doi.org/10.1109/TUFFC.2013.2592

Marc, R. E., Jones, B. W., Watt, C. B., & Strettoi, E. (2003). Neural remodeling in retinal degeneration. *Progress in Retinal and Eye Research*, *22*(5), 607–655. https://doi.org/10.1016/S1350-9462(03)00039-9

Masvidal-Codina, E., Illa, X., Dasilva, M., Calia, A. B., Dragojević, T., Vidal-Rosas, E. E., Prats-Alfonso, E., Martínez-Aguilar, J., De La Cruz, J. M., Garcia-Cortadella, R., Godignon, P., Rius, G., Camassa, A., Del Corro, E., Bousquet, J., Hébert, C., Durduran, T., Villa, R., Sanchez-Vives, M. V., … Guimerà-Brunet, A. (2019). High-resolution mapping of infraslow cortical brain activity enabled by graphene microtransistors. *Nature Materials*, *18*(3), 280–288. https://doi.org/10.1038/s41563-018-0249-4

Masvidal-Codina, E., Smith, T. M., Rathore, D., Gao, Y., Illa, X., Prats-Alfonso, E., Corro, E. D., Calia, A. B., Rius, G., Martin-Fernandez, I., Guger, C., Reitner, P., Villa, R., Garrido, J. A., Guimerà-Brunet, A., & Wykes, R. C. (2021). Characterization of optogenetically-induced cortical spreading depression in awake mice using graphene micro-transistor arrays. *Journal of Neural Engineering*, *18*(5), 055002. https://doi.org/10.1088/1741-2552/abecf3

Mathieson, K., Loudin, J., Goetz, G., Huie, P., Wang, L., Kamins, T. I., Galambos, L., Smith, R., Harris, J. S., Sher, A., & Palanker, D. (2012). Photovoltaic retinal prosthesis with high pixel density. *Nature Photonics*, *6*(6), 391–397. https://doi.org/10.1038/nphoton.2012.104

Matteucci, P. B., Barriga-Rivera, A., Eiber, C. D., Lovell, N. H., Morley, J. W., & Suaning, G. J. (2016). The Effect of Electric Cross-Talk in Retinal Neurostimulation. *Investigative Opthalmology & Visual Science*, *57*(3), 1031. https://doi.org/10.1167/iovs.15-18400

Maya-Vetencourt, J. F., Ghezzi, D., Antognazza, M. R., Colombo, E., Mete, M., Feyen, P., Desii, A., Buschiazzo, A., Di Paolo, M., Di Marco, S., Ticconi, F., Emionite, L., Shmal, D., Marini, C., Donelli, I., Freddi, G., Maccarone,

R., Bisti, S., Sambuceti, G., … Benfenati, F. (2017). A fully organic retinal prosthesis restores vision in a rat model of degenerative blindness. *Nature Materials*, *16*(6), 681–689. https://doi.org/10.1038/nmat4874
Mayevsky, A., Doron, A., Manor, T., Meilin, S., Zarchin, N., & Ouaknine, G. E. (1996). Cortical spreading depression recorded from the human brain using a multiparametric monitoring system. *Brain Research*, *740*(1–2), 268–274. https://doi.org/10.1016/S0006-8993(96)00874-8
Medeiros, N. E., & Curcio, C. A. (2001). Preservation of ganglion cell layer neurons in age-related macular degeneration. *Investigative Ophthalmology & Visual Science*, *42*(3), 795–803.
Merrill, D. R., Bikson, M., & Jefferys, J. G. R. (2005). Electrical stimulation of excitable tissue: Design of efficacious and safe protocols. *Journal of Neuroscience Methods*, *141*(2), 171–198. https://doi.org/10.1016/j.jneumeth.2004.10.020
Milek, J. T. (1971). Silicon Nitride-Silicon Dioxide Combinations. In J. T. Milek, *Silicon Nitride for Microelectronic Applications* (pp. 100–118). Springer US. https://doi.org/10.1007/978-1-4684-6162-6_4
Mishra, A. M., Ellens, D. J., Schridde, U., Motelow, J. E., Purcaro, M. J., DeSalvo, M. N., Enev, M., Sanganahalli, B. G., Hyder, F., & Blumenfeld, H. (2011). Where fMRI and Electrophysiology Agree to Disagree: Corticothalamic and Striatal Activity Patterns in the WAG/Rij Rat. *The Journal of Neuroscience*, *31*(42), 15053–15064. https://doi.org/10.1523/JNEUROSCI.0101-11.2011
Mody, I., Lambert, J. D., & Heinemann, U. (1987). Low extracellular magnesium induces epileptiform activity and spreading depression in rat hippocampal slices. *Journal of Neurophysiology*, *57*(3), 869–888. https://doi.org/10.1152/jn.1987.57.3.869
Montaldo, G., Tanter, M., Bercoff, J., Benech, N., & Fink, M. (2009). Coherent plane-wave compounding for very high frame rate ultrasonography and transient elastography. *IEEE Transactions on Ultrasonics, Ferroelectrics and Frequency Control*, *56*(3), 489–506. https://doi.org/10.1109/TUFFC.2009.1067
Muqit, M. M. K., Velikay-Parel, M., Weber, M., Dupeyron, G., Audemard, D., Corcostegui, B., Sahel, J., & Le Mer, Y. (2019). Six-Month Safety and Efficacy of the Intelligent Retinal Implant System II Device in Retinitis Pigmentosa. *Ophthalmology*, *126*(4), 637–639. https://doi.org/10.1016/j.ophtha.2018.11.010
Musk, E. & Neuralink. (2019). An Integrated Brain-Machine Interface Platform With Thousands of Channels. *Journal of Medical Internet Research*, *21*(10), e16194. https://doi.org/10.2196/16194
Nabaei, V., Panuccio, G., & Heidari, H. (2020). Neural Microprobe Device Modelling for Implant Micromotions Failure Mitigation. *2020 IEEE International Symposium on Circuits and Systems (ISCAS)*, 1–5. https://doi.org/10.1109/ISCAS45731.2020.9180497
Nasretdinov, A., Lotfullina, N., Vinokurova, D., Lebedeva, J., Burkhanova, G., Chernova, K., Zakharov, A., & Khazipov, R. (2017). Direct Current Coupled Recordings of Cortical Spreading Depression Using Silicone Probes. *Frontiers in Cellular Neuroscience*, *11*, 408. https://doi.org/10.3389/fncel.2017.00408
Nathaniel, E. J. H., & Nathaniel, D. R. (1981). The Reactive Astrocyte. In *Advances in Cellular Neurobiology* (Vol. 2, pp. 249–301). Elsevier. https://doi.org/10.1016/B978-0-12-008302-2.50012-2
Nebel, C. E., Rezek, B., Shin, D., Uetsuka, H., & Yang, N. (2007). Diamond for bio-sensor applications. *Journal of Physics D: Applied Physics*, *40*(20), 6443–6466. https://doi.org/10.1088/0022-3727/40/20/S21
Negi, S., Bhandari, R., Rieth, L., & Solzbacher, F. (2010). *In vitro* comparison of sputtered iridium oxide and platinum-coated neural implantable microelectrode arrays. *Biomedical Materials*, *5*(1), 015007. https://doi.org/10.1088/1748-6041/5/1/015007
Nemes-Baran, A. D., & DeSilva, T. M. (2021). Quantification of microglial contact and engulfment of oligodendrocyte progenitor cells in the rodent brain. *STAR Protocols*, *2*(2), 100403. https://doi.org/10.1016/j.xpro.2021.100403
Nguyen, D., Valet, M., Dégardin, J., Boucherit, L., Illa, X., De La Cruz, J., Del Corro, E., Bousquet, J., Garrido, J. A., Hébert, C., & Picaud, S. (2021). Novel Graphene Electrode for Retinal Implants: An in vivo Biocompatibility Study. *Frontiers in Neuroscience*, *15*, 615256. https://doi.org/10.3389/fnins.2021.615256
Nguyen, D., Valet, M., Dégardin, J., Boucherit, L., Illa, X., de la Cruz, J., del Corro, E., Bousquet, J., Garrido, J. A., Hébert, C., & Picaud, S. (2021). Novel Graphene Electrode for Retinal Implants: An in vivo Biocompatibility Study. *Frontiers in Neuroscience*, *15*, 615256. https://doi.org/10.3389/fnins.2021.615256
Nimmerjahn, A., Kirchhoff, F., & Helmchen, F. (2005). Resting Microglial Cells Are Highly Dynamic Surveillants of Brain Parenchyma in Vivo. *Science*, *308*(5726), 1314–1318. https://doi.org/10.1126/science.1110647
Noailles, A., Fernández-Sánchez, L., Lax, P., & Cuenca, N. (2014). Microglia activation in a model of retinal degeneration and TUDCA neuroprotective effects. *Journal of Neuroinflammation*, *11*(1), 186. https://doi.org/10.1186/s12974-014-0186-3
Noailles, A., Maneu, V., Campello, L., Gómez-Vicente, V., Lax, P., & Cuenca, N. (2016). Persistent inflammatory state after photoreceptor loss in an animal model of retinal degeneration. *Scientific Reports*, *6*(1), 33356. https://doi.org/10.1038/srep33356
Novoselov, K. S., Geim, A. K., Morozov, S. V., Jiang, D., Zhang, Y., Dubonos, S. V., Grigorieva, I. V., & Firsov, A. A. (2004). Electric Field Effect in Atomically Thin Carbon Films. *Science*, *306*(5696), 666–669. https://doi.org/10.1126/science.1102896
Nune, G., Arcot Desai, S., Razavi, B., Agostini, M. A., Bergey, G. K., Herekar, A. A., Hirsch, L. J., Lee, R. W., Rutecki, P. A., Srinivasan, S., Van Ness, P. C., Tcheng, T. K., & Morrell, M. J. (2019). Treatment of drug-resistant epilepsy in patients with periventricular nodular heterotopia using RNS® System: Efficacy and description of chronic electrophysiological recordings. *Clinical Neurophysiology*, *130*(8), 1196–1207. https://doi.org/10.1016/j.clinph.2019.04.706
Ochoa, M., Wei, P., Wolley, A. J., Otto, K. J., & Ziaie, B. (2013). A hybrid PDMS-Parylene subdural multi-electrode array. *Biomedical Microdevices*, *15*(3), 437–443. https://doi.org/10.1007/s10544-013-9743-2

Odom, J. V., Bach, M., Brigell, M., Holder, G. E., McCulloch, D. L., Mizota, A., Tormene, A. P., & International Society for Clinical Electrophysiology of Vision. (2016). ISCEV standard for clinical visual evoked potentials: (2016 update). *Documenta Ophthalmologica*, *133*(1), 1–9. https://doi.org/10.1007/s10633-016-9553-y

Offenhäusser, A., Sprössler, C., Matsuzawa, M., & Knoll, W. (1997). Field-effect transistor array for monitoring electrical activity from mammalian neurons in culture. *Biosensors and Bioelectronics*, *12*(8), 819–826. https://doi.org/10.1016/S0956-5663(97)00047-X

Paknahad, J., Kosta, P., Bouteiller, J.-M. C., Humayun, M. S., & Lazzi, G. (2021). Mechanisms underlying activation of retinal bipolar cells through targeted electrical stimulation: A computational study. *Journal of Neural Engineering*, *18*(6), 066034. https://doi.org/10.1088/1741-2552/ac3dd8

Palanker, D., Le Mer, Y., Mohand-Said, S., Muqit, M., & Sahel, J. A. (2020). Photovoltaic Restoration of Central Vision in Atrophic Age-Related Macular Degeneration. *Ophthalmology*, *127*(8), 1097–1104. https://doi.org/10.1016/j.ophtha.2020.02.024

Palanker, D., Le Mer, Y., Mohand-Said, S., & Sahel, J. A. (2022). Simultaneous perception of prosthetic and natural vision in AMD patients. *Nature Communications*, *13*(1), 513. https://doi.org/10.1038/s41467-022-28125-x

Palanker, D., Vankov, A., Huie, P., & Baccus, S. (2005). Design of a high-resolution optoelectronic retinal prosthesis. *Journal of Neural Engineering*, *2*(1), S105–S120. https://doi.org/10.1088/1741-2560/2/1/012

Panetsos, F., Sanchez-Jimenez, A., Cerio, E. D., Diaz-Guemes, I., & Sanchez, F. M. (2011). Consistent Phosphenes Generated by Electrical Microstimulation of the Visual Thalamus. An Experimental Approach for Thalamic Visual Neuroprostheses. *Frontiers in Neuroscience*, *5*. https://doi.org/10.3389/fnins.2011.00084

Pellegrino, G., Hedrich, T., Chowdhury, R., Hall, J. A., Lina, J.-M., Dubeau, F., Kobayashi, E., & Grova, C. (2016). Source localization of the seizure onset zone from ictal EEG/MEG data: wMEM for Ictal Source Imaging. *Human Brain Mapping*, *37*(7), 2528–2546. https://doi.org/10.1002/hbm.23191

Petoe, M. A., Titchener, S. A., Kolic, M., Kentler, W. G., Abbott, C. J., Nayagam, D. A. X., Baglin, E. K., Kvansakul, J., Barnes, N., Walker, J. G., Epp, S. B., Young, K. A., Ayton, L. N., Luu, C. D., Allen, P. J., & for the Bionics Institute and Centre for Eye Research Australia Retinal Prosthesis Consortium. (2021). A Second-Generation (44-Channel) Suprachoroidal Retinal Prosthesis: Interim Clinical Trial Results. *Translational Vision Science & Technology*, *10*(10), 12. https://doi.org/10.1167/tvst.10.10.12

Petrossians, A., Whalen Iii, J. J., Weiland, J. D., & Mansfeld, F. (2011). Electrodeposition and Characterization of Thin-Film Platinum-Iridium Alloys for Biological Interfaces. *Journal of The Electrochemical Society*, *158*(5), D269. https://doi.org/10.1149/1.3559477

Pezaris, J. S., & Eskandar, E. N. (2009). Getting signals into the brain: Visual prosthetics through thalamic microstimulation. *Neurosurgical Focus*, *27*(1), E6. https://doi.org/10.3171/2009.4.FOCUS0986

Pham, P., Roux, S., Matonti, F., Dupont, F., Agache, V., & Chavane, F. (2013). Post-implantation impedance spectroscopy of subretinal micro-electrode arrays, OCT imaging and numerical simulation: Towards a more precise neuroprosthesis monitoring tool. *Journal of Neural Engineering*, *10*(4), 046002. https://doi.org/10.1088/1741-2560/10/4/046002

Pierson, H. O. (1993). *Handbook of carbon, graphite, diamond, and fullerenes: Properties, processing, and applications*. Noyes Publications.

Piper, R. D., Lambert, G. A., & Duckworth, J. W. (1991). Cortical blood flow changes during spreading depression in cats. *American Journal of Physiology-Heart and Circulatory Physiology*, *261*(1), H96–H102. https://doi.org/10.1152/ajpheart.1991.261.1.H96

Piret, G., Hébert, C., Mazellier, J.-P., Rousseau, L., Scorsone, E., Cottance, M., Lissorgues, G., Heuschkel, M. O., Picaud, S., Bergonzo, P., & Yvert, B. (2015). 3D-nanostructured boron-doped diamond for microelectrode array neural interfacing. *Biomaterials*, *53*, 173–183. https://doi.org/10.1016/j.biomaterials.2015.02.021

Poland, C. A., Duffin, R., Kinloch, I., Maynard, A., Wallace, W. A. H., Seaton, A., Stone, V., Brown, S., MacNee, W., & Donaldson, K. (2008). Carbon nanotubes introduced into the abdominal cavity of mice show asbestos-like pathogenicity in a pilot study. *Nature Nanotechnology*, *3*(7), 423–428. https://doi.org/10.1038/nnano.2008.111

Polikov, V. S., Tresco, P. A., & Reichert, W. M. (2005). Response of brain tissue to chronically implanted neural electrodes. *Journal of Neuroscience Methods*, *148*(1), 1–18. https://doi.org/10.1016/j.jneumeth.2005.08.015

Prévot, P.-H., Gehere, K., Arcizet, F., Akolkar, H., Khoei, M. A., Blaize, K., Oubari, O., Daye, P., Lanoë, M., Valet, M., Dalouz, S., Langlois, P., Esposito, E., Forster, V., Dubus, E., Wattiez, N., Brazhnikova, E., Nouvel-Jaillard, C., LeMer, Y., … Picaud, S. (2019). Behavioural responses to a photovoltaic subretinal prosthesis implanted in non-human primates. *Nature Biomedical Engineering*, *4*(2), 172–180. https://doi.org/10.1038/s41551-019-0484-2

Provansal, M., Labernède, G., Joffrois, C., Rizkallah, A., Goulet, R., Valet, M., Deschamps, W., Ferrari, U., Chaffiol, A., Dalkara, D., Sahel, J. A., Tanter, M., Picaud, S., Gauvain, G., & Arcizet, F. (2021). Functional ultrasound imaging of the spreading activity following optogenetic stimulation of the rat visual cortex. *Scientific Reports*, *11*(1), 12603. https://doi.org/10.1038/s41598-021-91972-z

Purves, D. (Ed.). (2018). *Neuroscience* (Sixth edition). Oxford University Press.

Ratner, B. D. (2015). The Biocompatibility of Implant Materials. In *Host Response to Biomaterials* (pp. 37–51). Elsevier. https://doi.org/10.1016/B978-0-12-800196-7.00003-7

Reddy, D., Register, L. F., Carpenter, G. D., & Banerjee, S. K. (2011). Graphene field-effect transistors. *Journal of Physics D: Applied Physics*, *44*(31), 313001. https://doi.org/10.1088/0022-3727/44/31/313001

Ren, Y., Cong, F., Ristaniemi, T., Wang, Y., Li, X., & Zhang, R. (2019). Transient seizure onset network for localization of epileptogenic zone: Effective connectivity and graph theory-based analyses of ECoG data in temporal lobe epilepsy. *Journal of Neurology*, *266*(4), 844–859. https://doi.org/10.1007/s00415-019-09204-4

Renaudin, N., Demené, C., Dizeux, A., Ialy-Radio, N., Pezet, S., & Tanter, M. (2022). Functional ultrasound localization microscopy reveals brain-wide neurovascular activity on a microscopic scale. *Nature Methods*, *19*(8), 1004–1012. https://doi.org/10.1038/s41592-022-01549-5

Renz, A. F., Lee, J., Tybrandt, K., Brzezinski, M., Lorenzo, D. A., Cerra Cheraka, M., Lee, J., Helmchen, F., Vörös, J., & Lewis, C. M. (2020). Opto-E-Dura: A Soft, Stretchable ECoG Array for Multimodal, Multiscale Neuroscience. *Advanced Healthcare Materials*, *9*(17), 2000814. https://doi.org/10.1002/adhm.202000814

Rizzo, J. F. (2011). Update on Retinal Prosthetic Research: The Boston Retinal Implant Project. *Journal of Neuro-Ophthalmology*, *31*(2), 160–168. https://doi.org/10.1097/WNO.0b013e31821eb79e

Rodriguez, A., Meyerson, H., & Anderson, J. M. (2008). Quantitativein vivo cytokine analysis at synthetic biomaterial implant sites. *Journal of Biomedical Materials Research Part A*. https://doi.org/10.1002/jbm.a.31939

Roessler, G., Laube, T., Brockmann, C., Kirschkamp, T., Mazinani, B., Goertz, M., Koch, C., Krisch, I., Sellhaus, B., Trieu, H. K., Weis, J., Bornfeld, N., Röthgen, H., Messner, A., Mokwa, W., & Walter, P. (2009). Implantation and explantation of a wireless epiretinal retina implant device: Observations during the EPIRET3 prospective clinical trial. *Investigative Ophthalmology & Visual Science*, *50*(6), 3003–3008. https://doi.org/10.1167/iovs.08-2752

Rosenfeld, J. V., Wong, Y. T., Yan, E., Szlawski, J., Mohan, A., Clark, J., Rosa, M., & Lowery, A. (2020). Tissue response to a chronically implantable wireless, intracortical visual prosthesis (Gennaris array). *Journal of Neural Engineering*. https://doi.org/10.1088/1741-2552/ab9e1c

Sahel, J.-A., Boulanger-Scemama, E., Pagot, C., Arleo, A., Galluppi, F., Martel, J. N., Esposti, S. D., Delaux, A., De Saint Aubert, J.-B., De Montleau, C., Gutman, E., Audo, I., Duebel, J., Picaud, S., Dalkara, D., Blouin, L., Taiel, M., & Roska, B. (2021). Partial recovery of visual function in a blind patient after optogenetic therapy. *Nature Medicine*, *27*(7), 1223–1229. https://doi.org/10.1038/s41591-021-01351-4

Sakaguchi, H., Kamei, M., Fujikado, T., Yonezawa, E., Ozawa, M., Cecilia-Gonzalez, C., Ustariz-Gonzalez, O., Quiroz-Mercado, H., & Tano, Y. (2009). Artificial vision by direct optic nerve electrode (AV-DONE) implantation in a blind patient with retinitis pigmentosa. *Journal of Artificial Organs*, *12*(3), 206–209. https://doi.org/10.1007/s10047-009-0467-2

Salzmann, J. (2006). Subretinal electrode implantation in the P23H rat for chronic stimulations. *British Journal of Ophthalmology*, *90*(9), 1183–1187. https://doi.org/10.1136/bjo.2005.089110

Savage, J. C., Carrier, M., & Tremblay, M.-È. (2019). Morphology of Microglia Across Contexts of Health and Disease. In O. Garaschuk & A. Verkhratsky (Eds.), *Microglia* (Vol. 2034, pp. 13–26). Springer New York. https://doi.org/10.1007/978-1-4939-9658-2_2

Schaffrath, K., Lohmann, T., Seifert, J., Ingensiep, C., Raffelberg, P., Waschkowski, F., Viga, R., Kokozinski, R., Mokwa, W., Johnen, S., & Walter, P. (2021). New epiretinal implant with integrated sensor chips for optical capturing shows a good biocompatibility profile in vitro and in vivo. *BioMedical Engineering OnLine*, *20*(1), 102. https://doi.org/10.1186/s12938-021-00938-9

Schiavone, G., Kang, X., Fallegger, F., Gandar, J., Courtine, G., & Lacour, S. P. (2020). Guidelines to Study and Develop Soft Electrode Systems for Neural Stimulation. *Neuron*, *108*(2), 238–258. https://doi.org/10.1016/j.neuron.2020.10.010

Sekirnjak, C., Hottowy, P., Sher, A., Dabrowski, W., Litke, A. M., & Chichilnisky, E. J. (2006). Electrical Stimulation of Mammalian Retinal Ganglion Cells With Multielectrode Arrays. *Journal of Neurophysiology*, *95*(6), 3311–3327. https://doi.org/10.1152/jn.01168.2005

Seo, J.-M., Kim, S. J., Chung, H., Kim, E. T., Yu, H. G., & Yu, Y. S. (2004). Biocompatibility of polyimide microelectrode array for retinal stimulation. *Materials Science and Engineering: C*, *24*(1–2), 185–189. https://doi.org/10.1016/j.msec.2003.09.019

Shire, D. B., Kelly, S. K., Chen, J., Doyle, P., Gingerich, M. D., Cogan, S. F., Drohan, W. A., Mendoza, O., Theogarajan, L., Wyatt, J. L., & Rizzo, J. F. (2009). Development and Implantation of a Minimally Invasive Wireless Subretinal Neurostimulator. *IEEE Transactions on Biomedical Engineering*, *56*(10), 2502–2511. https://doi.org/10.1109/TBME.2009.2021401

Shire, D., Gingerich, M., Wong, P., Skvarla, M., Cogan, S., Chen, J., Wang, W., & Rizzo, J. (2020). Micro-Fabrication of Components for a High-Density Sub-Retinal Visual Prosthesis. *Micromachines*, *11*(10), 944. https://doi.org/10.3390/mi11100944

Shung, K. K., Sigelmann, R. A., & Reid, J. M. (1976). Scattering of Ultrasound by Blood. *IEEE Transactions on Biomedical Engineering*, *BME-23*(6), 460–467. https://doi.org/10.1109/TBME.1976.324604

Sieu, L.-A., Bergel, A., Tiran, E., Deffieux, T., Pernot, M., Gennisson, J.-L., Tanter, M., & Cohen, I. (2015). EEG and functional ultrasound imaging in mobile rats. *Nature Methods*, *12*(9), 831–834. https://doi.org/10.1038/nmeth.3506

Simon, R. P. (1985). Physiologic Consequences of Status Epilepticus. *Epilepsia*, *26*(s1), S58–S66. https://doi.org/10.1111/j.1528-1157.1985.tb05725.x

Skarpaas, T. L., Jarosiewicz, B., & Morrell, M. J. (2019). Brain-responsive neurostimulation for epilepsy (RNS® System). *Epilepsy Research*, *153*, 68–70. https://doi.org/10.1016/j.eplepsyres.2019.02.003

Slavcheva, E., Vitushinsky, R., Mokwa, W., & Schnakenberg, U. (2004). Sputtered Iridium Oxide Films as Charge Injection Material for Functional Electrostimulation. *Journal of The Electrochemical Society*, *151*(7), E226. https://doi.org/10.1149/1.1747881

Smith, J. M., Bradley, D. P., James, M. F., & Huang, C. L.-H. (2006). Physiological studies of cortical spreading depression. *Biological Reviews*, *81*(4), 457–481. https://doi.org/10.1017/S1464793106007081

Sofroniew, M. V., & Vinters, H. V. (2010). Astrocytes: Biology and pathology. *Acta Neuropathologica*, *119*(1), 7–35. https://doi.org/10.1007/s00401-009-0619-8

Sokolov, A. N., Roberts, M. E., & Bao, Z. (2009). Fabrication of low-cost electronic biosensors. *Materials Today*, *12*(9), 12–20. https://doi.org/10.1016/S1369-7021(09)70247-0

Soloukey, S., Vincent, A. J. P. E., Satoer, D. D., Mastik, F., Smits, M., Dirven, C. M. F., Strydis, C., Bosch, J. G., Van Der Steen, A. F. W., De Zeeuw, C. I., Koekkoek, S. K. E., & Kruizinga, P. (2020). Functional Ultrasound (fUS) During Awake Brain Surgery: The Clinical Potential of Intra-Operative Functional and Vascular Brain Mapping. *Frontiers in Neuroscience*, *13*, 1384. https://doi.org/10.3389/fnins.2019.01384

Somjen, G. G., Aitken, P. G., Czéh, G. L., Herrearas, O., Jing, J., & Young, J. N. (1992). Mechanisms of spreading depression: A review of recent findings and a hypothesis. *Canadian Journal of Physiology and Pharmacology*, *70*(S1), S248–S254. https://doi.org/10.1139/y92-268

Stafstrom, C. E., & Carmant, L. (2015). Seizures and Epilepsy: An Overview for Neuroscientists. *Cold Spring Harbor Perspectives in Medicine*, *5*(6), a022426–a022426. https://doi.org/10.1101/cshperspect.a022426

Steinmetz, J. D., Bourne, R. R. A., Briant, P. S., Flaxman, S. R., Taylor, H. R. B., Jonas, J. B., Abdoli, A. A., Abrha, W. A., Abualhasan, A., Abu-Gharbieh, E. G., Adal, T. G., Afshin, A., Ahmadieh, H., Alemayehu, W., Alemzadeh, S. A. S., Alfaar, A. S., Alipour, V., Androudi, S., Arabloo, J., … Vos, T. (2021). Causes of blindness and vision impairment in 2020 and trends over 30 years, and prevalence of avoidable blindness in relation to VISION 2020: The Right to Sight: an analysis for the Global Burden of Disease Study. *The Lancet Global Health*, *9*(2), e144–e160. https://doi.org/10.1016/S2214-109X(20)30489-7

Stence, N., Waite, M., & Dailey, M. E. (2001). Dynamics of microglial activation: A confocal time-lapse analysis in hippocampal slices. *Glia*, *33*(3), 256–266.

Stieglitz, T., Schuettler, M., Rubehn, B., Boretius, T., Badia, J., & Navarro, X. (2011). Evaluation of polyimide as substrate material for electrodes to interface the peripheral nervous system. *2011 5th International IEEE/EMBS Conference on Neural Engineering*, 529–533. https://doi.org/10.1109/NER.2011.5910602

Stingl, K., Bartz-Schmidt, K. U., Besch, D., Braun, A., Bruckmann, A., Gekeler, F., Greppmaier, U., Hipp, S., Hörtdörfer, G., Kernstock, C., Koitschev, A., Kusnyerik, A., Sachs, H., Schatz, A., Stingl, K. T., Peters, T., Wilhelm, B., & Zrenner, E. (2013). Artificial vision with wirelessly powered subretinal electronic implant alpha-IMS. *Proceedings of the Royal Society B: Biological Sciences*, *280*(1757), 20130077. https://doi.org/10.1098/rspb.2013.0077

Stone, J. L. (1992). Morphometric Analysis of Macular Photoreceptors and Ganglion Cells in Retinas With Retinitis Pigmentosa. *Archives of Ophthalmology*, *110*(11), 1634. https://doi.org/10.1001/archopht.1992.01080230134038

Strickland, E., & Harris, M. (2022, February 15). Their Bionic Eyes Are Now Obsolete and Unsupported. https://spectrum.ieee.org/bionic-eye-obsolete

Strong, A. J., Fabricius, M., Boutelle, M. G., Hibbins, S. J., Hopwood, S. E., Jones, R., Parkin, M. C., & Lauritzen, M. (2002). Spreading and Synchronous Depressions of Cortical Activity in Acutely Injured Human Brain. *Stroke*, *33*(12), 2738–2743. https://doi.org/10.1161/01.STR.0000043073.69602.09

Sun, Y., Lacour, S. P., Brooks, R. A., Rushton, N., Fawcett, J., & Cameron, R. E. (2009). Assessment of the biocompatibility of photosensitive polyimide for implantable medical device use. *Journal of Biomedical Materials Research Part A*, *90A*(3), 648–655. https://doi.org/10.1002/jbm.a.32125

Szarowski, D. H., Andersen, M. D., Retterer, S., Spence, A. J., Isaacson, M., Craighead, H. G., Turner, J. N., & Shain, W. (2003). Brain responses to micro-machined silicon devices. *Brain Research*, *983*(1–2), 23–35. https://doi.org/10.1016/S0006-8993(03)03023-3

Tabish, T. A., Pranjol, M. Z. I., Hayat, H., Rahat, A. A. M., Abdullah, T. M., Whatmore, J. L., & Zhang, S. (2017). *In vitro* toxic effects of reduced graphene oxide nanosheets on lung cancer cells. *Nanotechnology*, *28*(50), 504001. https://doi.org/10.1088/1361-6528/aa95a8

Tamim, I., Chung, D. Y., De Morais, A. L., Loonen, I. C. M., Qin, T., Misra, A., Schlunk, F., Endres, M., Schiff, S. J., & Ayata, C. (2021). Spreading depression as an innate antiseizure mechanism. *Nature Communications*, *12*(1), 2206. https://doi.org/10.1038/s41467-021-22464-x

Tang, L., Tsai, C., Gerberich, W. W., Kruckeberg, L., & Kania, D. R. (1995). Biocompatibility of chemical-vapour-deposited diamond. *Biomaterials*, *16*(6), 483–488. https://doi.org/10.1016/0142-9612(95)98822-V

Tanter, M., & Fink, M. (2014). Ultrafast imaging in biomedical ultrasound. *IEEE Transactions on Ultrasonics, Ferroelectrics, and Frequency Control*, *61*(1), 102–119. https://doi.org/10.1109/TUFFC.2014.2882

Tehovnik, E. J., & Slocum, W. M. (2007). Phosphene induction by microstimulation of macaque V1. *Brain Research Reviews*, *53*(2), 337–343. https://doi.org/10.1016/j.brainresrev.2006.11.001

Thalhammer, A., Edgington, R. J., Cingolani, L. A., Schoepfer, R., & Jackman, R. B. (2010). The use of nanodiamond monolayer coatings to promote the formation of functional neuronal networks. *Biomaterials*, *31*(8), 2097–2104. https://doi.org/10.1016/j.biomaterials.2009.11.109

Thorn, J. T., Chenais, N. A. L., Hinrichs, S., Chatelain, M., & Ghezzi, D. (2022). Virtual reality validation of naturalistic modulation strategies to counteract fading in retinal stimulation. *Journal of Neural Engineering*, *19*(2), 026016. https://doi.org/10.1088/1741-2552/ac5a5c

Thorn, J. T., Migliorini, E., & Ghezzi, D. (2020). Virtual reality simulation of epiretinal stimulation highlights the relevance of the visual angle in prosthetic vision. *Journal of Neural Engineering*, *17*(5), 056019. https://doi.org/10.1088/1741-2552/abb5bc

Turner, J. N., Shain, W., Szarowski, D. H., Andersen, M., Martins, S., Isaacson, M., & Craighead, H. (1999). Cerebral Astrocyte Response to Micromachined Silicon Implants. *Experimental Neurology*, *156*(1), 33–49. https://doi.org/10.1006/exnr.1998.6983

Vassanelli, S., & Fromherz, P. (1998). Transistor records of excitable neurons from rat brain. *Applied Physics A: Materials Science & Processing*, *66*(4), 459–463. https://doi.org/10.1007/s003390050695

Vera-González, A. (2022). Pathophysiological Mechanisms Underlying the Etiologies of Seizures and Epilepsy. In Department of Pathophysiology, Medical University of Lublin, Lublin, Poland & S. J. Czuczwar (Eds.), *Epilepsy*. Exon Publications. https://doi.org/10.36255/exon-publications-epilepsy-pathopysiology

Viana, D., Walston, S. T., Illa, X., Valle, J. del, Hayward, A., Dodd, A., Loret, T., Prats-Alfonso, E., Oliva, N. de la, Palma, M., Corro, E. del, Rodríguez-Meana, B., Bernicola, M. del P., Rodríguez-Lucas, E., Gener, T. A., Cruz, J. M. de la, Torres-Miranda, M., Duvan, F. T., Ria, N., … Garrido, J. A. (2022). *Graphene-based thin film microelectrode technology for in vivo high resolution neural recording and stimulation* (p. 2022.11.16.515761). bioRxiv. https://doi.org/10.1101/2022.11.16.515761

Vomero, M., Castagnola, E., Maggiolini, E., Ciarpella, F., Rembado, I., Goshi, N., Fadiga, L., Kassegne, S., & Ricci, D. (2016). *A Direct Comparison of Glassy Carbon and PEDOT-PSS Electrodes for High Charge Injection and Low Impedance Neural Interfaces*. 68–76. https://doi.org/10.4028/www.scientific.net/AST.102.68

Walter, P., Kisva´rday, Z. F., Go¨rtz, M., Alteheld, N., Rossler, G., Stieglitz, T., & Eysel, U. T. (2005). Cortical Activation Via an Implanted Wireless Retinal Prosthesis. *Investigative Opthalmology & Visual Science*, *46*(5), 1780. https://doi.org/10.1167/iovs.04-0924

Walton, F., Cerezo-Sanchez, M., McGlynn, E., Das, R., & Heidari, H. (2022). Cleanroom strategies for micro- and nano-fabricating flexible implantable neural electronics. *Philosophical Transactions of the Royal Society A: Mathematical, Physical and Engineering Sciences*, *380*(2228), 20210009. https://doi.org/10.1098/rsta.2021.0009

Wang, B.-Y., Chen, Z. C., Bhuckory, M., Huang, T., Shin, A., Zuckerman, V., Ho, E., Rosenfeld, E., Galambos, L., Kamins, T., Mathieson, K., & Palanker, D. (2022). Electronic photoreceptors enable prosthetic visual acuity matching the natural resolution in rats. *Nature Communications*, *13*(1), 6627. https://doi.org/10.1038/s41467-022-34353-y

Waschkowski, F., Hesse, S., Rieck, A. C., Lohmann, T., Brockmann, C., Laube, T., Bornfeld, N., Thumann, G., Walter, P., Mokwa, W., Johnen, S., & Roessler, G. (2014). Development of very large electrode arrays for epiretinal stimulation (VLARS). *BioMedical Engineering OnLine*, *13*(1), 11. https://doi.org/10.1186/1475-925X-13-11

Watanabe, T., Kobayashi, R., Komiya, K., Fukushima, T., Tomita, H., Sugano, E., Kurino, H., Tanaka, T., Tamai, M., & Koyanagi, M. (2007). Evaluation of Platinum-Black Stimulus Electrode Array for Electrical Stimulation of Retinal Cells in Retinal Prosthesis System. *Japanese Journal of Applied Physics*, *46*(4B), 2785–2791. https://doi.org/10.1143/JJAP.46.2785

Watson, B. D., Dietrich, W. D., Busto, R., Wachtel, M. S., & Ginsberg, M. D. (1985). Induction of reproducible brain infarction by photochemically initiated thrombosis. *Annals of Neurology*, *17*(5), 497–504. https://doi.org/10.1002/ana.410170513

Wei, Z., Gordon, C. R., Bergey, G. K., Sacks, J. M., & Anderson, W. S. (2016). Implant Site Infection and Bone Flap Osteomyelitis Associated with the NeuroPace Responsive Neurostimulation System. *World Neurosurgery*, *88*, 687.e1-687.e6. https://doi.org/10.1016/j.wneu.2015.11.106

Weiland, J. D., Anderson, D. J., & Humayun, M. S. (2002). In vitro electrical properties for iridium oxide versus titanium nitride stimulating electrodes. *IEEE Transactions on Biomedical Engineering*, *49*(12), 1574–1579. https://doi.org/10.1109/TBME.2002.805487

WHO. (2023, August 10). *Blindness and vision impairment*. https://www.who.int/news-room/fact-sheets/detail/blindness-and-visual-impairment

Wolpaw, J. R., Millán, J. D. R., & Ramsey, N. F. (2020). Brain-computer interfaces: Definitions and principles. In *Handbook of Clinical Neurology* (Vol. 168, pp. 15–23). Elsevier. https://doi.org/10.1016/B978-0-444-63934-9.00002-0

Woods, G. A., Rommelfanger, N. J., & Hong, G. (2020). Bioinspired Materials for In Vivo Bioelectronic Neural Interfaces. *Matter*, *3*(4), 1087–1113. https://doi.org/10.1016/j.matt.2020.08.002

Wykes, Rob. C., Masvidal-Codina, E., Guimerà-Brunet, A., & Garrido, Jose. A. (2022). The advantages of mapping slow brain potentials using DC-coupled graphene micro-transistors: Clinical and translational applications. *Clinical and Translational Medicine*, *12*(7). https://doi.org/10.1002/ctm2.968

Yang, K.-H., & Narayan, R. J. (2019). Biocompatibility and functionalization of diamond for neural applications. *Current Opinion in Biomedical Engineering*, *10*, 60–68. https://doi.org/10.1016/j.cobme.2019.03.002

Yanovitch, L., Raz-Prag, D., & Hanein, Y. (2022). *A new high-resolution three-dimensional retinal implant:* System design and preliminary human results [Preprint]. Bioengineering. https://doi.org/10.1101/2022.09.14.507901

You, Y., Klistorner, A., Thie, J., & Graham, S. L. (2011). Improving reproducibility of VEP recording in rats: Electrodes, stimulus source and peak analysis. *Documenta Ophthalmologica*, *123*(2), 109. https://doi.org/10.1007/s10633-011-9288-8

Yue, L., Weiland, J. D., Roska, B., & Humayun, M. S. (2016). Retinal stimulation strategies to restore vision: Fundamentals and systems. *Progress in Retinal and Eye Research*, *53*, 21–47. https://doi.org/10.1016/j.preteyeres.2016.05.002

Zakharov, A., Chernova, K., Burkhanova, G., Holmes, G. L., & Khazipov, R. (2019). Segregation of seizures and spreading depolarization across cortical layers. *Epilepsia*, *60*(12), 2386–2397. https://doi.org/10.1111/epi.16390

Zhang, M., Tang, Z., Liu, X., & Van Der Spiegel, J. (2020). Electronic neural interfaces. *Nature Electronics*, *3*(4), 191–200. https://doi.org/10.1038/s41928-020-0390-3

Zhang, X., Levy, D., Kainz, V., Noseda, R., Jakubowski, M., & Burstein, R. (2011). Activation of central trigeminovascular neurons by cortical spreading depression. *Annals of Neurology*, *69*(5), 855–865. https://doi.org/10.1002/ana.22329

Zhao, M., Suh, M., Ma, H., Perry, C., Geneslaw, A., & Schwartz, T. H. (2007). Focal Increases in Perfusion and Decreases in Hemoglobin Oxygenation Precede Seizure Onset in Spontaneous Human Epilepsy. *Epilepsia*, *48*(11), 2059–2067. https://doi.org/10.1111/j.1528-1167.2007.01229.x

Zrenner, E., Bartz-Schmidt, K. U., Benav, H., Besch, D., Bruckmann, A., Gabel, V.-P., Gekeler, F., Greppmaier, U., Harscher, A., Kibbel, S., Koch, J., Kusnyerik, A., Peters, T., Stingl, K., Sachs, H., Stett, A., Szurman, P., Wilhelm, B., & Wilke, R. (2011). Subretinal electronic chips allow blind patients to read letters and combine them to words. *Proceedings of the Royal Society B: Biological Sciences*, *278*(1711), 1489–1497. https://doi.org/10.1098/rspb.2010.1747

Zrenner, E., Bartz-Schmidt, K. U., Besch, D., Gekeler, F., Koitschev, A., Sachs, H. G., & Stingl, K. (2017). The Subretinal Implant ALPHA: Implantation and Functional Results. In V. P. Gabel (Ed.), *Artificial Vision* (pp. 65–83). Springer International Publishing. https://doi.org/10.1007/978-3-319-41876-6_6